PHD

Photonic microcells for quantum optics applications

Light, Philip

Award date:
2008

Awarding institution:
University of Bath

Photonic Microcells for Quantum Optics Applications

Philip Stephen Light

A thesis submitted for the degree of Doctor of Philosophy

University of Bath

Department of Physics

May 2008

Abstract

This thesis presents the development of photonic microcells for use as the host for coherent optics phenomena and related applications. A photonic microcell consists of a length of hollow-core photonic crystal fibre (HC-PCF) with a gas-filled core that is spliced to conventional optical fibre at either end to seal the gas within the fibre.

Towards the goal of demonstrating and assessing the coherence properties of quantum optical effects in photonic microcells, the fabrication of two types of HC-PCF is presented. The established photonic bandgap HC-PCF offers extremely low transmission loss of ~10 dB/km over kilometre distances. However, the fibre has a limited transmission bandwidth of ~50 THz and exhibits modal coupling unfavourable for many applications. Work is presented on the tailoring of this fibre by control and shaping of the core-surround in order to improve its modal properties. A second type of HC-PCF is based on a large-pitch lattice, whose guidance relies on a new mechanism. This fibre exhibits a much improved bandwidth (>1000 THz) and has a relatively higher but still practical loss of ~1 dB/m.

The development of photonic microcells at microbar pressure level and with low optical insertion loss is shown, an important step in the improvement of the technology for coherent optics applications which will take advantage of the extreme gas-laser interaction efficiency achieved in HC-PCF.

Finally, quantum optical effects are demonstrated in HC-PCF and photonic microcells loaded with both the molecular gas acetylene and atomic vapour rubidium. The observation of electromagnetically induced transparency (EIT) in acetylene-filled HC-PCF represents the first such observation in a molecular gas, while the use of a photonic microcell allows a comparison of many experimental configurations to explore the coherence properties of coherent optical systems in the core of a HC-PCF. Furthermore, EIT is observed unambiguously in a rubidium loaded HC-PCF for the first time, and the anti-relaxation effects of a polymer coating demonstrated in this configuration.

Preface

Since the fabrication of the first hollow-core photonic crystal fibre (HC-PCF) there has been extensive work on its development for many applications, including the optimisation of transmission loss with the aim to eventually replace conventional optical fibre in telecommunications systems. Among the applications of HC-PCF there is one use that stands out from the rest: as a host for extremely efficient light-matter interaction. F. Benabid proposed that gas or vapour loaded HC-PCF could be a compact and effective host for coherent optical effects.

HC-PCF is a silica optical fibre consisting of a hollow core surrounded by hundreds of micrometre scale air-holes running the entire length of the fibre, forming a photonic crystal structure and confining light to the core. Chapter 1 is an introduction to this type of optical fibre and provides details of its design, guidance mechanism and use for gas-laser interaction. The ability of HC-PCF to provide efficient light-matter interaction is the result of two main properties of the fibre: its tight confinement of light to the micrometre scale hollow-core and its low optical transmission loss, allowing the tight confinement to be maintained over kilometre lengths.

The fabrication methods of HC-PCF are detailed in Chapter 2, which also details the important linear characteristics of the fibre. A detailed look is taken at the effect of surface modes, or modes guided at the silica core interface, on the modal properties of the core modes. This is an important factor when considering the use of HC-PCF for metrology applications. Finally, Chapter 2 presents a method for tailoring the modal properties of drawn fibres through shaping of the core through chemical etching.

The benefits and limitations of using HC-PCF as a host for quantum optics are discussed in Chapter 3, which first provides an overview of quantum optical effects that will be seen experimentally in later chapters. This chapter considers the effect of the small diameter of the fibre core and large aspect ratio of the core compared with typical experimental configurations used for observing quantum optical effects.

The main body of this thesis is comprised of three chapters. Chapter 4 introduces the concept of the photonic microcell, an all-fibre gas-cell device. A photonic microcell

consists of a length of hollow-core photonic crystal fibre with gas-filled core, joined at each end to conventional optical fibre, thereby sealing the gas within the core. Photonic microcells are compact and extremely efficient devices for gas-laser interaction, which in addition are compatible with existing optical fibre systems. The development of the original technique for producing high-pressure microcells into a technique capable of achieving vacuum pressure cells with low insertion loss is presented.

Chapter 5 presents the results of the observation of electromagnetically induced transparency (EIT) in the molecular gas acetylene, initially within HC-PCF attached to bulky gas chambers, and later in a compact low-pressure photonic microcell. This represents the first observation of EIT in a molecular gas, unseen before due to the small transitional dipole-moments compared with those of atomic vapours, and made possible by the efficient gas-laser interaction within HC-PCF. This chapter presents a detailed study of acetylene EIT in four distinct experimental configurations, including the use of counter-propagating coupling and probe beams in which EIT has not been reported before due to the unfavourable Doppler shifts and resulting two-photon detuning. The results obtained are used to evaluate the sources of decoherence within a quantum optics system in a HC-PCF host.

The work on EIT in HC-PCF is extended from molecular gases to the atomic vapour of rubidium in Chapter 6. Atomic vapours are conventionally the medium of choice for quantum optics phenomena for many reasons, but the loading of HC-PCF with atomic vapours represents a significant challenge due to their highly reactive nature. Importantly it is shown that a technique is available to overcome one of the drawbacks of using HC-PCF as a host, namely the high rate of atomic collisions with the silica fibre core wall due to the micrometre scale diameter of the core.

The final chapter of this thesis presents a summary of the work and the suitability of photonic microcells for quantum optics applications, together with planned future work to further improve on the developments presented here.

Acknowledgements

First and foremost I would like to thank Dr. Fetah Benabid for providing guidance and support, and being an invaluable supervisor during the past three years. I am fortunate to have had such a great mentor throughout my time here at the University of Bath.

I would like to thank Philip St. J. Russell for the opportunity to do a PhD within the then Photonics and Photonic Materials Group. Without this offer I would not have been able to commence this research.

I also thank the many members of the Department of Physics at the University of Bath who have contributed in numerous ways. Foremost, I would like to thank my colleague François Couny who embarked on his PhD at the same time as me and with whom I worked on several projects. As well as being a great friend, François has provided invaluable input into many aspects of this thesis. I thank Prof. David Bird for many useful discussions on theoretical parts of this work. I would also like to acknowledge the work of Natalie Wheeler and Yingying Wang, two of our newer students, with whom I worked on some aspects of this work. I would like to thank Alan George, Wendy Lambson and Steve Renshaw for technical support in their various fields.

In addition to those at the university, I acknowledge Dr. P. John Roberts who not only performed much of the fibre modelling work presented in this thesis, but also provided critical assessment of experimental results.

Finally, I would like to thank my family for believing in me. I am grateful for their constant support and encouragement.

This thesis is dedicated to Tuan who I thank for his support, encouragement and patience over the past three years.

Table of Contents

Table of Figures

Table of Tables

Definition of Symbols

β	Axial component of wavevector k
c	Speed of light in a vacuum
h	Planck's constant
$\hbar$	Reduced Planck's constant ($h/2\pi$)
k	Wavevector, $1/\lambda$
k_B	Boltzmann constant
$k\Lambda$	Normalised frequency
Λ	Fibre cladding pitch
λ	Wavelength Mean-free-path
μ	Transitional dipole moment Kinematic viscosity
n	Refractive index
n_{eff}	Effective refractive index
r_0	Bore radius or fibre core radius

Abbreviations

DOPS	Density of photonic states
ECDL	Extended cavity diode laser
EIT	Electromagnetically induced transparency
HC-PCF	Hollow-core photonic crystal fibre
PBG	Photonic bandgap
PCF	Photonic crystal fibre
SA	Saturated absorption

Chapter 1

Hollow Waveguides

This chapter provides an overview of the requirement for hollow waveguides and their applications. The various manifestations of such waveguides are introduced, with particular attention to the guidance mechanism of photonic bandgap fibre.

The much enhanced gas-laser interactions made possible by hollow-core photonic crystal fibre, exploited experimentally in later chapters, are introduced.

1.1 Light Guidance in Air

Optical fibres provide the ability to guide light in a confined manner over length scales of many kilometres, through a glass material. Guiding light in a similar way, but confined to an air core, has proved to be a significant challenge. Total internal reflection, the effect that allows low-loss guidance in conventional optical fibre, cannot be used to confine light in air or vacuum. Although several methods have been attempted to guide light in air, it is the advent of hollow-core photonic crystal fibre that has finally made the confined low-loss guidance of light in air possible.

The ability to guide light in air overcomes limitations of the silica host of conventional optical fibres, as well as opening up a whole new area of investigation made possible by guidance of light through gaseous and liquid media on kilometre length scales.

The motivation for the ability to guide light in a hollow waveguide takes several forms. From a telecommunications perspective, the main limiting factor in the transmission performance of conventional optical fibre is the loss via Rayleigh scattering within the doped silica that such fibres are made from. Although reductions in this scattering that have been achieved by lowering draw temperature and changing the doping agent [1], Rayleigh scattering provides a fundamental, and not purely technical, limit. Today's state-of-the-art optical fibre has reached this fundamental limit, which is due to density fluctuations within the doped silica. In addition, guidance in silica also places limitations

on usable wavelength ranges due to material absorption, particularly below 0.4 μm in the UV and beyond 3 μm in the mid-infrared.

Guiding light in air or a vacuum, on the other hand, removes these limitations. Rayleigh scattering will be dramatically reduced together with material absorption, potentially allowing lower-loss guidance over a broader spectral range. A further advantage of air-guidance is for delivery of high optical power to confined spaces. Conventional optical fibres are limited in power that can be transmitted by heating of the fibre due to small but significant material absorption. Here, again, guiding light in air or vacuum would be an excellent solution.

Further motivation for hollow waveguides comes from the ability to fill the void with gaseous or liquid media. If the light is tightly confined in the waveguide, high intensities can be achieved even at relatively low powers; if the attenuation is low, effective interaction between light and the medium in the waveguide may occur over many metres or kilometres. It is this ability that provides the motivation for the work presented in this thesis: hollow-core photonic crystal fibre (HC-PCF) provides the ability to guide light in a confined manner in a hollow gas-filled core over distances of many kilometres, for quantum optics and many other applications.

This section discusses the historical attempts at achieving the goal of confined guidance of light in air, leading to the development of hollow-core photonic crystal fibre. Later in the chapter, section 1.2 introduces different types of HC-PCF and their wave-guiding mechanisms. In section 1.3 the exceptional light-matter interaction properties provided by HC-PCF are discussed in detail.

1.1.1 Hollow Capillaries

The development of the laser in early 1960s led to much interest in guided propagation of light. Among the earliest proposed waveguides were the hollow-metal and dielectric tube waveguides. These waveguides had been successfully used at microwave wavelengths, but due to metal being a poor conductor at optical frequencies the theory developed for these waveguides was not valid in the optical domain. Marcatili developed a theory applicable to such waveguides in the optical domain [2].

The lowest loss mode for a 1 mm core diameter silica waveguide, the EH_{11} mode, was shown to have a 1.85 dB/km loss at a wavelength of 1.0 μm. This figure was however found to be extremely sensitive to bending of the waveguide, with a bend radius of just 10 *kilometres* calculated to double the loss. Furthermore, the difficulty in coupling light efficiently to the low-loss mode in a waveguide of such large diameter makes such a

waveguide impractical. Using a smaller diameter capillary improved the coupling, but the waveguide loss for a hollow-dielectric waveguide scales as λ^2/r_0^3 and the loss therefore increases dramatically as the core radius is reduced. For a 10 μm core the calculated loss is ~1 dB *per millimetre*, even before considering bend loss. Here λ is wavelength of light, and r_0

1.1.2 Bragg Reflection Waveguides

Yeh and Yariv showed that in principle lossless guidance is possible in a low index slab bounded by periodic layers of alternative higher refractive index, as shown in Figure 1-1 [3]. In this structure light is confined to the central region of index n_g, bound by alternating planes of high index (n_2) and low index (n_1) media. The relationship between the refractive indices is thus $n_g < n_1 < n_2$. Although Yeh and Yariv were first to suggest a hollow Bragg-reflection waveguide, the use of planar Bragg reflectors was at the time already commonplace in distributed feedback and distributed Bragg reflection lasers.

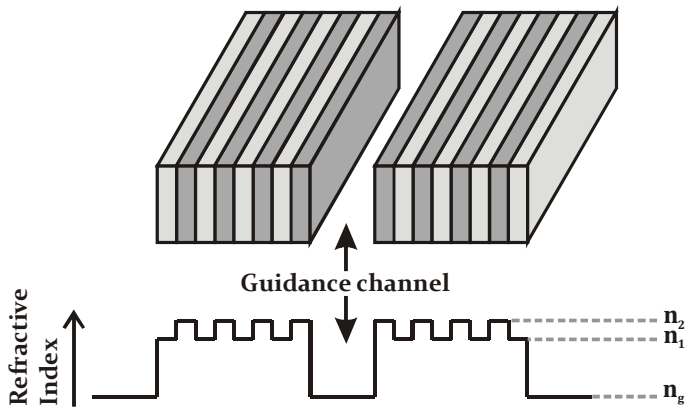

Figure 1-1: *Schematic of a slab Bragg reflection waveguide (top) and its refractive index profile (bottom). In this structure light can be guided in the central low index channel.*

Neglecting material absorption, a waveguide of this type formed with an infinite number of periodic layers would be expected to provide lossless guidance, but due to the rapid evanescent decay of the field through the periodic layers the number of layers required to provide a good approximation is small. It has been shown that the optimal layer thickness, obtaining the minimum loss for a given number of layers, is one-quarter of a wavelength [4].

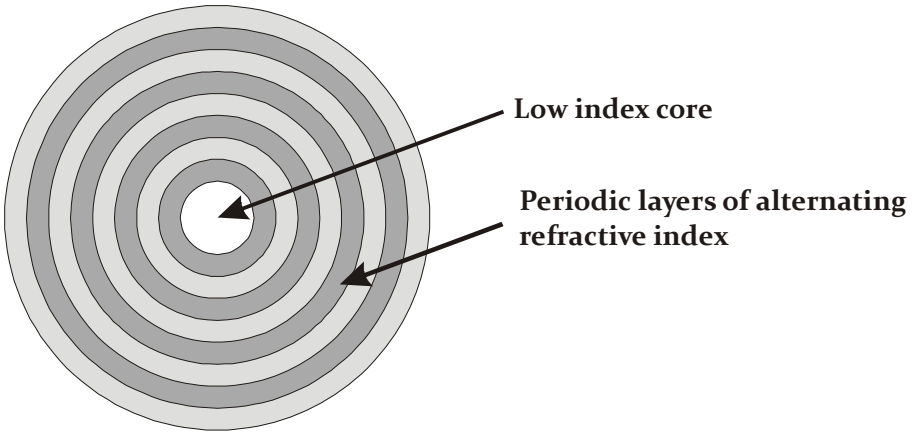

Figure 1-2: *Diagram of a Bragg-reflector type optical fibre. This fibre consists of a low-index core (white), and alternating layers of higher but different refractive index.*

The same authors also extended the theory to a radially symmetric Bragg reflector structure, or Bragg fibre [5], illustrated in Figure 1-2, showing that such a structure should provide guidance similar to the periodic slab waveguide. The results, obtained using a transfer matrix technique, were however inconclusive in determining the optimal refractive indices and pitches (or layer thicknesses) required to achieve low-loss guidance.

With the advent of the photonic bandgap concept, the early proposals of Yeh were revisited by Fink et al. [6] who designed and fabricated a short (10 cm) multimode cylindrical Bragg guide operating at a central wavelength of 10 μm. The guide was formed by alternating layers of tellurium and polystyrene deposited on the inside of a ~2 mm silica tube. The layers were calculated to provide 100% reflection for a broad wavelength range at normal incidence, and better than 90% reflection over a similar range at grazing incidence. Transmission of 80% was obtained across a 2 μm bandwidth with a 90° bend in the 10 cm waveguide.

Due to the very weak dependence of reflection on incidence angle, the Bragg reflection waveguide fabricated by Fink et al. was termed 'OmniGuide.' This class of waveguide was theoretically studied in detail by Johnson et al. [7], and there is now a wealth of varied theoretical work on OmniGuide waveguides. Experimental work is more limited, and mainly concentrated on guidance in the mid-infrared. Omniguide fibres with an attenuation ~1 dB/m have been demonstrated at 10.6 μm [8], with higher losses of ~5 dB/m in the near-infrared [9] in several-metre-long lengths of fibre.

1.2 Hollow-Core Photonic Crystal Fibre

The hollow-waveguide that has attracted the most interest over the past ten years, and that used in the experimental work in this thesis, is hollow-core photonic crystal fibre (HC-PCF). This fibre consists of a hollow-core, surrounded by a periodic two-dimensional photonic crystal cladding, as shown schematically in Figure 1-3. The ability of the structure to confine and guide light was proposed by Russell in 1991 [10], and later demonstrated theoretically by Birks et al. [11]. While the existence of in-plane photonic bandgaps (PBGs) in photonic crystal structures was well known and substantially investigated [12, 13], through HC-PCF Birks et al. introduced the concept of out-of-plane PBGs (see section 1.2.1 below).

There are in fact two distinct classes of HC-PCF, and these will be treated separately in the following sub-sections. The first of these is photonic bandgap (PBG) HC-PCF introduced above, in which the cladding structure provides a photonic bandgap. These fibres exhibit very low loss but limited bandwidth guidance, and the guidance properties of these fibres will be considered in section 1.2.1.

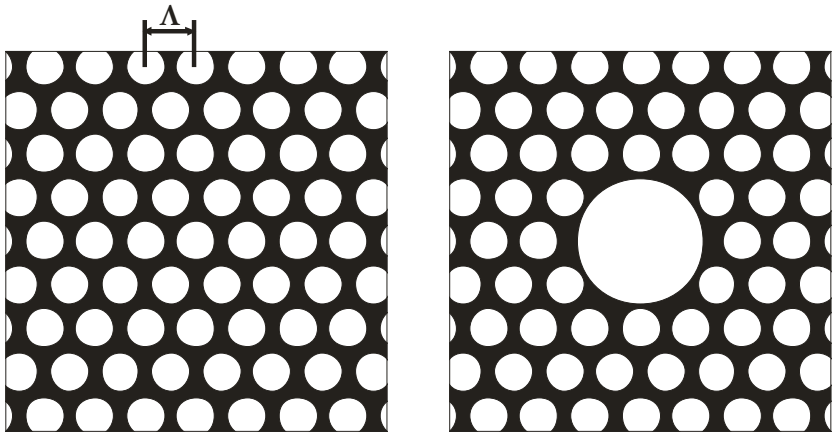

Figure 1-3: *A two-dimensional photonic crystal structure (left). The introduction of a defect to the structure (right) leads to the formation of guided modes within the defect. This example consists of air holes (white) in a silica background (dark grey). The introduced defect is an air hole of larger diameter than those forming the periodic structure. The hole-to-hole spacing Λ is termed the pitch of the fibre.*

The second class of HC-PCF has a photonic crystal cladding that does not possess a photonic bandgap at the guidance wavelengths. This class of HC-PCF was first reported by Benabid et al. [14] in 2002. This fibre provides broadband guidance (over the visible and near-infrared) with relatively low attenuation, and comparable to that of PBG

HC-PCF at short wavelengths. The guidance of this class of fibre is due to inhibited coupling between cladding and core modes [15], and will be explored in section 1.2.2.

1.2.1 Photonic Bandgap HC-PCF

Here we consider the guidance of the class of HC-PCF that rely on the formation of an out-of-plane photonic bandgap in the photonic crystal cladding structure; the existence of such bandgaps in a silica/air structure was theoretically demonstrated by Birks et al. in 1995 [11]. The term out-of-plane refers to the presence of a photonic bandgap for wave-vectors k with a non-zero component β in the non-periodicity plane. Two cladding structures of bandgap HC-PCF fibre, fabricated by the author, are shown in Figure 1-4; the triangular structure is the standard cladding structure of HC-PCF, with identical holes sizes throughout the structure. The double-period fibre has a cladding structure with two hole dimensions achieved by stacking capillaries of identical outer diameter but with two different inner diameters (see Chapter 2 for fabrication details).

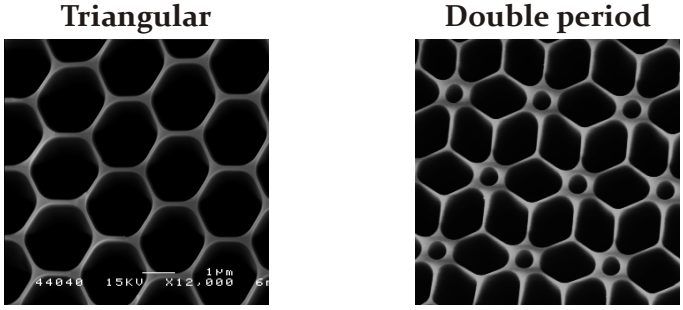

Figure 1-4: *Electron micrographs of two types of bandgap HC-PCF fibre. Left: standard triangular stack with interstitial rods for low loss HC-PCF. Right: 'double-period' fibre, using two thicknesses of capillary.*

The location of photonic bandgaps for a given periodic structure is illustrated in a plot of density of photonic states (DOPS). The DOPS is typically plotted against both normalised frequency[1] ($k\Lambda$) and normalised axial wave-vector ($\beta\Lambda$) or effective refractive index (n_{eff})[2]. The schematic diagram in Figure 1-5 illustrates the position of full photonic bandgaps (black regions). The diagonal lines in this figure mark the boundary between allowed and forbidden propagation in a particular medium; below the line the axial wave-number is greater than the free-space wave-number and therefore

[1] Although $k\Lambda$ is the normalised wavevector, it is usually referred to as normalised frequency since $k\Lambda = (\omega/c)\Lambda$ and is thus directly proportional to frequency.

[2] The effective index is given by the ratio between the axial component of the wavevector and the free-space wavevector, i.e. $n_{\text{eff}} = \beta/k$.

propagation is forbidden. The vacuum line is given by $\omega = ck$ (or equivalently $\beta = k$), and the silica line with a dependence on the refractive index of silica by $\omega = \frac{ck}{n_{SiO_2}}$ (or $\beta = n_{SiO_2}k$). It can be seen that the photonic bandgaps extend into the white region, where propagation is allowed in air ($k\Lambda \geq \beta\Lambda$). It is in these regions that band-gap guidance in a hollow-core is possible; light is free to propagate in the air core, but unable to escape into the cladding since there are no supported photonic states.

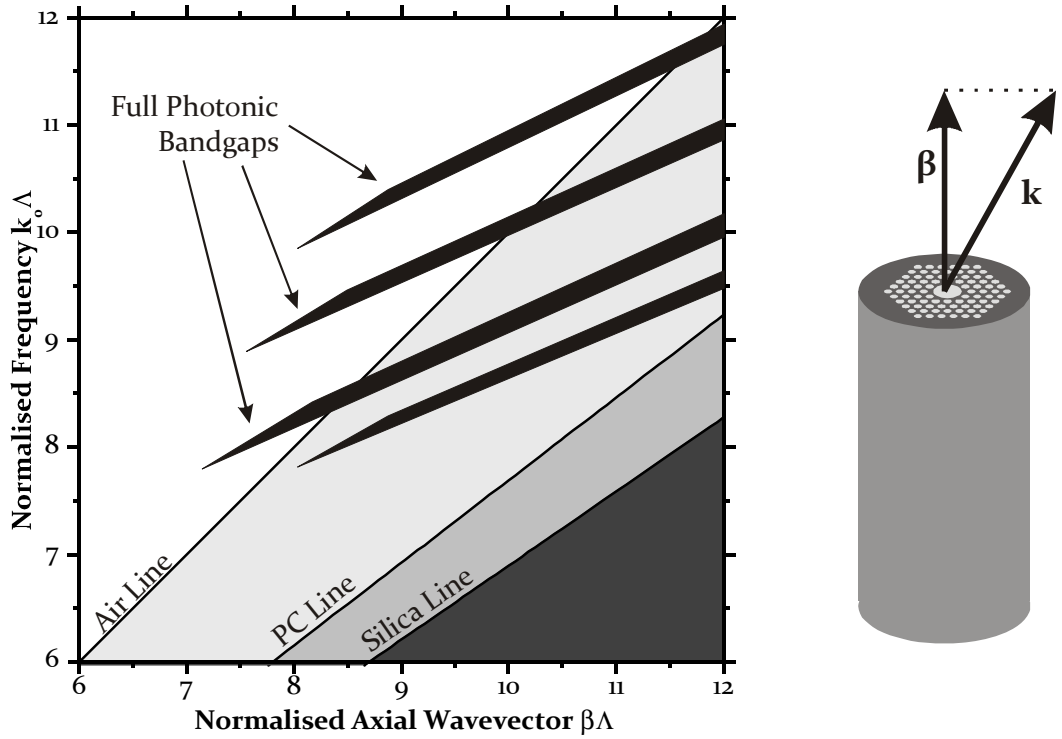

Figure 1-5: *Left: A band-edge diagram or 'finger-plot' illustrating the position of photonic bandgaps in terms of normalised frequency and normalised wavevector. The diagonal 'light-lines' are a boundary below which light is evanescent and is unable propagate in the respective medium. Right: Indication of wavevector k and the axial component of the wavevector, β.*

Examples of numerically calculated DOPS plots are shown in Figure 1-6[3]. The grey-scale is linear from black representing a minimum of photonic states, to white for a maximum of states. For clarity, regions with zero photonic states are hatched; this shows the location of the bandgap. Normalised frequency is plotted against $(\beta - k)\Lambda$, such that the air-line is horizontal as indicated in the plots.

[3] The DOPS was calculated using the plane wave expansion method using code developed by T. Hedley, G. J. Pearce and D. Bird.

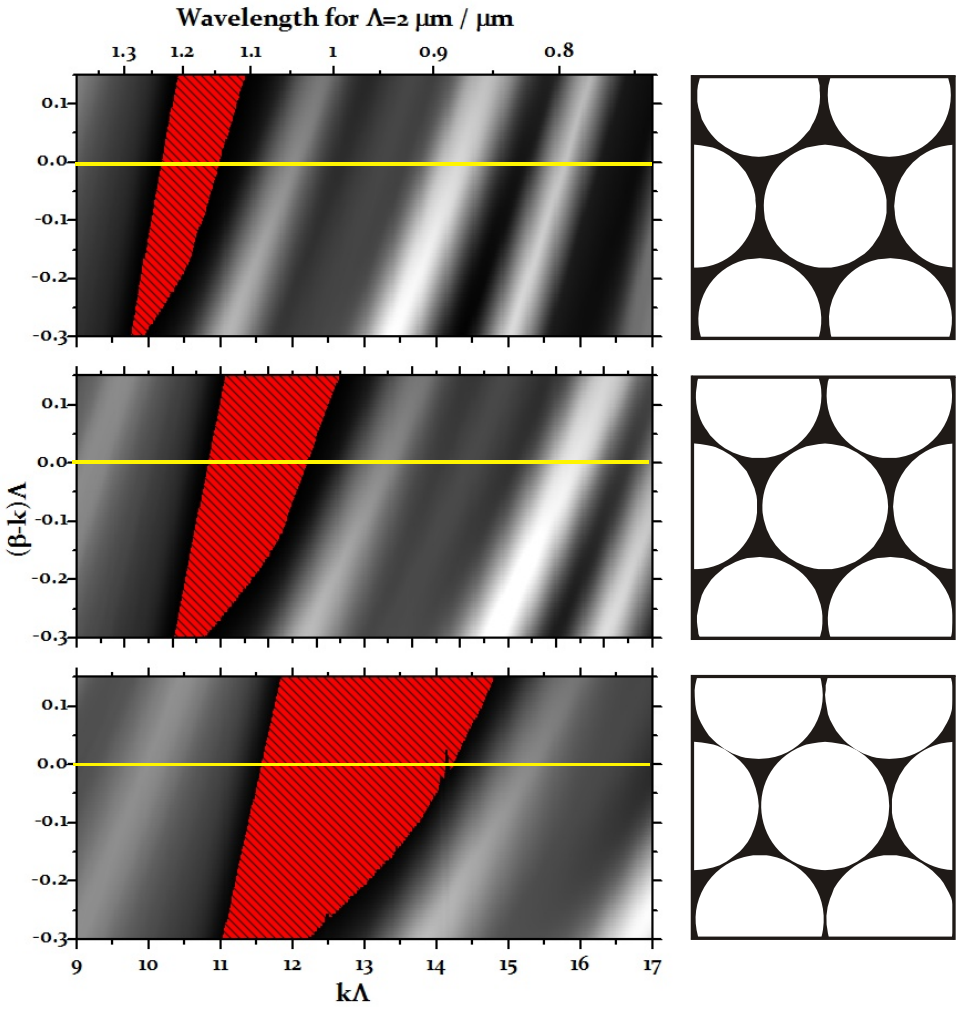

Figure 1-6: *Density of photonic states plots for the three cladding structures, with ratio of hole diameter to pitch of 0.94, 0.96 and 0.98 from top-to-bottom. The grey-scale represents the density-of-states from low (black) to high (white); zero density is highlighted by the red hatched regions, and shows the bandgap of the fibre. The yellow-line is the air-line, $\beta = k$. As a guide, a wavelength scale for a 2 μm pitch is given at the top of the figure.*

The plots in this figure are calculated for a simple triangular lattice photonic crystal, formed by identical circular air-holes in a silica background. The three plots correspond to a ratio between hole diameter and pitch (d/Λ) of 0.94, 0.96 and 0.98 respectively. The code used to perform these calculations is based on the plane wave expansion method [16].

For this structure the width of the bandgap as a function of air-filling fraction ($\pi[d/\Lambda]^2/2\sqrt{3}$) is shown in Figure 1-7; for an air-filling fraction of 88%, for example, a bandwidth of 14 THz is expected. The bandwidth displays an exponential dependence on air-filling fraction, which has recently been elucidated theoretically through the development of a

photonic model akin to the solid state tight-binding model [17]. This model will be introduced later in the section.

Although extremely large bandwidth would be obtained for very high air-filling fraction, the making of fibre with large air-filling fraction is difficult. The fabrication process for HC-PCF will be explained in Chapter 2.

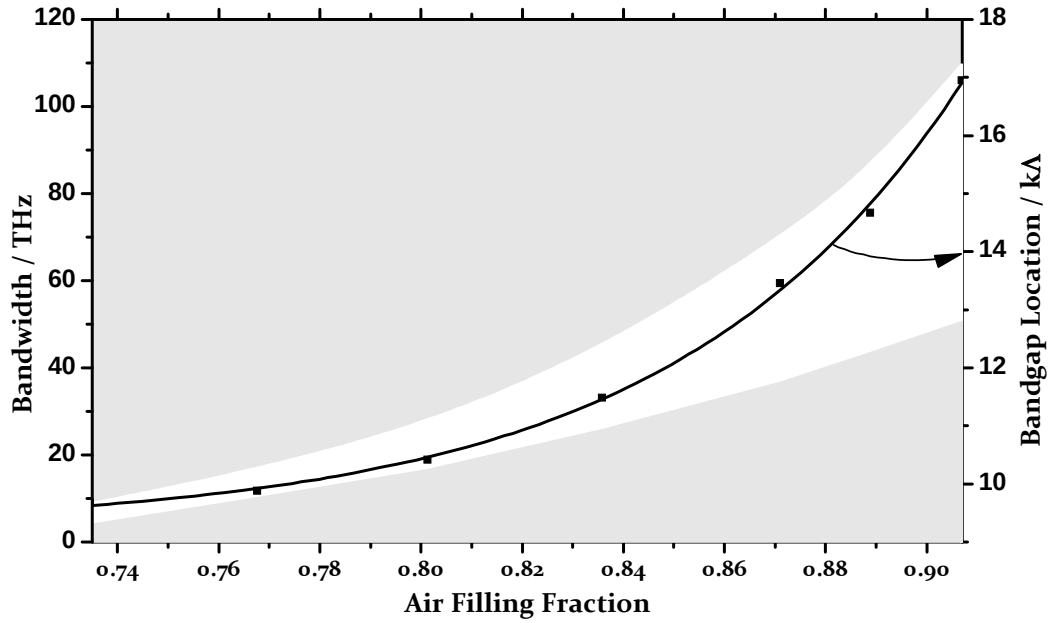

Figure 1-7: *Solid line: calculated bandgap width as a function of air-filling fraction for a cladding structure formed by uniform circular holes. The white band illustrates the central bandgap location along the air-line in units* of kΛ.

The introduction of a defect into the photonic crystal cladding structure (i.e. the core of a HC-PCF) introduces guided modes within the defect. Calculated modes[4] for a fabricated fibre are shown superimposed on a DOPS plot in Figure 1-8. The core-guided modes have a shallow spectral gradient as seen by the mode branches for fundamental (HE_{11}) core-mode and higher order core modes as labelled on the diagram. In addition to modes localised in the core, further guided modes exist at the interface between the hollow-core and silica core-surround, called surface modes. Surface modes are seen in the figure as the diagonal trajectories.

[4] These calculations were completed by P. J. Roberts.

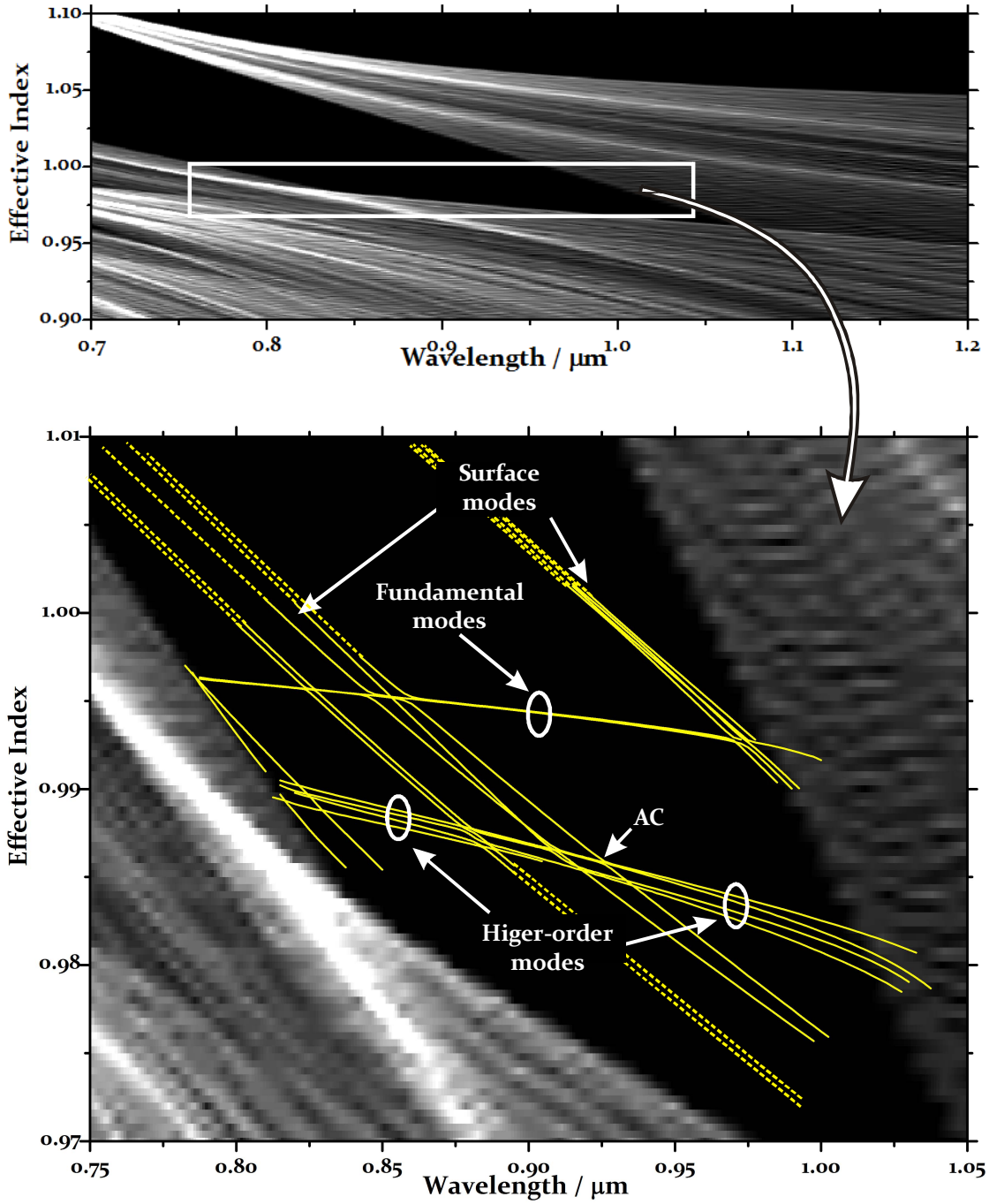

Figure 1-8: *Calculated guided modes of a HC-PCF superimposed on a density of photonic states. The lower graph is a detail of the top graph to more clearly show the modes. The extension of the guided modes out of the bandgap is due to the DOPS being calculated for the average cladding hole diameter, while the modes are calculated for the actual structure with slight variations in hole diameter across the cladding. Due to the computational time required, the dashed curves are obtained by extrapolation based on the calculated behaviour of surface modes in similar structures.*

The presence of surface modes is a source of loss for the fundamental-like (and other core-guided) modes. At anti-crossings between core and surface modes, such as the point marked AC in the figure, power can couple from the fundamental mode to the lossy surface-mode to which it is phase-matched (i.e. of the same β value). Experimentally the surface modes have the effect of reducing the usable bandwidth of the fibre. As an example, Figure 2-12 in Chapter 2 shows the attenuation of a 7-cell HC-PCF with a bandgap centred at 1550 nm. The three loss peaks visible at the short-wavelength end of the spectrum are due to surface-mode anti-crossings, and reduce the exploitable bandwidth of the fibre by 70 nm. The interaction between core-modes and surface-modes and the resulting changes in modal properties near anti-crossing points are explored in Chapter 2.

The experimentally measured spatial intensity profile of core-guided and surface modes of a 19-cell HC-PCF are shown in Figure 1-9. In this figure (A) is the fundamental core mode, and (B) and (C) are higher-order core modes. To a very good approximation the intensity profile of HC-PCF core modes are the same as those of a hollow capillary of the same diameter [2].

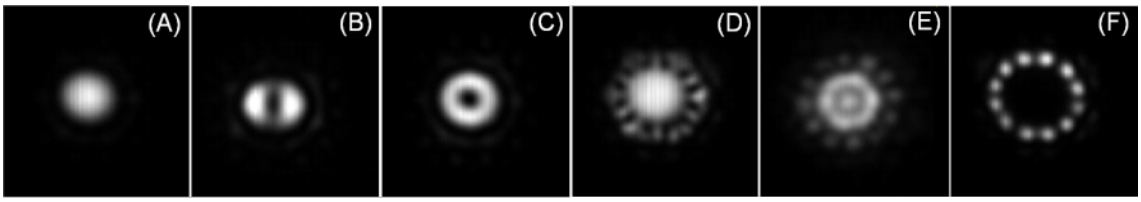

Figure 1-9: *Measured guided mode intensity profiles for a 19-cell HC-PCF with bandgap centred at 1550 nm.*

Since the bandgap position is normalised to the pitch of the fibre, the spectral location can be chosen by appropriate scaling of the cladding structure, and thus the core size of a particular fibre depends not only on the number of cells removed to form the core defect, but also the wavelength at which the fibre guides.

Although we have seen above that it is the presence of an out-of-plane bandgap in the cladding structure that allows HC-PCF to guide light in a hollow core, the numerical simulations provide no physical interpretation of its origin. There are several works that consider the relevance of cladding states, dating back to Yeh and Yarivs' Bragg reflection waveguide [5]. In that work it was qualitatively observed that the allowed bands in the cladding structure were formed from several modes, predominantly confined in the higher-index layers, the number of modes being determined by the number of layers.

This observation indicated the role of the resonance properties of the high-index layers in the formation of the bandgap.

Later, the anti-resonant reflective optical waveguide (ARROW) model was introduced by Duguay [18]. This model was originally applied to simple planar waveguides, considering the resonance properties for the transverse component of the wavevector of the high-index confining layers. The layers act as Fabry-Perot resonators, and as such high-reflection is obtained for anti-resonant wavelengths. The ARROW model has more recently been applied to Bragg-reflection fibres and a particular class of photonic crystal fibres [19, 20]. In the case of PCF the studies considered high-index circular inclusions in a low index background, and show that the transmission bands and bandgaps are determined by the modal properties of the individual inclusions, which act as waveguides. In this approximate model, valid for $\lambda \ll \Lambda$, the band structure is independent of the lattice constant, and dependent solely of the geometry of the inclusions. While the ARROW model provides important insights, it is not able to accurately model PCFs.

Birks *et al.* introduced a method for calculating band structure that is an intermediate approach between full numerical simulation and the ARROW model [21], and provides further insight into the guidance mechanism of Bragg fibres and all-solid PCF. The proposed model is analogous to the cellular method used in solid state physics, and unlike the ARROW model, where the band structure is independent of pitch, this model does take account of the low-index regions that separate the high-index rods. For this reason it is able to provide good approximations to the true band structure.

Couny et al. [17] have extended the analogy with solid-state physics to the tight-binding model, which gives additional information about the guidance mechanism, and of the origin of the photonic bandgap formation in complex structures such as that of triangular lattice HC-PCF.

Photonic Tight-binding Model

In solid-state physics the tight-binding model [22] has been successfully used to determine the origin of allowed and forbidden electronic bands. The tight-binding electronic states of a crystal are the result of "bringing together" isolated and identical atomic sites within the structure. In this model, as the isolated sites are brought closer together the well localised wavefunctions of the individual sites split to form bands of energy levels with delocalised wavefunctions, or Bloch functions; these bands are allowed bands, while the gap between them is a bandgap. It is found that the upper energy-level of each band is formed by an anti-symmetric wavefunction, while the lower

energy-edge of the band is defined by a symmetric wavefunction. This model can be applied to certain classes of PCF (such as that studied by Birks et al. [21]), where it provides a wealth of information on the formation of photonic bandgaps for certain structures.

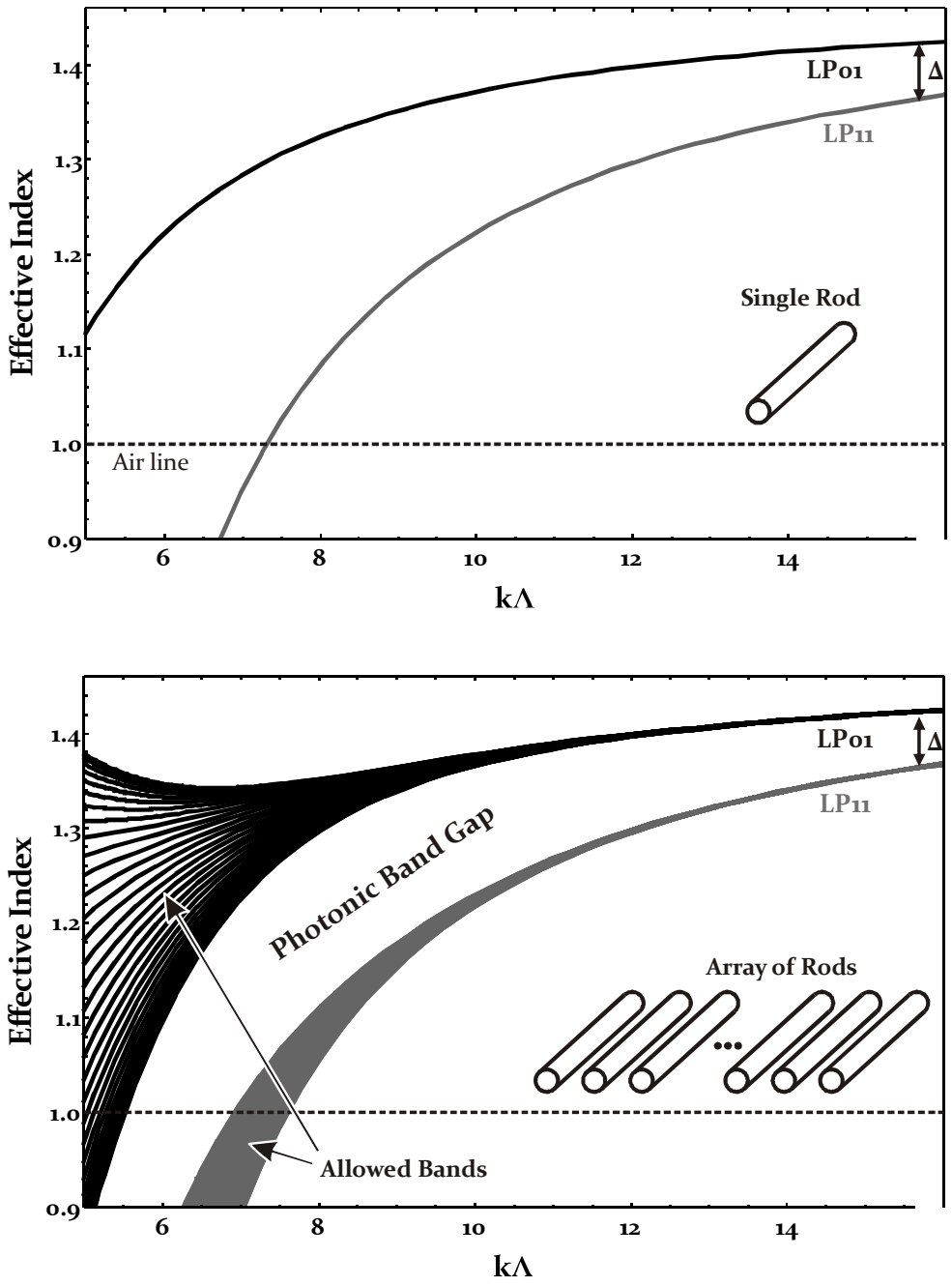

Figure 1-10: *Top: dispersion curves of the fundamental (black) and first higher-order (grey) modes of an isolated silica rod. Bottom: For an array of identical rods spaced by pitch Λ the dispersion curves broaden to form allowed bands.*

Due to the complex interconnected structure of the silica-air cladding of HC-PCF, the identification of optical resonators responsible for the formation of a bandgap is challenging. To illustrate the photonic tight-binding model, Benabid et al. [15] considered a 1-dimensional array of silica rod waveguides, as explained below.

The initial stage of the model considers the dispersion curves of an isolated silica rod. The top graph of Figure 1-10 illustrates the dispersion curves of the fundamental LP01 and higher order LP11 modes of an isolated rod of diameter d. These are calculated using an approximate analytical expression by Snyder *et al.* [23] given in equation 1-1.

$$\beta^2 = (n_{rod}k)^2 - \frac{U_\infty^2}{d^2}\frac{k^2}{\left(k+\frac{\eta}{d}\right)^2} \qquad 1\text{-}1$$

Here k is the wavevector, and η is a function of the refractive indices of the rod and background materials given by $\eta = (1-\Delta)/\left(n_{rod}\sqrt{2\Delta}\right)$ with $\Delta = \left(n_{rod}^2 - n_{bg}^2\right)/2n_{rod}^2$. The modes of the figure are calculated for a silica rod in air background. U_∞ is the first zero of the zeroth-order Bessel function for the LP01 mode, and of the first-order Bessel function for the LP11 mode.

For a 1-dimension array of identical rods, illustrated inset in the lower graph of Figure 1-10, the dispersion curves may be calculated by considering the coupling between rods. The figure shows the calculated curves for rods of diameter $d = 0.45\Lambda$, where Λ is the pitch of the array. It is calculated for an array of 1000 rods, and for ease of calculation the rods are assumed to have a Gaussian refractive index profile and to couple only to nearest-neighbour rods. It is observed that the allowed frequencies for a single rod broaden into allowed bands for the array, particularly at small normalised frequency. The plot also shows the existence of a photonic bandgap that importantly extends into the region $n_{\text{eff}} < 1$ below the air-line.

At large normalised frequency $k\Lambda$, i.e. for $\lambda \ll \Lambda$, it is observed that the difference in effective index between the fundamental LP01 mode and the higher-order LP11 mode tends to a constant value, as indicated by Δ in Figure 1-10. This is the regime in which the ARROW model holds, and explains its observed independence on pitch.

The tight-binding model illustrates the formation of photonic bandgap within the cladding structure. The findings of the model have been verified experimentally through observations made using a scanning near-field optical microscope [24]. Figure 1-11 shows the calculated density of states of a HC-PCF guiding at 800 nm, where the lower and upper frequency edges of the bandgap are shown by the red and blue/green dispersion

curves respectively. Modes calculated at the points (E), (F) and (G) as labelled are shown to the right of the figure. These clearly shown that the red, green and blue edges of the bandgap are due to cladding modes which guide predominantly in the silica apexes, silica struts and air-holes of the cladding structure.

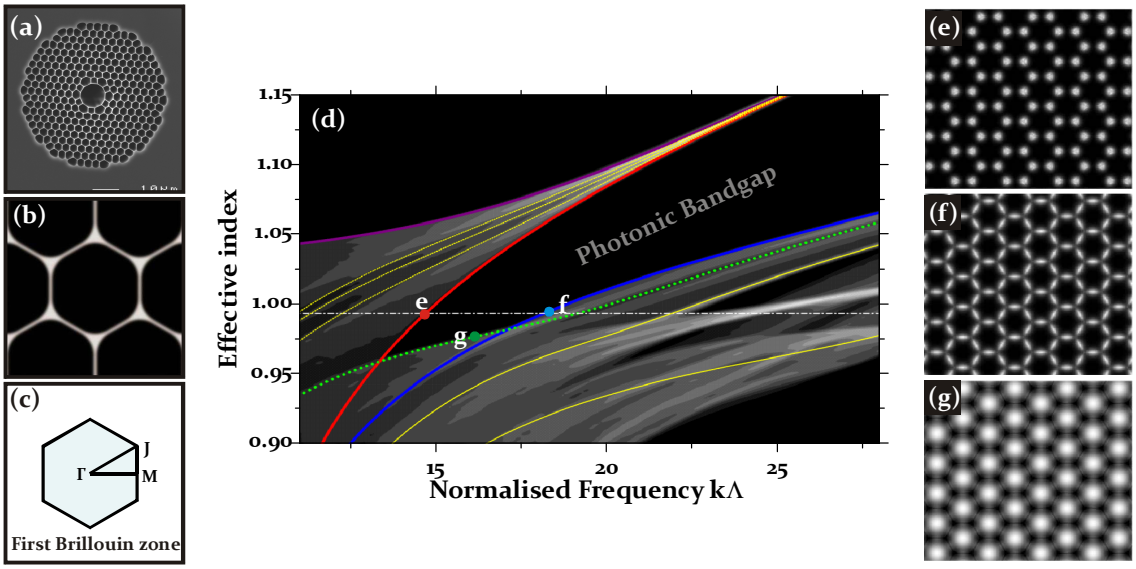

Figure 1-11: *(a) Electron micrograph of a HC-PCF guiding at 800 nm with a detail of the structure used for simulation (b). The Brillouin zone symmetry points are shown in (c). The calculated density of states is shown in (d) with the cladding modes at the points indicated shown in (e-g).*

While the photonic model provides excellent insight into the guidance obtained by hollow-core photonic bandgap fibre, as revealed earlier there is a second type of HC-PCF which offers broadband low-loss optical guidance without the presence of a bandgap in the cladding structure. This guidance mechanism behind this second class of HC-PCF is explained in the following section.

1.2.2 Broadband Guidance in HC-PCF

The second class of HC-PCF provides broadband guidance without the cladding structure having a photonic bandgap. This type of guidance was first observed in a fibre with a kagomé lattice structure by Benabid et al. [14]. This lattice structure consists of tessellating hexagons and triangles as seen in the centre of Figure 1-12; the scanning electron micrograph at the left of the figure is the original working fibre of this type, with a pitch of ~10 µm.

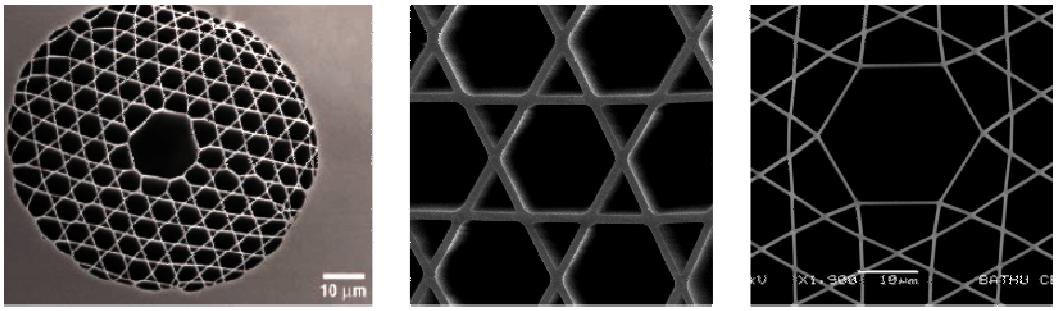

Figure 1-12: *Left: electron micrograph of the original kagomé lattice fibre. Centre and right: details of the cladding structure and core of a single-cell core large-pitch kagomé fibre.*

HC-PCF with this cladding structure has been shown to provide low-loss guidance over a broad spectral range, much greater than that achieved with fibre based on the standard HC-PCF cladding. Transmission loss of <3 dB/m was observed from 400 nm to 1700 nm in a kagomé fibre with 10 µm pitch, and similar transmission is obtained for 12 µm pitch kagomé structure fibre [25] fabricated for use in this thesis. The optical characteristics of this fibre will be considered further in Chapter 2, but it is observed that the low attenuation, chromatic dispersion and bend loss are similar to those in PBG HC-PCF.

The broadband guidance achieved in the large-pitch kagomé fibre is not limited to this structure. Triangular and square lattice fibres of similar pitch are found to have similar characteristics. Chapter 2 presents the fabrication of large-pitch kagomé fibres, with a typical pitch of 12 µm. The fibre provides two broad bands of guidance located in the visible and near-infrared, and corresponds to large normalised frequency between ~50 and 200. The fibre has a loss of ~1 dB/m throughout these regions; although this is significantly higher than bandgap HC-PCF in the infrared, it is comparable in the visible guidance band.

As stated above, despite the excellent transmission bandwidth obtained by the large-pitch kagomé fibre, the cladding structure does not exhibit photonic bandgaps. Instead, the guidance is attributed to the inhibited coupling between core-modes and cladding modes as is explained further below. For completeness the DOPS plot for the kagomé lattice is shown in Figure 1-13, which illustrates the absence of a photonic bandgap for normalised frequency below 160. It is also worth mentioning that the existence of a relatively low-loss core guided mode, as observed experimentally, is verified by full numerical simulation, but does not explain its origin.

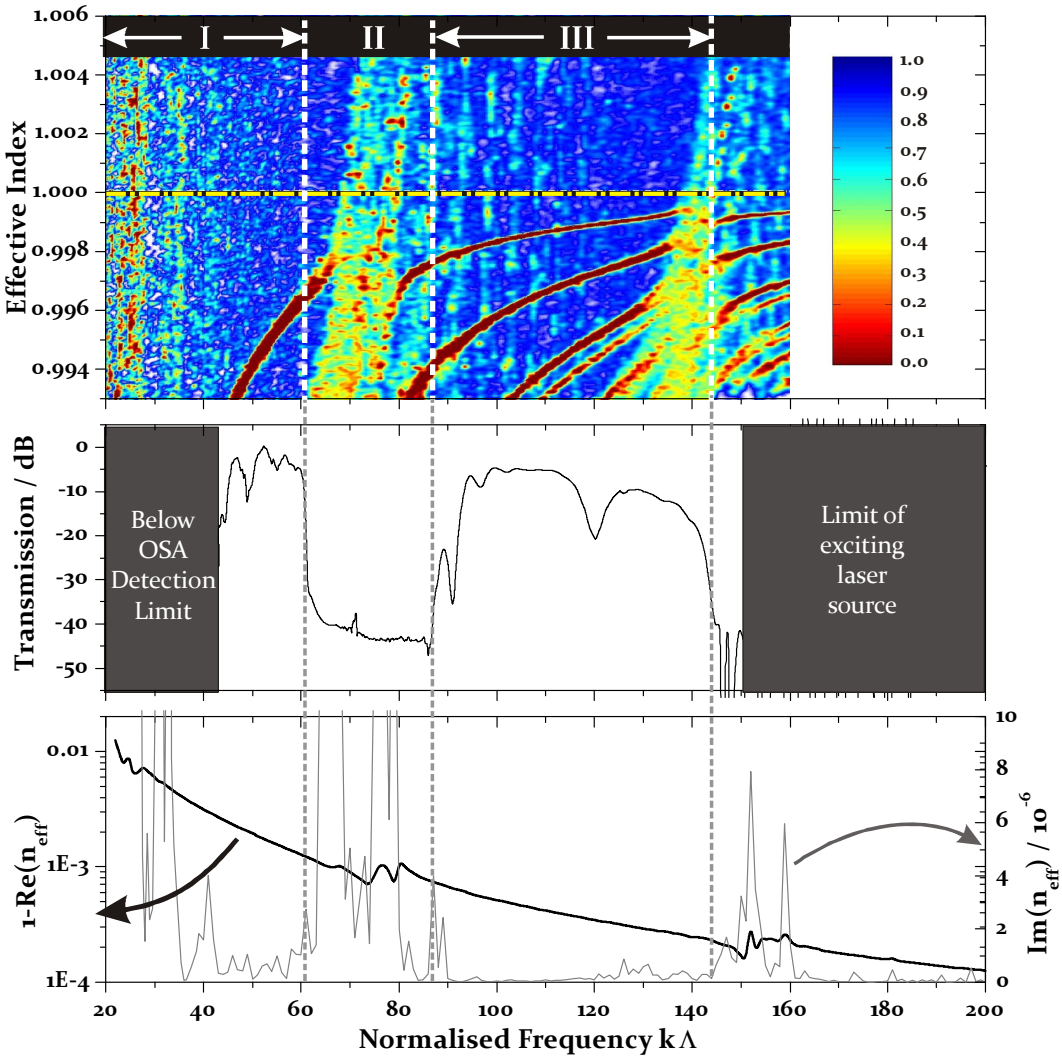

Figure 1-13: *Top: density of photonic states for the kagomé lattice structure. There is no photonic bandgap present. The horizontal yellow line indicates the air-line. Middle: transmission spectrum of a fabricated kagomé lattice fibre of the same structure as that simulated to obtain the DOPS. I and III are bands of high-transmission in the core, and II is a band of low transmission in the core. Bottom: calculated real (thick black) and imaginary (thin red) parts of the effective index of the fundamental HE11-like core mode; the imaginary part is related to the loss of this mode.*

The broadband guidance of these large-pitch fibres is attributed to inhibition interaction between core and cladding modes. This, as for the guidance of bandgap HC-PCF, can be explained by analogy with solid-state physics.

In the early days of quantum mechanics, von Neumann and Wigner proposed that a bound or quasi-bound state could exist within a continuum [26]. This remained unverified experimentally until 1992 when Capasso et al. observed an electronic bound state above the potential barrier in a layered semiconductor structure [27]. Due to the

successful photonic analogue of the solid-state cellular model and tight-binding models, this observation raises the question of whether the photonic analogue of bound states within a continuum also exists. It turns out that the photonic equivalent of von Neumann and Wigner's proposal is able to explain the guidance of the second class of HC-PCF.

In the photonic model, the localised guided mode represents a quasi-bound state with a given frequency and effective index that lies within the continuum of propagating modes provided by the cladding structure of the HC-PCF. The guidance is attributed to the inhibited interaction (or non-coupling) between the transversely fast-oscillating modes associated with the silica cladding, and the slowly-varying modes in the air-core.

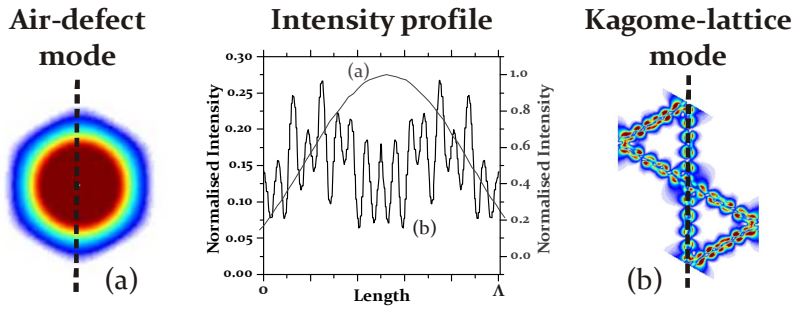

Figure 1-14: *Intensity profiles of (a) the guided core-mode of a kagomé lattice fibre, and (b) a cladding mode of the same fibre. The graph plots the transverse intensity variation of both modes over a distance equal to the cladding pitch.*

The weak interaction between core and cladding mode that are phase-matched longitudinally is due to the large transverse field mismatch, as seen by the fast intensity oscillations of the cladding mode compared with the slowly varying intensity of the core mode in Figure 1-14. The fast phase oscillations of the cladding mode occur away from resonances which occur approximately at the normalised frequency expressed in equation 1-2, where t is the thickness of the glass in the cladding, and m is a positive integer.

$$k\Lambda = \frac{\pi m(\Lambda/t)}{\left(n_{\text{silica}}^2 - n_{\text{air}}^2\right)^{1/2}} \qquad 1\text{-}2$$

Returning to Figure 1-13, the bands labelled I and III correspond to regions of high-transmission in the core, and II to a region of low transmission due to a resonance described by equation 1-2. Experimentally it is observed that a fundamental core-guided mode exists even in the low-transmission region II. Modes calculated for each of these

regions are shown in Figure 1-14. In the high-transmission bands, it is clear that the core and cladding modes are well confined to the core and cladding respectively, and exhibit very little overlap; this is the region for the low-loss guidance in these regions. In band II there is a large overlap between core and cladding modes, and as a result there is greater attenuation of the core mode in this region. This region corresponds to the lowest frequency resonance described by equation 1-2.

The measured intensity profile of the core mode of a kagomé lattice HC-PCF is shown in Figure 1-15, and shows that power in silica at the edge of the core is 30 dB below the maximum power. For a bandgap HC-PCF of the same mode area the power is silica is calculated to be just 20 dB below maximum. This highlights the small interaction between core- and cladding-modes in the large-pitch broadband HC-PCF.

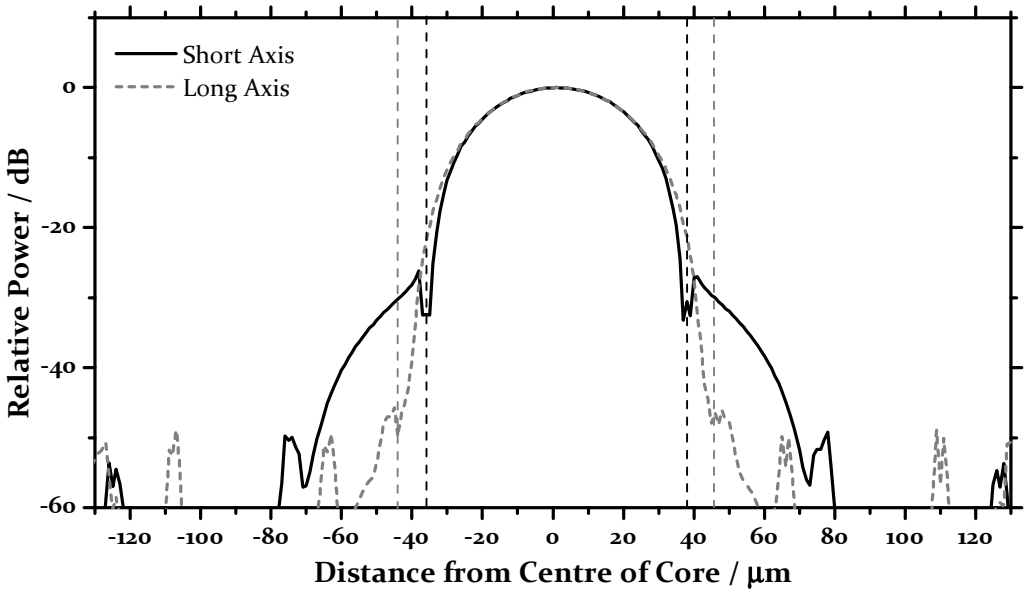

Figure 1-15: *Measured intensity of the fundamental HE11-like mode of a large-pitch kagomé lattice fibre a function of distance from the centre of the core. The solid line corresponds to a cross-section through the longest part of the (approximately hexagonal) core, and the dotted line to a cross-section through the shortest part. The vertical dashed lines indicate the position of the silica core-surround in both cases.*

Experimentally broadband HC-PCFs are found to be extremely insensitive to bending; this can also be explained by the model described here. By analogy with fibres with cylindrical symmetry, the fast-oscillating cladding modes are associated with a large effective number m that governs the azimuthal variation. A fibre bend is associated with a change in m of 1, whereas coupling between core and cladding modes requires a large Δm, and therefore bend-loss is negligible.

Further discussion of the von Neumann-Wigner guidance model can be found in [15] and the supplementary material of [17].

1.3 Laser-Matter Interactions

The main subject of this thesis, and a major application of hollow-core fibre, is the investigation of light-matter interactions. Conventional experiments maximise the interaction by tightly focusing a laser beam (Figure 1-16), thereby increasing intensity as much as possible. This technique however has a major drawback, in that the light only remains tightly focused over the rather short Rayleigh length ($z_R = w_0^2/\lambda$, where w_0 is the beam waist) along which the "effective" interaction occurs over this distance. Typically this length is of the order of 200 μm (1550 nm; 10 μm beam-waist). A short interaction length means low signal-to-noise ratio, and the subsequent difficulty in detection. A longer interaction length may be obtained by looser focusing of the beam, but this is at the expense of a reduction in intensity.

The conventional method of focusing light through a gaseous medium is therefore a trade-off between high intensity and good interaction length. To compare the techniques that have been proposed in order to increase the efficiency, a figure-of-merit, f_{om}, is introduced. In general this is given by the expression $f_{om} = L_{int}\lambda/A_{eff}$, where L_{int} is the constant intensity interaction length, and A_{eff} is the effective cross-sectional area of the beam.

One technique that improves on such a scheme is the use of hollow-capillaries (see section 1.1.1). Light may be guided in such a capillary maintaining a respectable beam waist, typically hundreds of micrometres to several millimetres, and provide an increased interaction length over the simple focusing method. The usable capillary length is determined by the loss of the capillary waveguide, and is typically only a few centimetres. The figure-of-merit for such a waveguide is given by equation 1-3 [14]. Here r_0 is the bore radius, and n the refractive index of the dielectric capillary waveguide.

1-3
$$f_{om}^{cap} = \frac{6.8 r_0 (n^2 - 1)}{\lambda \pi \sqrt{n^2 + 1}}$$

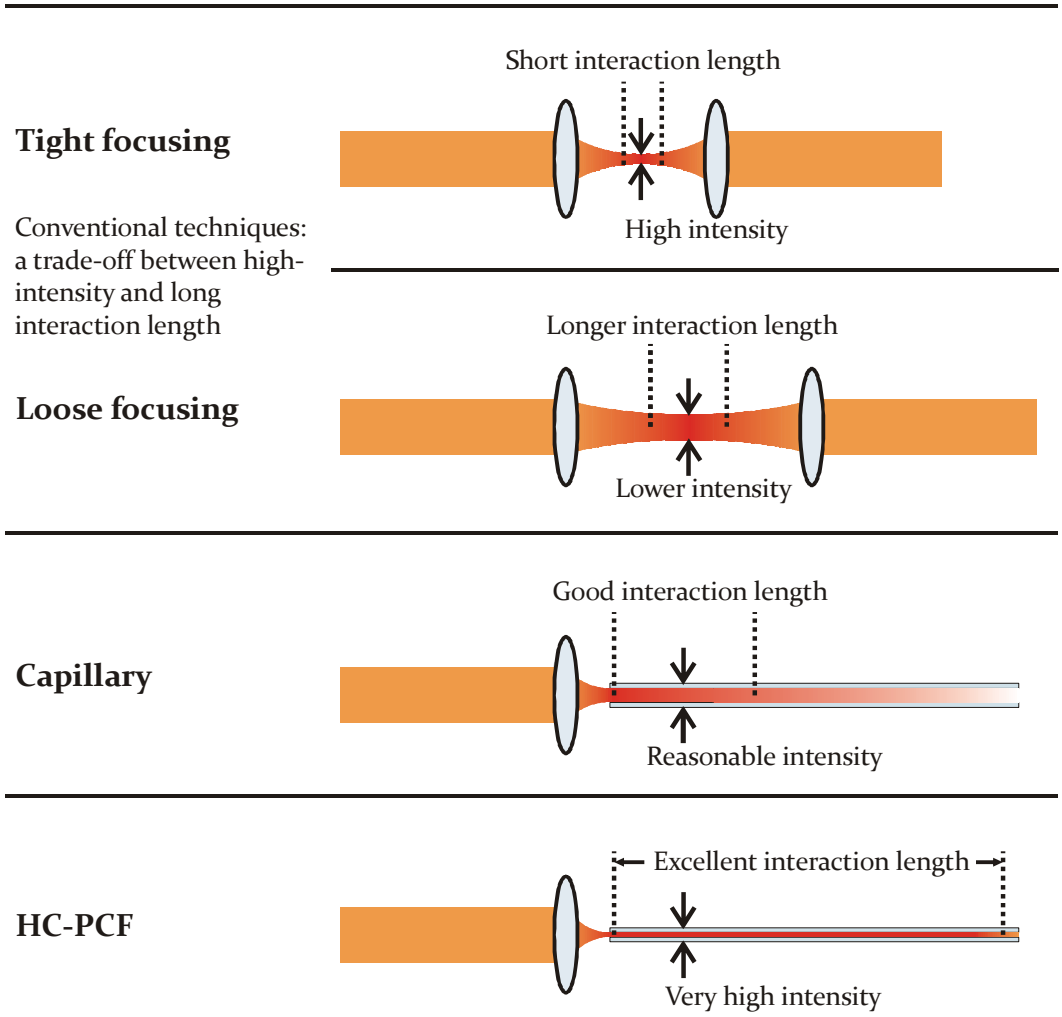

Figure 1-16: *Comparison of techniques for gas-laser interaction in a single-pass configuration. Ideally there should be a long interaction length and small effective area.*

Alternatively, a multi-pass cavity also provides a length enhancement. This offers the advantage of reduced loss compared with a capillary, but more complex alignment and no improvement in intensity. A further technique used to enhance gas-laser interaction is the use of optical cavities, offering a power enhancement, again at the expense of ease-of-use due to the alignment required, and still offering only limited interaction length.

Hollow-core photonic crystal fibre allows a large increase in interaction efficiency to be obtained compared with the above techniques. It provides low-loss guidance over metres or kilometres of fibre, thereby achieving long interaction lengths, while maintaining an extremely small mode area over the entire length of interaction. The figure-of-merit for HC-PCF is described by equation 1-4 in terms of the fibre attenuation α.

1-4 $$f_{om} = \frac{\lambda}{\pi r_0^2 \alpha}$$

Figure 1-17 summarises the figure-of-merit for a free-space beam, capillary, and HC-PCF of various losses as a function of the core or bore radius.

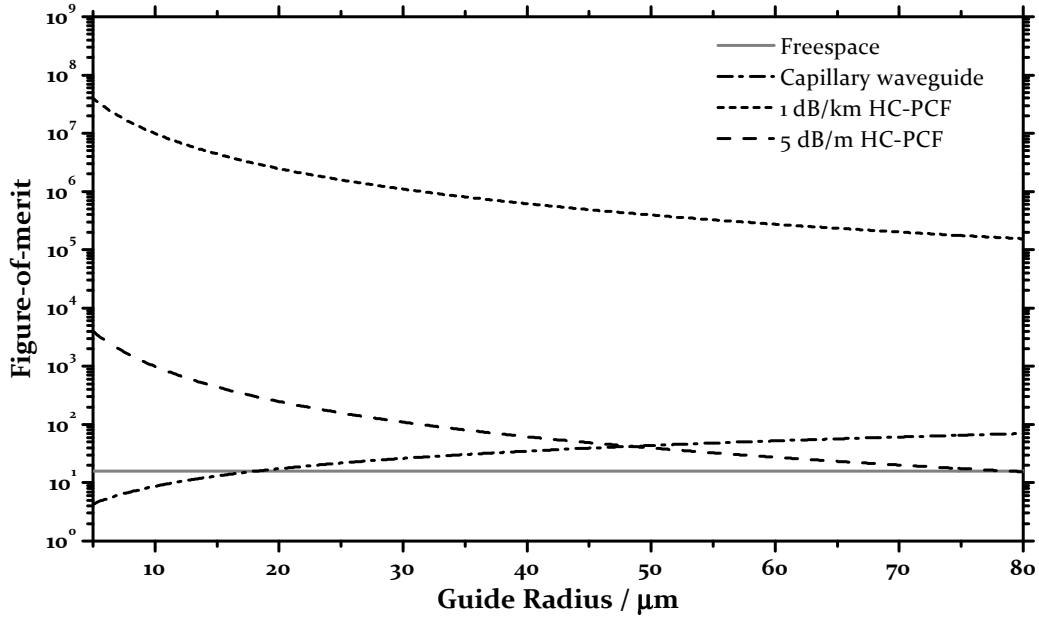

Figure 1-17: *Figure-of-merit describing the relative efficiency of light-matter interaction in free-space (grey), a hollow-capillary (dot-dash), and HC-PCF of 5 dB/m loss (long dash) and 1 dB/km loss (short dash). The curves are calculated for a wavelength of 1550 nm.*

At bore radii below 45 μm, even HC-PCF with a high loss of 5 dB/m provides a greater figure-of-merit than both free-space beams and capillaries. As bore radius and fibre loss are further reduced, the figure-of-merit of HC-PCF increases dramatically. For a core radius 6 μm and loss 1 dB/km, realistic for a fibre guiding at 1550 nm, the figure-of-merit is more than six orders of magnitude greater than a free-space beam.

It is this high figure-of-merit provided by HC-PCF that makes it ideal for investigation of gas-laser interactions. With HC-PCF, the waveguide itself forms the gas-cell, and it is this that allows it to achieve laser-matter interaction with unprecedented efficiency.

While the figure-of-merit gives an accurate estimation of the efficiency of interaction in a system, it does not consider physical geometric effects of the system. The geometry of the gas-filled core of a HC-PCF is significantly different to that of conventional gas cells, particularly with respect to the aspect ratio. A conventional cell will be of similar length

in all three dimensions, whereas the core of HC-PCF is of the order 10 μm in diameter, and at least 10 m in length, an aspect ratio of one *million*.

The large aspect ratio of HC-PCF manifests itself in a number of ways when using it as a host for laser-matter interaction and quantum optical effects. Firstly, the filling of such a channel with gas presents a number of hurdles; these will be considered in Chapter 4 which presents the creation of photonic microcells, gas-filled lengths of HC-PCF sealed by splicing at either end to conventional optical fibre. Second, at low gas-pressures (sub-millibar), there is a significant rate of collisions between the gas molecules and the silica core wall of the fibre; this affects the coherence properties of coherent optical effects, as will be explained in Chapter 3. This rate of decoherence is experimentally determined in the quantum optics experiments carried out in gas-filled HC-PCF in Chapters 5 and 6.

1.4 Summary

This chapter has introduced hollow-core photonic crystal fibre, and its guidance mechanisms. It has also shown that filling the hollow-core of the fibre with a gas or liquid will allow for extremely efficient interaction between light and the medium introduced into the core. The following chapter introduces the fabrication process of HC-PCF, and explores the linear transmission properties of the fibre.

In chapter 4 we will see how the fibre is filled with gas, and how all-fibres gas-cells consisting of HC-PCF spliced at either end to conventional optical fibre, or *photonic microcells*, are formed. These HC-PCF based cells are used in later Chapters for the observation of coherent optical effects. Chapter 5 presents the first observation of electromagnetically induced transparency (EIT) in a molecular gas, and a detailed study of the system. In Chapter 6 EIT is obtained in rubidium loaded HC-PCF. The polymer coating of the inside of the fibre core allows linewidths to be obtained that are lower than those to be expected from a fibre of small diameter, and thus demonstrate that the diameter of HC-PCFs need not be a hurdle.

Chapter 2

Hollow-Core PCF Fabrication and Characterisation

This chapter explains the fabrication process for hollow-core photonic crystal fibre, and the controls that are available in achieving the properties required of the fibre for its many applications.

Characterisation of the linear properties, including attenuation and chromatic dispersion is then considered. A spatially resolved dispersion measurement method is presented that allows the discrimination of the dispersion of core modes from that of surface modes.

A later section considers post-processing of a fibre, where etching of the silica core-surround is used to further tailor the properties of a drawn fibre. It is shown that such a method is able to shift the spectral position of surface modes within the bandgap, and has the potential to improve the fibre characteristics in other ways.

Finally, the modal properties in the region of anti-crossings between core-guided and surface-modes are explored both theoretically and experimentally.

2.1 Introduction

This chapter covers the different steps of fabrication of hollow-core photonic crystal fibre and the optical characterisation to determine suitability for the many varied applications. The fibre fabrication process is described in section 2.2, which details the various controls available throughout the process that determine the structure of the final fibre.

The next section describes optical characterisation of a fabricated fibre, including transmission spectra, attenuation measurements and chromatic dispersion. This section also shows the ability to explore spatially resolved dispersion measurements, making it possible to determine separately the dispersion of higher order and surface modes experimentally.

Section 2.5 explores the possibility of altering the structure of the drawn fibre through acid etching of the silica to tailor and improve the optical characteristics of the fibre. Experimental results are presented which illustrate the ability to shift the spectral location of surface modes, achieved by patterning the silica core surround. Techniques similar to those shown here also increase the air-filling fraction of the cladding structure, thus broadening the transmission spectrum and decreasing attenuation.

The final section of this chapter looks at how the spatial properties of guided modes of HC-PCF are affected by anti-crossings between core modes and surface modes.

2.2 Fabrication Techniques

There are two techniques available for producing the periodic structure of HC-PCF: extrusion [28] and stack-and-draw [29]. Typically extrusion is used for soft glasses such as SF_6, and stack-and-draw for silica, although both methods have been used for both classes of material. This chapter concentrates on the stack-and-draw technique as the fabrication method used by the author.

2.2.1 Stack-and-draw

The basic aim of the stack-and-draw technique is to start with a large scale version of the structure required formed by stacking capillaries, and then heating and stretching this structure to form the final fibre. An overview of the process is shown in Figure 2-1.

Stack Design

The first stage in this fabrication process is to design the initial *stack* from which the fibre will be drawn. An example design for a standard HC-PCF is shown in Figure 2-2. HC-PCF is usually fabricated with a triangular lattice cladding, but other structures are possible, as described in section 1.2. The triangular structure is formed from hollow circular capillaries, rather than tessellating hexagonal capillaries. The reasons for this are two-fold: firstly, by appropriate choice of drawing parameters the hexagonal structure can be drawn from a stack of circular silica capillaries, as shown in Figure 2-2. These capillaries are drawn from commercially available silica tubes, 10-20 mm in diameter. Secondly, hexagonal silica tubes with suitable tolerances are not readily commercially available, and would be unlikely to maintain their shape sufficiently when being drawn into capillaries.

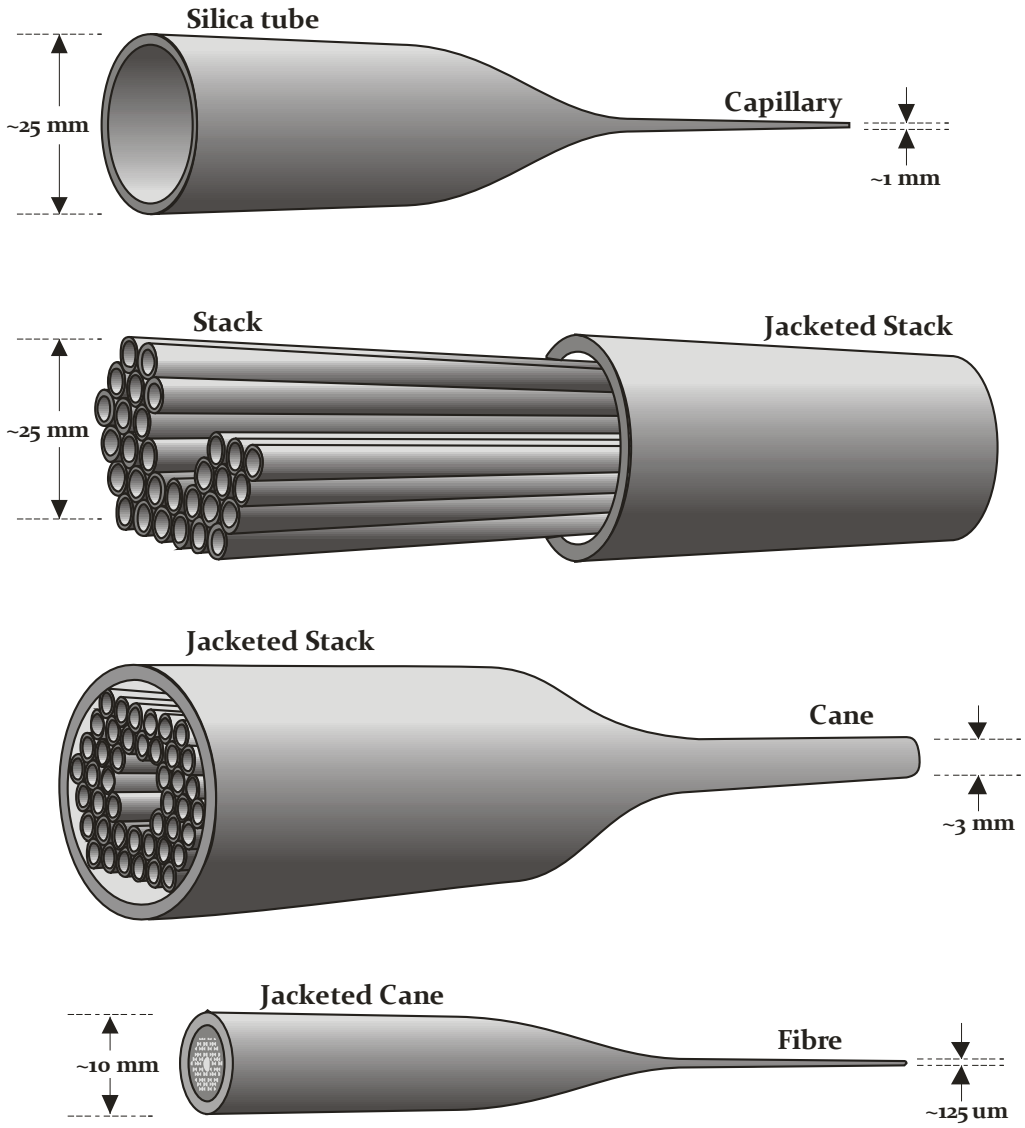

Figure 2-1: *An overview of the entire stack-and-draw fibre fabrication process.*

The stack is designed to fit within a thick silica jacket tube. In order to maintain the symmetry, the periodic structure must be packed by either smaller capillaries or rods (as illustrated in Figure 2-2) to maintain the structure within the jacketing tube. This packing is a very important part of the fabrication process, as insufficient packing results in the cladding structure not 'sticking' to the jacket, resulting in severe distortions in the cross-section of the fibre drawn. The core of the fibre is usually formed by removing the central 7 or 19 capillaries from the structure, as shown in Figure 2-3. The capillaries removed to form the core are usually replaced with a large thin core capillary to hold the structure, as illustrated.

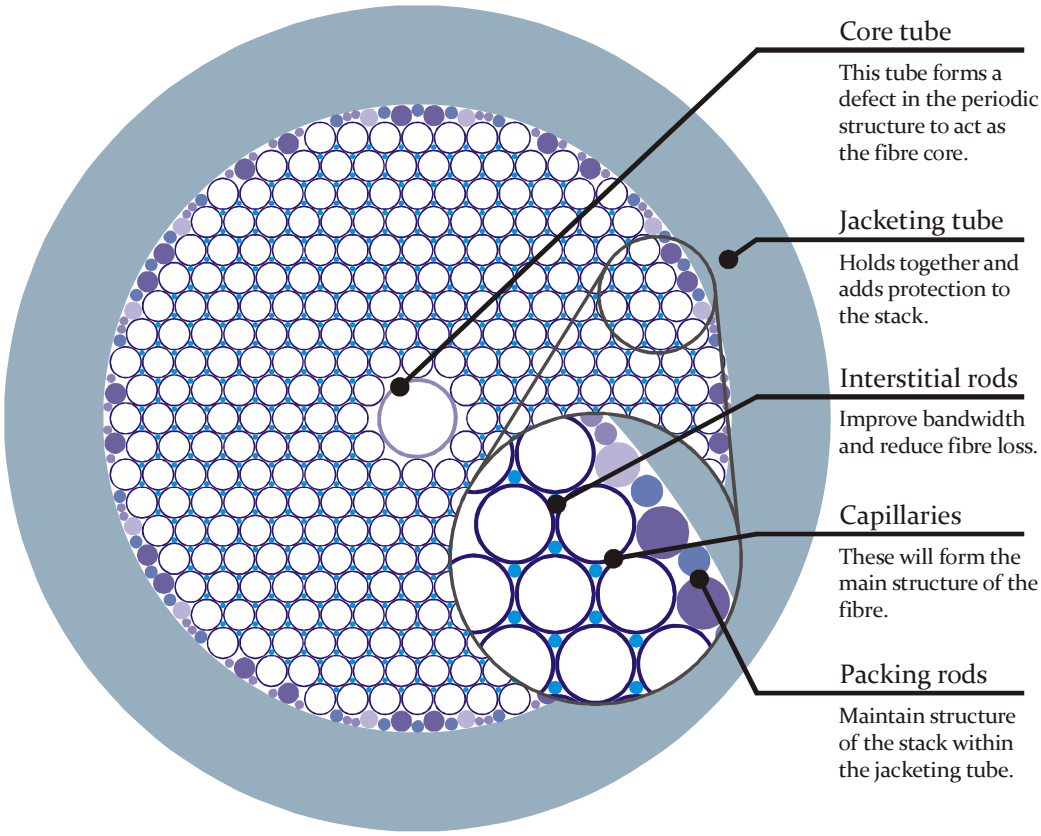

Figure 2-2: *Initial design of a stack for producing standard triangular lattice HC-PCF. This design illustrates how the stack of capillaries that will form the cladding of the fibre is held in place in a large jacketing tube through the use of packing rods.*

If a thin silica core surround is required, it is possible to use a supporting core capillary at either end of the stack, with a section in the centre left without the additional tube.

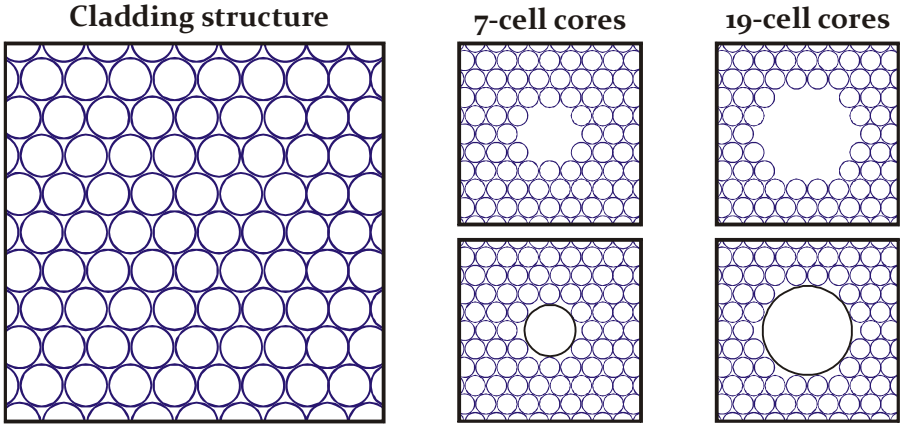

Figure 2-3: *The core of a HC-PCF is usually formed by removing the central 7 or 19 capillaries from the periodic cladding structure, and optionally replacing them with a single larger diameter capillary.*

The Drawing Tower

An important piece of equipment in the fabrication process is the fibre drawing tower, shown in Figure 2-4. The main component of this is the furnace, which is used to heat silica to 1800-2100°C, softening the glass so it is able to be drawn. The draw-down ratio achieved is altered by changing both the rate at which glass is fed into the furnace by the preform feeder, and the rate at which it is pulled out by the tractor or capstan.

The drawing process can also be controlled by altering the furnace temperature, and by pressurisation at various stages of the drawing process; further discussion of the parameters are given in the following sub-sections.

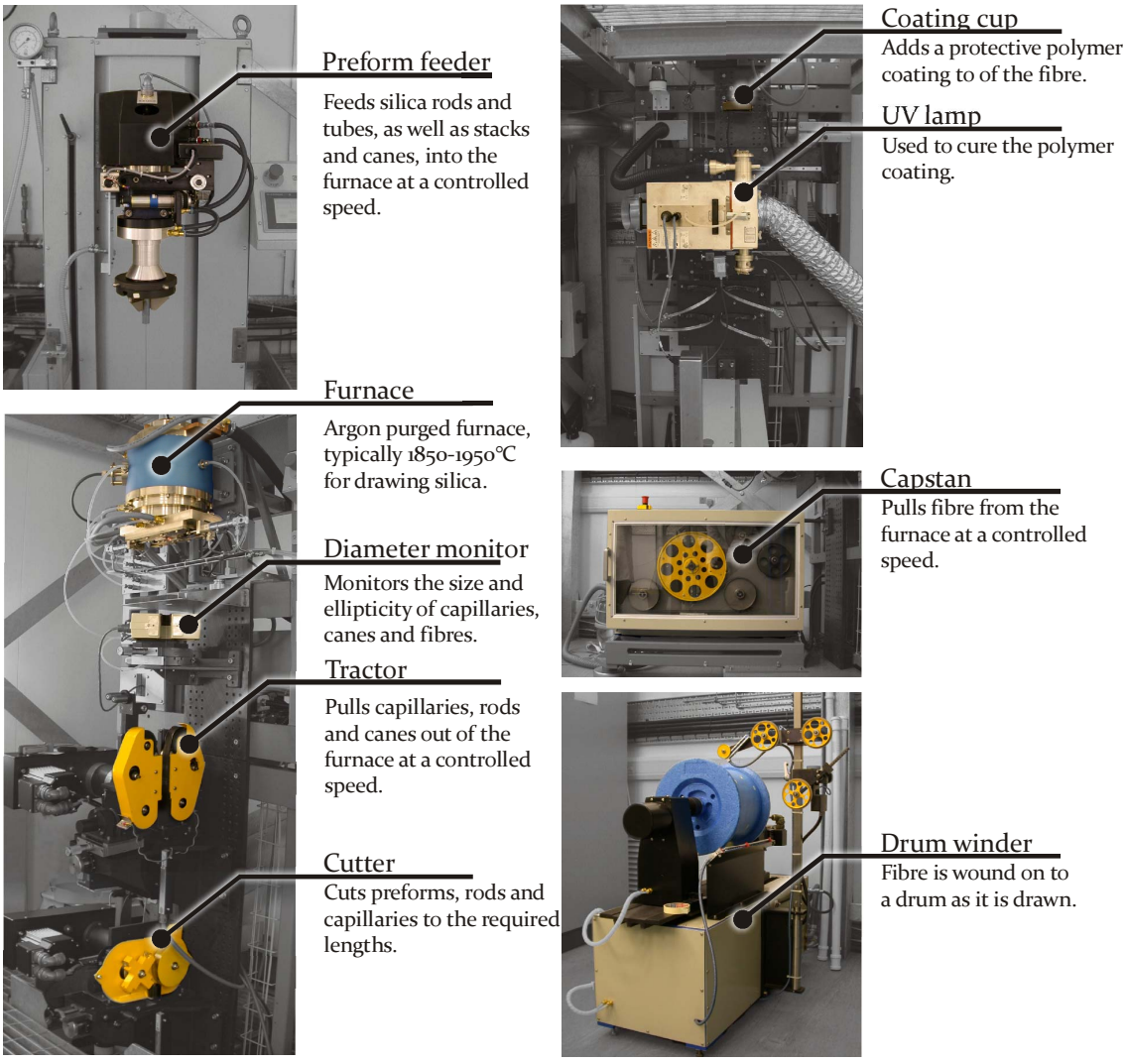

Figure 2-4: *Annotated photograph of the fibre drawing tower.*

Stack Fabrication

The capillaries and rods required for the stack are drawn on the fibre drawing tower from large silica tubes and rods, typically 15-25 mm in diameter and 1 m in length. The capillaries are usually drawn such they have the same relative thickness (thickness/diameter) as the tube being drawn. If thinner capillaries are required, such as for use as the core capillary, it is possible to pressurise the inside of the silica tube with nitrogen gas while it is being drawn. Whilst pressuring the tube, the speed of the tractor pulling the capillary through the furnace is increased to maintain the correct outer diameter.

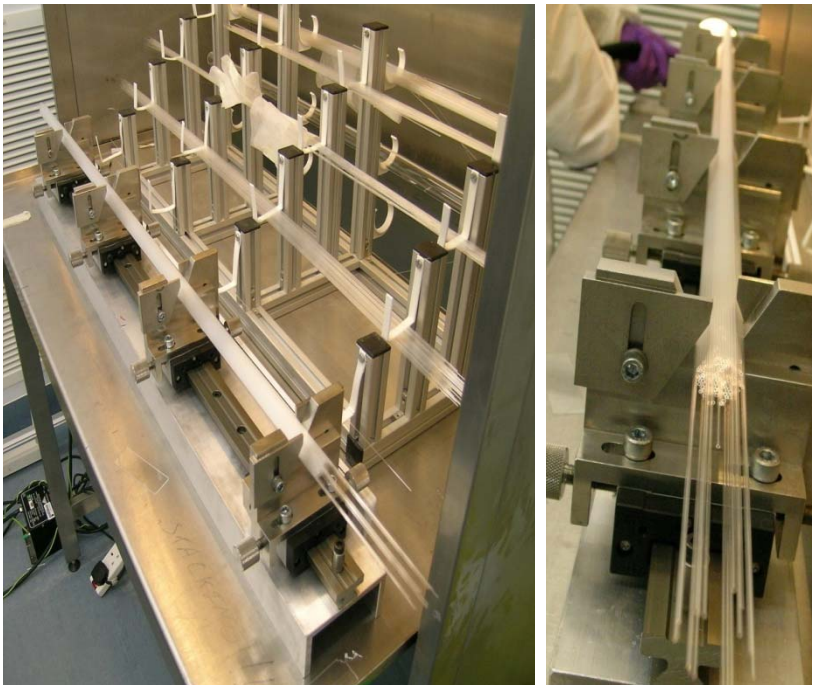

Figure 2-5: *The stacking rig used to hold capillaries as they are stacked one-by-one into the required structure. The completed stack in the rig can be seen on the right; the left-hand photograph also shows spare capillaries stored behind the stacking rig.*

Once drawn, the capillaries are stacked one-by-one onto a *stacking rig* designed to form a hexagonal structure (Figure 2-5). As the rig will only securely hold a hexagonal cross-section structure, additional capillaries to those shown in the design in Figure 2-2 are added to the stack at this stage.

Once the stack is complete, it is fitted into a thick jacketing tube. During this process the additional capillaries added to the stack to make the structure hexagonal are removed. Once inside the jacket tube, packing rods (as seen in the original stack design) are added to secure the structure within the circular jacket. If required, small diameter rods are

inserted in the interstitial holes throughout the stack formed between the circular capillaries. These are used to increase the aspect ratio between the silica struts and apexes in the final fibre to more closely resemble the structure modelled in section 1.2.1. Photographs of completed stacks are shown in Figure 2-6.

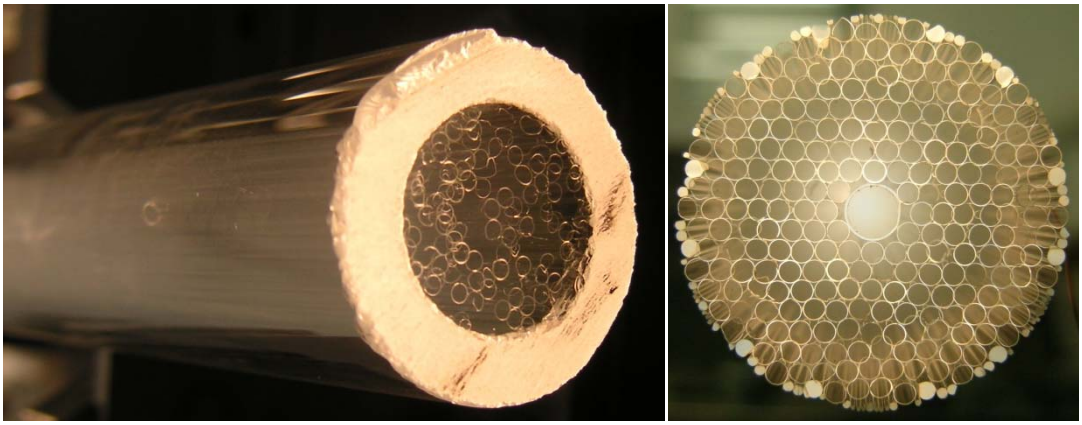

Figure 2-6: *Left: photograph of a completed stack within a thick jacketing tube. Right: hollow-core stack removed from jacketing tube to show the packing rods used to fit the circular tube.*

Cane Pulling

The drawing of the stack to fibre is done in two stages, as the overall draw-down ratio of ~200 (diameter of ~25 mm to ~125 µm) is difficult to control in one step. The use of an intermediate stage also gives greater possibilities in fibre design options.

The stack will be drawn from its initial diameter of ~25 mm to a *cane* of 2 mm - 5 mm diameter. When drawing standard HC-PCF the top of the stack is collapsed, completely sealing the stack at this end. During this draw a vacuum is applied through a slot in the side of the jacket tube and between the capillaries forming the stack in order to ensure that the capillaries fuse both to each other, and to the jacket tube. This also closes the interstitial holes between capillaries, which are unwanted in the final fibre. Kagomé structure stacks are not sealed at the top as it is important that the interstitial holes remain open. The draw temperature of these canes is adjusted in these cases to ensure capillaries fuse both to each other and the jacketing tube.

In addition to the vacuum, it is also possible to pressurise the cladding and core capillaries to obtain higher air-filling fraction in the canes drawn. Differential pressures are used in the core and cladding to maintain the correct size of core relative to the cladding structure; the typical pressures used range up to ~20 kPa. A selection of canes

for standard triangular lattice fibre, double-period fibre, and kagomé fibre is shown in Figure 2-7.

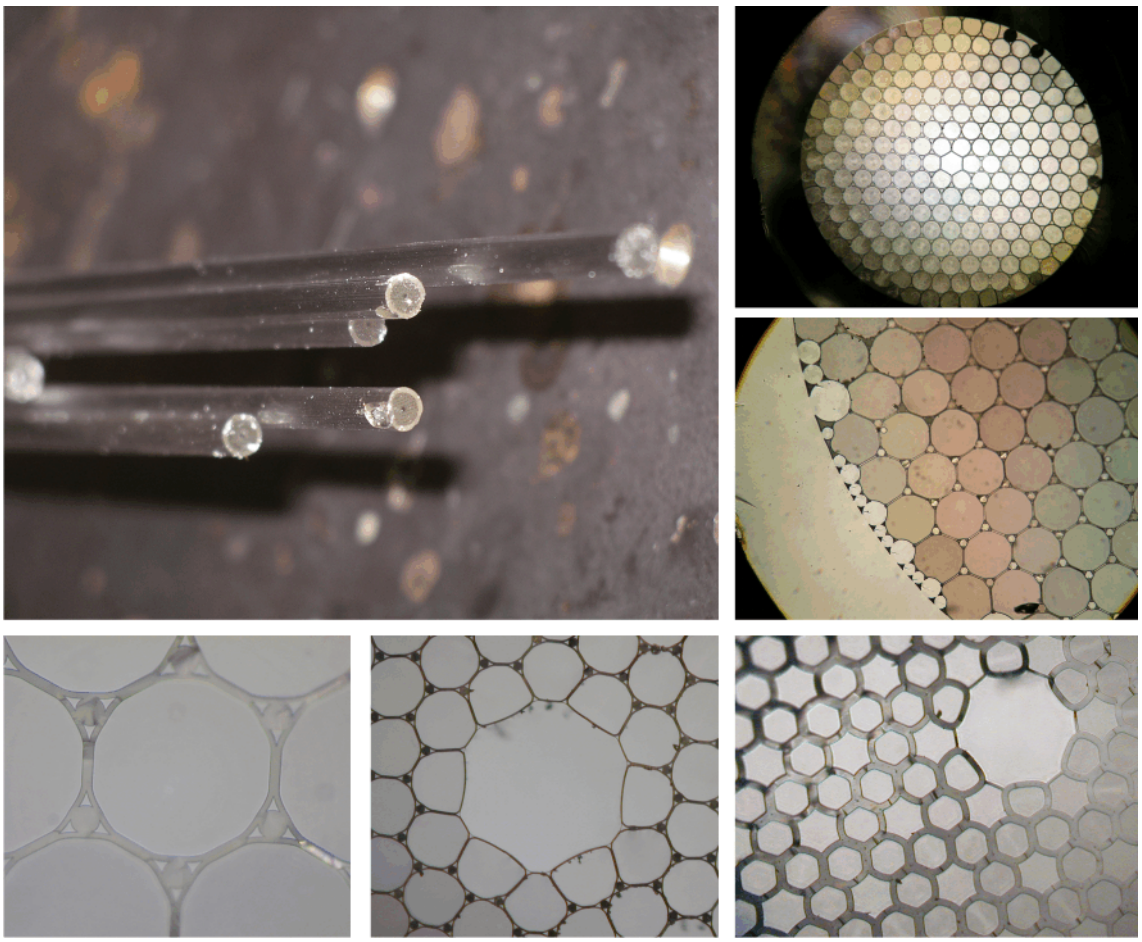

Figure 2-7: *Main photograph: HC-PCF canes. Cane cross-sections clockwise from top right: full cross-section of a 1-cell kagomé lattice cane; detail of a kagomé cane showing the packing rods fused to the jacket tube; a 7-cell double period cane; thin-core triangular lattice HC-PCF cane with interstitial rods; detail showing the interstitial rods.*

Fibre Drawing

The final stage of the fabrication process is to draw the cane to fibre. The cane is inserted into a second jacketing tube, in order to obtain a reasonable outer diameter (~125 μm) when the structure is drawn down to the required pitch. The jacketed cane can then be drawn to fibre. Similar to the cane pulling, a vacuum is applied between the cane and the jacket. Pressures may also be applied to the core and cladding region of the canes; this pressurisation allows control of the air-filling fraction of the fibre, and also ensures that the core maintains the correct dimensions with respect to the cladding structure. Independent pressures are applied to the cladding, hollow core and between the cane and jacketing tube using the pressurisation holder described in Figure 2-8.

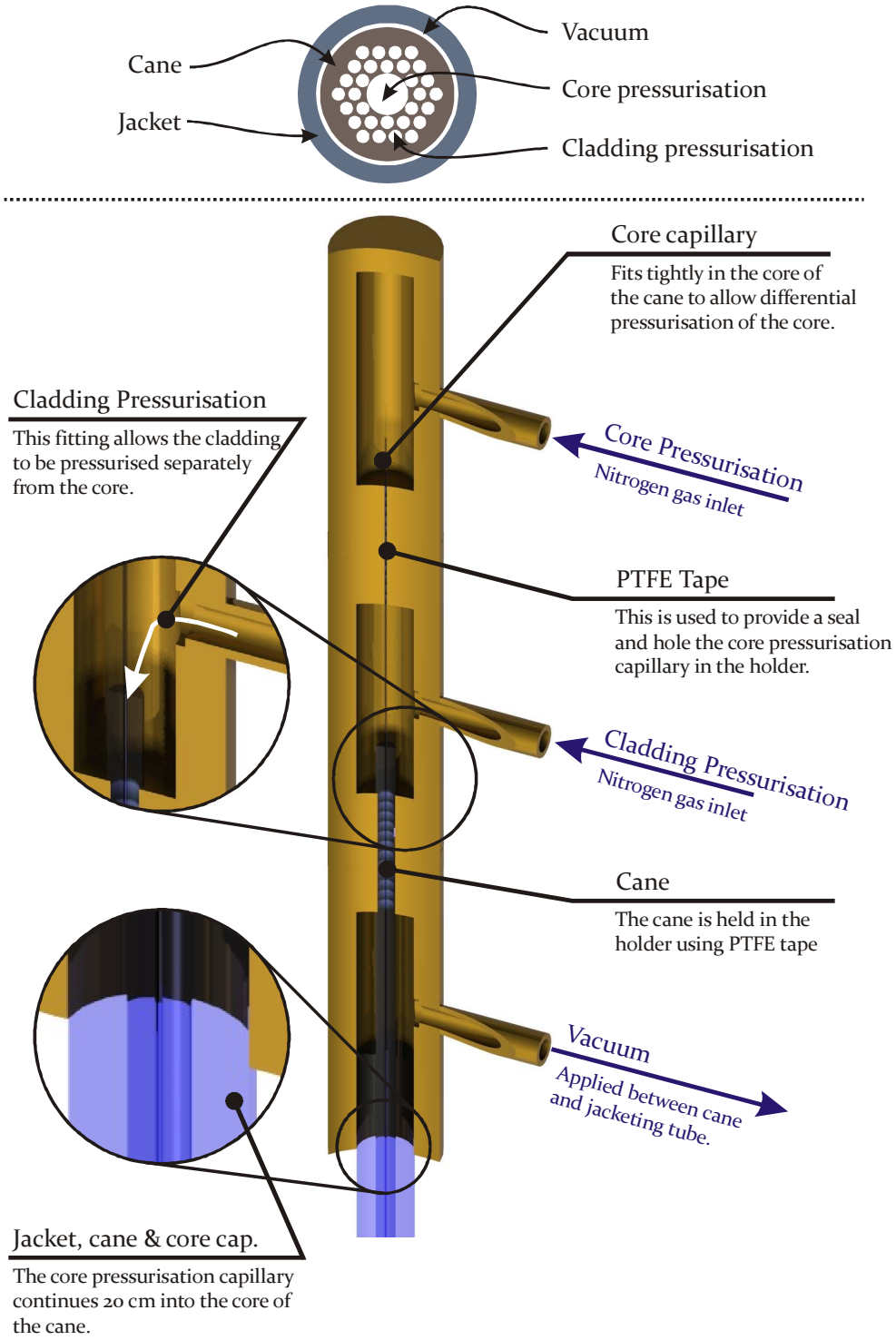

Figure 2-8: *Top: while drawing a cane to fibre independent pressures are applied to the core hole and cladding holes, and a vacuum is applied between the cane and jacketing tube. Main image: a cross-section through the holder used to provide the differential pressure between core and cladding.*

The fibre structure obtained is dependent on several other factors. The furnace temperature controls the tension at which fibre is pulled out of the furnace: if the

tension is too low the structure will have a tendency to be unstable; too high and the fibre will break. The speed at which the cane is fed into the furnace can also be adjusted. This changes the amount of time the cane spends in the hot-zone of the furnace and affects the final structure of the fibre. Obtaining the desired fibre structure requires careful balancing of all of these factors.

In the final stage of fibre fabrication a protective polymer coating is just before the fibre is wound onto a drum. To maintain compatibility with conventional optical fibres and their components, the outer diameter of the fibre is ~125 μm with the polymer coating bringing the overall diameter to ~250 μm.

A photograph of drawn fibre rewound onto a spool is shown in Figure 2-9, which also shows cross-sections of three hollow-core fibres. Once drawn the fibre is optically characterised as discussed in the following section.

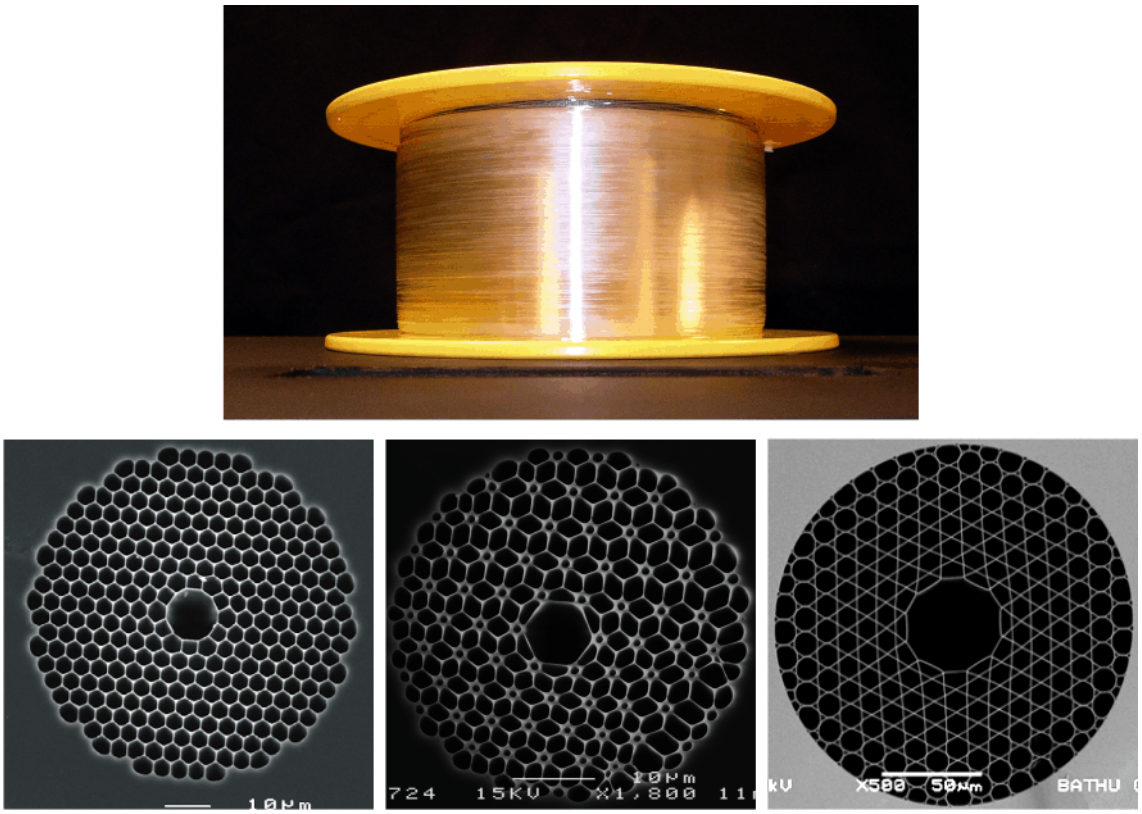

Figure 2-9: *Top: HC-PCF wound on a spool. Bottom: scanning electron micrographs of 7-cell core fibre cross-sections, from left-to-right: triangular lattice HC-PCF, double-period HC-PCF; kagomé lattice fibre.*

2.3 Linear Optical Fibre Properties

After fabrication, the drawn fibre is optically characterised to determine the suitability for its desired applications. This section describes typical measurement techniques to characterise the linear optical properties.

Transmission

A fundamental measurement of the guidance of an optical fibre is the transmission spectrum and optical loss. To obtain a broadband spectrum, an optical spectrum analyser is used. A supercontinuum light source [30] provides sufficient spectral power density to allow narrow-resolution measurements with the OSA, even with moderate fibre attenuation. A simple setup for measuring transmission is shown schematically in Figure 2-10.

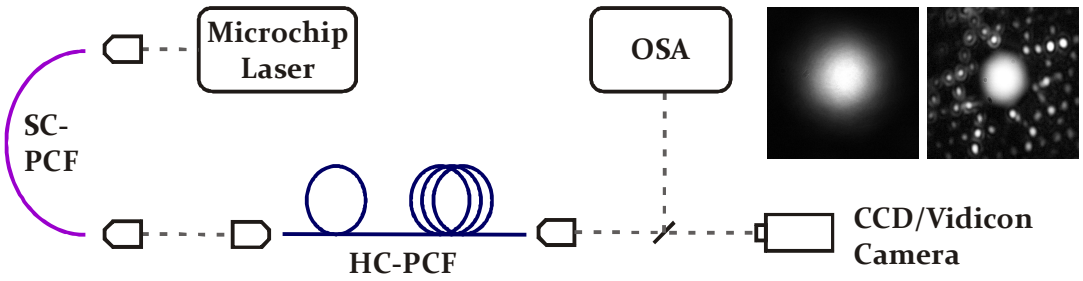

Figure 2-10: *Schematic of the fibre linear transmission and attenuation measurement scheme. OSA: optical spectrum analyser; SC-PCF: supercontinuum generating PCF. Inset: images of fibre output of a standard HC-PCF (left) and kagomé lattice HC-PCF (right) with the source deliberately defocused to highlight the cladding guidance.*

A CCD or vidicon camera is used to ensure good coupling to the mode of interest, which is usually the fundamental-like core mode. This is particularly important when using short lengths of fibre in which significant intensity may remain in the cladding, or kagomé fibre which also guides light in the silica cladding. The power of the microscope objective used to couple light from the supercontinuum source into the fibre is chosen to optimise coupling efficiency.

The transmission spectrum is typically measured using tens or hundreds of metres of fibre, depending on its attenuation. Loss measurements are performed using the *cut-back* technique. First, the transmission of a long length of fibre is measured. The fibre is then cut-back from the output end (typically to around one tenth of its original length), without altering the input coupling in any way. The transmission of the shorter length can then be used with the earlier measurement to determine the linear loss of the fibre.

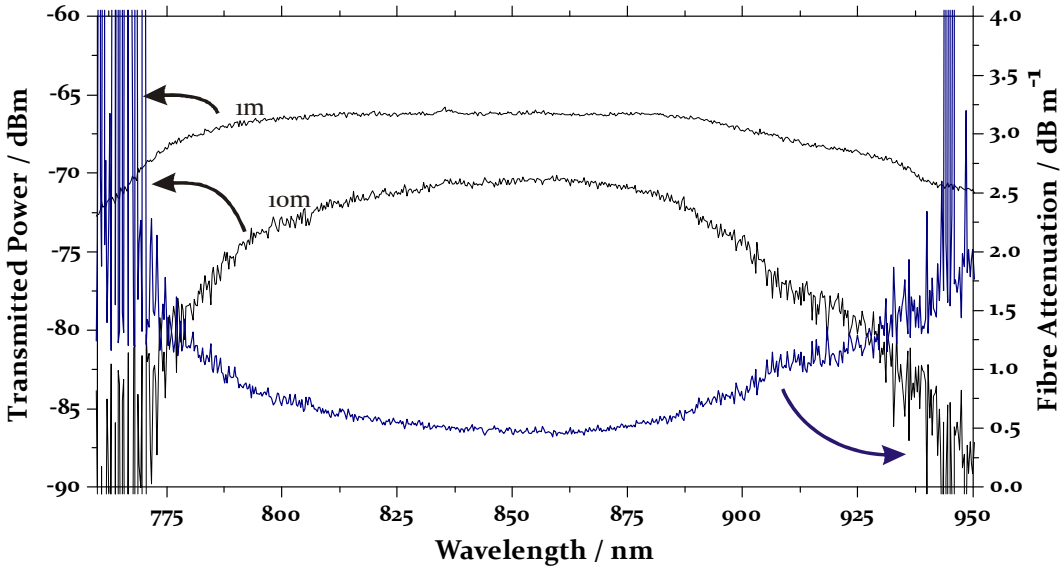

Figure 2-11: *Attenuation measurement of a HC-PCF. Thin and thick black curves are transmitted power through 1 m and 10 m of fibre respectively. The linear attenuation calculated from these is shown by the blue curve.*

Figure 2-11 shows the measurements taken to determine the loss of HC-PCF with bandgap centred at 850 nm; the black curves show the transmission of 1 m and 10 m of fibre, and the grey curve the calculated loss. Attenuation measurements of several fibres are compared in Figure 2-12. The right-hand and left-hand columns show the transmission of 7-cell core and 19-cell core fibres respectively. Each row corresponds to a different spectral bandgap location.

By comparing the minimum attenuation values shown it is clear that the shorter wavelength fibre exhibits significantly greater loss than at longer wavelengths. For the three 19-cell fibres presented in the graph, the minimum losses are 190, 20 and 10 dB/km respectively at 850 nm, 1060 nm and 1550 nm. This dependence is a result of scattering due to surface roughness of the silica, calculated to have an r.m.s. value of ~0.1 nm [31]. The actual roughness of the silica results from surface capillary waves that occur on the liquid silica surface as the fibre is drawn, which are themselves a result of surface tension. The roughness leads to a variation in effective refractive index and therefore the scattering of light from core modes to leaky cladding modes, which creates a source of attenuation.

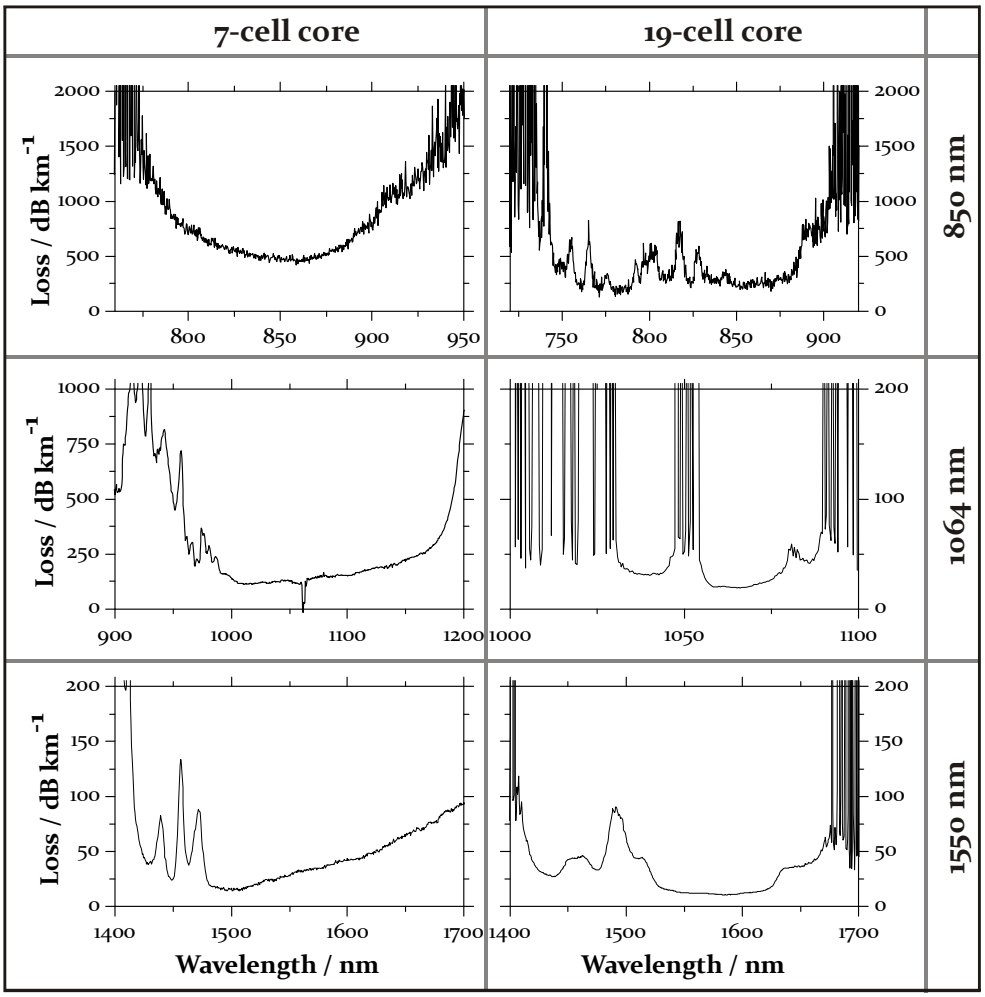

Figure 2-12: *Attenuation spectra for several triangular lattice HC-PCFs. Left and right hand columns are for 7-cell core and 19-cell core fibre respectively. From top to bottom the bandgaps are centred at ~850 nm, 1064 nm and 1550 nm.*

Reference [31] shows that the transmission loss due to surface roughness scales as $1/\lambda^3$, and that this is now the main source of attenuation in the lowest-loss HC-PCFs that have been reported. The $1/\lambda^3$ dependence has been observed experimentally; Figure 2-13 plots minimum loss against wavelength for the fibres of Figure 2-12, with open triangles for 7-cell fibre, and open diamonds for 19-cell fibre. The solid squares show the attenuation of other reported 7-cell core fibres, and the solid curve is a λ^{-3} fit to these points. The peak at 1064 nm in the 7-cell fibre is an artefact resulting from saturation of the OSA by the unconverted supercontinuum pump laser.

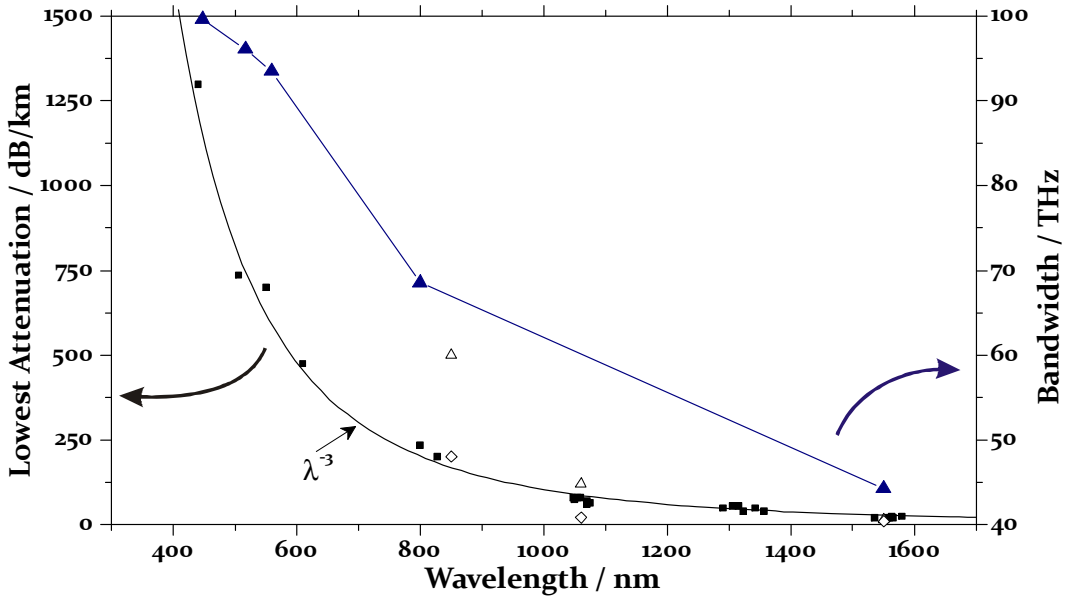

Figure 2-13: *The minimum losses for the fibres of Figure 2-12 are shown by open triangles and open diamonds for 7-cell and 19-cell fibres respectively. Solid squares are the lowest reported HC-PCF attenuation at a range of wavelengths, and the solid curve shows the expected λ^{-3} dependence of attenuation on wavelength.*

In addition to the wavelength dependence of attenuation, it is also evident that 19-cell core fibre has a lower attenuation than 7-cell fibre. This is particularly evident at shorter wavelength where at 800 nm, for example, the loss of 7-cell and 19-cell HC-PCFs are of the order 500 dB/km and 200 dB/km respectively.

The transmission of a 19-cell fibre across the bandgap is however not as smooth as that of a 7-cell fibre due to the many attenuation peaks throughout the transmission band, indicative of loss due to coupling with surface modes at the core wall. This reduces the useable bandwidth of such fibre.

The above results apply to triangular lattice photonic bandgap fibre. Kagomé lattice fibres, introduced in section 1.2.2 and shown in Figure 2-14, show significantly different transmission characteristics. Such fibres have broadband transmission, providing low-loss guidance throughout the majority of the visible and near-infrared. The transmission spectra of two kagomé lattice fibres, with 4 μm and 12 μm pitches are shown in Figure 2-15.

Kagomé HC-PCF, and indeed other cladding structure HC-PCFs with a pitch much greater than the wavelength of the core-guided light, demonstrate a loss of 1-2 dB/m across the guidance region, with occasional peaks of increased loss as explained in section 1.2.1. At wavelengths below ~550 nm the kagomé fibre has a loss similar to, or

even better than, PBG HC-PCF guiding at the same wavelength, while at the same time offering a much broader guidance region.

The low-loss guidance (compared to, for example, a hollow capillary) can be seen in the transmission spectrum of kagomé fibre with 12 μm cladding pitch shown in **Figure 2-15**. The guidance range corresponds to over 1000 THz, in comparison to a maximum of 100 THz in photonic bandgap HC-PCF.

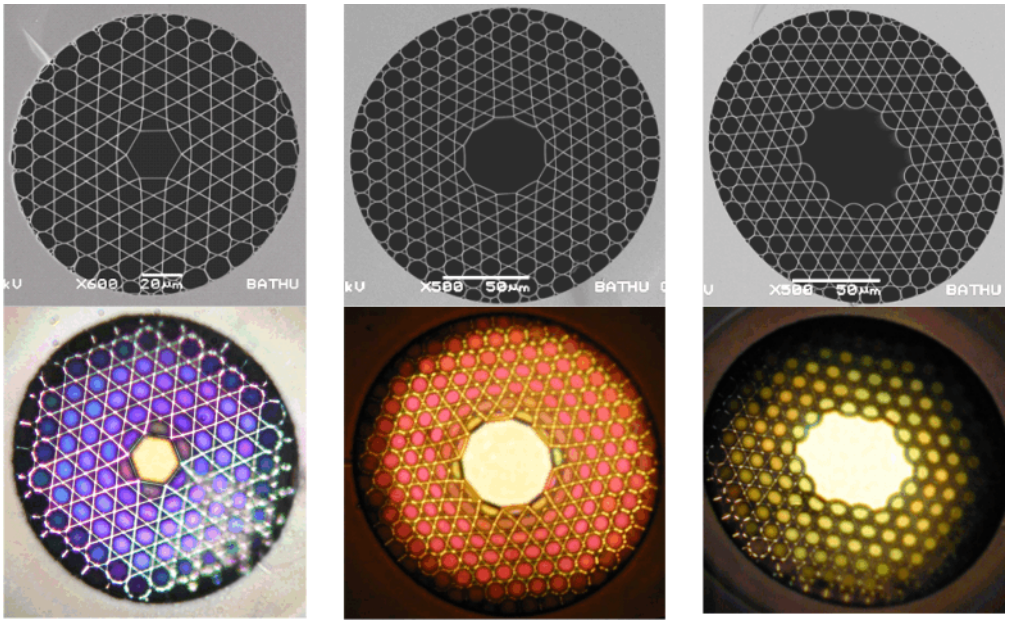

Figure 2-14: *Scanning electron micrographs (top) and optical transmission (bottom) of large-pitch kagomé lattice fibre with 1-cell (left), 7-cell (centre) and 19-cell (right) cores.*

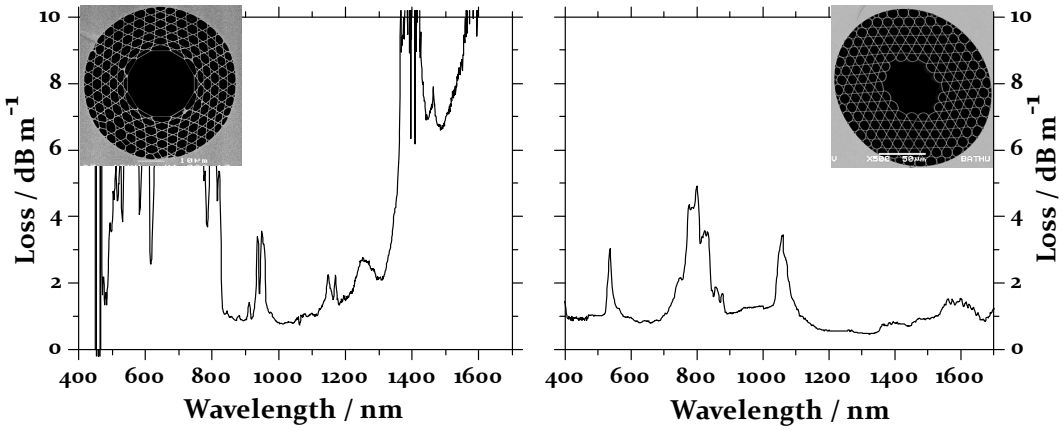

Figure 2-15: *Attenuation spectra of (left) 4 μm pitch and (right) 12 μm pitch kagomé lattice hollow-core fibre. Electron micrographs of each fibre are shown inset.*

Chromatic Dispersion

Another basic optical property of HC-PCF is the chromatic dispersion. This describes how the phase velocity $v(\omega) = \omega/\beta$ varies with wavelength throughout the transmission band of a fibre. As such, it determines the change in shape of a polychromatic pulse of light as it propagates along a fibre. The dispersion can be both detrimental and beneficial depending on the application; the exact dispersion can be tailored to a certain extent in the fibre design and fabrication process.

The dispersion of a propagating optical pulse is described by the group velocity dispersion (GVD). Experimentally this is determined through measurements of group delay, related to dispersion through equation 2-1.

$$D = \frac{\partial \beta_1}{\partial \lambda} \qquad 2\text{-}1$$

Here $\beta_1 = \partial\beta/\partial\omega$ is the group delay, or inverse of group velocity. The group delay is measured using a Mach-Zehnder interferometer with controllable reference arm length [32] (Figure 2-16). As used for measuring fibre transmission, a super-continuum source is coupled through a length of fibre placed in one arm of the interferometer, and a camera used to optimise the coupling to the fundamental mode. A typical length of fibre used for a group delay measurement is 15-50 cm; the dispersion is proportional to the length of the fibre.

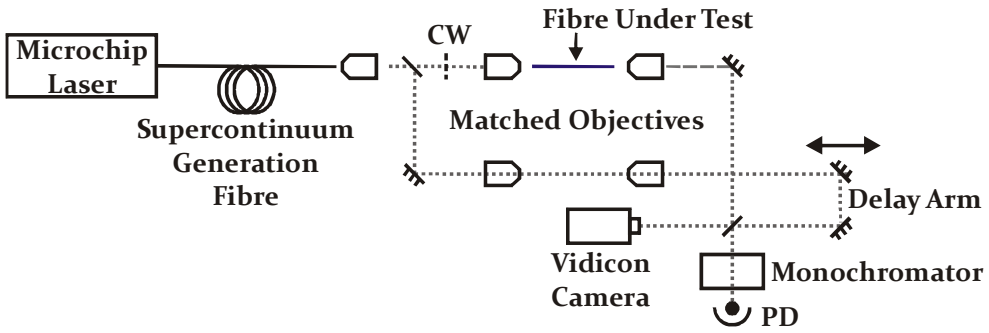

Figure 2-16: *Experimental setup for the measurement of fibre dispersion characteristics, based on a Mach-Zehnder interferometer. PD: photodiode; CW: chopper wheel.*

To improve the sensitivity of the interferometer, a chopper wheel is placed in the fibre arm, and phase-sensitive detection is used. A monochromator positioned after recombination of the two arms is used to select the wavelength range at which the group delay is to be measured; the monochromator has a 3 nm resolution. To match the path lengths of the two arms, a retro-reflector is positioned on a precision translation stage in

one arm. The arm length is swept under computer control, while monitoring the signal at the photodiode. The appearance of fringes as the arm length is swept indicates the matched arm lengths; a typical trace is shown in Figure 2-17.

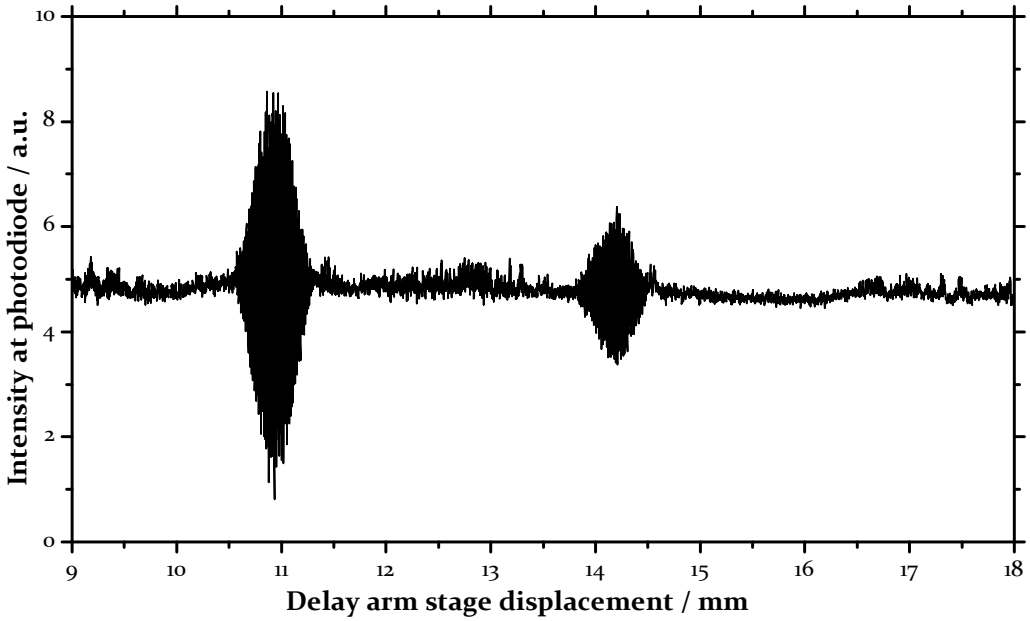

Figure 2-17: *Group delay measurement for a 15 cm 7-cell HC-PCF at 1070 nm, plotting the intensity at the photodiode as a function of retro-reflector displacement. The change in arm length of the reference arm of the interferometer is twice the mirror displacement. The left-hand set of fringes corresponds to matching arm lengths for the fundamental mode, and the second set of fringes for a higher-order or surface mode.*

The large set of fringes at ~11 mm corresponds to a matching length of the arms for the fundamental core mode of the fibre. Further fringes occur due to higher-order modes and surface modes, such as those at 14.2 mm. These are smaller in amplitude than the main set of fringes as the input coupling was optimised to excite these modes as little as possible. The group delay is determined from the mirror displacement by $t_{gd} = 2d_m/c$, where d_m is the mirror displacement.

This group delay measurement is repeated at small wavelength intervals. The dispersion is then obtained by fitting a curve to the group delay data, and differentiating with respect to wavelength. A subset of the data for one particular fibre (a 7-cell HC-PCF with bandgap centred at 1060 nm) is plotted in Figure 2-18. Each coloured trace is a measurement of intensity against mirror displacement for a single-wavelength, as shown on the x-axis. The black circles plot the measured group-delay as a function of wavelength for a full set of data.

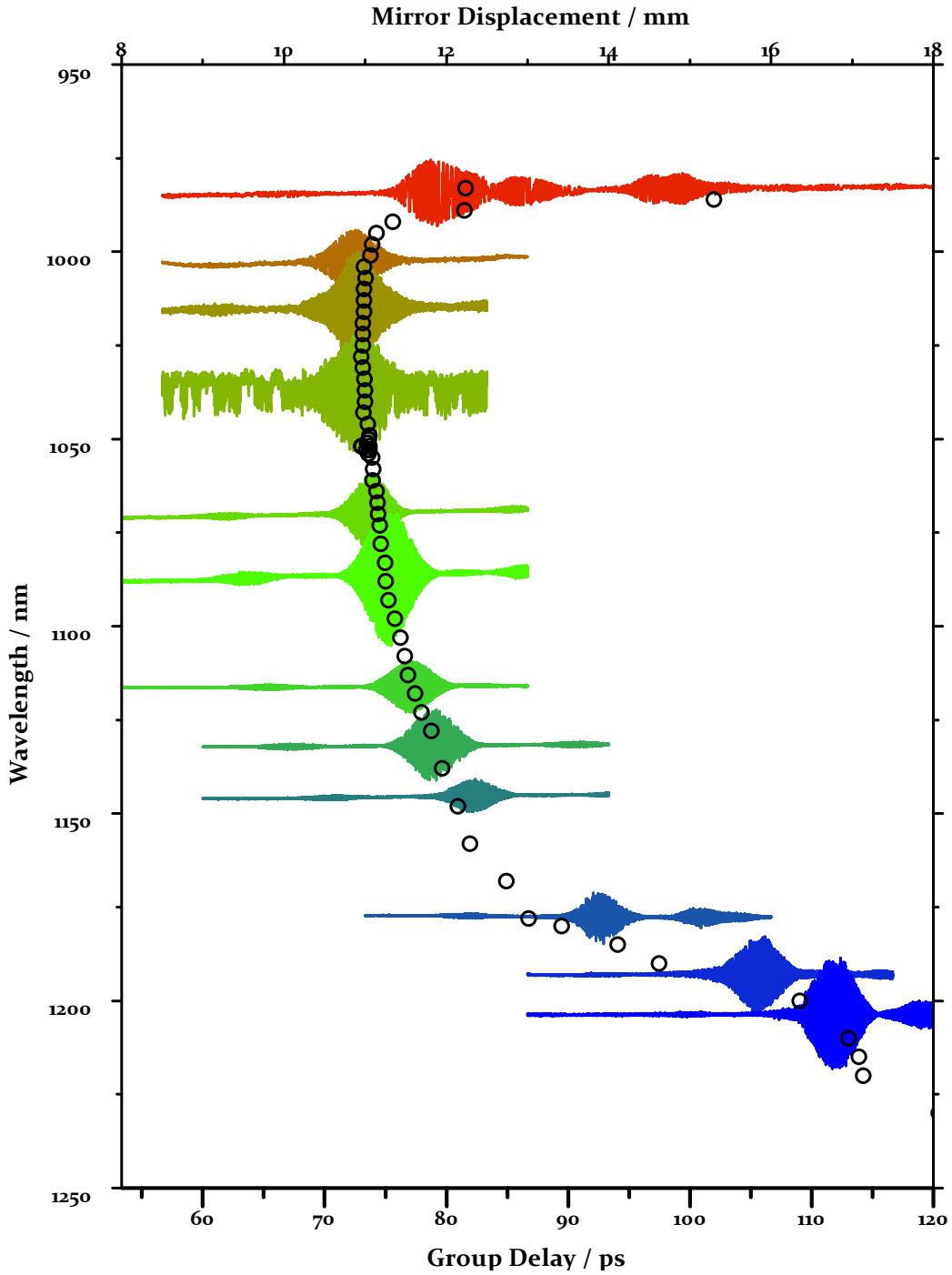

Figure 2-18: *Dispersion group delay measurements of a triangular lattice HC-PCF with bandgap centred at 1060 nm. Each trace represents the amplitude of the received signal as the arm length is scanned for a different wavelength, as indicated on the x-axis. The group delay is calculated from the position of the fundamental peak, and is plotted against wavelength (black circles).*

The dispersion is the wavelength derivative of the time delay ($D = dt_d/d\lambda$), and is typically expressed in ps nm^{-1} km^{-1}. HC-PCF typically has an 'S'-shaped dispersion curve, as would be expected from any resonator. In many fibres the dispersion is strongly

influenced by anti-crossings between core and surface modes of the fibre, leading to the behaviour shown in Figure 2-19 for a 7-cell fibre with bandgap centred at 1060nm. In the wavelength regions indicated by the boxes it can be seen that there are small increases in the fibre attenuation, and the dispersion points show more significant deviation from the fitted curve. Both of these effects are due to the presence of weak coupling between the fundamental core mode and surface modes.

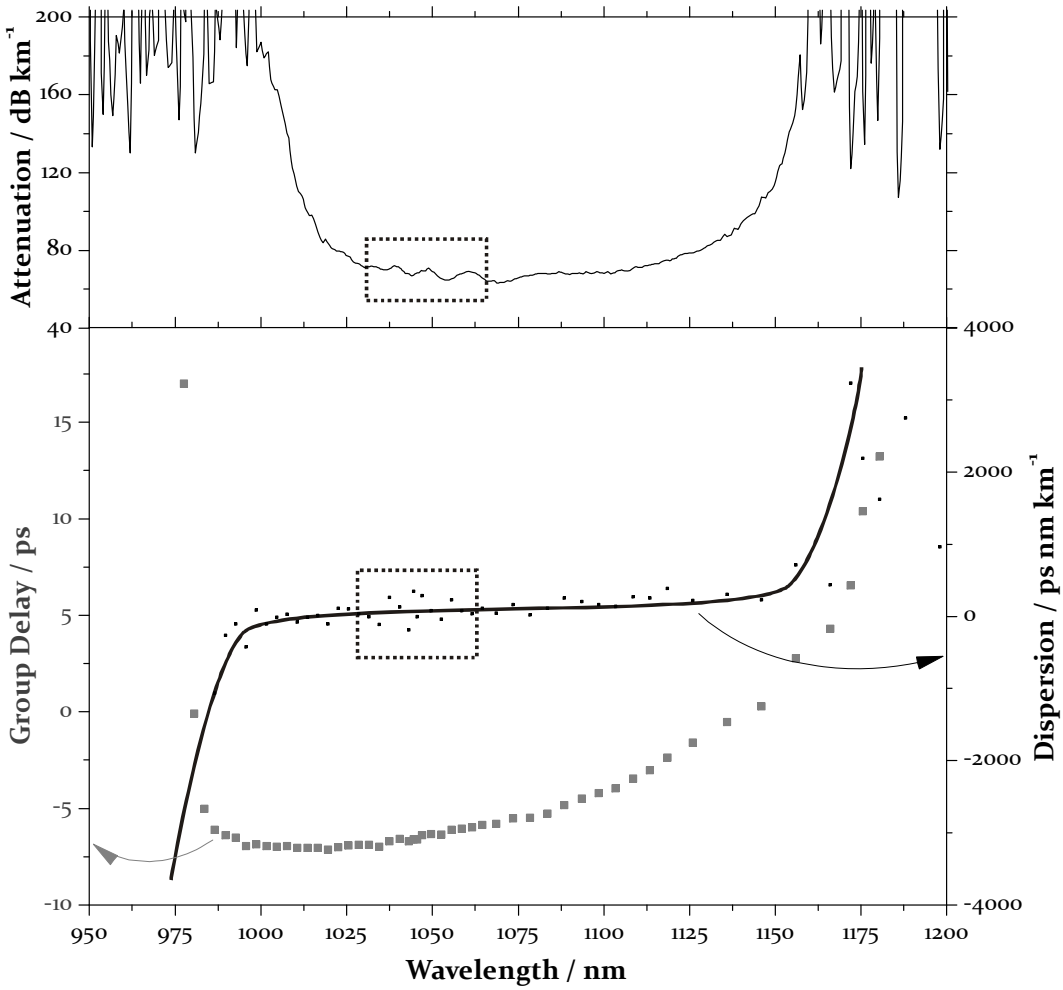

Figure 2-19: *Bottom: The dispersion curve (black line) is derived from group-delay measurements at regular wavelength intervals (grey points), in this case for a 7-cell HC-PCF with bandgap centred at 1075 nm. Top: attenuation spectrum for the same fibre.*

Spatially Resolved Measurements

In the previous sub-section we saw that dispersion measurements resulted in multiple sets of interference fringes due to multiple excited modes within the fibre. From the measurements taken it was not possible to determine which modes gave rise to each set of fringes, and therefore determine the dispersion of each individual mode, such as fundamental mode, higher-order core mode, or surface mode. This is particularly

difficult in the case where the propagation constant β of a surface mode is close to that of a core-mode, for example in the region of an anti-crossing event.

An imaging technique has been developed which allows the identification of the modes during the dispersion scan, and can therefore determine the dispersion of each mode. This is possible since core modes and surface modes are spatially resolvable. The technique involves capturing a video of the interference of the overlapped beams in the Mach-Zehnder interferometer, in the setup shown in Figure 2-16, as the reference arm length is scanned. Each frame of the video is then divided into regions corresponding to the spatial locations of the maximum intensity for each mode of interest, and the total intensity of each region calculated as a function of frame number and therefore arm length. In doing this, interference patterns are built up, as for the usual Mach-Zehnder interferometer technique discussed above; however, in this case there is an interferogram for each region the fibre is divided into. By suitable choice of regions, the dispersion of each mode can be separated.

The group delay is determined by matching the time at which the fringes occur in the video with the reference arm length at that time.

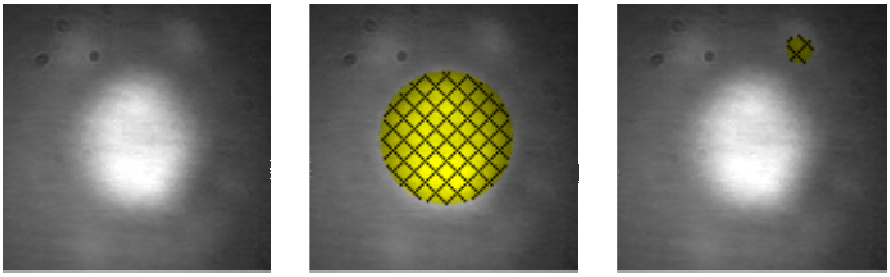

Figure 2-20: *Example frame (left) and masks used for spatially resolved dispersion measurement analysis. The centre and right-hand images show the regions chosen (hatched areas) to distinguish between core and surface modes.*

A typical set of masks used, and a sample frame, are shown in Figure 2-20. The central image shows the region chosen to monitor the fundamental core mode; the centre of the mode pattern is used as this is its point of maximum intensity. The right-hand image shows the region selected for monitoring of a surface mode. The integrated intensity in these regions is plotted against video frame number and reference arm length in Figure 2-21.

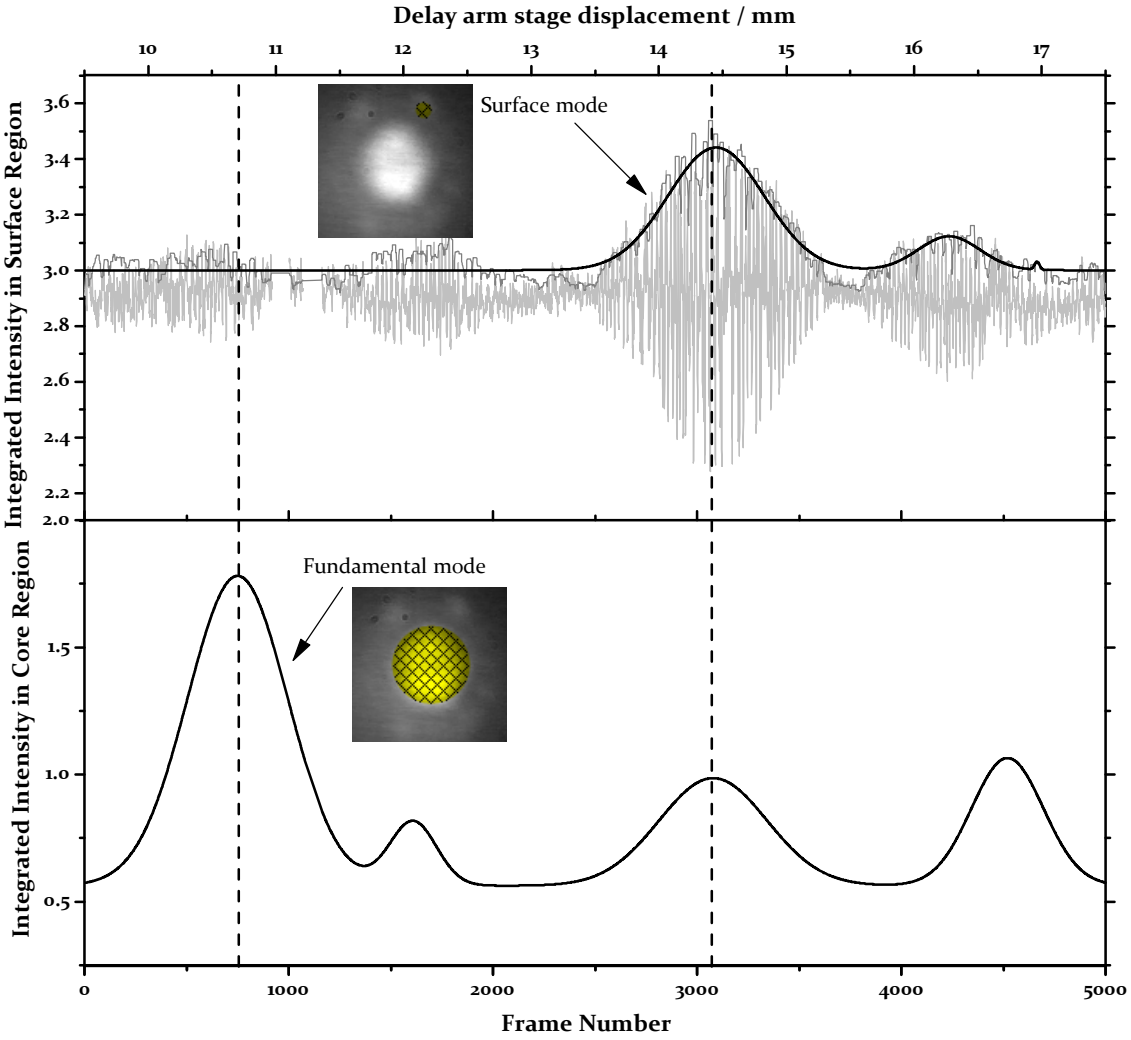

Figure 2-21: *Determination of dispersion using the spatially resolved technique. The top graph shows the steps of analysis for the surface data, as explained in the main text. The arms are matched in length for this mode at a stage displacement of 14.4 mm. The lower graph shows the result of analysis of the core region (highlighted inset); this shows a matched arm length of ~10.7 mm for the fundamental mode. The additional peaks are related to higher-order core modes, which also have a non-zero intensity in the masked region.*

The lower graph in Figure 2-21 shows a set of fringes for the surface region at the same location as the second set of fringes in Figure 2-17; from this it is then known that these fringes are the result of matched arm lengths for the surface mode.

This method allows the dispersion of the different modes to be measured. By appropriate choice of integration regions this technique can also be used to distinguish between matched arm lengths for higher-order core modes and surface modes, allowing the dispersion of the higher-order mode to be determined correctly.

2.4 Modal Properties at Anti-Crossings

As discussed in section 1.2, HC-PCF supports surface modes, and the coupling of light from core modes to such surface modes is a major source of attenuation. Typically this is seen in a transmission spectrum as loss peaks in an otherwise flat transmission. While strong coupling between core and interface modes leads to high loss, the effects of weaker coupling are more subtle, such as variations in group velocity dispersion. These effects can be detrimental in spectroscopic and coherent optics applications such as those considered later in chapters 5 and 6; in particular, the interaction between surface modes lifts the degeneracy between core modes and gives rise to the mode beating that can be seen experimentally in section 5.2.

The nature of the interactions between core modes and surface modes is therefore important in accessing the suitability of HC-PCF in applications. In this section, the effects of anti-crossing events on the modal electric field distribution of fundamental and higher-order core-modes are predicted theoretically and investigated experimentally.

Modelling results

To understand the effects of anti-crossing events that can be observed experimentally, it is important to consider theoretically the effect of such events. The calculations in this section are for a fabricated 7-cell HC-PCF with the bandgap centred at 850 nm; the analysis is valid for any bandgap HC-PCF of this structure by appropriate scaling. The modelled fibre and calculated density of photonic states are displayed in Figure 2-22.

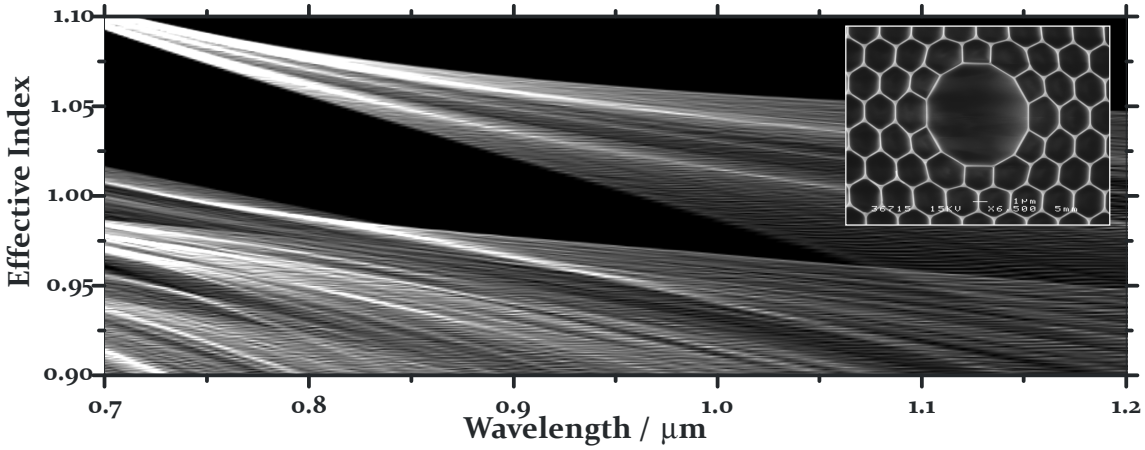

Figure 2-22: *Density of photonic states calculated for the cladding structure illustrated in the electron micrograph shown inset.*

The core and surface modes for the fibre have been calculated[5] at regular wavelength intervals across the bandgap, with a high-resolution interval of 0.25 nm in the regions of interest in which anti-crossing events occur between core and surface modes. In addition to the effective index, the electric and magnetic field distributions are calculated for each mode. Examples of the calculated field distributions and intensity profiles are shown in Figure 2-23 for a surface mode, fundamental core mode and higher order core mode.

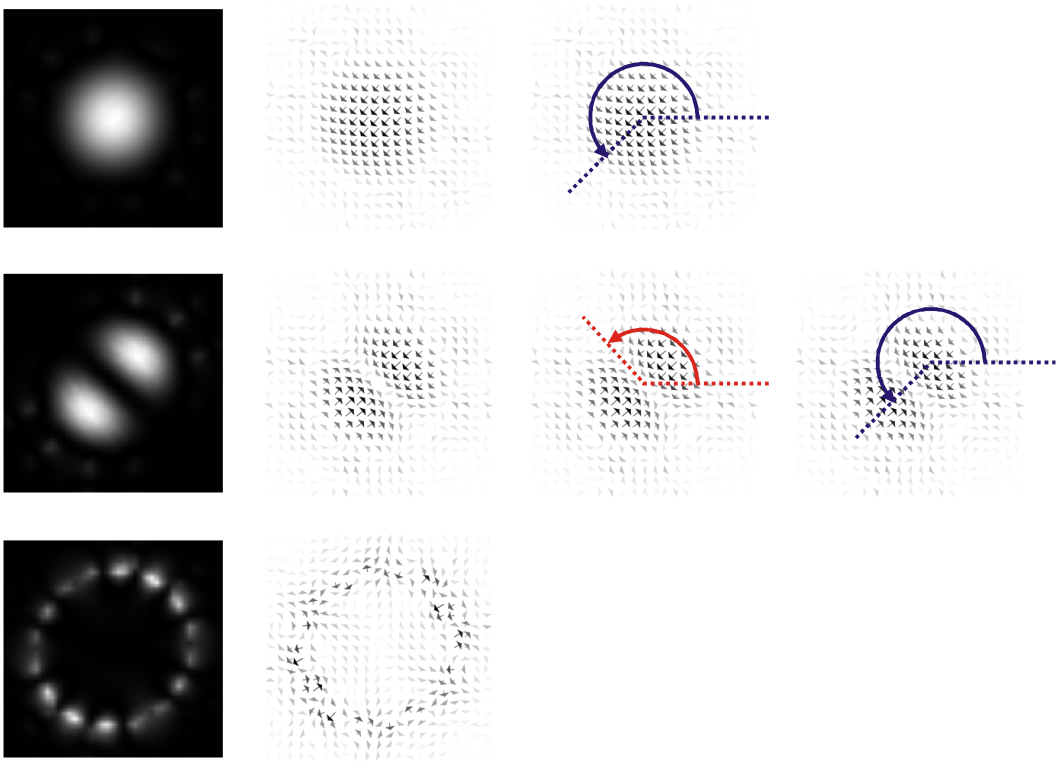

Figure 2-23: *Calculated intensity profiles and electric field distributions for (top) fundamental core mode, (middle) higher-order core mode and (bottom) surface mode. The definition of angles chosen to characterise fundamental and higher-order cores modes are shown to the right of the figure.*

Of interest theoretically and experimentally is the change of symmetry axis that occurs in the region of an anti-crossing event due to residual interaction of core and surface modes, which may be observed by the change in mode patterns. In order to evaluate the calculated mode patterns several angles are defined, as illustrated in Figure 2-23. For the

[5] The mode calculations were performed by P. J. Roberts. The modes are actually calculated at a particular normalised frequency kΛ, with the frequencies chosen to give regular wavelength spacing for the modelled fibre.

fundamental core mode a single angle is introduced, measuring the angle of the real part of the electric field at the centre of the core with respect to an arbitrarily chosen fibre axis (horizontal in the figure). For higher-order core modes, two angles are defined. First, the angle between the chosen axis and line of minimum electric field that lies between the two lobes of the mode pattern, and second, the angle of the electric field at the point of maximum intensity.

As stated earlier, the effective index of each mode has been calculated as a function of wavelength, and the mode locations (open circles) and the deduced mode trajectories (lines) are plotted in Figure 2-24. As discussed in Chapter 1, core-modes are associated with a small change in propagation constant with wavelength, and appear nearly horizontal on the plot, while surface modes have a much stronger dependence on wavelength. In the diagram the two polarisations of the fundamental HE11 modes have the highest effective index (~0.992-0.997), with the four nearly degenerate HE12 higher-order core modes having a lower effective index (0.982-0.990).

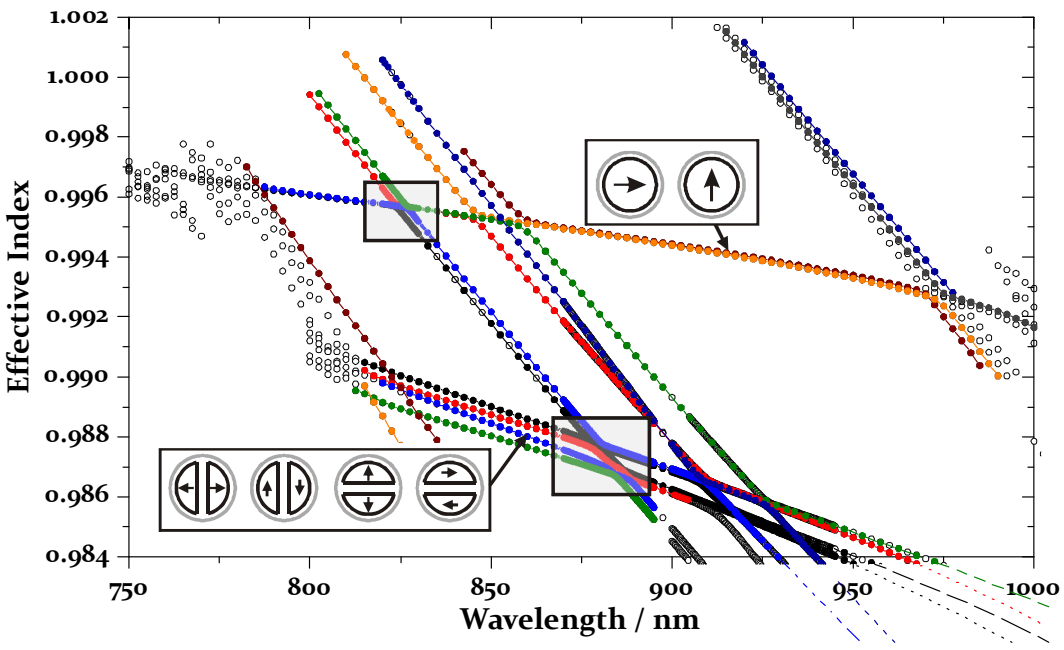

Figure 2-24: *Calculated mode co-ordinates of guided modes of a HC-PCF with bandgap centred at 850 nm. The regions highlighted indicated anti-crossings between surface modes (steep gradients) and either fundamental core modes or higher-order core modes.*

Highlighted in Figure 2-24 are two regions of interest where anti-crossings exist between core-guided mode and surface modes. The noticeable effect of the surface modes is the lifting of the degeneracy between the pair of fundamental core modes, and also the quartet of higher-order modes. However, the anti-crossing events also have an effect on

the mode pattern, and it is useful to consider the change in characteristic angles of the field patterns as introduced above.

Figure 2-25 includes a detail of the anti-crossing events between the fundamental core-mode and surface modes, where it is seen that one crossing (AC1 at 823.9 nm) is between a surface mode and one polarisation of the fundamental mode and the other crossing (AC2 at 827.0 nm) is between the second surface mode and orthogonal core mode. The electric field distribution of the core modes prior to, between and after the anti-crossings is illustrated, together with those of the surface modes away from the anti-crossing events.

The middle graph of Figure 2-25 plots the difference in refractive index, or equivalently difference in propagation constant (linearly proportional to Δn over this wavelength range) between the two modes involved at each anti-crossing, as a function of wavelength. This allows the point at which the anti-crossing modes are closest to be identified, and these wavelengths are indicated by the vertical grey lines on the figure (solid for AC1; dotted for AC2). The strength of the anti-crossing is also measured by $\Delta\beta$, where a larger value is indicative of a stronger anti-crossing.

The lower graph of Figure 2-25 plots the resultant direction (relative to a chosen fibre axis) of the real part of the electric field in the core region for each of the four mode trajectories; solid lines are used for the modes involved in the first anti-crossing, and dashed lines for modes involved in the second anti-crossing. It can be seen that at 820 nm the core-mode field angles are orthogonal (red and purple curves), as is expected to be the case for odd and even HE11 modes [33]. Away from the anti-crossing events this remains the case for core modes, as seen for the (red and green) core modes at 825 nm between the two anti-crossings, and the (green and blue) core modes at 830 nm.

It is observed that the field angles of the core modes before interaction with the surface modes occurs (225° and -45° for upper and lower branches respectively) are ~180° from those of the core modes after the anti-crossing events (40° and 130° at 830 nm). The 180° flip is a result of the method employed for calculating the field profiles[6]. Of interest is the fact that after accounting for this artefact, the field angles for the two core modes are identical before and after the interaction with the surface modes; this is observed to be true for additional anti-crossing events between fundamental core and surface modes that are not shown here.

[6] The field angle calculated is corrected to be consistent along each mode trajectory; the 180° flip in field angle is thus only observed relative to other mode trajectories, as is the case when, for example, comparing the field angle of the highest effective index core mode, which is given by different mode trajectories either side of the mode anti-crossings.

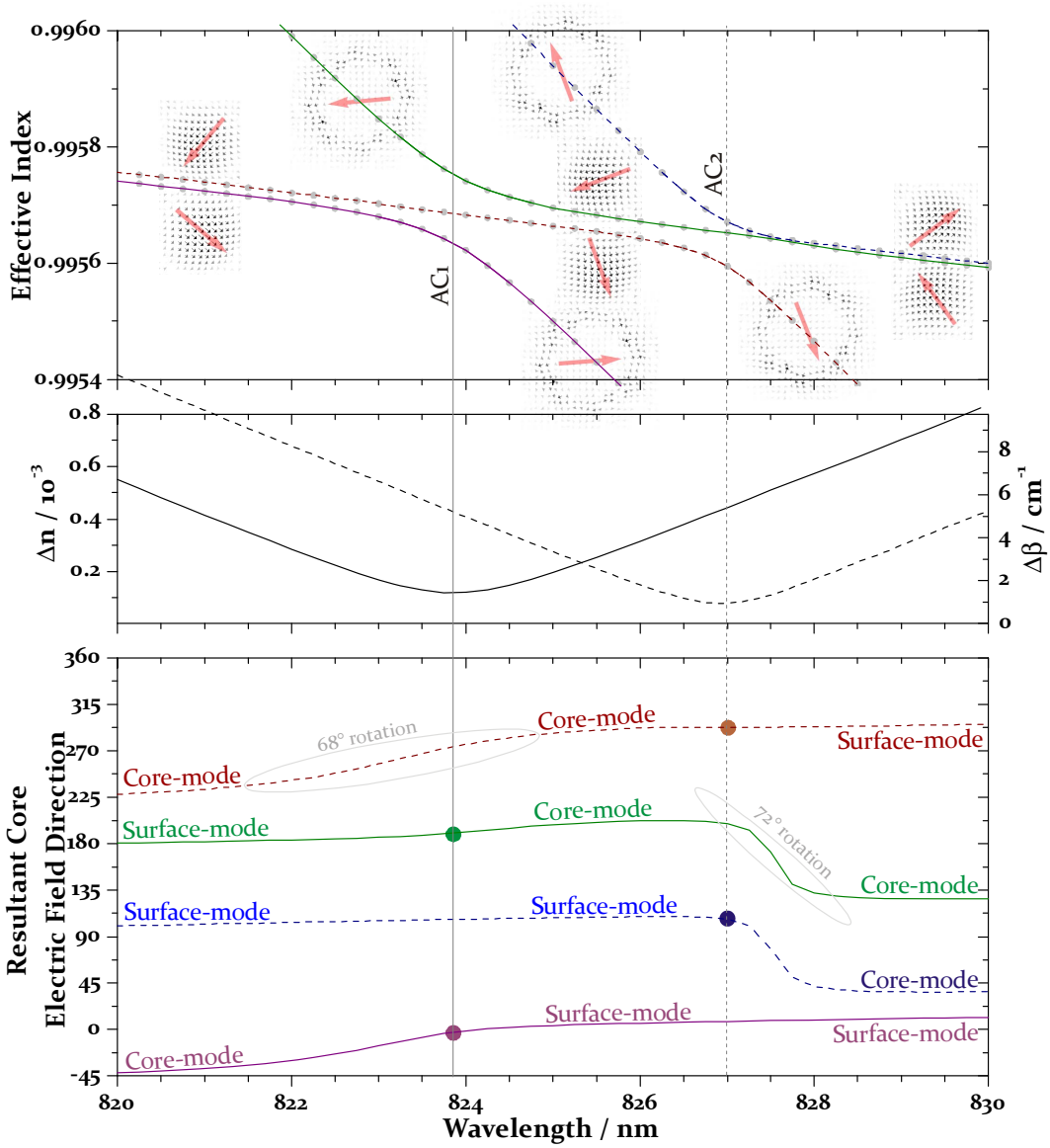

Figure 2-25: *Top: mode-trajectories showing two anti-crossings: AC1 between mode trajectories indicated by solid lines and AC2 between trajectories illustrated by dashed lines. Middle: Difference in effective index (Δn_{eff}) and propagation constant ($\Delta\beta$) between the modes involved in each anti-crossing. Bottom: Result electric field angle in the core region for each mode. The solid and dashed vertical lines indicate the wavelength of minimum $\Delta\beta$ between anti-crossing modes.*

Considering now the effect of the anti-crossings between core and surface modes, the surface mode field profiles away from the anti-crossing event are indicated on the top graph of Figure 2-25. In the anti-crossing regions (~823 nm to ~825 nm for AC1), coupling occurs between the anti-crossing modes, and the field profiles become a combination of core and surface modes. This is clearly seen in Figure 2-26 which shows the electric field and intensity profiles of each of the four mode trajectories at regular wavelength

intervals in the region of the anti-crossing events. At the central wavelength of AC1 (indicated by the dashed black box in the figure), the anti-crossing modes have similar power in both the core and surface regions.

Returning to consideration of the predominant core field angle, illustrated in the lower graph of Figure 2-25, the field of the interacting core mode at AC1 (purple curve) is observed to rotate in the 4 nm on the short wavelength side of the anti-crossing. Interestingly, the non-interacting core mode is also observed to undergo a rotation, as is required to maintain the orthogonality condition between the two fundamental core modes ($\int d^2r(\boldsymbol{E}_1 \times \boldsymbol{H}_2^*) \cdot \hat{z} = 0$). A similar rotation of the core modes is seen on the long-wavelength side of AC2.

In addition to being of scientific interest in its own right, the rotation of field direction at anti-crossing events offers an experimental means to potentially observe even weak anti-crossings, which may have undesired effects when HC-PCF is used for applications such as precision spectroscopy and quantum optics. The examination of anti-crossings between higher-order core modes and surface modes is now considered, as the intensity profile of such modes allow the rotation of field in the region of anti-crossing to be observed more clearly.

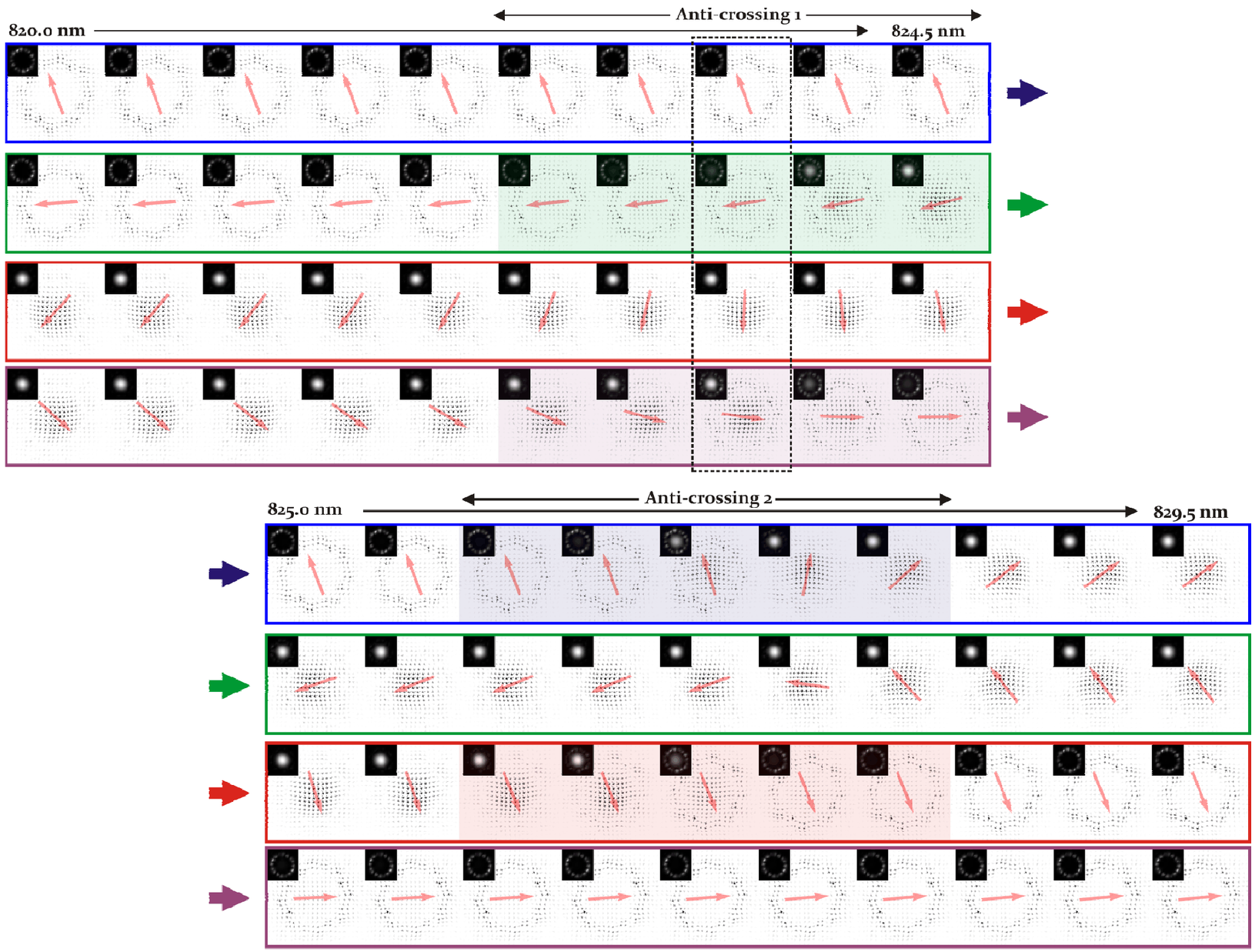

Figure 2-26: *Electric field distribution as a function of normalised frequency for the guided modes shown in Figure 2-25. The red arrow in each plot shows the average field direction within the core region. The inset images display the intensity profile of each mode. The greyscale represents minimum to maximum field amplitude in a given image, and thus the strengths are not directly comparable between images.*

As discussed above and illustrated in Figure 2-27, the LP11 higher-order set of four nearly-degenerate modes are formed by linear combinations of the TE01, TM01 and HE21 modes.

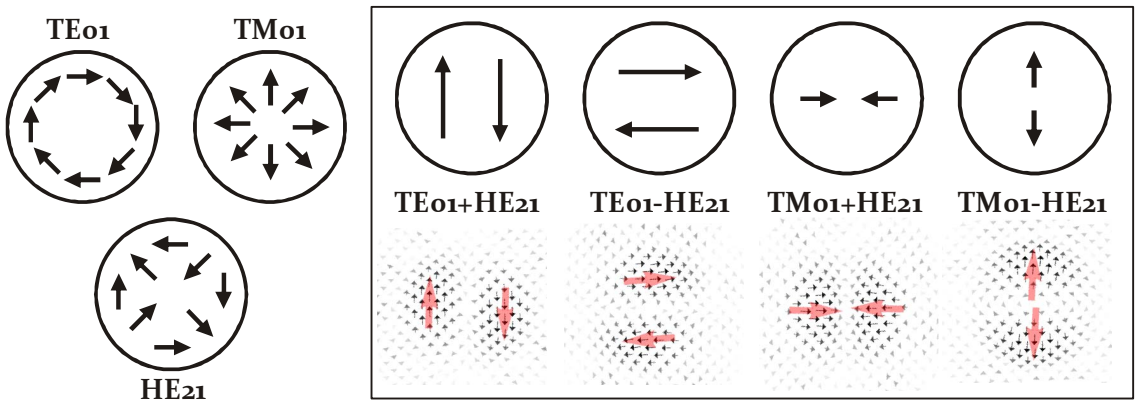

Figure 2-27: *Formation of the LP11 higher order modes of HC-PCF. Each mode is a linear superposition of TE01, TM01 and HE21 modes, shown both schematically and numerically calculated for a fabricated HC-PCF.*

A detail of the mode trajectories modelled for the HC-PCF in the region of anti-crossings between these higher order modes and two surface modes is shown in Figure 2-28. The dotted black lines represent the extrapolated paths that the mode trajectories would take in the absence of coupling between the core- and surface-modes. As for the analysis of the fundamental mode anti-crossing above, the transverse electric field profile of each mode either side of the anti-crossing region (at 870 nm and 895 nm) is also shown in the figure. The four higher order core mode, from highest to lowest effective index, are TE01+HE21, TM01+HE21, TE01-HE21 and TM01-HE21 respectively.

To analyse this data two parameters introduced in figure Figure 2-23, the field angle and mode angle, will be used. The mode angle is the angle between the line of minimum intensity in the core, and a chosen fixed fibre axis. This gives an angle between 0° and 180°, but the resolution (in wavelength) of the simulated modes is sufficient that rotation of the mode angle be smoothly followed. The field angle is the direction of the field at point of maximum intensity in the core region. For higher-order core modes there are clearly two maxima with equal and opposite electric field; one maximum is chosen arbitrarily at the shortest wavelength, and followed as the wavelength in increased in small steps.

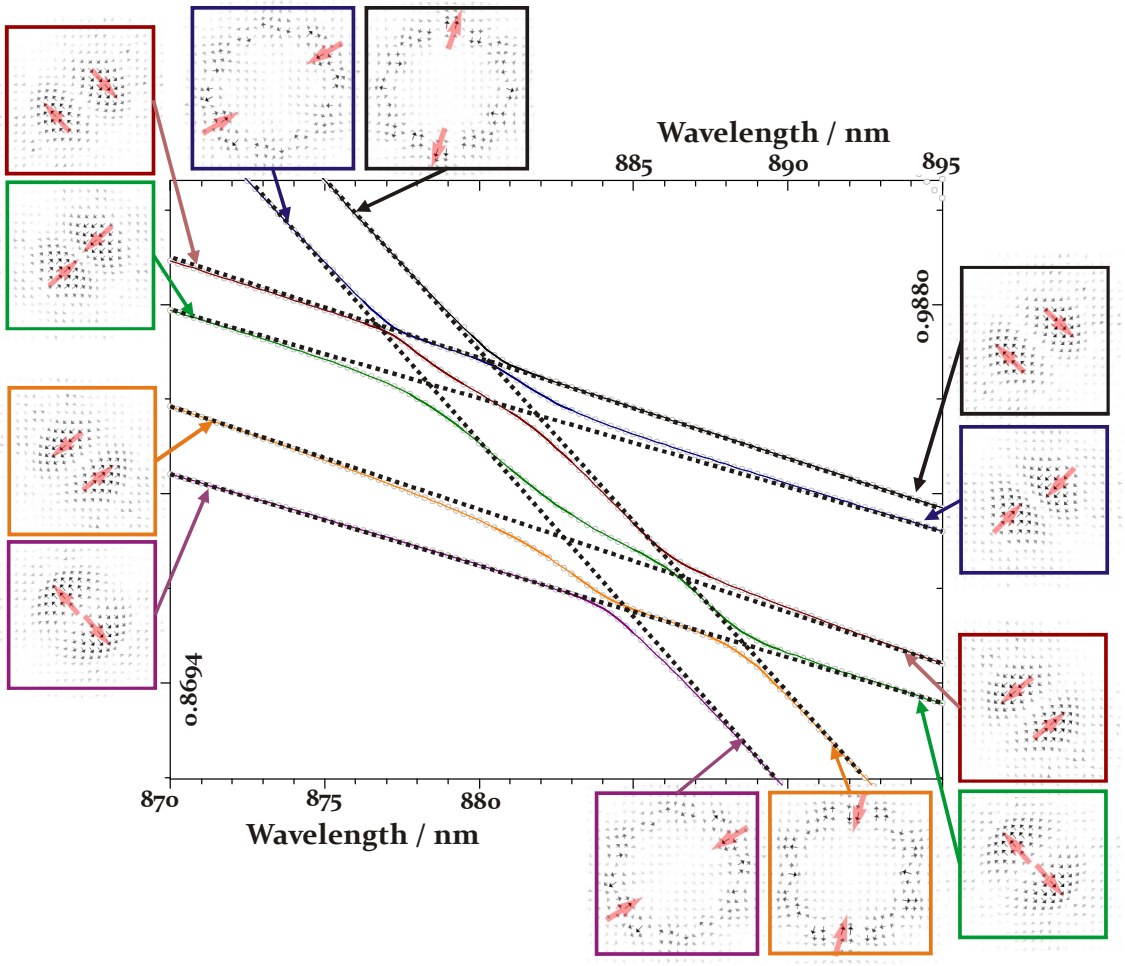

Figure 2-28: *Detail of anti-crossings between LP11 higher-order core modes and two surface modes. The electric field distribution of each mode is shown at 870 nm and 895 nm.*

The determined mode and field angles for each mode trajectory are shown in Figure 2-29. The top graph in this figure plots the effective index difference between each pair of interacting trajectories; the line style in this graph matches the line style of the vertical grey lines that show the location of each anti-crossing event throughout the figure. The three strongest anti-crossing events are labelled 1, 2 and 3 respectively. The middle graph plots the mode angle for each trajectory, and the lower graph the field angles.

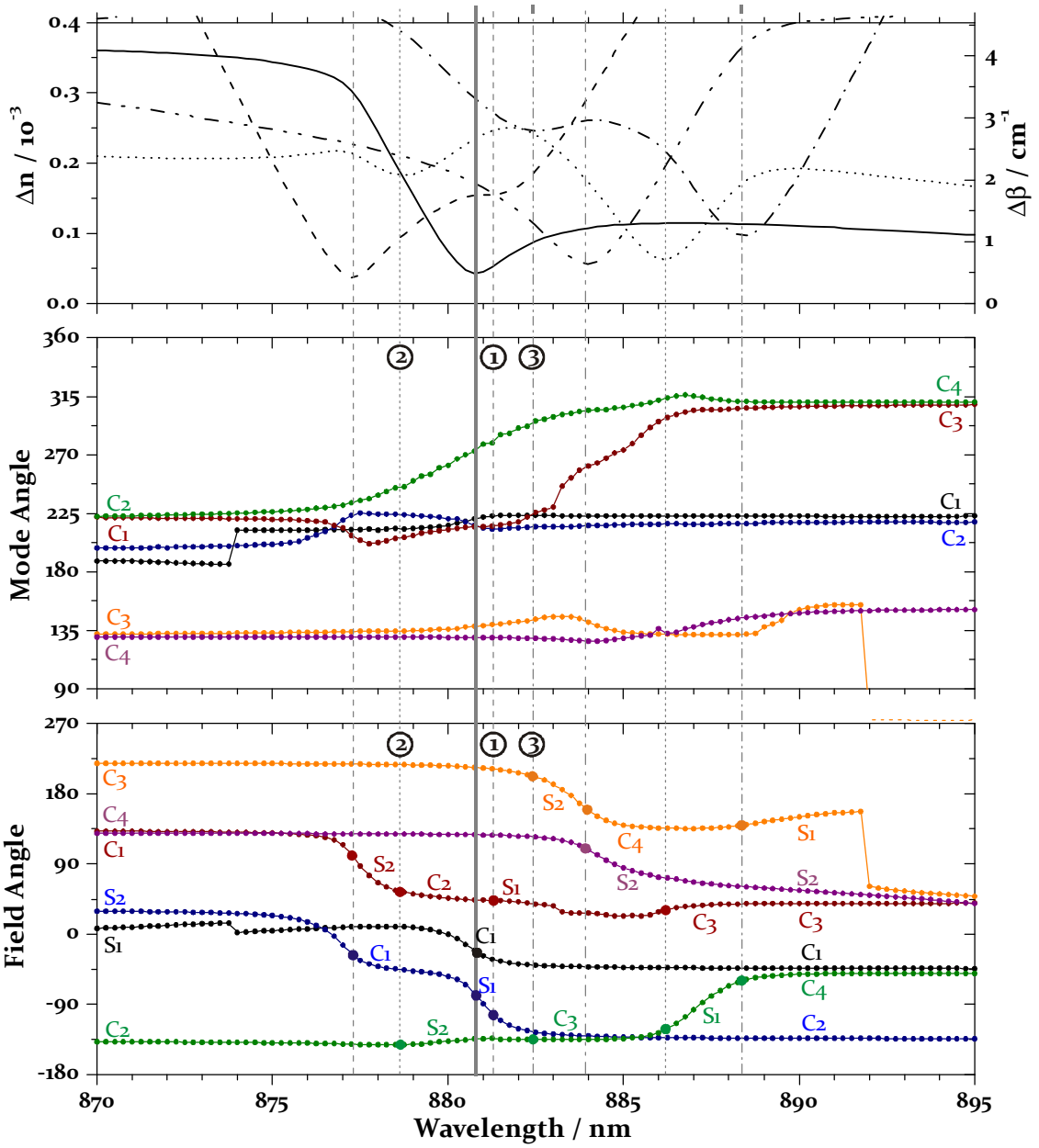

Figure 2-29: *Top: effective index difference between each pair of modes. Solid: black & blue; dashed: blue & red; dotted: red & green; dot-dash: green & orange; dot-dot-dash: orange and purple. Middle: Mode angle (as defined in main text) for each mode as a function of wavelength. Bottom: Field angle as a function of wavelength for each mode.*

Considering the two highest index core-modes at 870 nm, and again at 895 nm, it is seen that their mode angles are identical both before and after the anti-crossings; the same is true for the lower index pair of core-modes. In each of these cases the field angles are orthogonal both before and after the anti-crossings.

As observed for anti-crossing involving the fundamental modes, the higher-order mode anti-crossings also result in a rotation of field angle and mode angle. The most

significant changes in mode angle are observed for the red and green trajectories, which indicate the highest-index core-modes at short wavelengths and lowest-index core-modes at long wavelengths. The field angle for these modes rotates by 90° moving across the two anti-crossings.

To simulate the effect of the anti-crossings experimentally, it is useful to consider superpositions of the modes. The results below assume equal coupling to each higher-order core mode; experimentally this is difficult to achieve, but the results for asymmetric coupling to each mode show a similar behaviour.

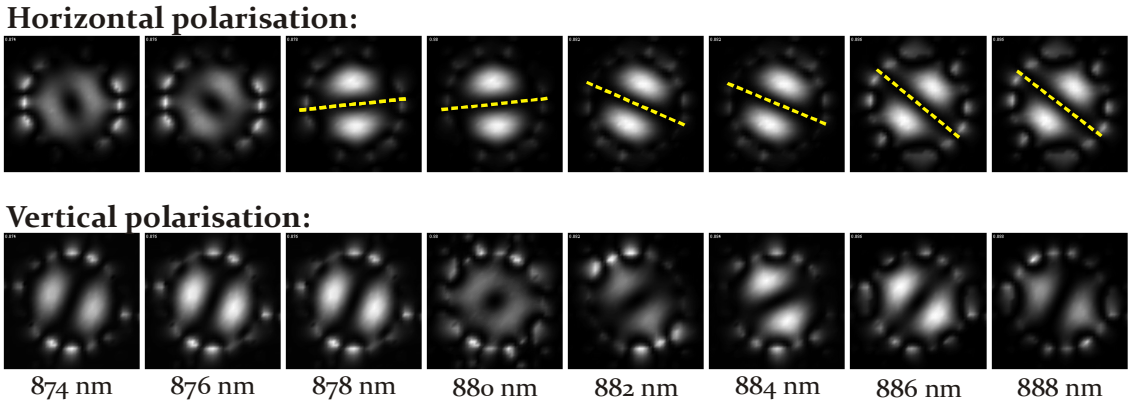

Figure 2-30: *Superpositions of each higher-order and surface modes as a function of wavelength. The two strips of images represent filtering through orthogonal polarisers.*

The simulated intensity profiles shown in Figure 2-30 show a rotation in the resultant mode angle, and changes from a clear two-lobed mode profile such as that seen at 880 nm for the horizontal polarisation to a 'doughnut' shape intensity profile such as that seen at 876 nm, also for a horizontal polarisation. Away from regions of anti-crossing events there is no such rotation observed. The observation of the mode-angle intensity experimentally should therefore provide an indication of the spectral location and strength of anti-crossing events.

Experimental mode rotation

Theoretically we have seen that changes, particularly rotation, of the spatial mode profile of core-guided modes occur where that mode crosses with a surface mode.

The effect may be observed experimentally using setup shown in Figure 2-31. Light from a tuneable extended cavity diode laser (ECDL) is selectively coupled into higher-order core modes of a 10 m length of triangular-lattice HC-PCF (inset of Figure 2-31). Selective coupling to these modes is achieved by launching light at an angle to the fibre axis, and an extinction ratio of >20 dB between the higher-order and fundamental core modes obtained. A half-wave plate rotates the linear-polarization of the laser to allow preferential coupling to only two of the quartet of higher-order modes. Since in general only one of the higher-order modes will interact with an interface mode in a given region of normalised frequency, the fact that the light is not coupled to a single mode is not detrimental to the observation of mode-pattern rotation; the output will be a superposition of the two-modes, one of which has a constant field distribution. At the output of the fibre, a Glan-Thompson polarizer (GTP) selects a single polarization, and the mode-pattern is recorded using a vidicon camera.

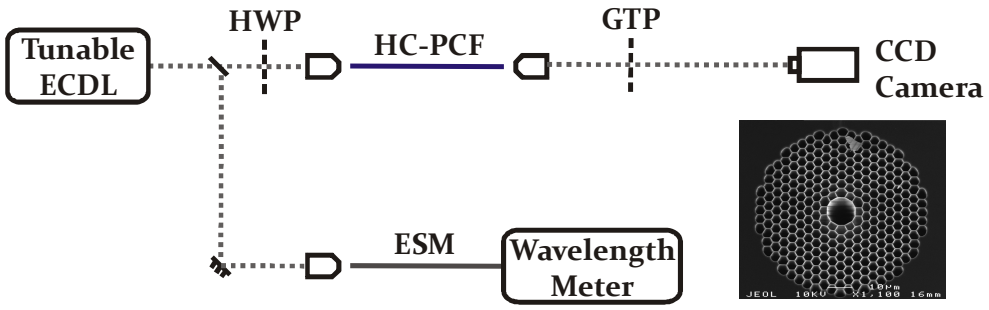

Figure 2-31: *Experimental setup for the observation of mode pattern rotation at anti-crossing events. ECDL: extended-cavity diode laser; HWP: half-wave plate; GTP: Glan-Thompson polarizer; ESM: endlessly single-mode photonic crystal fibre. Inset: Electron micrograph of the 7-cell 1500 nm HC-PCF used.*

Data is acquired by slowly scanning the laser frequency in the vicinity of an anti-crossing event, and a wavelength-meter (with relative accuracy of 20 MHz) is used to ensure smooth mode-hop-free frequency scanning. Figure 2-32 shows the output mode-pattern as a function of frequency detuning over a wavelength range of 0.1 nm.

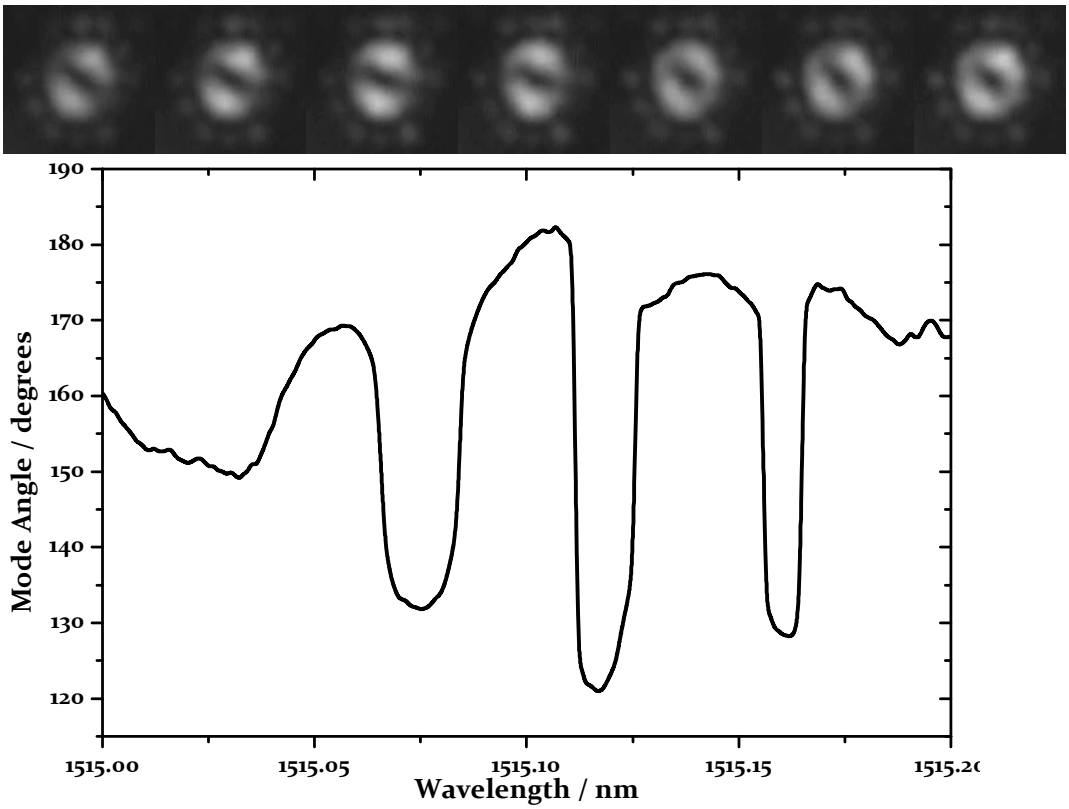

Figure 2-32: *Experimentally measured mode angle as a function of wavelength for a 7-cell 1550 nm HC-PCF. Top: sequence of near-field images illustrating the rotation.*

These results show that weak anti-crossing events, short-ranged in terms on wavelength can occur within a bandgap. Although such weak events are not observed in a course resolution transmission spectrum, such as obtained using a white-light source and optical spectrum analyser (see section 2.3), these events may be responsible for local variations in dispersion behaviour.

The following section details a technique of altering the core-shape of drawn HC-PCF. One application of this technique is to shift the spectral location of surface modes, and even move them completely outside of the bandgap

2.5 Post-Processing of Fibre Structure by Etching

The stack-and-draw technique described in section 2.2.1 allows for a wide range of structure to be produced. However, certain structures that have been shown to have advantageous properties through modelling are not easily fabricated using this technique. In particular, very high air-filling fraction cladding structures and optimised core shapes, are difficult to achieve.

This section presents experimental work[7] on optimising the silica core surround through etching of drawn fibre by hydrogen fluoride (HF). The technique is however not limited only to the core, and optimisation of the cladding structure should also be achievable. Preliminary work on the optimisation of canes through HF etching has also been undertaken, although this section will concentrate principally on the results obtained for processed fibre.

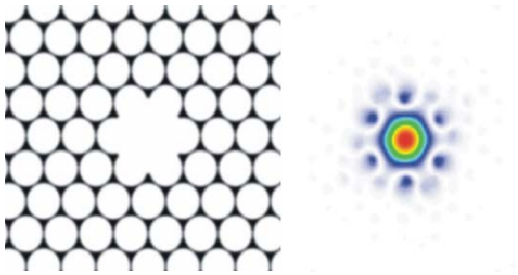

Figure 2-33: *Left: HC-PCF structure that is calculated to have no surface modes in the bandgap region. Right: fundamental core-mode intensity profile for the structure.*

The existence of surface modes is detrimental to many quantum optics applications, as well as often limiting the useful bandwidth of HC-PCF. The positions of the surface modes within the bandgap can however be controlled by the shape and thickness of the silica core surround [28, 29]. Etching offers a means to finely control the exact thickness and shape of the core ring.

Core Etching of HC-PCF

The etching technique involves allowing a flow of HF solution through the core of a section of fibre; the sample length was limited to 20 cm in this experiment. To prevent flow of HF through the fibre cladding, the cladding structure was collapsed using a filament fusion splicer, leaving only the core hole open at both ends of the fibre (see

[7] This work was performed with Yingying Wang, also at the University of Bath.

section 4.4.1 for further details of this technique). The flow through the fibre is maintained by applying a difference pressure between the ends of the fibre.

There are two main considerations in the choice of solution used for etching: the etching must be uniform along the length of the fibre to maintain a constant transmission spectrum, and the roughness of the silica must not be increased significantly beyond that of the drawn fibre as this would increase loss due to scattering. To obtain longitudinal uniformity, the etch rate should be slower than the rate of flow through the fibre. Buffered HF (a solution containing HF and the buffering agent NH_4F) maintains the pH of the solution as etching is performed and therefore helps to maintain a constant etching rate throughout the process.

The required concentration of the HF solution can be calculated using equations 2-2 and 2-3. The acid density D and etching rate have an exponential dependence on time, given by the constant α which itself depends on the internal surface area and volume of the fibre core [34]. Laminar flow is applicable for the HF solution in a fibre core, and the 'flow-through' time for a fibre of diameter d and length L under a differential pressure P between fibre ends is given by equation 2-3.

2-2 $$D(t) = D(0)\exp(-\alpha t)$$

2-3 $$\tau = \frac{32\mu_0}{d^2}\frac{L^2}{P}$$

A commercially available buffered HF solution is used, with a 1:100 ratio of 49% HF to 40% NH_4F, with a quoted silica etching rate of ~7.5 nm/minute [34]. This was further diluted in water in a 1:30 volume ratio, resulting in an experimentally determined etching rate of 0.18 nm/minute. Using a low concentration solution is expected to give the additional advantage of achieving a low surface roughness [35]. The condition that the decay time ($1/\alpha$) be much smaller than the flow through time is satisfied, with $\tau\alpha \approx 100$.

Scanning electron microscope (SEM) images of unetched and etched fibres are shown in Figure 2-34. Comparison of (a) and (b) shows the reduced thickness of the silica core ring obtained by etching. A more extreme example is shown in (c) when the thinner sections of the core ring have been completely removed. The non-uniformity of the core thickness around the circumference of the core in the original fibre results from the use of circular capillaries in the stacking process during fabrication.

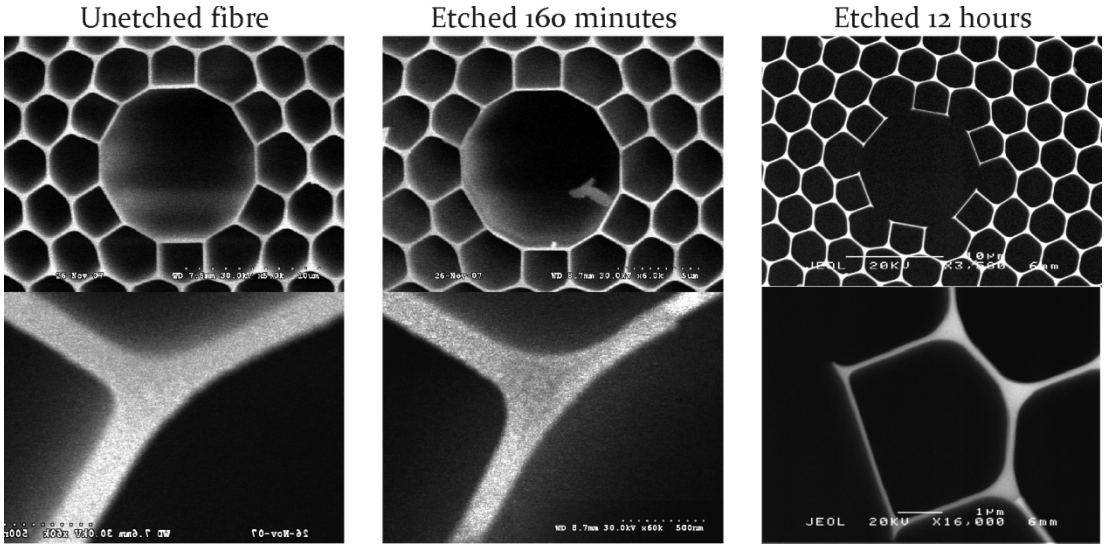

Figure 2-34: *Electron micrographs of 7-cell HC-PCF. (a) Unetched fibre, as drawn. The entire core is shown in the top image, with a detail of the core surround below. (b) and (c) show fibres after 160 minutes and 12 hours of etching respectively.*

The effects of altering the core surround are clearly observed when comparing the transmission spectra of samples etched for varying lengths of time (Figure 2-35). The transmission spectrum of the unetched fibre shows three loss peaks towards the short-wavelength end of the spectrum that may be attributed to coupling of the fundamental mode with surface modes. As the core of the fibre is reduced in thickness by etching, these three loss peaks are observed to shift further toward the blue end of the spectrum, and gradually out of the transmission band.

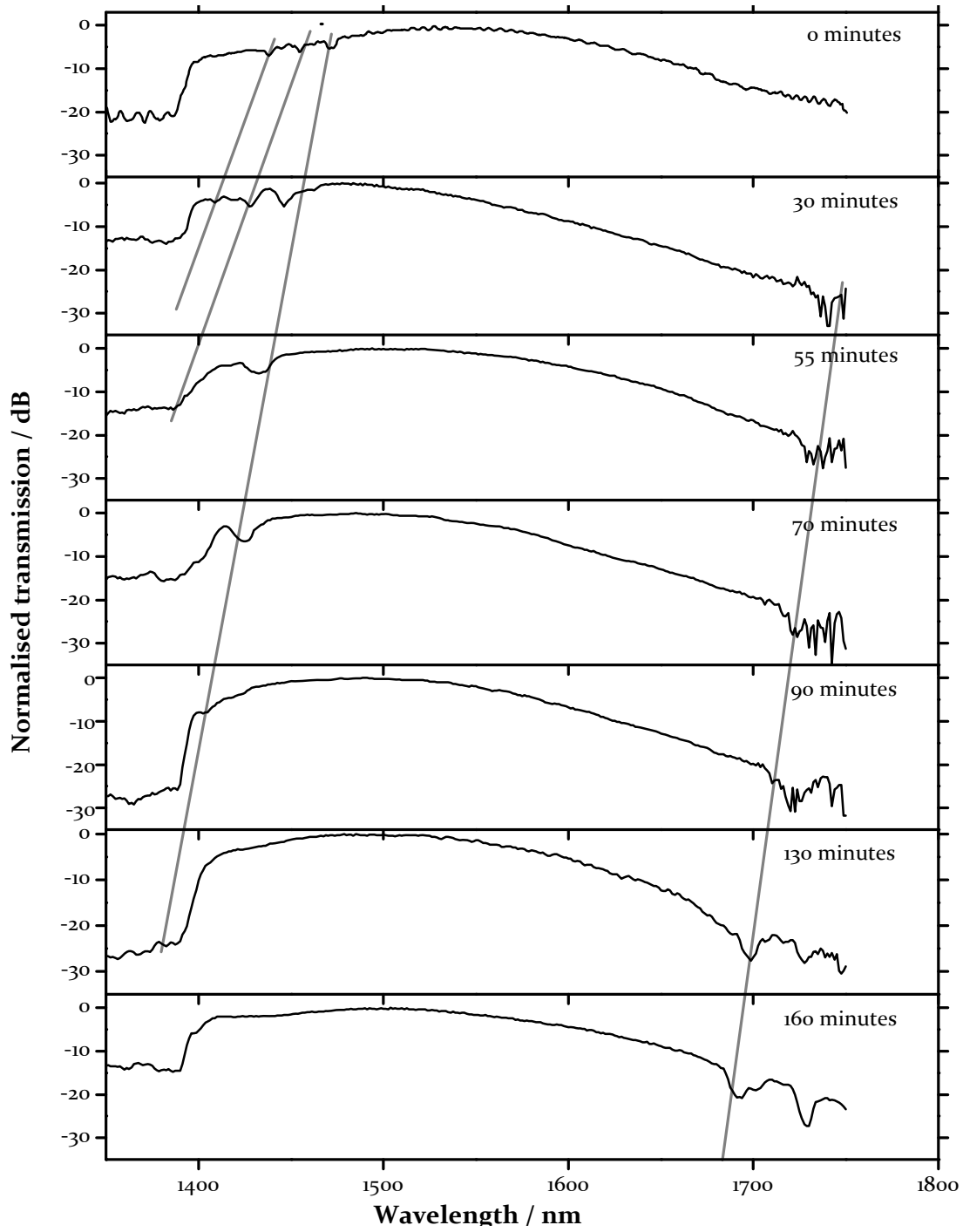

Figure 2-35: *Transmission spectra of etched and unetched fibre samples. The top spectrum is of the unetched fibre. Subsequent spectra are for fibre with core etched for 30, 55, 70, 90, 135 and 160 minutes respectively. The grey lines are a guide to the eye illustrating the shift of surface modes towards the blue end of the spectrum. After 160 minutes the etch depth is measured to be 30 nm.*

At the long wavelength end of the bandgap, new loss peaks are observed, which again move to shorter wavelengths as the thickness of the core surround is reduced. A detail of the transmission spectrum is shown in Figure 2-36 to highlight the surface mode shift.

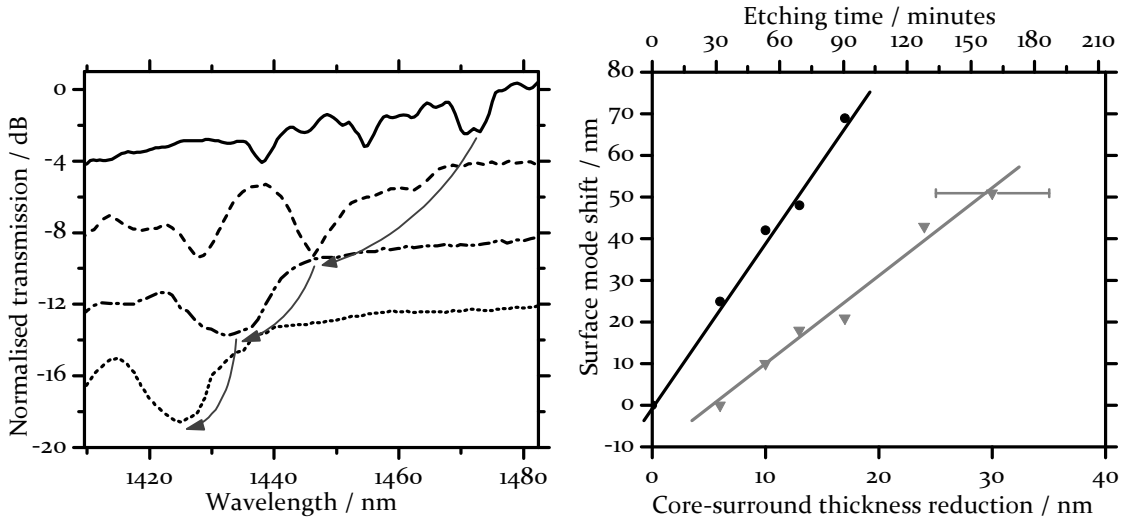

Figure 2-36: *Left: Detail of the surface mode shift, from top-to-bottom unetched, and etched for 30, 55 and 70 minutes respectively. Right: Surface mode shift as a function of etching time and etch depth for a surface at the blue-end of the bandgap (black) and red-end of the bandgap (grey). The error bar represents the uncertainty in thickness reduction due to limited resolution of the electron microscope.*

This figure also plots the shift of one of the short wavelength surface modes (black circles) and of the long wavelength surface mode (grey triangles) as a function of etching time. The thickness reduction in this data was measured using a electron microscope after 160 minutes of etching, and the remaining thickness reductions by linear interpolation; the linear relationship between surface mode shift and thickness reduction agrees with theory [36], validating this assumption.

Due to the short length of the samples investigated, extensive measurements of possible increases in the fibre attenuation due to increased roughness or longitudinal non-uniformity on the etching have not been possible. However, no decrease in the width of the transmission band is observed in the 20 cm etched samples suggesting that the etching is indeed uniform. Further work is planned to further evaluate this promising technique.

Cane Etching

An alternative approach to etching the fibre is to etch the cane. This has both advantages and disadvantages over fibre etching. Since many kilometres of fibre may be drawn from

a single cane, the cane etching approach is favourable where long lengths of fibre are required. Indeed etching of the cane should allow high air-filling fraction fibre to be achieved without reducing the thickness of the capillaries used during the stacking stage. The drawing of very thin capillaries with good circularity is difficult, and an alternative approach is therefore useful.

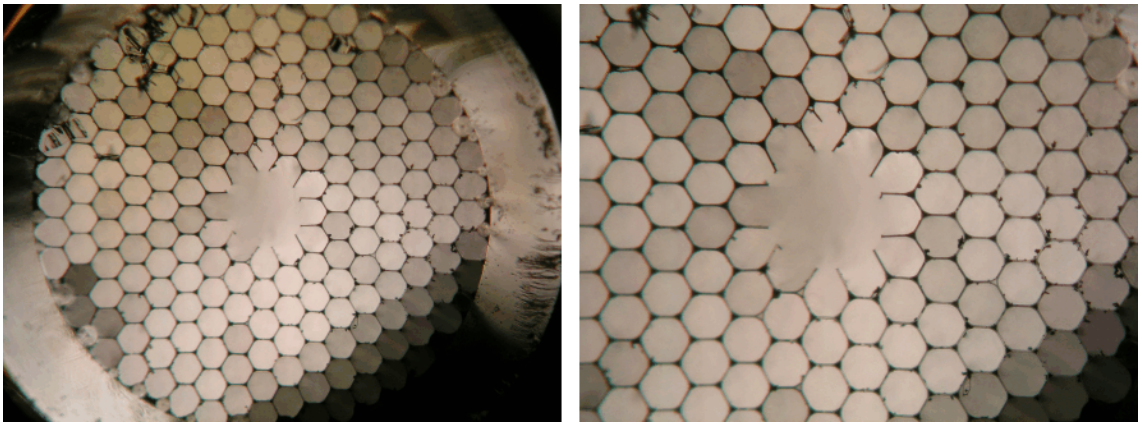

Figure 2-37: *Photographs of a cane etched using hydrofluoric acid. The shape of the core surround is altered to reduce the coupling to surface modes in fibre drawn from these canes.*

On the other hand, the structures achievable in fibre drawn from etched canes will be more limited than those obtained from direct fibre etching due the fact that surface tension will change features in the cane as it is drawn to fibre.

Etching is a promising technique for tailoring the properties of fibre, particularly with respect to surface mode locations.

2.6 Summary

This chapter has presented the fabrication techniques for producing hollow-core photonic crystal fibre. These techniques have been used in producing the fibre used in later chapters, such as the triangular lattice HC-PCF used for observing electromagnetically induced transparency in acetylene in Chapter 5 and kagomé lattice fibre used to observe EIT in rubidium vapour in Chapter 6.

The tailoring of fibre properties through post-processing has been demonstrated to be a viable technique, at least for short lengths of fibre. For many applications only short lengths of fibre are required, although there is potential to extend the etching technique to lengths of the scale of metres.

Chapter 3

Hollow-Core PCF for Coherent Optics

This chapter gives an introduction to the field of optics in coherent media. An overview of previous work is given, and the parameters required for understanding the effects introduced.

Following this, applications made possible by the coherent effects are introduced, and the use of hollow-core photonic crystal as a host for the gases is discussed.

The final section of this chapter considers the advantages and possible limitations presented by the use of HC-PCF, with particular regard to the small diameter and large aspect ratio of the fibre.

3.1 Historical Background

Coherent optics considers systems in which a laser induces *coherence* between atomic states. The coherence can be thought of as a fixed phase relationship between atomic states, and is induced by one or more laser fields on or close to resonance with atomic transitions. The presence of atomic coherence leads to the possibility of interference effects. However, while in classical waves it is the field amplitudes that are interfering, atomic coherence and interference requires the consideration of parameters such as probability amplitudes. A wealth of effects results from this interference, and these have prospects both in fundamental and applied physics.

Among these interference effects we find electromagnetically induced transparency (EIT), the main topic of interest in this thesis, in which a powerful coupling laser tuned to one transition is used to create a transparency within a second transition probed by a weaker probe laser. EIT involves a system with two transitions and therefore three energy levels, and can thus be observed in three possible distinct configurations,

illustrated in Figure 3-1. These schemes, for obvious reasons, are known as lambda (Λ), vee (V) and ladder (or cascade) respectively.

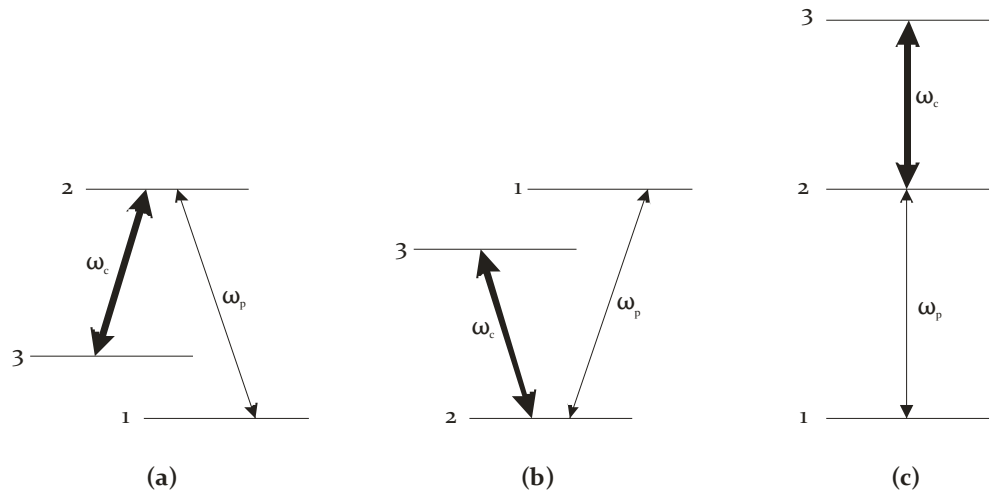

Figure 3-1: *The three energy level schemes in which EIT may be observed: (a) lambda scheme, (b) vee scheme and (c) cascade or ladder scheme.*

Before explaining more about EIT, it is useful to first introduce the concept of atomic coherence, and other atomic coherence phenomena related to EIT.

The most basic system which can exhibit atomic coherence is a simple two energy-level system (Figure 3-2, left), in which optical decay from the excited to ground state is neglected. When this system is excited by a laser close to resonance with the level separation, a sinusoidal transfer of population occurs from the lower to upper energy level and back in a process termed Rabi flopping (Figure 3-2, right). This process is in contrast to what would be expected from incoherent excitation (following the Einstein rate equations), where oscillation would not occur, and at most half the population would be excited to the upper state.

The frequency of the Rabi flopping oscillations, or angular *Rabi frequency*, is given by $\Omega_R = \mu E/\hbar$, or more generally by equation 3-1 when the laser frequency is detuned from resonance with the transition by $\Delta = \omega_c - \omega_{12}$.

3-1
$$\Omega_R = \sqrt{\Delta^2 + \left(\frac{\mu E}{\hbar}\right)^2}$$

Here μ is the transitional dipole-moment and E the electric field strength. This equation shows that as the laser is further detuned from resonance with the transition, the Rabi frequency increases and oscillation period decreases such that at large detuning the field

has no effect on the atom. The definition of Rabi frequency is useful as it takes into account both laser intensity and the strength of the transition.

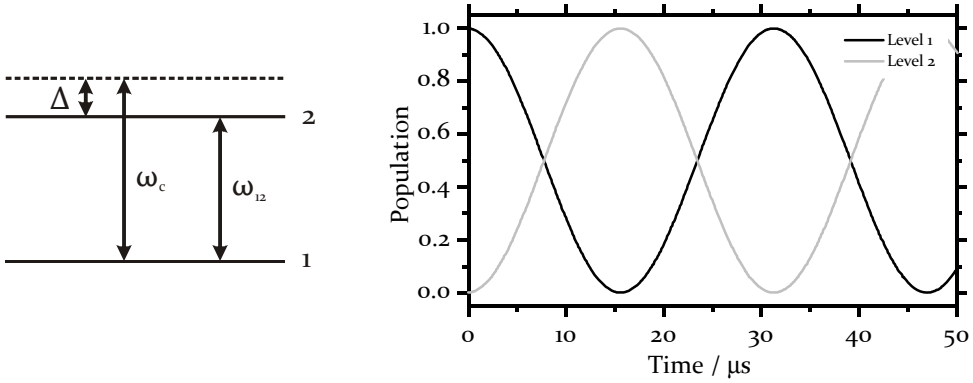

Figure 3-2: *Left: the simplest system in which to observe atomic coherence. ω_{12} is the transition frequency, ω_c the frequency of the applied field, and Δ the frequency detuning. Right: evolution of the population of level 1 (black curve) and level 2 (grey curve) with time under the influence of the applied field.*

3.1.1 Quantum Optics Phenomena

This section explores coherent effects that have been defined over the last 50 years. To introduce the terminology associated with these effects, it is useful to consider them in a chronological order. All of the effects are manifestations of the interference of probability amplitudes within an atom or molecule.

Autler Townes Splitting

An important effect that will be useful in explaining electromagnetically induced transparency is Autler-Townes splitting [37]. In this, the application of a coupling field, which may be either optical, or as in the initial observation, radio frequency, results in the splitting of an energy level, such that a probe laser sees a resultant doublet state. The splitting occurs due to the modulation of the dipole moment by Rabi oscillations.

Autler-Townes splitting is illustrated in Figure 3-3, where a strong *coupling* laser ω_c couples levels $|1\rangle$ and $|2\rangle$.

With a probe laser in the absence of the coupling beam a single absorption peak is observed (dashed line), but the addition of the coupling field results in a splitting of this peak (solid line). The strength of the splitting (in term of frequency difference between the two components) is determined by the Rabi frequency of the coupling field: if it is on exact resonance with the transition, then the splitting is exactly equal to the Rabi frequency. It the coupling field is off resonance, the splitting becomes asymmetric.

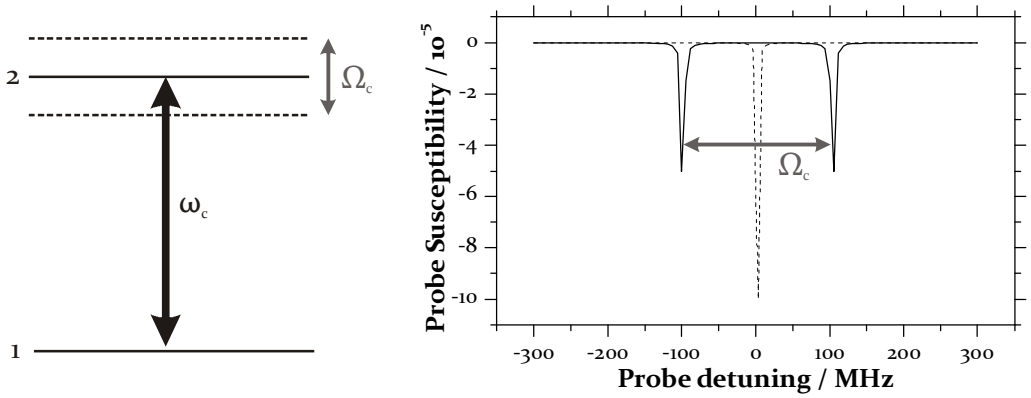

Figure 3-3: *Left: energy level scheme for observing Autler-Townes splitting. Right: observed probe transmission in the presence of the strong coupling field (solid line). The coupling beam forms a doublet, resulting in an absorption peak either side on its usual location (zero probe detuning).*

Autler-Townes splitting is a dynamic version of the Stark effect that gives rise to the shift of energy-levels under the application of an applied static electric field. The splitting can be predicted by considering the eigenstates of the full Hamiltonian of the system, comprising the base-atom Hamiltonian and interaction Hamiltonian due to the applied field; this approach will be considered when we come to consider EIT later in this section.

Fano interference

In 1961, Fano [38] realised that when states of an atom are coupled by multiple pathways or transitions, interference between the amplitudes of these transitions may lead to either an enhancement or a reduction in the total probability amplitude; indeed, a complete cancellation of the transition probability is possible via destructive interference.

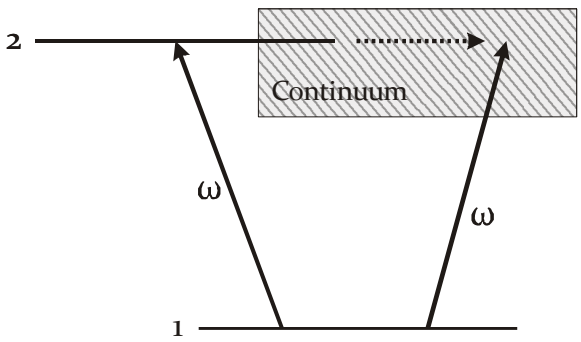

Figure 3-4: *Configuration for observing Fano interference.*

Figure 3-4 shows the configuration of Fano's experiment that demonstrated interference effects within an atom for the first time. There are two routes via which a continuum state may be reached from the ground state $|1\rangle$. The first and obvious route is by direct excitation. The second route is via excitation to an autoionising state (a bound state within the continuum) $|2\rangle$, which is coupled via Coulomb interaction to a continuum state. Fano showed that interference (both constructive and destructive) between these two excitation pathways lead to a frequency dependent enhancement or suppression being observed in the photo-ionisation cross-section.

Ramsey Fringes

Another of the earliest examples of atomic coherence was the observation of Ramsey fringes in the microwave domain [39]. In this observation, atoms pass through two spatially separated microwave fields. The first field imposes atomic coherence to an atom, which then acquires a phase shift as it travels to the second microwave field, dependent on both the time-of-flight between the regions and atomic transition frequencies. Interaction in the second field then leads to modulation of the absorption spectrum (fringes), dependent on the phase shift between the atom and the second microwave field.

In the optical domain Ramsey fringes have been observed in two distinct configurations. One of these uses a scheme of spatially separated optical fields, similar to the configuration used in the microwave domain. Bergquist *et al.* observed fringes on a sub-Doppler saturation absorption feature in sodium vapour [40]. The first observation of optical Ramsey fringes, however, used short coherent time delayed pulses. In the scheme used by Salour *et al.* [41] the fringes are observed in the profile of Doppler-free two-photon resonances of sodium vapour. The pulses used (~5 ns) are shorter than the lifetime (~50 ns) of the atomic states involved, and importantly also shorter than the transit time of an atom through the laser beam (~100 ns), such that the transit time plays no role. The Ramsey fringes obtained have a frequency spacing $1/2T$, where T is the time delay between the pulses, which can be much smaller than the spectral width of the of the transform-limited pulses.

Coherent Population Trapping

In 1976, Alzetta experimentally observed an effect termed *coherent population trapping* (CPT)[42]. This was shortly followed by theoretical explanations of the phenomenon by Whitley and Stroud [43] and Orriols and Arimondo [44]. CPT refers to the ability to trap population in a so-called dark state.

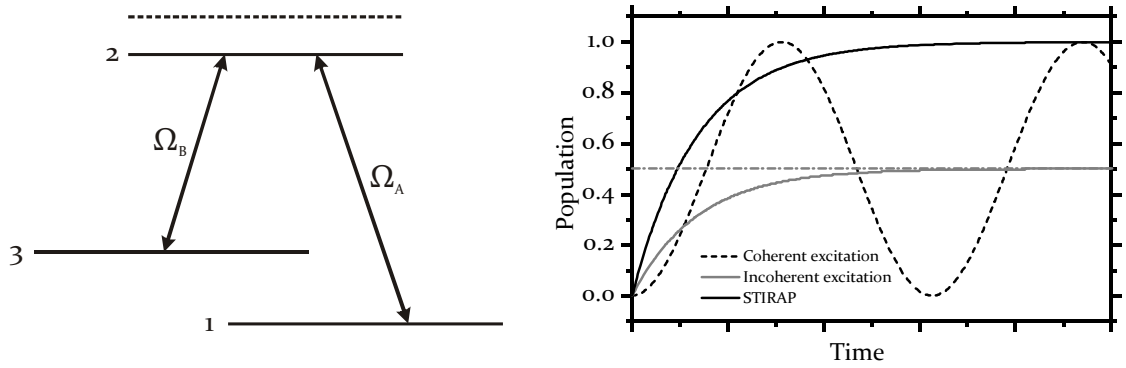

Figure 3-5: *Left: Typical energy level scheme for coherent population trapping. Right: Incoherent excitation will at most transfer 50% of the population from* $|1\rangle \rightarrow |3\rangle$. *Coherent excitation results in oscillating population, while the STIRAP technique allows full transfer of population from* $|1\rangle \rightarrow |3\rangle$.

A typical scheme for observing CPT is shown in Figure 3-5. In this scheme, the two fields Ω_A and Ω_B of similar intensity couple the transitions $|1\rangle \rightarrow |2\rangle$ and $|3\rangle \rightarrow |2\rangle$. The presence of the fields changes the eigenstates of the system's Hamiltonian such that they are linear superpositions of the bare atom eigenstates:

$$
\begin{aligned}
|a_+\rangle &= \sin\theta \sin\phi|1\rangle + \cos\phi\,|2\rangle + \cos\theta \sin\phi|3\rangle \\
|a_0\rangle &= \cos\theta|1\rangle - \sin\theta\,|3\rangle \\
|a_-\rangle &= \sin\theta \cos\phi|1\rangle - \sin\phi\,|2\rangle + \cos\theta \cos\phi\,|3\rangle
\end{aligned}
\qquad 3\text{-}2
$$

These superpositions are expressed in terms of *mixing angles*, dependent on the Rabi frequencies of the two fields [45]. The mixing angle thus determines the eigenstates of the system. Assuming fields on resonance with the bare-atom transitions:

$$
\begin{aligned}
\tan\theta &= \frac{\Omega_p}{\Omega_c} \\
\tan 2\phi &= \sqrt{\Omega_p^2 + \Omega_c^2}
\end{aligned}
\qquad 3\text{-}3
$$

The state $|a_0\rangle$, a coherent superposition of the two lower states containing no component of the upper state $|2\rangle$, is known as the *dark state* as there is no possibility of excitation to the upper state. Any population in this state is therefore trapped. The dark state itself may be populated by optical decay from $|2\rangle$.

In a similar way to Fano interference, CPT can be considered in as interference between pathways, in this case destructive interference between the two pathways $|1\rangle \rightarrow |3\rangle$ and $|2\rangle \rightarrow |3\rangle$.

An useful of application of CPT allows population to be transferred from $|1\rangle$ to $|3\rangle$ (still with reference to Figure 3-5) without populating $|2\rangle$ during the process; this process is termed stimulated Raman adiabatic passage (STIRAP) [46, 47]. Such a process has many applications, since alternative techniques for transferring population are limited. As shown in Figure 3-5, incoherent excitation can at most transfer 50% of the population between the two states. Coherent excitation with two laser of equal Rabi frequency tuned to the two allowed transition result in oscillating population transfer between $|1\rangle$ and $|3\rangle$; although in principle a π-pulse could be used to stop this transfer when all of the population is in $|3\rangle$, in practice this is only useful in certain situations since the 'size' of a pulse depends on molecular orientation, and also Rabi frequency is not constant across the profile of a laser beam. The use of STIRAP avoids these difficulties.

The STIRAP process is illustrated in Figure 3-6. A pulse resonant with the transition between unpopulated levels $|2\rangle$ and $|3\rangle$ prepares the system, before a partially overlapping second pulse resonant with the $|1\rangle \rightarrow |2\rangle$ transition then drives the population from $|1\rangle$ into $|3\rangle$. In the literature, the first pulse is termed the Stokes pulse, and the second the pump pulse.

The process can be understood by considering the eigenstates of the atom and field system, given in equation 3-2 [45]; note that unlike CPT, the assumption of equal Rabi frequencies for the two lasers is not made. The mixing angles originally defined above are now time dependent.

$$\tan\theta(t) = \frac{\Omega_B(t)}{\Omega_A(t)}$$
$$\tan 2\phi(t) = \sqrt{\Omega_B^2(t) + \Omega_A^2(t)} \qquad 3\text{-}4$$

The aim of STIRAP is to adiabatically change the dark state $|a_0\rangle$ from being identical to $|1\rangle$ until it is identical to $|3\rangle$, thus transferring population between the two states without populating the leaky state $|2\rangle$. By considering the mixing angle θ it is seen that when $\theta = 0$, corresponding to $\Omega_B = 0$, the dark-state $|a_0\rangle$ is equivalent to $|1\rangle$. Similarly, when $\theta = \pi/2$, corresponding to $\Omega_A = 0$, the dark state is equivalent to the state the population is to be transferred to, $|3\rangle$.

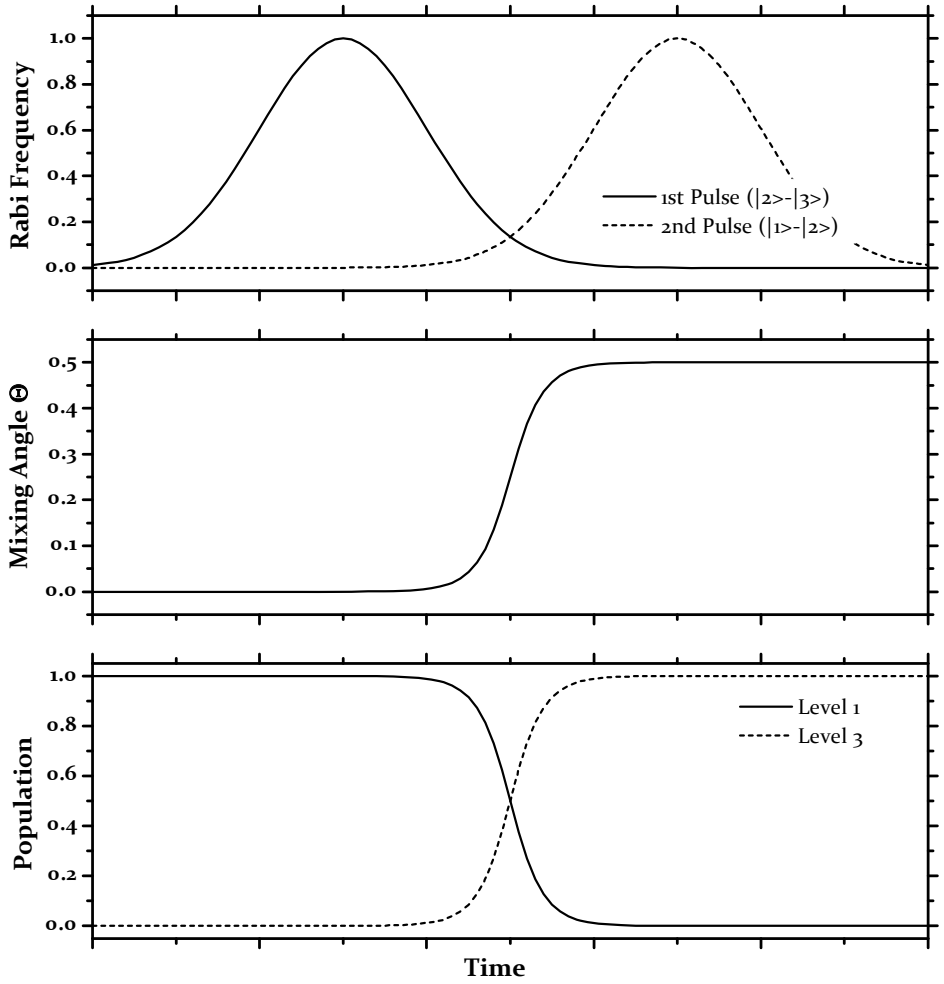

Figure 3-6: *Stimulated Raman adiabatic passage (STIRAP). Top: Relative Rabi frequency of laser tuned to the* |2⟩ → |3⟩ *transition (solid) and* |1⟩ → |2⟩ *transition (dashed). Middle: Mixing angle as a function of time. Bottom: Population of states* |1⟩ *(solid line) and* |3⟩ *(dashed line), showing the full transfer of population.*

The dark-state can be adiabatically moved from the initial to final state by slowly changing the mixing angle by changing the relative power of the two laser fields; recall that the mixing angle determines the eigenstates of the system, and that an adiabatically changing mixing angle corresponds to a system always at equilibrium. This is illustrated in Figure 3-6, where the top graph shows the time evolution of the intensity of Stokes and pump pulses. The middle graph illustrates the smooth evolution of mixing angle, and the lower graph the transfer of population from |1⟩ to |3⟩ (where it is assumed that all population is initially in the ground state. Without this explanation, the process seems counter-intuitive since the first applied field is between |2⟩ and |3⟩, both of which are initially unpopulated.

STIRAP is useful as it allows the transfer of population between two states of the same parity (such that the transition is dipole forbidden) without detrimental effects due to decay of the intermediate state, which itself remains unpopulated. We shall see shortly that EIT closely resembles the initial stages of the STIRAP process, where the two applied laser fields are highly asymmetric in power.

Electromagnetically Induced Transparency

As stated at the beginning of this chapter, EIT is a coherent effect where a coupling laser is used to induce a transparency within an absorption dip probed by a second laser. It is useful to start with an illustration of the effect, and the first experimental observation of EIT by Harris *et al.* [48], in strontium vapour, is shown in Figure 3-7.

In this experiment a weak probe laser scans across the $|1\rangle \rightarrow |3\rangle$ transition resulting in the transmission profile Figure 3-7 (a). The addition of a strong coupling laser tuned to the $|2\rangle \rightarrow |3\rangle$ transition induced a transparency within the observed transparency peak, shown in profile Figure 3-7 (b). The authors found that the transmission of a probe beam (when on resonance with the $|1\rangle \rightarrow |3\rangle$ transition) increased from exp(-20) to exp(-1) when the coupling laser was switched on.

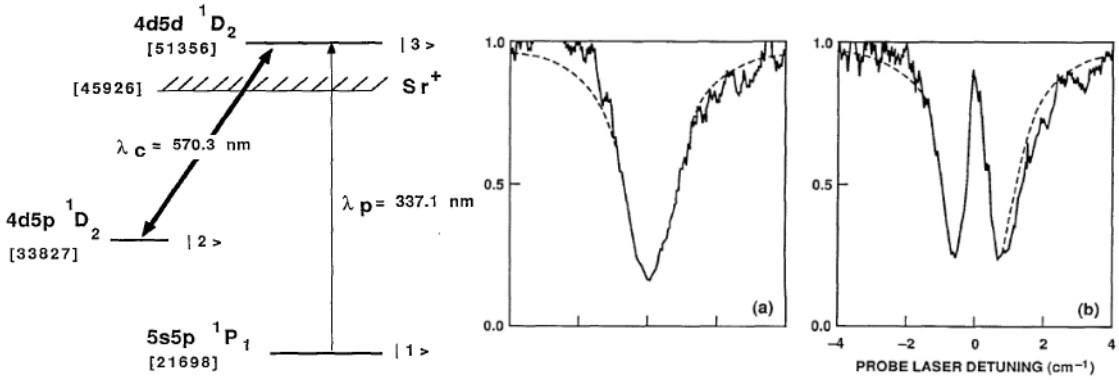

Figure 3-7: *The first experimental observation of EIT. Left: level diagram. Right: Probe transmission in (a) absence and (b) presence of the coupling laser. Figure taken from Boller et al., Phys. Rev. Lett. 66 (1991) 2593-2596.*

EIT was proposed before this experimental observation independently by both Kocharovskaya [49] and Harris [50], and both papers describe the effect as a means to achieve lasing without inversion (LWI). The term *electromagnetically induced transparency* itself was coined in a later paper from Harris' group, concerning further applications of the effect [51].

There are several ways of explaining the phenomenon of EIT. One of these is to consider a dressed state [52] picture, as used for the explanation of CPT earlier in the chapter. If we consider the Λ energy level scheme, we see in Figure 3-7 that essentially the same configuration as is used in CPT; the one major difference is that instead of the two fields being of the same power, they are highly asymmetric in power. The two fields are labelled Ω_P and Ω_C for probe (low power) and coupling (high power) beams respectively.

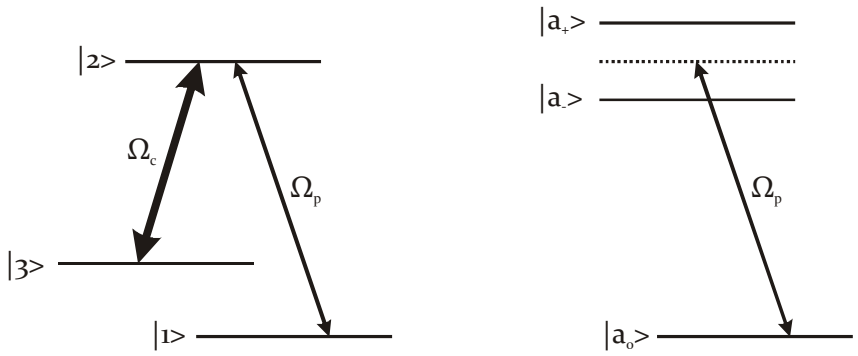

Figure 3-8: *Left: Λ energy level scheme for EIT. Right: The same scheme in the dressed-state basis.*

Due to much larger strength of the coupling field compared to the probe field, in the dressed state basis, considering the atom and field system as a whole, the upper levels form a coherent superposition, as shown in Figure 3-8. Assuming again on resonance fields, and that $\Omega_c \gg \Omega_p$, equation 3-2 reduces to equation 3-5.

$$|a_+\rangle = \cos\phi\,|2\rangle + \sin\phi|3\rangle = \frac{1}{\sqrt{2}}(|3\rangle + |2\rangle)$$

$$|a_0\rangle = |1\rangle \qquad \text{3-5}$$

$$|a_-\rangle = -\sin\phi\,|2\rangle + \cos\phi\,|3\rangle = \frac{1}{\sqrt{2}}(|3\rangle - |2\rangle)$$

The dark state $|a_0\rangle$ is thus identical to the ground state of the three-level lambda scheme, from which there will be no excitation as long as the on-resonance condition is maintained. From this treatment it is clear that absorption of the probe will not occur, and therefore a transparency is induced in the absorption line. In the next section a full density-matrix approach to the system is considered, removing the approximations made here. This will be important in interpreting the experimental EIT results in Chapters 5 and 6.

The transition amplitude from $|1\rangle$ to the dressed states is then given by the sum of the amplitudes to each dressed state individually. If the probe is resonant with the $|1\rangle \rightarrow |2\rangle$ bare-atom transition, then the contribution from the dressed states will be equal and opposite, and thus there will be no absorption of the probe laser.

A perhaps more intuitive way to view EIT is by returning to a bare atom picture with interacting fields, and considering the *coherence* between each pair of energy levels [53]. The coherence can be thought of as being associated with the oscillating electric dipole between pairs of energy levels, driven by fields resonant or near-resonant with the transition. If the oscillating dipole can be excited in several ways, interference can occur between the different contributions. If the sum is zero, such that the overall dipole-moment is zero, then there will be no absorption on the corresponding transition. The coherences will be introduced formally in section 3.2, where a density matrix approach is taken.

As well as the appearance of a transparency peak, EIT also dramatically alters dispersion in the vicinity of the transparency. This leads to the unusual situation of strong dispersion in a frequency range where there is little attenuation; this is illustrated in Figure 3-9 where the theoretical variation in refractive index (Δn) from the background index (n) is plotted in the region of an induced transparency. Although strong dispersion is to be expected in the region of an absorption line, it is under normal circumstances not possible to take advantage of these due to the strong absorption. EIT provides strong dispersion in a region of transparency, which allows slow-light to be achieved, as will be discussed later in this chapter (section 3.4).

The curves in Figure 3-9 are calculated for acetylene gas, with coupling Rabi frequency of 200 MHz, and other parameters matching those of the experimental conditions used in chapter 5, with the exception of decoherence rates which are taken to be slightly lower than experimentally in order to highlight the effect. In this example the group index in the transparency region is ~8.7, corresponding to a group velocity of 3.4×10^7 m/s. This will be considered further in the following sections.

This section has introduced the field of quantum optics, and the most common effects, but of course there are many applications in which the effects play an important role. Section 3.4 is devoted to presenting some of these applications, and looking at the configuration of experiments where these applications have been investigated.

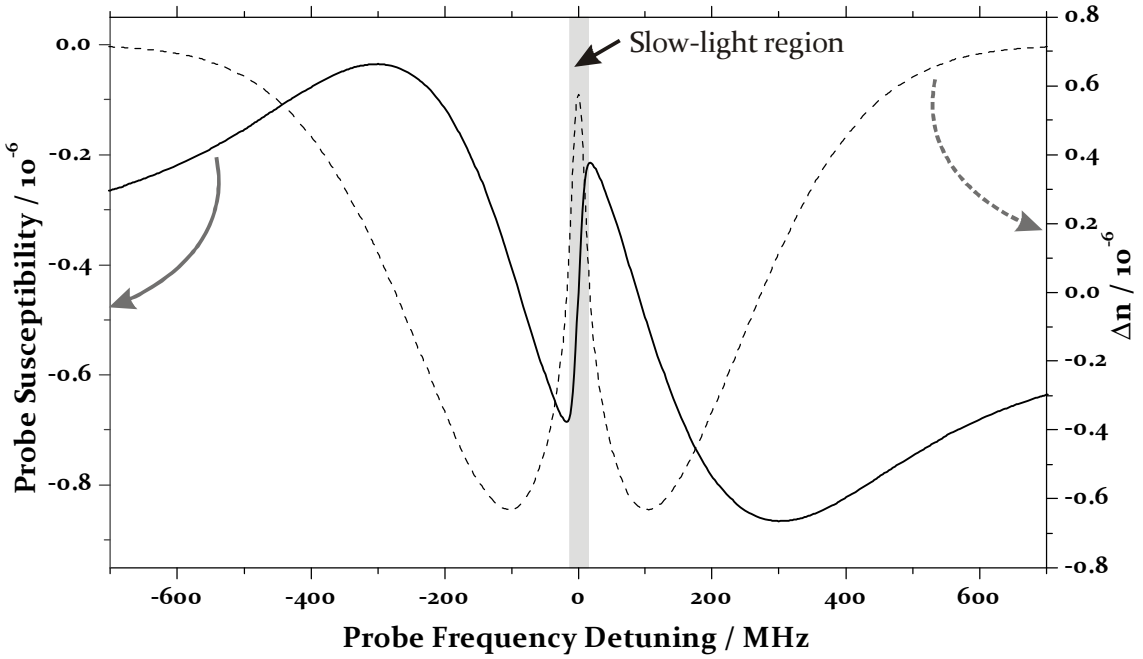

Figure 3-9: *Theoretical probe transmission (grey curve) and change in refractive index (black curve) illustrating the strong dispersion occurring across the frequency range of the induced transparency peak in an EIT system.*

Before this, in the following we will take a closer look at the density matrix formalism and the effects of decoherence. This allows the evaluation in section 3.3 of the properties required of both the medium chosen for quantum optical effects, and also of the host or container of this medium. In particular, the benefits and potential drawbacks of HC-PCF as the host will be considered.

3.2 The Density Matrix

For the experiments and applications considered in this thesis, the physical system consists of an ensemble of atom or molecules, and cannot therefore be described by a quantum mechanical wave function. The behaviour of such systems can be described through the use of the density operator ρ [54]. This operator describes the average state of the ensemble, including level populations and the phase relationship (*coherence*) between each pair of energy levels.

Absorption and dispersion characteristics of the system are fully contained within the density vector. The linear susceptibility for a given transition is given by equation 3-6.

3-6 $$\chi_{ij} = \frac{\mu_{ij}\rho_{ij}N}{\varepsilon_0 E}$$

Absorption is then proportional to the imaginary part of the susceptibility (equation 3-7), and dispersion is proportional to the real part of the susceptibility (equation 3-8). N is the atomic density, and n_0 the background refractive index due to off-resonance transitions. χ' and χ'' represent real and imaginary parts of the complex susceptibility respectively.

3-7 $$\alpha = \frac{\omega_p n_0 \chi'}{c}$$

3-8 $$\beta = \frac{\omega_p n_0 \chi''}{2c}$$

The time evolution of the density vector under the action of applied fields is determined by the Liouville equation:

3-9 $$\dot{\rho}(t) = -\frac{i}{\hbar}[H(t), \rho(t)]$$

Here $H(t)$ is the time dependent Hamiltonian of the system. As an example, consider a two-level atom with an applied field of optical frequency ω_C and Rabi frequency Ω_C. The Hamiltonian is then given by equation 3-10, and the time evolution can be found using the Liouville equation. The diagonal elements of this matrix are related to the energy levels of the atom or molecule through $E_i = \hbar\omega_i$.

3-10 $$H(t) = \begin{pmatrix} \hbar\omega_1 & \hbar\Omega_C \exp[i\omega_C t] \\ \hbar\Omega_C \exp[-i\omega_C t] & \hbar\omega_2 \end{pmatrix}$$

For the purposes of including optical decay and decoherence, it is useful to express ρ as a column vector rather than a square matrix. In this case the evolution of the system is given by $\dot{\rho}(t) = \boldsymbol{M}\rho$. The square matrix $\boldsymbol{M}$ will be referred to as the density matrix. In the example system the resultant expression is given by equation 3-11, after making the rotating wave approximation to remove the time dependence due to the quickly oscillating laser field [55].

3-11
$$\begin{pmatrix}\dot{\rho}_{11}\\ \dot{\rho}_{12}\\ \dot{\rho}_{21}\\ \dot{\rho}_{22}\end{pmatrix}=\begin{pmatrix}0 & i\Omega_C & -i\Omega_C & 0\\ i\Omega_C & -i\Delta & 0 & -i\Omega_C\\ -i\Omega_C & 0 & i\Delta & \mathrm{i}\Omega_C\\ 0 & -\mathrm{i}\Omega_C & \mathrm{i}\Omega_C & 0\end{pmatrix}\begin{pmatrix}\rho_{11}\\ \rho_{12}\\ \rho_{21}\\ \rho_{22}\end{pmatrix}$$

Here $\Delta=(\omega_2-\omega_1)-\omega_C$ is the detuning from resonance of the laser field. At this stage optical decay and sources of decoherence can be added to the matrix $\boldsymbol{M}$ phenomenogically. Optical decay (γ) appears on off-diagonal elements and decoherence (Γ) on diagonal elements. The full matrix for the two level system is shown in equation 3-12.

3-12
$$\mathbf{M}=\begin{pmatrix}0 & i\Omega_C & -i\Omega_C & \gamma_{21}\\ i\Omega_C & -i\Delta-\Gamma_{12} & 0 & -i\Omega_C\\ -i\Omega_C & 0 & i\Delta-\Gamma_{21} & \mathrm{i}\Omega_C\\ 0 & -\mathrm{i}\Omega_C & \mathrm{i}\Omega_C & -\gamma_{21}\end{pmatrix}$$

The optical decay terms here only affect population, and have no effect on the coherence terms $(\rho_{i\neq j})$. From the matrix it is clear to see that ρ_{11} gains population at a rate $\gamma\rho_{22}$, i.e. a rate proportional to the population of the upper state, while population is lost from the upper level at the same rate. The system is closed and therefore population must be conserved.

3.2.1 Decoherence

The decoherence terms Γ_{ij} relate to loss of coherence on the respective transition. Decoherence, or *dephasing*, results from external factors that are not accounted for in the derivation of the density matrix. One such source is optical decay: as well as transfer of population, this also affects the coherence, and therefore is a component of the relevant Γ terms.

Another cause of decoherence is atomic or molecular collisions. If an atom within the system undergoes a non-elastic collision, then this atom will no longer be in phase with the rest of the system, and therefore must contribute to the decoherence. The magnitude of decoherence from collisions is considered later in this chapter.

The laser linewidths are an additional source of decoherence in real systems.

3.3 Media and Hosts for Quantum Optics

For quantum optics applications, in addition to choice of media used, it is also important to consider the host or container of the medium, with particular regard to the physical

dimensions. This section considers both of these, and how the use of HC-PCF as a host may expand the range of suitable media.

The choice of medium is driven by the requirements for applications which, as we shall see in the following section, are the ability to obtain narrow and stable sub-Doppler features. These requirements require the decoherence in the system to be as low as possible. A further consideration is of the Rabi frequency required to observe the coherent optics effects; this is dependent on the dipole-moments of the transitions involved, and as such high intensities may be required if the dipole strength is weak.

Decoherence is largely determined by the inter-atomic or inter-molecular collision rate, and thus low pressure gases are preferred to keep this source of decoherence to a minimum. Historically atomic vapour has been the medium of choice for quantum optics applications, in part due to low collisional decoherence rates, and in part to the large transitional dipole-moments, which are often of the order of 1 Debye. Atomic vapours also hold the advantage of a simple energy level structure, with stable transitions.

In contrast, molecular gases have complex energy structures, including many vibrational and rotational modes and their overtones. This is a particular advantage over atomic vapours in many applications as the availability of transitions at a particular optical wavelength, for example for frequency stabilisation, is almost guaranteed. However, the use of molecular gases for coherent optics has been extremely limited, especially when compared with the wealth of publication involving coherent optics in atomic vapours; previous work involving molecular gases is explored in section 5.1. The reason for this is that the molecular dipole-moments are several orders of magnitude lower than those of atomic vapours, of the order 10^{-3} Debye. Also the more complex energy structures of molecules mean that systems used for quantum optics cannot be considered as closed, making the analysis of such system more complicated.

To obtain similar Rabi frequency in a molecular vapour as in an atomic vapour therefore requires the intensity to be several orders of magnitude greater. Conventionally this requires both the use of high peak-power pulses, and tight focusing; this is at the expense of interaction length, and it is useful to consider the figure-of-merit introduced in section 1.3.

The figure-of-merit describes the efficiency with which coherent optical effects are observed, in terms of beam area and interaction length. A small cross-sectional area gives high intensity, while a long interaction length increases the signal-to-noise ratio (or contrast) achievable. A long interaction is particularly important for molecular gases,

where the small dipole-moment and low-pressure mean little absorption of a probe beam. The figure-of-merit is determined by the experimental configuration and choice of host, which will be considered shortly.

With regard to the choice between atomic vapour and molecular gas, a further benefit offered by molecular gases is that they are often less reactive that atomic vapours. The most commonly used atomic vapours, such as rubidium and caesium, are highly reactive, and require careful handling.

For completeness, while the use of gases is of primary interest in this thesis, the use of solid media is now considered. Solids typically have broad optical linewidths and large decoherence rates due to the density of atoms within the solid. However, coherent effects can be achieved in solids when cooled to minimise the dephasing rate. Ham *et al.* were able to observe EIT in a rare-earth crystal of Pr^{3+} doped Y_2SiO_5 at a temperature of 5.5 K [56]. Ultraslow and trapped light have been obtained in the same crystal, although the limitation on operating temperature remains [57]. More recently ultraslow light propagation has been observed in a ruby crystal at room temperature [58] using coherent population oscillations. There has recently been much work in this area since the techniques used allow the production of stored or stopped light.

We now consider the host of a gaseous medium to be used for coherent optics. In many experiments a bulk gas cell is used, with dimensions of the order of centimetres. For such configurations, free-space beams are used, and there is a compromise between high-intensity and long interaction length as was discussed in section Figure 1-3. While signal-to-noise ratio may be improved by operating at higher gas pressures, and therefore greater optical depth, this comes at the expense of increased collisional dephasing.

Ideally low-pressure must be combined with long interaction length, and gas-filled HC-PCF offers just this. HC-PCF acts not only as a container of the atomic vapour or molecular gas, but also a waveguide. It is able to maintain high intensity at low-power due to the micrometer scale of the fibre-core over interaction lengths on the scale of metres, thus providing excellent signal-to-noise ratio even with weak molecular transitions. We will see in Chapter 5 that these properties have allowed EIT to be observed in a molecular gas for the first time. These advantages also hold for atomic vapours, and the fibre allows a significant reduction in the optical powers required over conventional techniques.

HC-PCF also offers additional advantages to both atomic vapour and molecular gas based systems. It is also a compact host for quantum optics applications, and is easily

integrated into optical fibre systems. This avoids alignment difficulties associated with free-space optics and multi-pass cells, especially when combined with technologies such as fibre lasers. The small fibre core has a volume of only ~80 nanolitres per metre, making the use of most toxic or harmful gases safe due to the small quantities required.

There are however both technological and fundamental hurdles in the implementation of HC-PCF as a host for quantum optics application. Chapter 4 describes the fabrication techniques that have been developed for producing *photonic microcells,* all-fibre gas-cells formed from gas-filled HC-PCF. The chapter covers the technical obstacles that have been successfully overcome to produce sealed all-fibre cells, with low optical insertion loss and micro-bar level gas pressure.

It is the small diameter of the fibre core, allowing high intensity at low power, which also presents the main, but not insurmountable, drawback of the use of HC-PCF in quantum optics applications.

3.3.1 Dephasing Effects of Confined Geometry

It has already been said that inter-atomic and inter-molecular collisions can represent a large source of dephasing, even at modest millibar level operating pressures, and it is for this reason that quantum optics experiment are usually carried out at the lowest possible operating pressure.

When operating at high pressures, collisions between gas atoms and the wall of the containing gas cell are insignificant since collisions between gas atoms are much more likely. As gas pressure is reduced, collisions of gas atoms with the wall become increasingly more likely.

Figure 3-10 plots the collision rate between gas atoms as a function of pressure, and also the rate of collisions with the wall for two cell diameters: a 2 cm bulk cell, and a 10 μm diameter cell representing HC-PCF geometry. The calculations are for acetylene gas at 300 K, representing the experimental conditions of the results presented in Chapter 5.

The atom-wall collision rate is calculated from equation 3-13 [59], where R_c is the diameter of the circular cell, c is 6.8 in the hard-sphere limit, D is the diffusion constant and $K = \lambda/R_c$ is the Knudsen number which simply relates the mean-free-path λ to the diameter. These parameters will be considered further in the context of gas-flow in Chapter 4. The diffusion constant can be calculated using equation 3-14, where σ is the collision cross-section and M_M the molar mass.

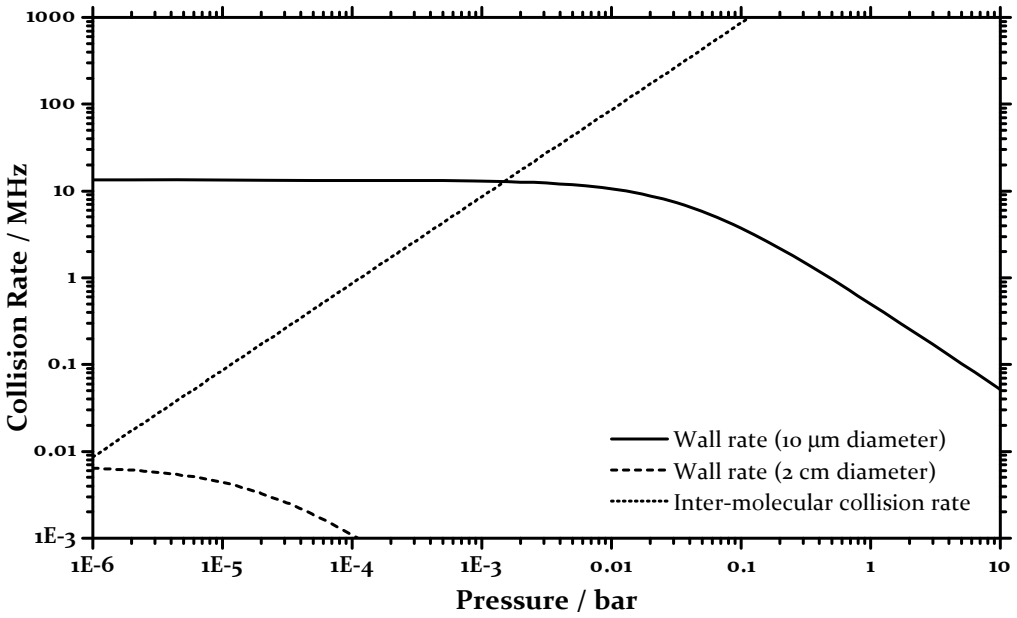

Figure 3-10: *Collisions rates for acetylene gas at 300 K as a function of pressure for a fibre of 10 μm core diameter (solid line) and for a bulk-cell of 2 cm diameter (dashed line).The dotted curve is the inter-molecular collision rate.*

The atom-wall collision rate is calculated from equation 3-13 [59], where R_c is the diameter of the circular cell, c is 6.8 in the hard-sphere limit, D is the diffusion constant and $K = \lambda/R_c$ the Knudsen number which simply relates the mean-free-path λ to the diameter. These parameters will be considered further in the context of gas-flow in Chapter 4. The diffusion constant can be calculated using equation 3-14, where σ is the collision cross-section and M_M the molar mass.

3-13
$$\gamma_{coll}^{wall} = \frac{2.405^2 D}{R_c^2}\left(\frac{1}{1+cK}\right)$$

3-14
$$D = \frac{1.86 \times 10^{19}\, T^{\frac{3}{2}}}{1.296\, P\, \sigma^2 M_M^{\frac{1}{2}}}$$

The dotted line of Figure 3-10 shows the inter-molecular collision rate which favours a low operating pressure for a low collision rate. The wall collision rates for a 2 cm diameter bulk cell and 10 μm diameter HC-PCF are shown by the dashed and solid curves respectively. These plateau below a certain pressure, which corresponds to the gas molecules having a mean-free-path equal to the diameter of the gas-cell; in effect the mean-free-path can no longer increase due to the presence of the wall. In a bulk cell the

plateau corresponds to a kHz collision rate; in the 10 μm core HC-PCF however, the collision rate plateaus at a collision rate orders of magnitude larger, ~15 MHz. This leads to large decoherence rates, which will limit the linewidth achievable in the various quantum optics phenomena. In EIT for example, this will also reduced the steepness of the dispersion in the transparency region, which will be detrimental for several applications.

There are, however, opportunities to reduce the number of collisions that actually result in dephasing of the atom. For many years it has been known [60] that by coating the walls of bulk cells with paraffin and various other polymers, elastic spin preserving collisions can be obtained for atomic vapours, which do not result in dephasing. In Chapter 6 this has been applied to the core of HC-PCF, where an EIT linewidth is obtained that is below that which would be expected for an uncoated fibre.

One means by which to reduce the wall collision rate is by laser cooling. This is discussed in Chapter 7 as planned future work.

The following section considers applications of coherent optics, and considers how the use of a HC-PCF host may offer improvements for these applications.

3.4 Applications

There are many applications in which the coherent effects discussed in this chapter have been put to use. The applications discussed below have two main requirements: that of firstly narrow, and secondly stable, transitions. It will be noticed that the majority of applications use atomic vapours.

Frequency Stabilisation

There are many applications where the frequency stability of a laser source is important, which involve locking the laser frequency to that of a well identified atomic resonance. While the locking may be performed using a number of techniques, such as the Pound-Drever-Hall technique, all require narrow and stable resonances. The use of sub-Doppler resonances, such as a saturated absorption feature, is common when using atomic vapours as a frequency reference. Coherent optical effects are a further means of achieving sub-Doppler features suitable for laser frequency stabilisation.

For many applications, such as telecommunications, atomic vapours do not provide references at appropriate wavelengths. Molecular gases on the other hand, as will be seen in section 5.1, offer regularly spaced absorption lines throughout the visible and near-infrared spectral regions. For example, many acetylene lines lie within ~1 GHz of ITU

(International Telecommunications Union) WDM grid lines, and it therefore seems ideal for use as a frequency reference in such systems.

While the Doppler broadened acetylene absorption lines may be used, in Chapter 5 acetylene-filled HC-PCF is used to observed the sub-Doppler EIT feature in acetylene for the first time; this is made possible by the tight-confinement and long interaction length offered by the fibre. This sub-Doppler feature offers a narrower frequency reference, and promises to improve stability compared with the use of a Doppler broadened line alone.

HC-PCF also offers advantages for other techniques for achieving sub-Doppler linewidths, such as saturated absorption [61]. Such setups conventionally use bulk gas-cells, Fabry-Perot cavities, and have the associated free-space optics and alignment difficulties associated with this. Saturated absorption can be observed in acetylene photonic microcells (see section 5.9) which as all-fibre devices can be easily integrated into optical-fibre based systems, a prospect which is particularly attractive to use in telecoms systems.

Metrology

Atomic clocks, based on microwave transitions in caesium, rubidium and hydrogen have proved to have unsurpassed long-term precision, and are frequently used where such precision is required. Primary standards, such as NIST-F1, are caesium fountain clocks and have large space and power requirements.

There are many applications, such as GPS receivers and telecommunications systems, where portable frequency standards would be of use and efforts are now being made to miniaturise technology, and make system easier to use for both industrial and laboratory applications. While substantial progress has been made in this area, commercially available atomic clocks have a footprint of at least 100 cm^3.

Recently there has been an effort to take advantage of coherent population trapping (section 3.1.1) to implement small-scale atomic frequency standards and atomic clocks. The use of CPT removes the need for the usual microwave cavity that is required to probe the stable microwave frequency as defined for example by the hyperfine splitting of the ground state of ^{87}Rb of ~6.8 GHz. Chip-scale atomic clocks developed at NIST and based on CPT have been shown to have a short-term (1 second) frequency stability of 1.5×10^{-10}. These chip scale devices however have the drawback of offering only limited interaction length, and correspondingly signal-to-noise ratio.

This is an area in which the use of HC-PCF has an advantage. Replacing the chip-scale gas-cell with a photonic microcell would increase the interaction length available and

therefore improve the signal-to-noise ratio, while still presenting a comparatively compact device.

Considering again large scale atomic clocks, another technique used is Ramsey interference in atomic fountain clocks. While the geometry of such experiments, which relies on the freefall of atoms over a distance of ~1 m, is clearly not suited for the confined geometry of HC-PCF, a second technique of obtaining Ramsey fringes is of interest. Zanon [62] reported the observation of Raman-Ramsey fringes in a double lambda atomic system. In contrast to the microwave techniques, instead of two spatially separated driving fields which allow the free evolution of atomic coherence between the fields, this technique uses a pulsed arrangement, with a long preparation pulse followed by a period of free evolution, and finally a short interrogation pulse. This particular scheme is also immune from optical pumping due to the double lambda configuration, and can potentially be achieved in gas-filled HC-PCF.

In addition to frequency standards, there are several other metrological applications that can take advantage of effects such as EIT and CPT. Magnetometers based on CPT in atomic vapour cells, for example, have been demonstrated to have sensitivities rivalling those of competing techniques such as superconducting quantum interference devices [63]. The use of photonic microcells again offers the potential to increase signal-to-noise ratio in such devices, and to achieve this in a compact millimetre scale package.

Slow Light

As shown in section 3.1.1, electromagnetically induced transparency achieves a sharp change in refractive index across the transparency. This steep dispersion is of importance for slow-light and its related applications. The parameters of interest in such application are the phase and group velocities, given by equations 3-15 and 3-16 respectively.

3-15
$$v_p = \frac{c}{n(\omega)}$$

3-16
$$v_g = \left.\frac{c}{n(\omega) + \omega \frac{dn(\omega)}{d\omega}}\right|_{\omega=\omega_c}$$

The denominator of equation 3-16 gives the group index n_g. The group velocity relates to a pulse of light with central frequency ω_c. If $dn(\omega)/d\omega$ is large, then slow group velocities, relating to propagation speed of speed of the polychromatic pulse, are achieved; it is not necessary for the phase index to vary significantly from the background value.

This presence of steep dispersion in EIT was discussed theoretically by Harris et al. in 1992 [64]. They found that the refractive index near the probe wavelength, whilst remaining close to that of the background, would exhibit a steep slope leading to strong dispersion. Based on the configuration of an earlier EIT experiment in Pb vapour [65] they calculated an expected group velocity of $c/250$; this would lead to an optical delay of 83ns for a pulse propagating in the transparency region in that configuration.

Experimentally, the dispersive properties of EIT were first measured directly by Xiao [66] for EIT in hyperfine levels of the D_2 transition in rubidium. From their dispersion measurements, a probe group velocity of $c/13.2$ was deduced. More recently, EIT has been used to demonstrate a group velocity of just 17 ms^{-1} [67].

Although not currently used in commercial applications, slow-light has uses in applications such as optical signal processing, where it may be useful for optical signal retiming and in the future optical buffering. Of importance here is the delay that can be obtained, and also the tuneability of the delay time.

EIT in HC-PCF is promising for use in such applications. On the basis of experimental molecular EIT results in Chapter 5, a group index of ~7 is expected to be achieved using EIT in an acetylene photonic microcell. While significantly greater group indices have been achieved in atomic vapour, HC-PCF offers interaction lengths order of magnitude greater than in such experiments. Slow light in HC-PCF has been demonstrated by Ghosh *et al.*, who observed a 800 ps delay using EIT in a 1.3 m long acetylene filled fibre.

3.5 Summary

Quantum optical effects are of interested in many applications, including frequency stabilisation, metrology and slow-light devices. Choices must be made between atomic vapours on one hand, offering limited narrow transitions, and molecular gases on the other, with a plethora of available transitions, but weak dipole-moments.

It has been shown that HC-PCF has excellent potential as a host for quantum optics applications due in part to strong confinement offering high intensity at lower power, and in part to its long metre scale interaction lengths.

Chapter 4 explores the technological development of the photonic microcell into a gas-cell with low optical insertion loss able to operate at pressures from microbar level or lower, to tens of bar.

One of the first demonstrations of molecular EIT is presented in Chapter 5, made possible by the use of an acetylene photonic microcell. The sources of decoherence and

the possible energy level schemes are explored with a view to obtaining the narrowest possible induced transparency. The use of HC-PCF has also made possible the first observation of EIT with counter-propagating probe and coupling beams in V and Λ energy level schemes, and this is valuable in evaluating the use of HC-PCF as a host.

In Chapter 6, the use of HC-PCF as a host for atomic vapours is considered. Here it is shown that the high wall collision rate occurring in HC-PCF need not be a limitation to the use of such fibre as a host for quantum optics phenomena: a polymer coating applied to the core of the host fibre reduces the linewidth of the induced transparency below that which would be expected due to decoherence from wall collisions alone.

Chapter 4

Photonic Microcells

Photonic microcells are compact, flexible, gas cells formed from hollow-core photonic crystal fibre. They provide extremely efficient light-matter interaction in an easy to use all-fibre device.

This chapter describes the development of low optical insertion loss photonic microcells suitable for all pressures from microbar or below to tens of bar. Ultra-low pressure cells are formed using a simple yet novel technique that relies on the fast diffusion of helium through silica, and removes the need to produce the microcell in a protected environment.

The gas-flow regimes for filling and evacuating HC-PCF are explored, which are significantly different to those of bulk cells due the substantial aspect ratio of the fibre core, whose length may be six orders of magnitude greater than the diameter.

Finally, the challenges of filling a HC-PCF with the atomic vapour of rubidium are explained, and the methods used to overcomes these problems and successfully achieve this goal are presented.

4.1 Gas Cells

There are many applications that rely on the interaction of gas and light. These range from observing quantum optical effects such as electromagnetically induced transparency and related applications as discussed in the preceding chapter, to more simple applications such as gas sensing. There are also many gas-medium based lasers, particularly at short wavelengths, such as excimer lasers, and in the infrared, such as CO_2 lasers.

Depending on the particular application, the cells used vary in dimension, but are often large, bulky and inflexible. Multi-pass configurations may be used to obtain long interaction lengths while limiting the physical dimensions of the cell; in doing so however the alignment becomes more critical and still does not solve the problem of diffraction.

Conventional gas and vapour cells have typical dimensions of centimetres or tens of centimetres in each dimension, and gas requirements of hundreds of millilitres to tens of litres.

HC-PCF based photonic microcells have the potential to replace many bulk gas-cells with a device that is compact, flexible, and even offers further advantages over conventional cells. The main advantages of HC-PCF are due to the fact that the waveguide itself forms the gas cell.

Photonic Microcells

A photonic microcell consists of a length of HC-PCF filled with gas, and spliced at either end to conventional single-mode fibre (SMF) to seal the cell; these cells were first developed by Benabid et al. [68]. Such a cell brings with it all of the advantages of HC-PCF for laser-matter interaction such as long interaction length and sustained high intensity at low power along the length of the fibre; refer to section 1.3 for further details. Furthermore, photonic microcells (Figure 4-1) are compact, light and flexible, making them suitable for use in confined or awkwardly shaped spaces.

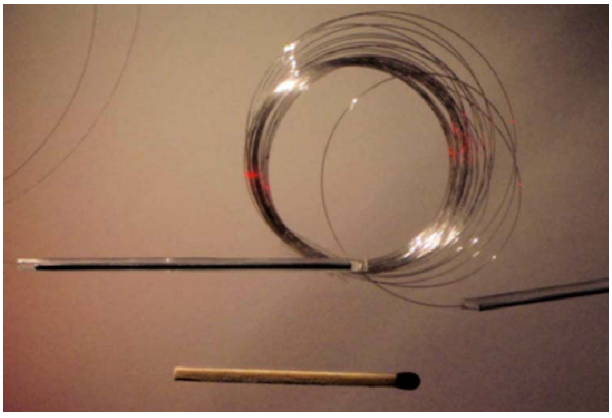

Figure 4-1: *Photograph of a photonic microcell, next to a matchstick for scale. This compact cell provides an interaction length of 5 metres [68].*

A further advantage of photonic microcells is their volume: the core of the fibre forming the cell has a volume of just 80 nanolitres per metre, assuming a 10 μm core diameter. This small capacity means that the use of toxic gases in such a cell is generally inherently safe, unlike their use in conventional gas-cells with much greater volumes. As an example, a typical gas reference cell [69] has a capacity of ~40 ml, and thus requires an amount of gas four orders of magnitude greater than a 10 metre photonic microcell while providing less than one hundredth of the interaction length.

The production of photonic microcells requires the filling of the fibre core with gas, and due to the large aspect ratio of this channel particular attention must be given to this filling process. Conventional gas cells are usually of a similar size in all three dimensions, while photonic microcells may be 10s of metres long but only several micrometres in diameter, an aspect ratio of 10^6. For this reason gas flow within the core of HC-PCF is considered theoretically and verified experimentally in the next section.

Following this, in section 4.3, the methods of fabricating photonic microcells are described, including a novel technique relying on the diffusion of helium through silica that allows both low-pressure and low optical loss cells to be formed. The ability to form vacuum-pressure microcells is of extreme importance for the use of photonic microcells in quantum-optics experiments, and will be used in Chapter 5 for the observation of EIT in acetylene gas.

4.2 Gas Flow dynamics in Micro-channels

The large aspect ratio of the core of HC-PCF, of order 10^6 for a fibre several metres long with a 10 μm diameter core, represents a considerable deviation from that of conventional gas cells that are typically of the same order length in each dimension. This section considers gas-flows rates in HC-PCF both theoretically and experimentally, in order to determine the timescale involved in gas-loading and assembly of photonic microcells.

4.2.1 Theoretical Flow Rates

The core of a HC-PCF is approximately circular, and as such the laminar flow of a fluid through the core is described as Poiseuille flow [59]. Whether the flow through the fibre is laminar or turbulent is determined by the Reynolds number, which gives the ratio of inertial forces to viscous forces. It is given by $R_e = \rho\, v_s L/\mu$, where v_s is the mean fluid velocity, μ the dynamic fluid viscosity, ρ the fluid density, and L a characteristic length given here by the diameter of the fibre core. In circular cross-section channels, for $R_e < \sim 2300$ flow is laminar, while for $R_e > \sim 2300$ the flow is turbulent.

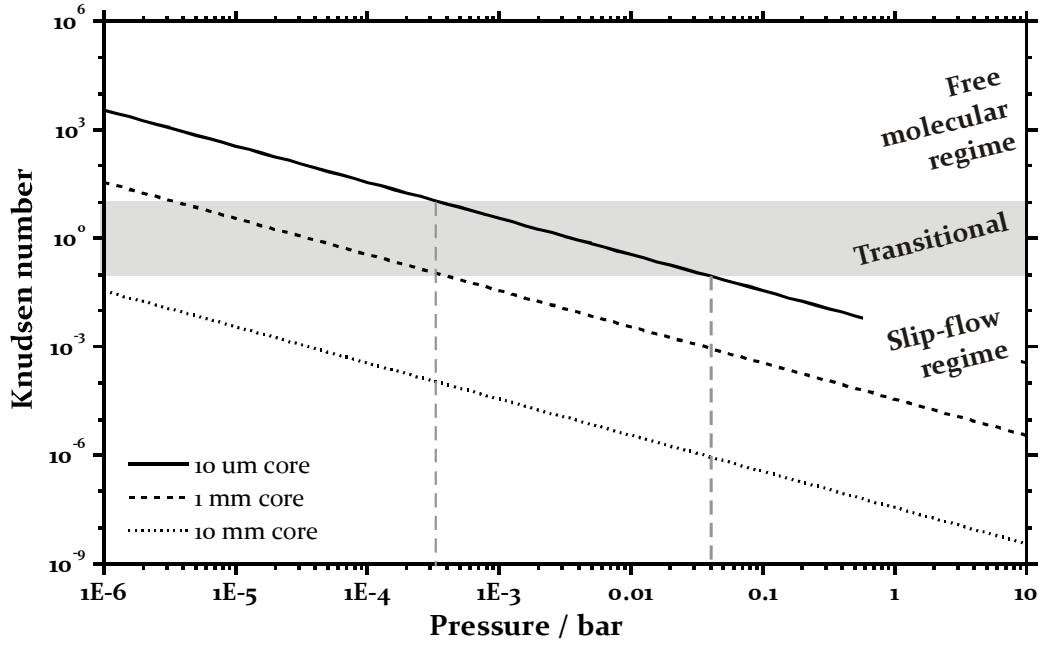

Figure 4-2: *Knudsen number as a function of pressure for core diameters of 10 μm, 1 mm and 1 cm, calculated for acetylene gas at room temperature. The grey bar represents the transition between free-molecular and slip-flow gas flow regimes.*

Considering acetylene gas which will be used in experiments in Chapter 5, its viscosity of $\mu = 9.35 \times 10^{-6}$ Pa. s [70] and assuming a fibre core diameter of 12 μm means that the flow will be laminar at all reasonable gas pressure and flow rates. For example, at a pressure of 1 bar and flow rate of 10 m/s, the Reynolds number of 13.4 is significantly below the critical value, and is reduced further as pressure is reduced. It is thus not necessary to consider turbulent flow in the use of HC-PCF.

Knowing that the flow is laminar, the flow regime may be free-molecular, transitional, or hydrodynamic, depending on the pressure of gas within the fibre. With large pressure differential between the two ends of the fibre, the flow could even encompass each of these regimes at different points along the fibre. Figure 4-2 plots the flow regime for acetylene gases as a function of the Knudsen number relating mean-free-path to the diameter of the channel and defined as $K_n = \lambda/2r_0$; for other gases the value will not differ by more than an order of magnitude from those of acetylene. Here, λ is the mean free path of the particular molecule (defined by equation 4-1 [71]) and r_0 the radius of the circular cross-section channel. The symbols P, T, m and μ are pressure, temperature and molecular mass and dynamic viscosity of the gas respectively.

$$\lambda = \frac{\sqrt{\pi}\mu}{2P}\left(\frac{2K_BT}{m}\right)^{1/2} \qquad 4\text{-}1$$

The flow calculations in this chapter have been carried out below using a slip-flow model suitable for use at arbitrary Knudsen numbers [72], and are valid throughout the range of pressures considered experimentally. The mass flow rate $\dot{q}_z$, determined by equation 4-2, depends on pressure both directly, and through the inverse Knudsen number ($D = 1/K_n$). The subscript z refers to distance along the fibre. The parameters a, b, c, d are constants determined by boundary conditions for the slip-flow model. Here these are taken to be 0.49, 1.28, -1.0669 and -0.03 respectively as determined in [72] for a high-order slip-flow model. It is important to note that these values were determined experimentally for a specific flow channel and fluid; they are not exact values for the flow of gas within HC-PCF, but do give an order-of-magnitude value for the mass-flow rate.

4-2 $$\dot{q}_z = \frac{\pi \rho {r_0}^4}{2\mu} \frac{\partial \rho}{\partial z} \left[\frac{1}{4} + \frac{2a}{\sqrt{\pi}} D^{d-1} + \frac{b}{2} D^c \right]$$

Similarly the velocity distribution along the channel is determined by equation 4-3.

4-3 $$u_z = -\frac{{r_0}^2}{4\mu} \frac{\partial \rho}{\partial z} \left[1 - \left(\frac{r}{r_0} \right)^2 + \frac{4a}{\sqrt{\pi}} D^{d-1} + bD^c \right]$$

These expressions can be used to determine the pressure distribution and mass flow speeds along the length of a fibre, as the result of a differential pressure between the fibre ends.

The results and timescales determined from these equations will be considered as required in the fabrication process of a photonic microcell in section 4.3. Throughout the section simulated results for a HC-PCF of 5 m in length and with 12 μm core diameter will be presented. Before this, in the following section experimental measurements of gas-flow are considered

4.2.2 Gas-flow Measurements

To verify the theoretical gas-flow calculations, measurements of the flow of hydrogen gas through various lengths have been made. The setup consists of a length of HC-PCF (11 μm core diameter) between two gas control chambers of volume 2 cm^3. The fibre is initially flushed with hydrogen and allowed to reach a stable pressure of 1 bar over a period of several days. The pressure in one chamber is increased to 13 bar, and the pressure in the two chambers allowed to reach equilibrium.

The results are shown in Figure 4-3 (points and solid curves) with the curves being the fit to the data points. The results of the simulations, neglecting the cladding, for each fibre length are indicated by dashed curves. Experimentally the equalisation of pressure

between the two chambers is found to be slower by a factor of 1.6, despite the presence of cladding holes that would be expected to increase the flow rate.

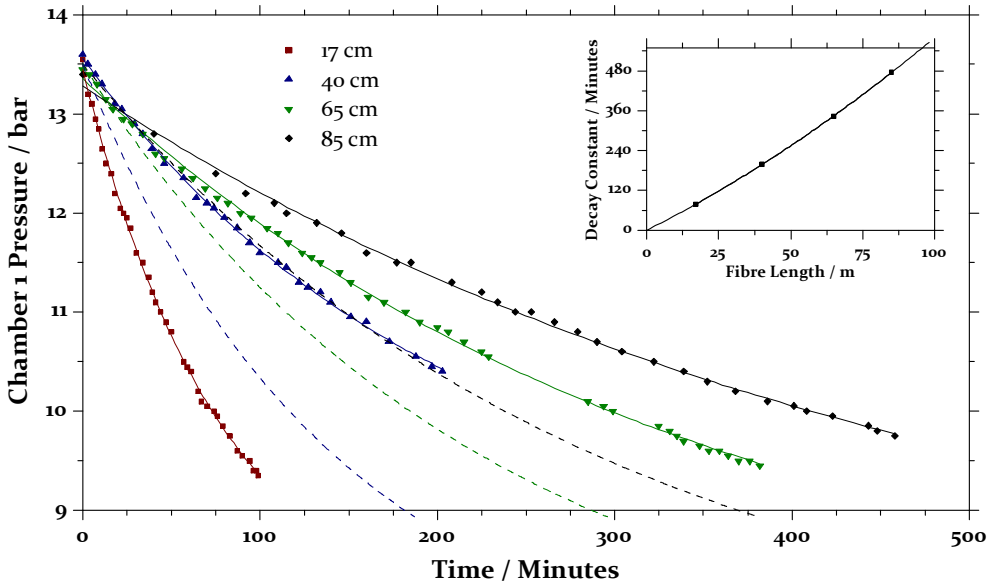

Figure 4-3: *Experimental hydrogen gas flow through several lengths of HC-PCF with core diameter of 11 μm. The points represent the pressure in each gas-control chamber, initially at 13.5 bar and 1 bar respectively. Solid lines are an exponential fit to the points, with dashed lines from simulation. Inset: measured decay constant as a function of fibre length with fitted parabola.*

The decay constant for the fitted curves is plotted against fibre length inset in Figure 4-3, with a fitted parabola. The equation of this fit is $t_d = 4.361l + 0.0144l^2$ where t_d is the decay constant and l the fibre length. This deviates from the l^2 dependence of the simple Poiseuille flow formula, but is in agreement with that determined from equation 4-2 when the fibre length is scaled by a factor of 2.

Thermal Clamp

It may be useful to temporarily interrupt the flow of gas along the fibre in certain situations, for example during the sealing process of the fabrication of a photonic microcell. Due to the small diameter of HC-PCF, it is possible to cool small sections of the fibre very quickly, and in doing so also cool the gas present in that section of the fibre. Experimentally it is seen that the condensation of gases at this point is effective at stopping the flow of gas along the fibre, even under conditions of high differential pressure.

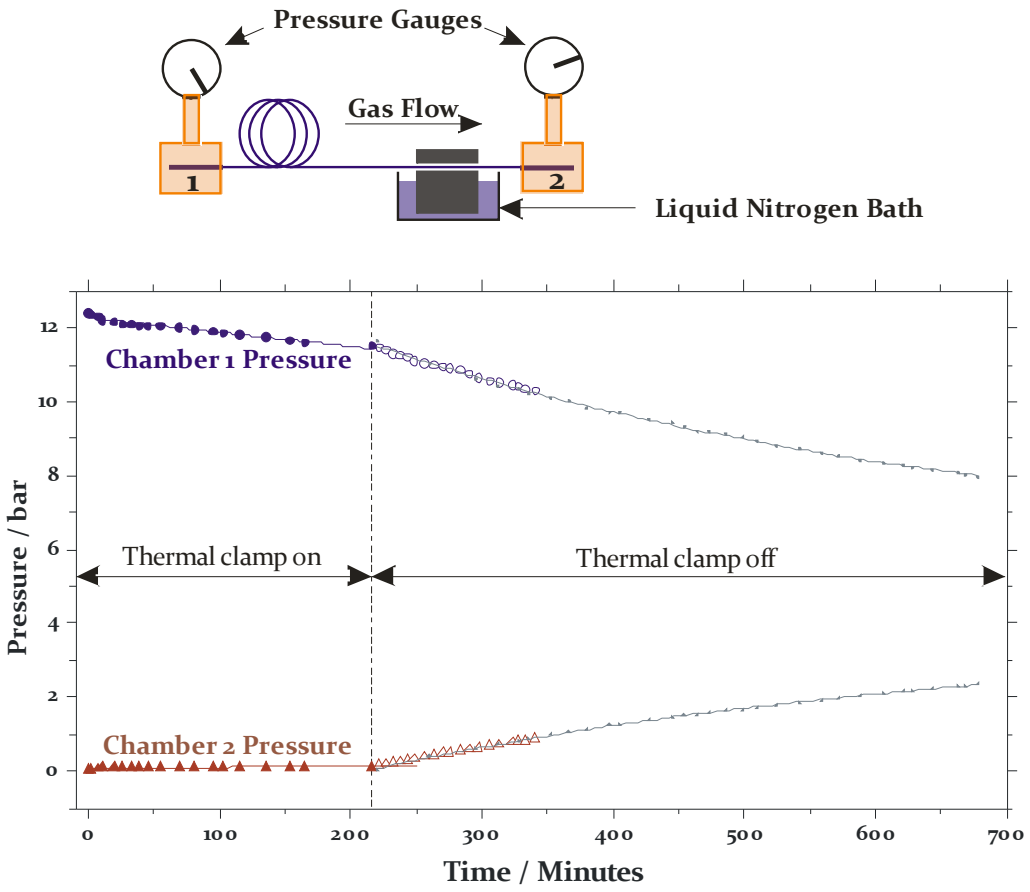

Figure 4-4: *Top: schematic of the thermal clamp arrangement. Bottom: hydrogen gas flow through 85 cm of fibre. Blue and red points show pressure in input and output chambers respectively. For the first 210 minutes (solid points) a 5 cm section of fibre close to one gas control chamber is cooled to ~100 K. After this time (open points) the fibre is allowed to return to room temperature. The grey points and curve are for the same length of fibre where a clamp has not been used, offset by 210 minutes.*

Figure 4-4 illustrated the operation of a thermal clamp, and plots the gas flow between two chambers (described in section 4.3.1) linked by an 85 cm length of HC-PCF. Initially a 5 cm section of fibre close to one chamber is cooled to ~100 K, by cooling a block of aluminium with liquid nitrogen; the fibre is trapped between this and a second block of aluminium. The chamber at the opposite end of the fibre to the thermal clamp is filled at 13.5 bar with hydrogen gas. The gas flow is monitored for 210 minutes before the thermal clamp is removed and the fibre is allowed to return to room temperature.

While the clamp is in place, there is no observed rise in pressure in the second chamber. The decrease in pressure in the first chamber is due to leaks within the chamber. Immediately after the clamp is removed after 210 minutes, gas flow is observed between the two chambers (open points). The grey points and curves are data collected from a

setup with the same initial conditions, but without thermal clamp, and shifted to start at the time the clamp was removed. The flow rate after the thermal clamp is removed matches that from the fibre without clamp, suggesting that the fibre temperature quickly recovers.

This thermal clamp is a convenient method of preventing gas flow within a fibre. The temperature required to cool the fibre to stop the flow will depend strongly on the gases present within the fibre. The small diameter of the fibre means that the fibre can however be cooled quickly, and the fibre can be safely cooled to liquid nitrogen temperatures without physical damage to the structure. Furthermore, the thermal clamp technique can be used to enhance the pressure gradient between two ends of a HC-PCF and hence the gas loading process.

4.3 Fabrication of Photonic Microcells

Having considered the flow of gases in micro-channels, this section explains each stage of fabrication on a photonic microcell. The preparation of the fibre is explained first, together with the gas control chambers that are used to both evacuate and fill the cells. Following this different techniques for sealing the fibre are explained, included a novel techniques that allows vacuum-pressure microcells to be created easily and inexpensively.

4.3.1 Fibre Preparation

Gas Control Chambers

The introduction of gas into and the evacuation of gas from the hollow-core fibre are achieved through the use of gas-control chambers, shown in Figure 4-5. The brass chamber is used for molecular gases, while the stainless steel chamber is designed to achieve the lowest possible pressures and for use with atomic vapours.

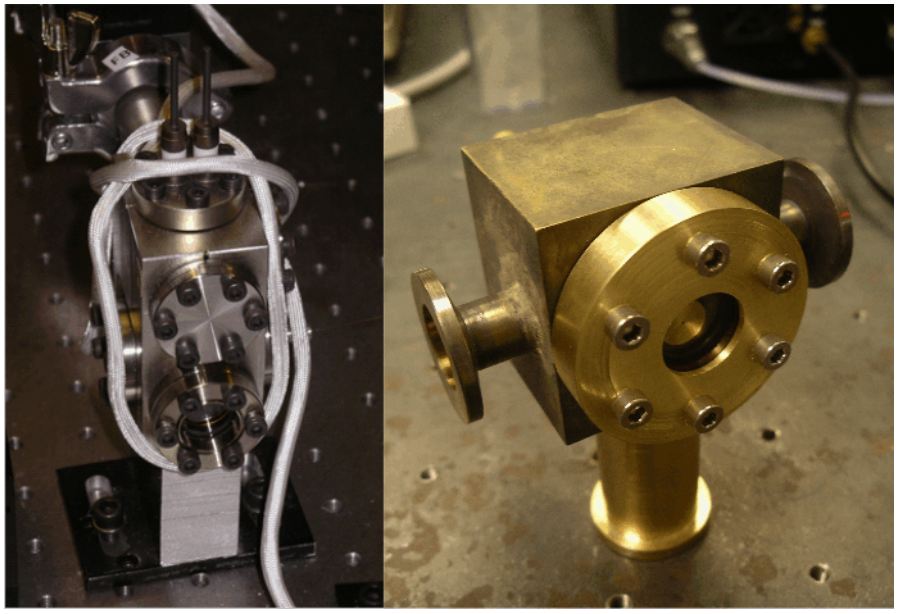

Figure 4-5: *Photograph of the gas-control chambers used for evacuating and filling HC-PCF. Left: stainless steel chamber used for atomic vapours at high-vacuum levels. Right: brass chamber used for molecular gases. The fibre end is hermetically sealed inside the chamber, and an optical window allows for the coupling of light into the fibre.*

Each end of the fibre is hermetically sealed in a separate chamber; the seal is formed by compressed Viton gaskets, as shown in Figure 4-6 and Figure 4-7.

The first stage in the fabrication of a photonic microcell is to flush the fibre to remove water vapour and other impurities that may exist in the fibre, and affect the loading process. To do this, one end of the fibre is attached to gas chamber filled with high purity argon or nitrogen, typically at ~5 bar. The fibre is heated to 120°C to ensure the vaporisation of water, and is removed by the gas flow through the fibre. For a 10 m length of fibre, a period of 4-5 hours is allowed for this flushing process.

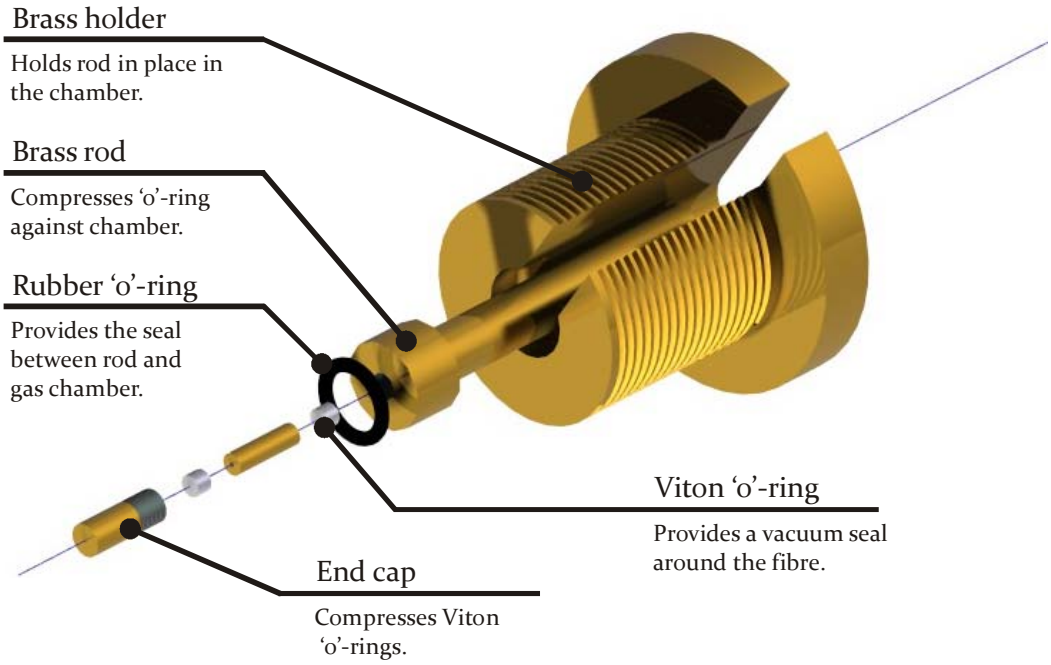

Figure 4-6: *This assembly allows the fibre end to be hermetically sealed within the gas control chamber, and easily removed without damage when required. The vacuum seal is provided by the compression of Viton 'o'-rings around the fibre. This design is used for loading fibres with molecular gases.*

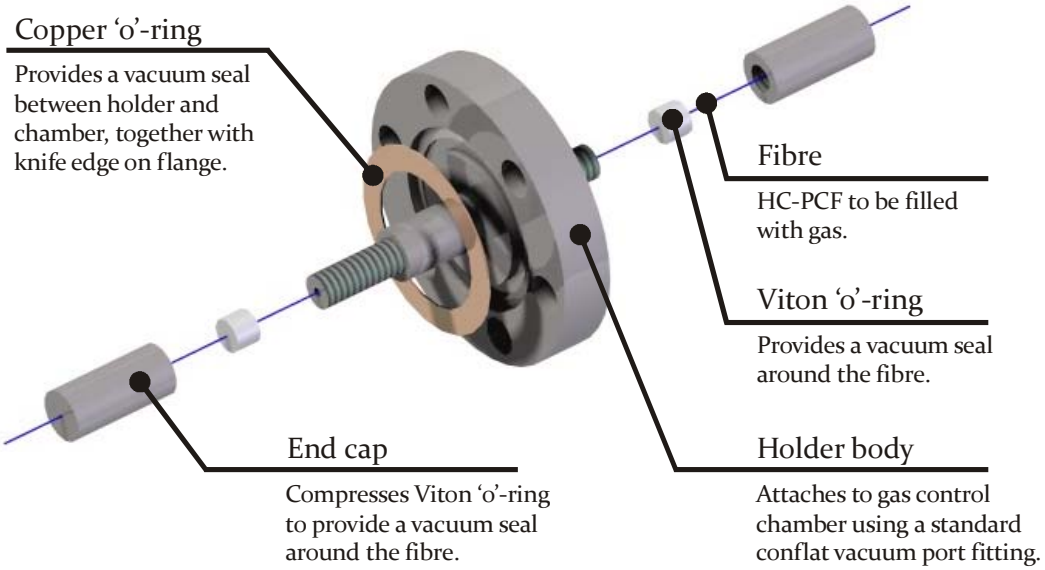

Figure 4-7: *This improved assembly is used to be hermetically seal a fibre within the stainless steel gas chambers used for loading rubidium vapour. The standard knife-edge seal on the flange allows UHV connection to a vacuum port.*

4.3.2 Gas Loading

After flushing, the required gas can be loaded into the fibre. For this process each end of the fibre is attached to a separate gas control chamber, to which it will remain attached until the microcell is sealed. To achieve the best possible purity, the fibre is flushed with the required gas by filling one chamber at high pressure, and evacuating from the second chamber. The next steps depend on the desired gas pressure in the completed microcell.

For fabrication of high-pressure photonic microcells, the pressure in the first gas chamber is reduced to the required pressure, and evacuation of the second chamber is stopped. The flow of gas through the fibre is monitored by observing the pressure in both gas-control chambers, until the pressure in both chambers is identical. In this way, the pressure of the gas inside the fibre is certain to be the same as that inside the chambers. The timescale for filling fibres in this way is discussed later in this section.

Low pressure microcells, below a few millibar, will usually require further monitoring in order to ensure correct gas pressure. For these, optical monitoring of the width of a suitable absorption line is used to determining the gas pressure, rather than relying on mechanical gauges with their associated dependence on gas type. When monitoring the pressure in this way it is important to consider additional broadening of absorption lines due to collisions between gas molecules and the fibre core wall, discussed in section 3.3.1, which become significant at sub-millibar pressures.

Also of particular importance for low pressure microcells is the time taken for the pressure to reach equilibrium throughout the length of the fibre, which may be on the scale of many hours. The following sub-sections consider the filling and evacuation of fibre.

Simulated Evacuation

The first regime considered is the evacuation of fibre initially filled uniformly at 1.2 bar. The pumping speed is such that a pressure of 1 μbar is maintained in the gas-control chambers at either end of the fibre. This is the situation when a fibre to be used as a low-pressure gas-cell is overfilled with gas. Figure 4-8 plots the pressure distribution along the length of the fibre as a function of time. Also plotted is the pressure that would be reached in the fibre if it was sealed at that time and allowed to reach equilibrium.

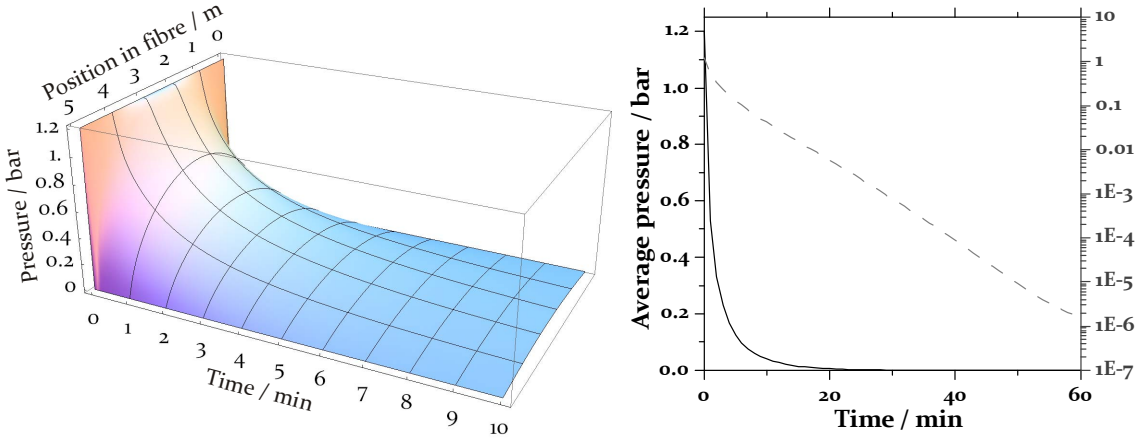

Figure 4-8: *Left: theoretical acetylene pressure distribution within a 5 m long, 12 µm diameter fibre as a function of time. The fibre is initially filled at 1.2 bar, and the chambers at 0.1 µbar. Right: average pressure in the fibre as a function of time on linear (solid line) and logarithmic (dashed line) scales.*

It can be seen that after 1 minute the pressure has reached 600 mbar. To reach pressures of 1 millibar and 1 microbar takes approximately 30 minutes and 60 minutes respectively; this illustrates the difficulty in obtaining the correct gas pressure inside the fibre when creating low-pressure gas-cells.

In order to have an order-of-magnitude guide to the time required to reach a certain pressure, the dependence of evacuation speed on fibre length is shown in Figure 4-9. The fibre is taken to be at a uniform 1.2 bar initially, and attached to chambers kept at a constant pressure of 1 µbar. The points plot the time taken to reach a given pressure (1 mbar, 100 µbar and 10 µbar) within the fibre. The fitted curves are fits to the point determined by simulation; an approximate l^2 dependence on length is expected. The fit parameters are given in Table 4-1.

Target Pressure	l^2 coefficient / 10^{-4}	l^4 coefficient / 10^{-6}
1 mbar	2.058	-6.8
100 µbar	2.865	-9.9
10 µbar	3.324	-8.0

Table 4-1: *Fit parameters for curves in Figure 4-9.*

The time taken to evacuate a 5 m fibre to 1 mbar is ~25 minutes. If the fibre length is doubled the time taken increases to 2 hours, while increasing the fibre length another 5 metres, to 15 m, requires over 4 hours to evacuate to the same pressure.

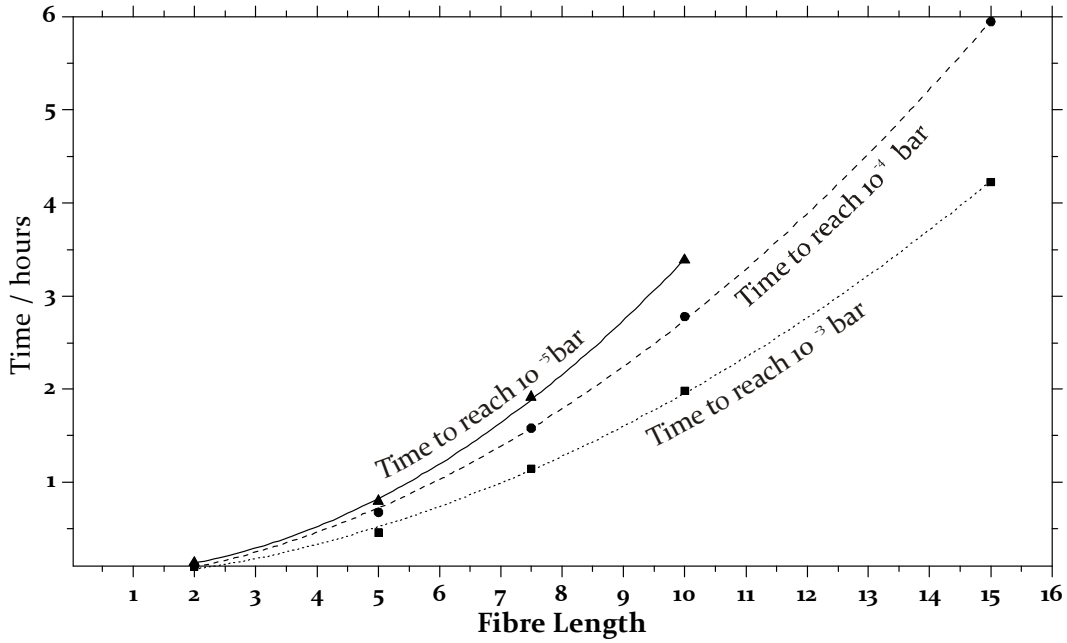

Figure 4-9: *Theoretical time (points) and exponential fits (lines) to evacuate a 12 µm diameter HC-PCF initially filled at 1.2 bar to pressures of 1 mbar (dotted line), 100 µbar (dashed line) and 10 µbar (solid line)*

The slow speed of evacuation is one reason why during preparation of the photonic microcell the fibre is flushed with the required gas: this process will remove impurity atoms more quickly than evacuating the fibre from either end.

Simulated Loading

Figure 4-10 is a similar calculation, filling the fibre with acetylene gas from both ends, with the gas control chambers filled at 1.2 bar. The initial pressure inside the core of the fibre is taken to be 1 µbar.

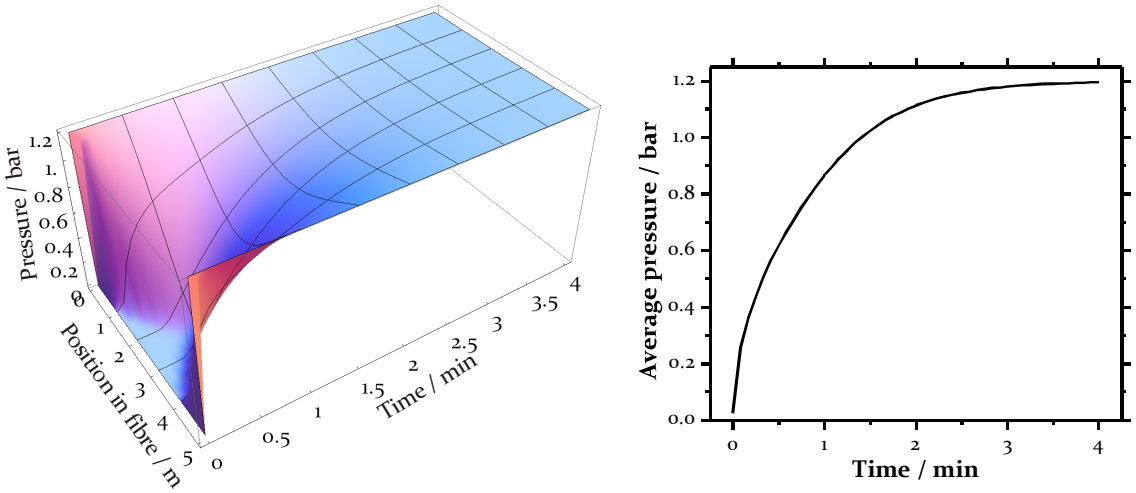

Figure 4-10: *Left: theoretical acetylene pressure distribution within a 5 m long, 12 µm diameter fibre as a function of time. The fibre is initially filled at 1 µbar, and the chambers at 1.2 bar. Right: average pressure in the fibre as a function of time.*

After just 4 minutes the pressure in the fibre reaches a uniform 1.2 bar. This calculation is also relevant to the filling of the fibre with helium to create a low-pressure low-loss photonic microcell, as will be described in the following section.

The reason for the asymmetry in time scales seen here (Figure 4-10) and in the evacuation of fibre (Figure 4-8) is the difference in flow regimes involved. When evacuating the fibre, at pressures below ~500 µbar the free-molecular regime is applicable. When filling a fibre however, the slip-flow regime is applicable due to the high pressure in the chambers at either end of the fibre, resulting in a different flow dynamic (see Figure 4-2).

4.3.3 Sealing a Photonic Microcell

The formation of a photonic microcell requires the gas-filled fibre to be sealed after being loaded with gas at the correct pressure. Although the aim of the sealing process is to splice the hollow-core PCF to solid SMF at either end, there are several techniques for this, depending on the gas-pressure. Each technique involves the use of a fibre splicer, and more details of the splicing method is given before considering the different techniques for sealing the microcell.

Fusion Splicing of HC-PCF

For joining HC-PCF to conventional single-mode fibre a filament fusion splicer is used. Throughout the work presented here a Vytran 2000 splicer has been used. It is also possible to use arc fusion splicers [73], but such splicers offer less control and

repeatability than filament splicer models. Photographs of a splice between HC-PCF and SMF are shown in Figure 4-11; the structure of the HC-PCF is visible in the fibre on the right, and the core of the SMF is visible in the fibre on the left of the image.

The typical splice loss achieved between a 7-cell HC-PCF guiding at 1550 nm, and Corning SMF-28 is 0.9dB. The greatest contribution to this figure is due to the mode-mismatch between the fibres; triangular lattice HC-PCF has a fundamental mode that does not perfectly match the Gaussian mode of a conventional single-mode fibre. Mismatch between core sizes of the two fibres also add to this contribution, which represents ~0.6 dB as the total loss in the example above. Further contributions arise from the Fresnel reflection [74] at the air-silica interface, typically giving a loss of ~0.15 dB.

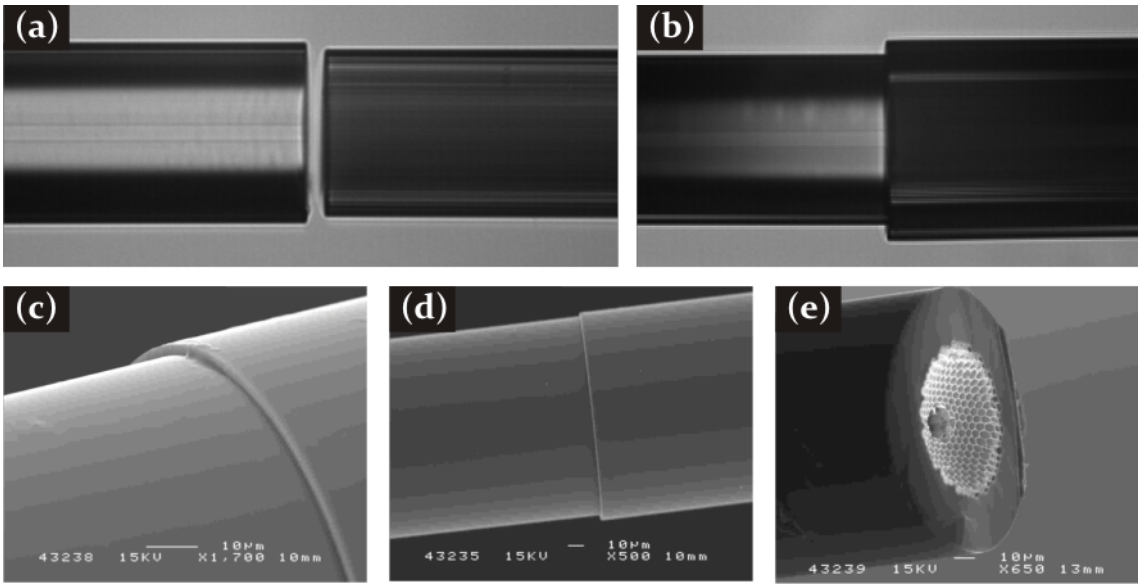

Figure 4-11: *(a) photograph taken before the splice of triangular lattice HC-PCF (right) and conventional solid single-mode fibre (left), as seen by the camera on a Vytran 2000 filament fusion splicer; (b) completed splice between a kagomé lattice fibre and SMF; (c) and (d) election micrographs of spliced fibre; (e) end face of HC-PCF when a splice is broken apart showing a curved surface.*

Figure 4-11(e) shows the end-face of HC-PCF as seen when a splice between SMF and SMF is broken. It can be seen that the cladding structure of the fibre has recessed, giving a curved face, which occurs due to surface tension effects during the splicing process as the fibre is heated. This effect can both lead to an increase or a decrease in the mode-field mismatch and therefore total splice loss.

The Fresnel reflection leads to a greater problem than the contribution to the splice loss; it is the light that the reflected and guided back along the fibre that can have a more detrimental effect. For example, reflection of laser power back inside the laser cavity leads to frequency instability. A more serious problem occurring in photonic microcells is the formation of cavity by the reflections at either end of the HC-PCF in the microcell. When scanning the frequency of a probe laser, this leads to a periodic modulation of the transmitted power through the microcell, with the period determined by the length of the HC-PCF (through $f = c/2L$, where L is the fibre length). For a typical microcell with fibre length of several metres, the modulation frequency is ~50-100MHz. This figure is comparable with the Doppler width of an acetylene absorption line at room temperature, and therefore interferes with the analysis of data in these conditions. This will be seen experimentally in Chapter 5.

To reduce the reflection, it is possible to perform an angled splice, with each fibre cleaved at a matching angle. By performing such a splice with each fibre cleaved at an angle of 8° it has been possible to reduce the reflection by 44dB, resulting in a return loss of <-60 dB compared with -16 dB for a normal splice. An angle splice is shown in Figure 4-12.

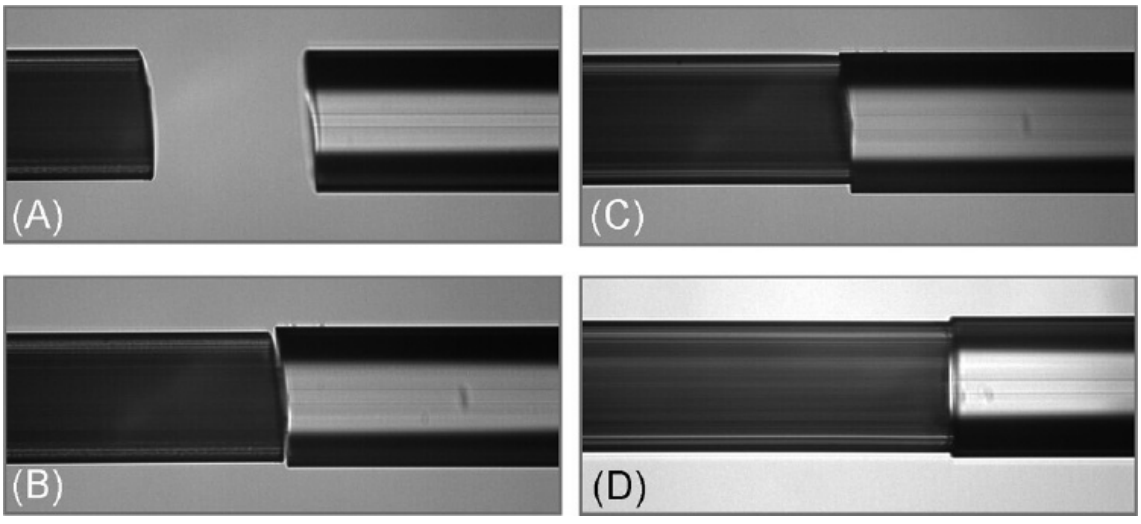

Figure 4-12: *(a) Angled cleaves of HC-PCF and SMF; (b) the fibres are rotated and butt-coupled ready for splicing; (c) side view and (d) top view of the angle-spliced fibres.*

There is however an increase in the transmission loss at such a splice, such that the typical transmission loss for an angled splice is 3dB, in comparison with 0.9dB for a perpendicular splice. The increased loss is attributed to the tendency of the HC-PCF to

produced a curved cleave, rather than the flat cleave observed for SMF; for flat cleaves an increase in loss of 1 dB is expected for each degree mismatch in cleave angle.

The greatly reduced return loss will nevertheless more than compensate for the small increase in transmission loss, as it will remove the etalon effects explained above that would be detrimental in many applications.

The following paragraphs expand on how the splicing technique fits into the complete procedures for sealing the gas within a photonic microcell. There are three techniques, the first only suitable for gas-pressures at or above atmospheric pressures. The second, developed for vacuum pressure cells, has limitations that led to the third novel technique involving the fast diffusion of helium through silica.

Direct Splice

The first, and simplest, technique for sealing a photonic microcell is to simply remove one end of the HC-PCF from a gas-control chamber, and splice to SMF. The same process is then repeated at the second end. Microcells formed using this technique have been used for stimulated Raman scattering in hydrogen gas and laser frequency stabilisation (section 3.4) in acetylene [68].

The drawback of this technique is that the end of the fibre is open to the atmosphere until the splice has been completed, a process that with practise can be completed in approximately 30-60 seconds. During this time, either gas will escape from a fibre filled at high-pressure, or air will enter into a fibre filled at low-pressure.

This is modelled by considering HC-PCF which is sealed at one end, and opened to the air at the other. Figure 4-13 and Figure 4-14 show the actual pressure obtained in the microcell as a function of the time taken to perform the sealing splice; the initial acetylene pressures inside the fibres are 10 bar and 1 mbar respectively.

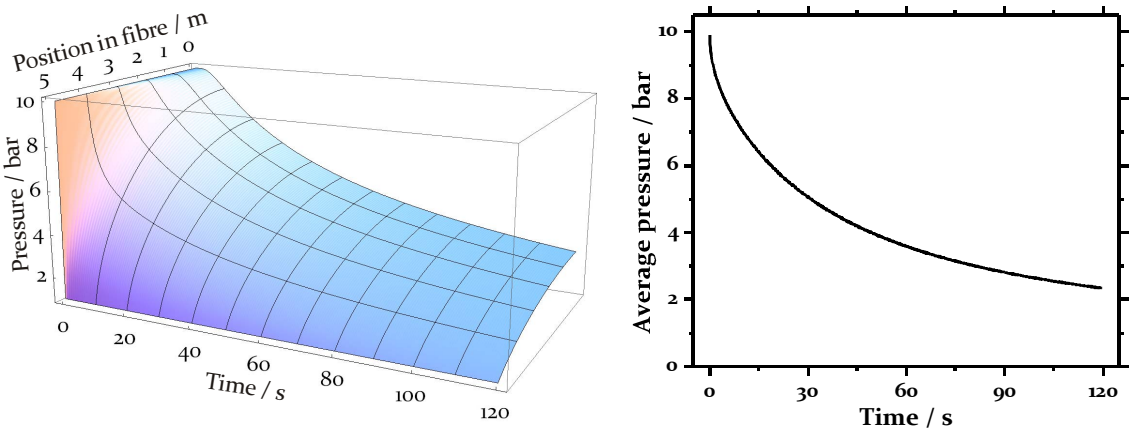

Figure 4-13: *Left: pressure distribution within a 5 long fibre with 12 µm core diameter as a function of time. The fibre is initially filled uniformly at 10 bar, and sealed at one end. The second end is open to a reservoir at 1 bar. Right: average pressure within the fibre at a function of time. This represents the usual situation in sealing a high-pressure photonic-microcell.*

The splicing procedure takes a minimum of ~30 seconds, and in this time, the pressure in the fibre initially at 10 bar will reduce to approximately 4.5 bar. When producing high-pressure cell the loss of gas can be approximately compensated for by initially filling the fibre at higher pressure than required, and does not present a problem in the fabrication of such microcells.

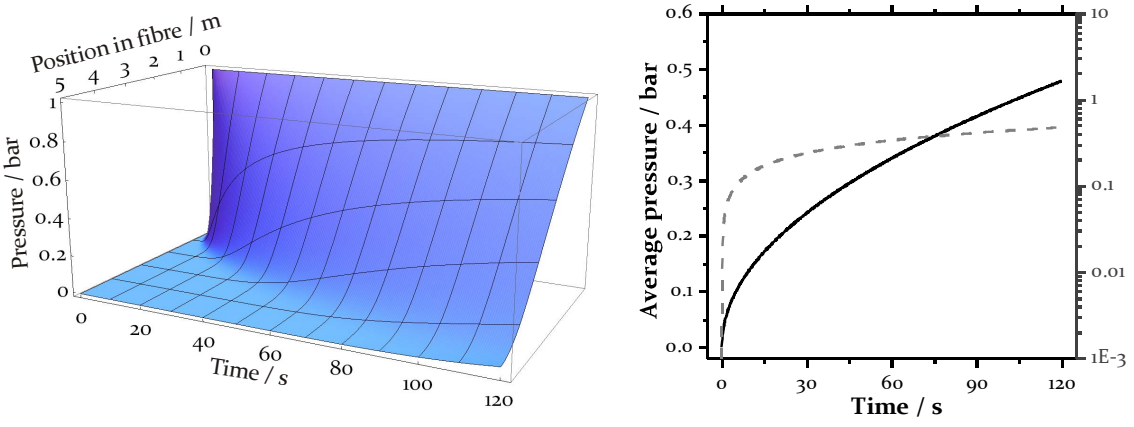

Figure 4-14: *Left: pressure distribution within a 5 m long fibre with 12 µm core diameter as a function of time. The fibre is initially filled uniformly at 1 mbar, and sealed at one end. The second end is open to a reservoir at 1 bar. Right: average pressure within the fibre at a function of time, on a linear scale (black) and logarithmic scale (grey). The average pressure rises to 100 mbar within just a few seconds.*

Considering the low-pressure 5 m long fibre however, the pressure will rise to ~300 mbar in the 30 seconds taken to perform the splice. This would be unacceptable for coherent optics applications, where the excess pressure would lead to an increase in collisional broadening of absorption lines, and decoherence in the system (section 3.3.1) in additional to detrimental effects results from the loss of purity of the original gas.

Clearly the direct splicing technique is not suitable where low-pressure uncontaminated microcells are required, such as for the applications discussed in section 3.4 and the experimental work presented in Chapters 5 and 6.

Core Collapse

To address the contamination problem of the direct splicing technique, a new sealing procedure was developed, suitable for fabricating microcells with the low-pressure requirements for quantum-optics.

In this technique, the HC-PCF is spliced to SMF at one end after the fibre has been flushed and filled at high pressure, above 1 bar, with the required gas. The fibre is then evacuated from the open end, and filled with the required gas at the required pressure. Care must be taken with this process to ensure that the flushing gas is adequately evacuated – for a 5 m fibre ~1 hour of pumping is required to reach an average pressure of 10 μbar inside the fibre assuming a pressure of 1 μbar is maintained in the gas control chamber; further details are given in section 4.2.

Once the fibre is filled, it is sealed by collapsing a small section of the fibre close to the remaining gas chamber, by heating with a filament fusion splicer. With sufficient temperature, the entire structure of the HC-PCF collapses and fuses to form solid silica, as can be seen from Figure 4-15. The fibre is then cleaved at the point of collapse, and spliced to SMF in the usual way.

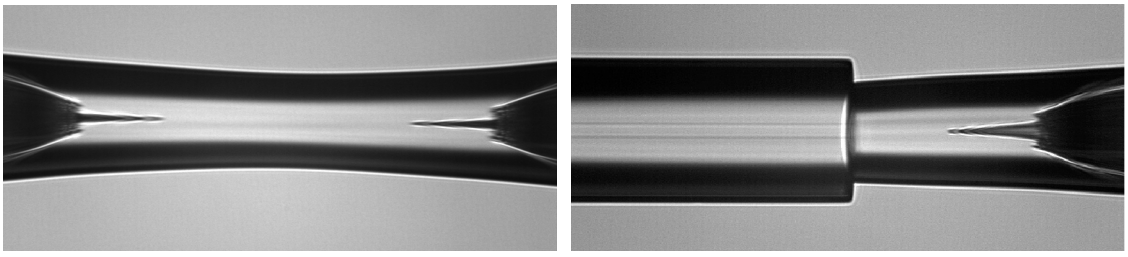

Figure 4-15: *Left: the collapse of the structure of a HC-PCF occurring when heated using a filament fusion splicer. The collapse of the cladding holes and core hole are clearly visible as different positions in the photograph. Right: the fibre can be cleaved at the point of collapse and spliced to SMF.*

This technique produces low-pressure microcells with no possibility of contamination during the sealing process. However, it is not without its disadvantages; the collapse of the cladding structure over a distance of ~300 μm at the splice gives rise to an optical transmission loss of ~10 dB.

Despite this relatively high loss in power, acetylene photonic microcells at millibar pressures formed using this technique are acceptable for many applications. For example, such microcells were used for the observation of saturated absorption in acetylene (section 5.9).

Helium Diffusion

To achieve the ultimate goal of vacuum-pressure photonic microcells with low optical insertion loss, a novel technique has been proposed by F. Benabid [75] and co-developed by the author [76], taking advantage of the fast diffusion of helium through silica. The rate of diffusion can be described through equation 4-4 [77], where q is the volume (cm^3) of gas at STP flowing through a wall of thickness d (mm) per unit surface area (cm^2) every second. The actual rate depends on the permeability constant K and gas pressure P (mmHg). For helium diffusing through silica this constant is 1.25×10^{-11} $cm^3/cm^2/mmHg$ at room temperature, many order of magnitude greater than for other gases [59].

$$q = \frac{KP}{d} \qquad 4\text{-}4$$

The fibre is initially prepared as detailed at the beginning of this section, with the fibre filled at the required pressure below 1 bar. High purity helium gas is then added to the fibre via the gas-control chambers, raising the total pressure to just above 1 bar. This allows the microcell to be sealed by direct splices to SMF without an inrush of air into the hollow-core fibre, since the total pressure is above atmospheric pressure.

The novelty of this technique is that the helium within the sealed fibre quickly diffuses through the silica cladding and polymer coating, leaving the required gas within the core of the fibre at the original fill pressure. The partial pressure of helium within the atmosphere is 5 μbar, and so a small quantity of helium will remain in the fibre; this of course applies to all silica based gas-cells, regardless of the production process. If this pressure of helium is detrimental it can be removed from the fibre by placing the microcell in an evacuated chamber, which will in any case increase the rate of diffusion of helium out of the fibre. Coating of the fibre with an appropriate material could then reduce the rate of helium back into the microcell once removed from the vacuum.

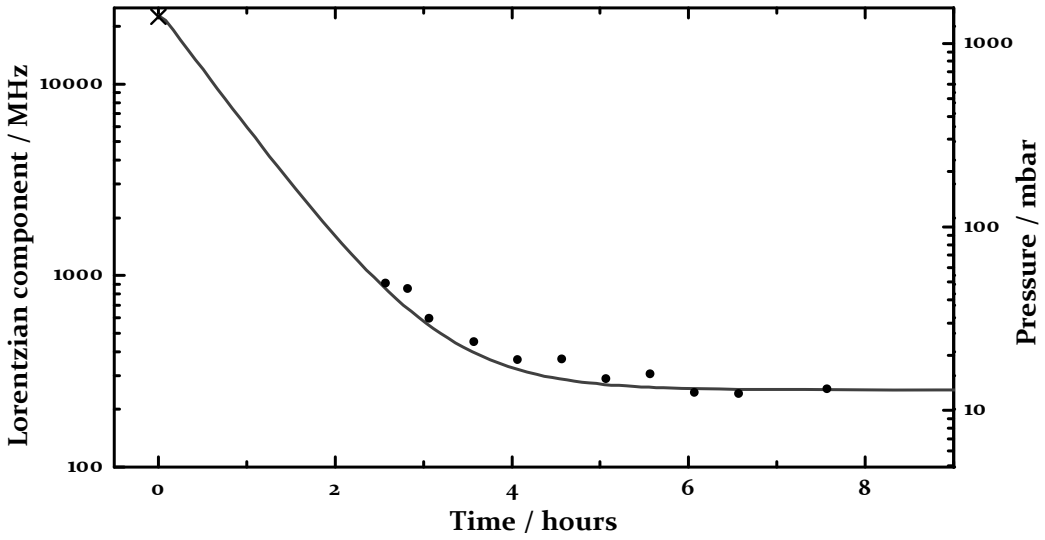

Figure 4-16: *Experimentally determined total pressure within a newly made acetylene gas cell, formed using the helium technique. The high-pressure point (cross) was measured with a Pirani pressure gauge; other pressure points (circles) are determined from the Lorenztian pressure-broadening component of an absorption line. Line: theoretical total pressure within a 5 m long HC-PCF as a function of time, assuming a 12 mbar acetylene partial pressure.*

The optical insertion loss of photonic microcells formed with this technique is low, as discussed in the direct splicing section above, and low-pressure cells for quantum optics applications can be formed.

Figure 4-16 shows the calculated rate of helium diffusion out of the fibre. The expected pressure after a given time can be calculated from equation 4-5, where r_{out} and r_{in} are internal and external radii of the silica cladding, P_{He} and P_{Gas} are initial pressures of helium and the microcell gas respectively, and $P(t)$ is total pressure at time t.

$$P(t) = P_{He} \exp\left[\frac{-Kt}{\pi(r_{out}^2 - r_{in}^2)}\right] + P_{Gas} \qquad 4\text{-}5$$

The same figure shows the experimentally determined rate of helium diffusion. Here the initial helium pressure was determined by a mechanical pressure gauge, with subsequent pressure measurements taken after sealing of the microcell determined optically by considering Lorentzian collisional broadening of an acetylene absorption line. The rate of collisional broadening is taken to be 12 MHz/Torr [78, 79]. Figure 4-17 shows a series of transmission profiles of the R15 acetylene absorption line, illustrating the reduction in linewidth over time.

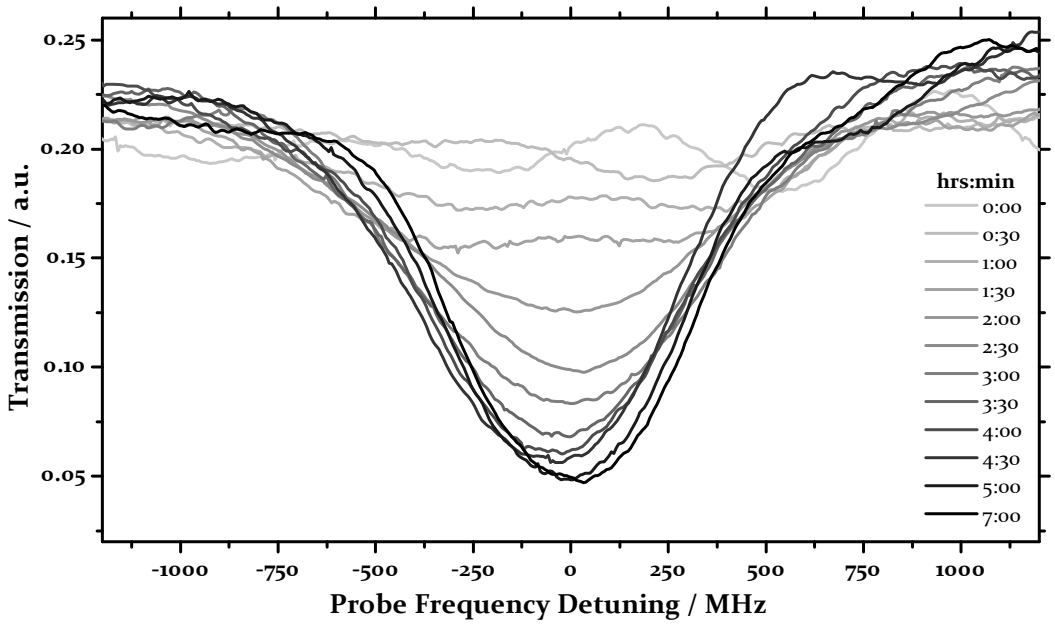

Figure 4-17: *Illustration of the reduction in linewidth of an acetylene absorption line (R15) over time, showing the reduction of pressure in a photonic microcell as the helium diffuses out of the fibre core.*

From these theoretical and experimental results, it can be seen that 12 mbar helium partial pressure is reached in 7 hours. The time for diffusion of helium out of the microcell is dramatically reduced by placing the microcell is a vacuum environment, where sub-millibar helium pressures are reached within 30 minutes. The rate of helium diffusion can similarly be increased by heating of the microcell.

The purity of the helium used for this technique is extremely important when low pressures are required, since any contaminants in the helium will remain in the microcell. The helium can be purified using techniques such as a liquid nitrogen trap in situations where low levels of contamination may be problematic.

The ultimate pressure achievable in a microcell is limited by the partial pressure of gases in the atmosphere that diffuse through silica at a non-negligible rate. Most other gases diffuse several orders of magnitude more slowly through silica than helium, such that the diffusion of those gases into or out of a microcell is not significant over a period of years. A notable exception to this is hydrogen, which diffuses through silica at a tenth of the rate of helium.

Demonstration that microbar pressure photonic microcells can be formed using this technique can be seen by considering the quantum optical effect of EIT in an acetylene filled HC-PCF both before and after creation of the microcell.

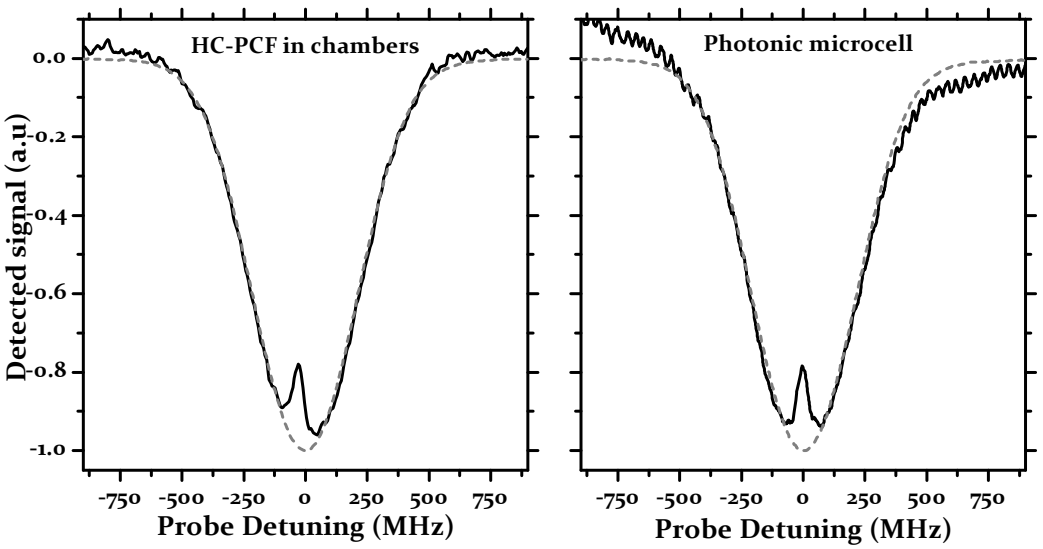

Figure 4-18: *Electromagnetically induced transparency under otherwise identical conditions in (left) fibre attached to chambers and (right) the completed photonic microcell after 24 hours have been allowed for the helium to diffuse out.*

Figure 4-18 compares experimental electromagnetically induced transparency in an acetylene filled fibre still attached to the gas control chambers (left), and in the completed microcell formed from this fibre, after allowing 24 hours for the silica to diffuse out of the fibre (right). The full experimental details are given in Chapter 5, but here it is sufficient to consider the fact that the width and height of the induced transparency peak seen at the centre of both spectra is much more sensitive to pressure than the width of the absorption line itself. It can be seen that the completed microcell has a transparency comparable in dimensions to that achieved before the fibre was filled with helium, and therefore that the acetylene pressure in the final microcell is at the same low pressure as it was in the filled fibre.

4.4 Atomic Vapour Loading

The loading of an alkali vapour into a HC-PCF, for the purpose of experiments described in Chapter 6, requires a more thorough approach than that used for loading unreactive gases described in the preceding section.

The highly reactive nature of alkali vapours necessitates an extremely clean environment, with low (sub-μbar) background pressure. Adsorption of the vapour, both physically and chemically, onto the silica of the fibre core must also be considered. Additionally, to counteract the broadening of absorption lines and loss of coherence due

to collisions between atoms and the fibre core wall due to the confined geometry (section 3.3.1), a polymer coating is applied to the inside the fibre core.

In order to minimise both leakage and degassing, gas-control chambers constructed from 316 stainless-steel and designed for high-vacuum are used for the loading of atomic vapours into HC-PCF. The chamber can be seen in Figure 4-5 and Figure 4-19.

Before use, the chambers are prepared by cleaning all components in an ultrasonic bath with a strong basic soap solution. The parts are then cleaned in distilled water, acetone, and finally methanol. Residual solvent is removed by baking at 400°C for several days. The system is then assembled, evacuated, and baked at ~150°C. This final process is important for removing hydrogen gas close to the surface of the stainless-steel chambers, which is the main degassing component that limits the pressure obtainable.

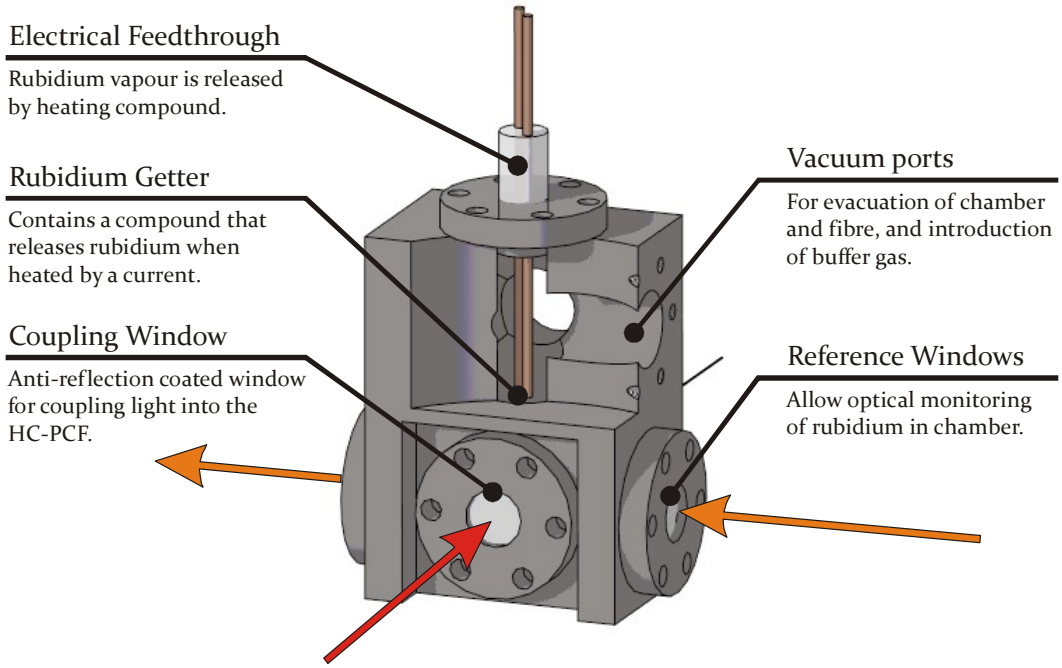

Figure 4-19: *Diagram of the gas control chamber used to load rubidium into HC-PCF.*

4.4.1 Polymer Coating of Core

The fibre to be used is first prepared as it would be for a standard photonic microcell (section 4.3.1) by flushing and heating. The additional step in the preparation of a fibre to be used with an atomic vapour is the coating of the inside of the core of the fibre with a layer of polymer to allow spin-preserving collisions between vapour atoms and the core wall. Several polymers have been shown to have this effect when used in bulk gas cells

[80, 81]. Polydimethylsiloxane (PDMS) has been chosen as suitable for coating the fibre core due to its proven properties and availability in various viscosities.

Since only a thin coating of the polymer is required on core wall of the fibre, the PDMS is prepared as a solution of 2% PDMS in diethyl-ether. The core of the fibre can then be filled with this solution and the ether allowed to evaporate, leaving a coating of PDMS. It is important to prevent coating of the cladding structure with the polymer as this negatively affects the guidance properties of the fibre. To avoid this, after flushing the fibre as described in section 4.3.2, the cladding structure is collapsed at each end of the HC-PCF, leaving only the core hole open. This is achieved by heating with a filament fusion splicer with the result can as seen in Figure 4-20; for a short section of fibre (~100 μm) the cladding holes are completely sealed.

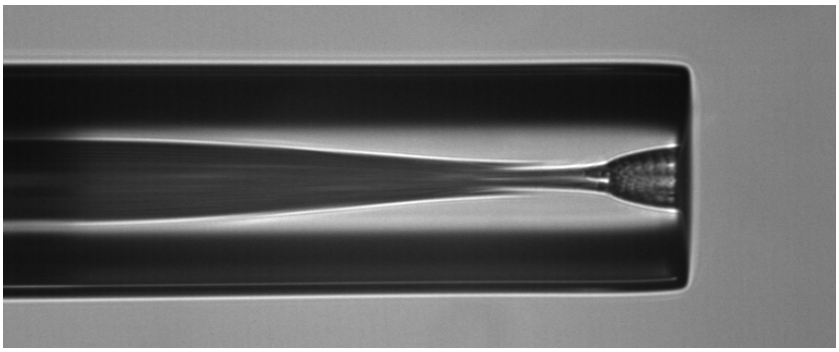

Figure 4-20: *Photograph of a HC-PCF with cladding structure collapsed using a filament fusion splicer. The cladding holes are sealed while the core hole remains open, allowing solely the core to be filled with gas or liquid.*

The fibre with collapsed cladding holes at either end is attached to a gas-control chamber at one end. The core of the fibre is filled with the polymer solution by dipping the loose end of the fibre in the solution, and evacuating the fibre via the gas control chamber (Figure 4-21). This process takes approximately one minutes for a fibre 1 m in length; it can be monitored via light scattered at the vacuum-solution interface by coupling light through into the fibre through the chamber. Once filled with the solution, the loose end is attached to a second gas control chamber, and the fibre evacuated from both ends.

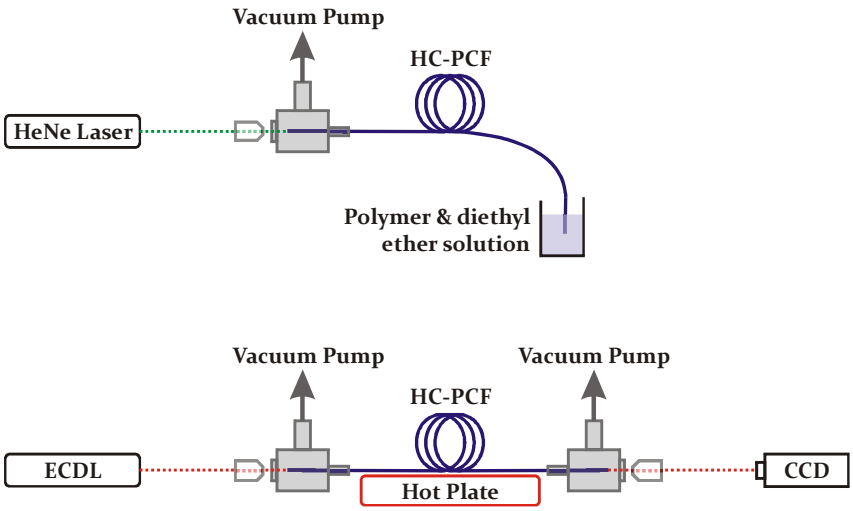

Figure 4-21: *Polymer coating of the HC-PCF core. Top: The fibre core is filled with a solution of PDMS in diethyl ether. The progress is monitored by the scattering of visible HeNe radiation at the vacuum/solution interface. Right: The ether evaporates, and is evacuated from both ends of the fibre to leave a polymer coating on the silica core wall. The fibre may be heated to speed this process.*

The ether is volatile, and is removed from the fibre on the timescale of 10s of hours. As the ether is evaporated, the PDMS is deposited onto the silica core walls. The evaporation of the ether is monitored optically by measuring the transmission spectrum of the fibre over time; within one day the transmission of the uncoated fibre is recovered. To speed up this process the fibre can be gently heated, keeping the temperature below the melting point of the PDMS (~200°C for the viscosity used). The recovery of guidance by the fibre as the ether evaporates is shown by the sequence of images in Figure 4-22: in (a) no core guidance of light is achieved, although apexes in the cladding structure are guiding (as is usual for this fibre), as clearly shown inset; (b) show the partial return of guidance after 3 hours of evacuation. When viewed on the CCD camera the light in the core is seen to shimmer; (c) after 24 hours the core guidance returns completely, as also confirmed by comparing transmission spectra from before and after the polymer coating process.

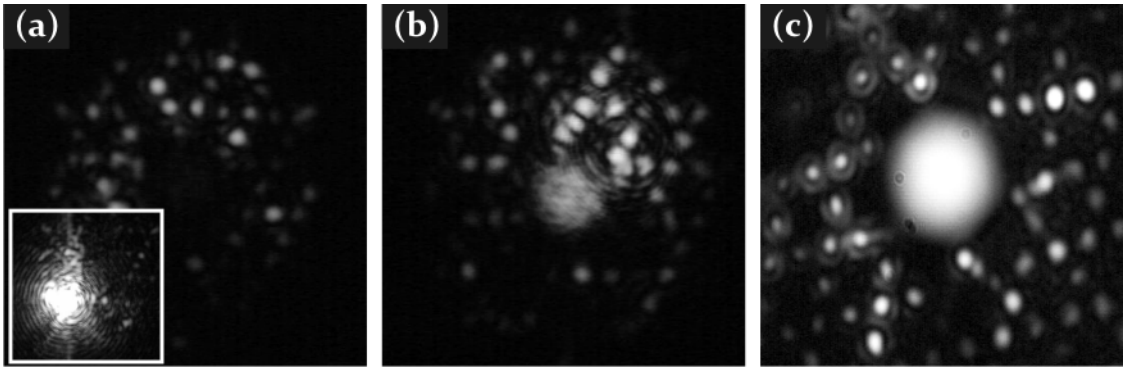

Figure 4-22: *A sequence of images of kagomé fibre illustrating the return of light guidance in the core as the ether evaporates from the PDMS solution. (a) immediately after filling with the solution core guidance is very poor; the inset figure shows guidance in a silica apex of the cladding. (b) core guidance starts to return after 3 hours of evacuation – the core of the fibre appears to shimmer as the fibre is heated. (c) Full guidance returns after 24 hours.*

Scanning electron micrographs of the fibre core (Figure 4-23) reveal that there are no large drops of PDMS deposited within the core. The resolution available is however insufficient to directly observe the properties of the polymer layer obtained. Further work is planned to evaluate and optimise the physical properties of the layer formed.

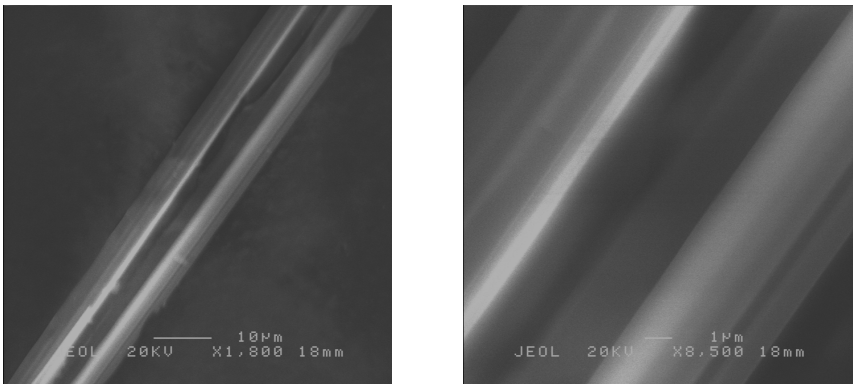

Figure 4-23: *Scanning electron micrographs of the PDMS coated HC-PCF core. The core is viewed in isolation from the remainder of HC-PCF structure.*

4.4.2 Vapour Loading

After flushing and polymer coating, the fibre is prepared to be loaded with the atomic vapour. The setup used is shown in Figure 4-24, with the chamber containing the rubidium source illustrated in Figure 4-19.

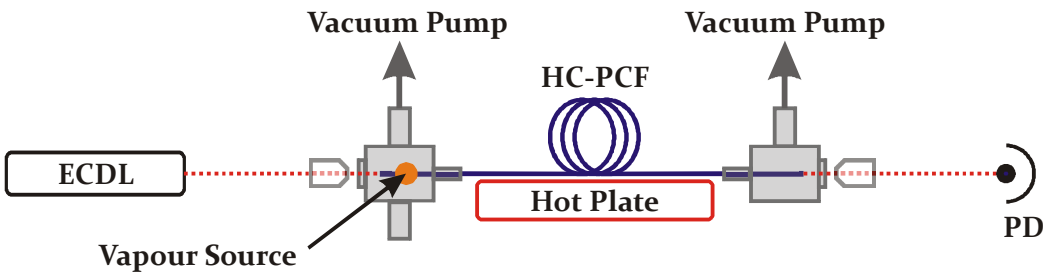

Figure 4-24: *Loading rubidium into HC-PCF. A natural rubidium source in one gas control chamber releases rubidium when heated by passing an electrical current through it.*

The gas control chambers are evacuated to 10^{-6} mbar at a temperature of ~150°C using a combination of turbo-molecular and ion-getter pumps. The system is left in this configuration for several days to ensure evacuation of the fibre to a suitable pressure level.

The experiments presented in Chapter 6 use rubidium vapour, and for this an Alvatec natural rubidium vapour source is used, containing ^{85}Rb and ^{87}Rb in ~3:1 ratio; rubidium is released from the source by a heating current which also allows the rate of release to be controlled.

In order to improve the rate of filling of the HC-PCF with rubidium, both the chambers and fibre are kept at a temperature of ~140°C during the filling process to maximise the vapour pressure; this will be discussed further in section 6.2. Monitoring of the vapour loading process, which is performed optically by monitoring the rubidium D_2 absorption lines, is also shown in this section.

The low vapour pressure of rubidium (2.9 µbar at 140°C) and large mean-free-path (~2.7 cm) in comparison with the diameter of the fibre core mean that molecular flow is applicable and that the loading process is relatively slow, although optical means are available to increase the loading rate (see Chapter 6). The loading of rubidium takes place over several days, with the source current being reduced until the rate of release matches the rate of adsorption; at this stage the current to the vapour source is reduced to 2-2.5 A. The loaded fibre is then suitable for use in observing quantum optical effect such as EIT, which will be shown in chapter 6.

4.5 Summary

This chapter has introduced hollow-core photonic crystal fibre based photonic microcells. The fabrication procedures for microcells of a wide range of pressures, from microbar to tens of bar, has been demonstrated. Such microcells, which are compact,

light and flexible, have the ability to replace bulk gas-cells in many situations. As all-fibre devices they are simple to include in optical fibre systems, simply by splicing. One role for photonic microcells in this situation is as frequency references, which are useful for example in dense wavelength division multiplexing systems used in telecommunications, where the frequency accuracy of the laser used is important.

Photonic microcells are also excellent for observing quantum optical effects. Acetylene microcells, at vacuum pressure and created using the helium diffusion technique, will be used for quantum optics in the following chapter, representing one of the first demonstrations of such effects in a molecular gas.

In Chapter 6 rubidium loaded HC-PCF is used to demonstrate electromagnetically induced transparency at extremely low power levels. This is made possible by the tight confinement of light and long interaction length offered by a HC-PCF, acting as both a waveguide and gas cell.

Chapter 5

Coherent Effects in Molecular Gases

This chapter presents the first experimental observation of electromagnetically induced transparency in acetylene gas with a cw coupling laser. This is achieved by the use of acetylene-filled HC-PCF to obtain the required intensity and interaction length at low gas pressure. The observation is also performed in an all-fibre system using a photonic microcell.

EIT is observed in V and Λ energy level schemes from transitions in the $\nu_1 + \nu_3$ ro-vibrational acetylene overtone band. Theory based on the density matrix model and multi-variate fitting allows the dephasing parameters of the experimental system to be determined.

Counter-propagating probe and coupling beams are also used to observe EIT in V and Λ schemes. Usually EIT is not observed in this geometry due to the large two-photon detuning, but the long interaction length of a photonic microcell enables it to be clearly observed.

The use of acetylene photonic microcells is also demonstrated for saturated absorption spectroscopy.

5.1 Molecular Gases as Frequency Standards

Despite the many potential applications of coherent effects such as electromagnetically induced transparency (EIT) discussed in section 3.4, such work has focused predominantly on atomic-vapour based systems. There are a number of advantages to the use of molecular gases, including excellent wavelength coverage, and ease-of-use from a practical point-of-view. The very weak molecular dipole moments, however, have hitherto limited their use. Molecular transitional dipole moments in the visible and near-infrared are typically of the order of 10^{-3} debye, in comparison with atomic dipole-moments of ~1 debye at similar wavelengths. This corresponds to saturation intensities 10^6 times higher in molecular gases.

The use of molecular gases as frequency standards is of interest due to their excellent coverage of telecommunications wavelength bands. As the spacing of channels used in

wavelength division multiplexing (WDM) is reduced in order to increase capacity, the stability of lasers used in such systems becomes ever more important; the International Telecommunication Union now specifies a grid with just 12.5 GHz spacing for dense WDM systems [82].

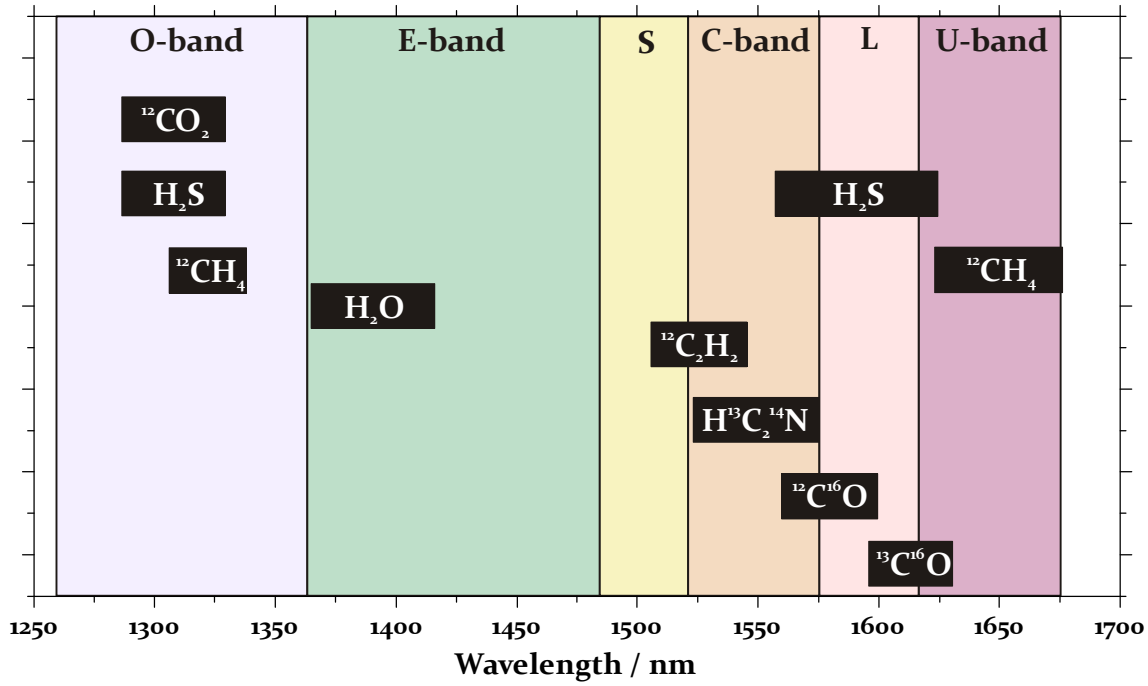

Figure 5-1: *Telecommunications wavelength bands and spectral coverage by molecular transitions.*

A combination of molecular gases provides regularly spaced frequency references in the range of this grid, and indeed other telecommunication bands; the coverage offered by just a few molecules is illustrated in Figure 5-1. Furthermore, the use of acetylene as a frequency reference has recently been recognised by its inclusion in the list of suitable references for practical realisation of the metre by Comité International des Poids et Mesures (CIPM) [83].

In addition to their excellent wavelength coverage, arising from the many vibrational and rotational modes and their overtones, molecular gases are often less reactive than atomic vapours making their use more straightforward. The commonly used atomic vapours of rubidium, caesium and calcium are all highly reactive alkali-earth metals.

5.1.1 Acetylene

The experimental work in the following sections of this chapter uses acetylene gas, chosen due to the ~60 regularly spaced absorption lines in the 1510 nm – 1545 nm

wavelength range. These can be seen in the transmission spectrum of a 1 m acetylene photonic microcell filled at ~100 mbar with $^{12}C_2H_2$ (Figure 5-2). The spectrum is obtained using a low-power broadband light-source and an optical spectrum analyser. It is noteworthy that the spectrum is obtained using only 80 nanolitres of gas.

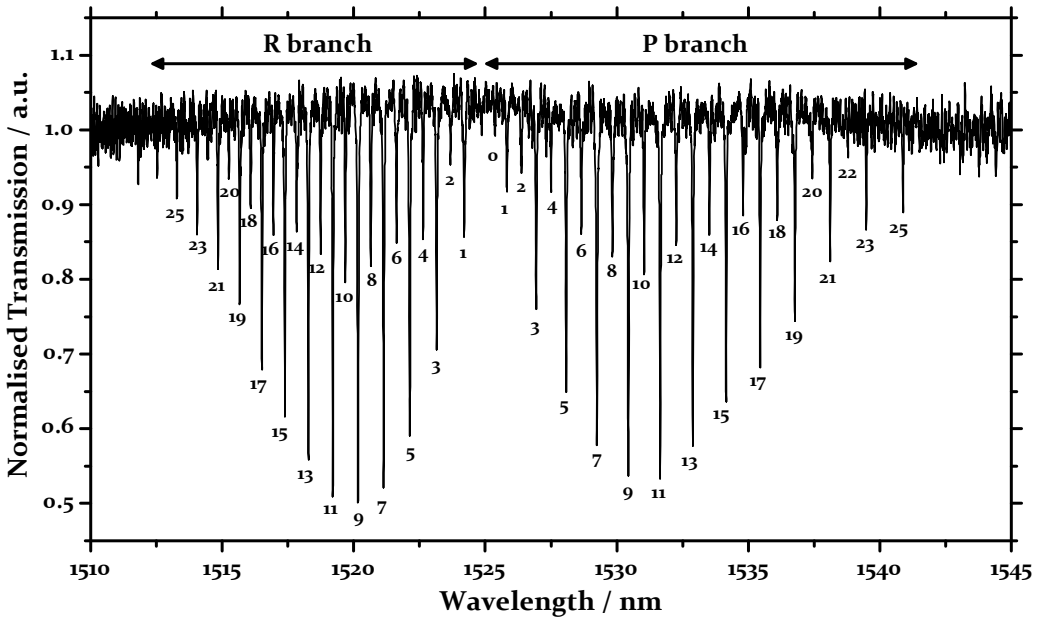

Figure 5-2: *Normalised transmission of a 1 m acetylene photonic microcell filled at a pressure of ~100 millibar, measured using a broadband light source and optical spectrum analyser.*

The source of the rich structure of molecular gases is the presence of many vibrational and rotational modes, together with their overtones. The vibrational modes of acetylene, a linear symmetric molecule, are shown in Figure 5-3. In general linear molecules will have $3N - 5$ vibrational modes, where N is the number of atoms. This is reduced to five modes in the case of acetylene due to its symmetry.

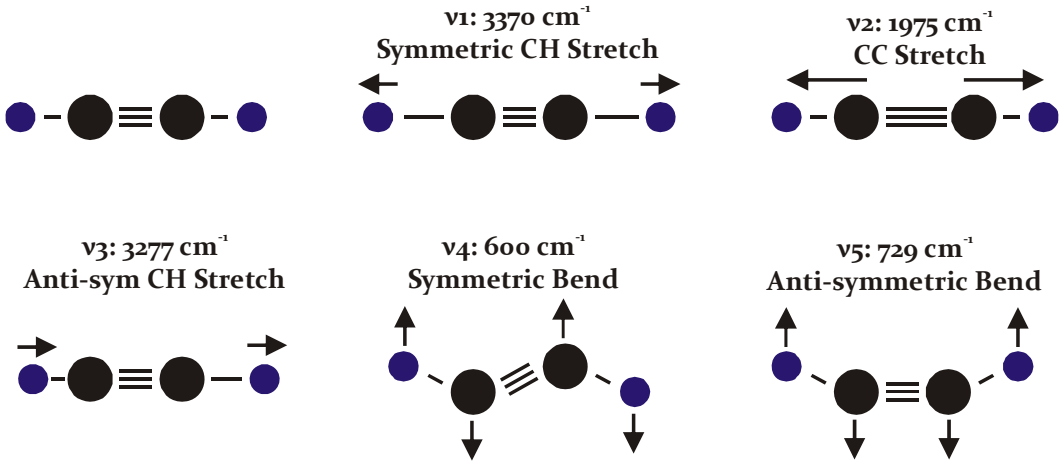

Figure 5-3: *The vibrational modes of the molecular gas acetylene. These modes and their overtones cover a wide range of optical frequencies. Each vibrational overtone provides a comb of transitions due to rotational modes.*

Commonly observed overtones of the fundamental vibrational modes that occur in the visible and near-infrared are given in Table 5-1. The highlighted overtone is of interest in this chapter, with a wavelength of 1538 nm.

Vibrational Overtone	Frequency / cm^{-1}	Wavelength / nm
$\nu_1 + \nu_5$	4092	2444
$\nu_2 + \nu_3$	5250	1904
$\nu_1 + \nu_3$	**6500**	**1538**
$3\nu_3$	9641	1037
$\nu_2 + 3\nu_3$	11599	862
$\nu_1 + \nu_2 + 3\nu_3$	14969	668
$\nu_2 + 5\nu_3$	17518	571

Table 5-1: *Energy and wavelengths of the fundamental vibrational modes of acetylene, and selected vibrational overtones in the visible and near-infrared [84].*

Rotational modes are of much smaller energy than the vibrational modes shown above, and give rise to a comb of spectral lines around each vibrational mode and overtone.

For the $\nu_1 + \nu_3$ overtone band of acetylene the rotational mode spacing is ~76 GHz, as was seen in Figure 5-2. The figure illustrates the P and R branches, corresponding to transitions with a change in rotational quantum number J of -1 or +1 respectively. The Q branch, corresponding to $\Delta J = 0$ is forbidden due to the symmetry of the acetylene molecule.

5.1.2 Quantum Optics in Molecular Gases

We now turn our attention to the ability to observe and use quantum optical effects in molecular gases. The ability to use such gases offers the potential to extend the wavelength ranges of applications for which atomic vapours have already demonstrated their suitability. It could also lead to the development of new applications, which have thus far not been considered due to the drawbacks of atomic vapours.

Coherent optics in molecular gases has thus far been little studied. Autler-Townes splitting has been observed in NO, CO, and H_2 gases [85-87], but in each case it required the use of pulsed lasers to obtain the intensity required. Taking the H_2 example, lasers with 5 ns pulses and 80 μJ pulse energy were used, corresponding to a peak power of ~16 kW.

Only recently was the first observation of Autler-Townes splitting in a molecule using cw lasers made. This was observed by Qi *et al.* [88] using triple resonance spectroscopy [89] in a four energy level scheme of molecular lithium. Furthermore, the same group have observed EIT in molecular lithium, using cw lasers and a cascade energy level scheme [90]. In this scheme the induced transparency was observed by monitoring the side fluorescence from the upper level of the system using modulation techniques and a cooled photomultiplier tube. These techniques were required due to the limited interaction length of the experimental setup providing low signal-to-noise ratio.

Extending the broad range of work covering atomic vapours to molecular gases promises to not only develop our understanding of coherent effects, but also to pave the way for many new technological applications including laser frequency stabilisation, and slow-light applications such as optical buffering. Use of HC-PCF as the host for quantum optics in molecular gases overcomes the difficulties associated with the weak dipole-strengths, as high-intensity can be obtained at low power, and the interaction maintained over length-scales of metres or more to hugely improve signal-to-noise ratio.

This chapter presents the experimental observation of EIT in acetylene gas in HC-PCF. Initial results are obtained at relatively high (millibar) pressure, with the fibre attached to gas-control chambers. To explore the coherence within the system further, microbar-pressure acetylene photonic microcells, providing an all-fibre system, are then used to explore the effect of energy-level configurations and beam propagating geometry. For the first time EIT is observed with counter-propagating beams in V and Λ energy level schemes, where the two-photon (residual) Doppler width is significantly larger than the coupling Rabi frequency.

5.2 EIT in Acetylene-Filled HC-PCF

As discussed in section 3.1.1, EIT is one of the most studied coherent effects, where the presence of a coupling beam induces a transparency in an absorption line scanned with a probe beam. The resulting sub-Doppler resonance, if available at the appropriate wavelengths, would be ideal for laser frequency stabilisation in telecommunication systems. The steep dispersion, seen in Figure 5-5, obtained in the transparency region also opens the possibilities of slow-light applications, such as optical buffering.

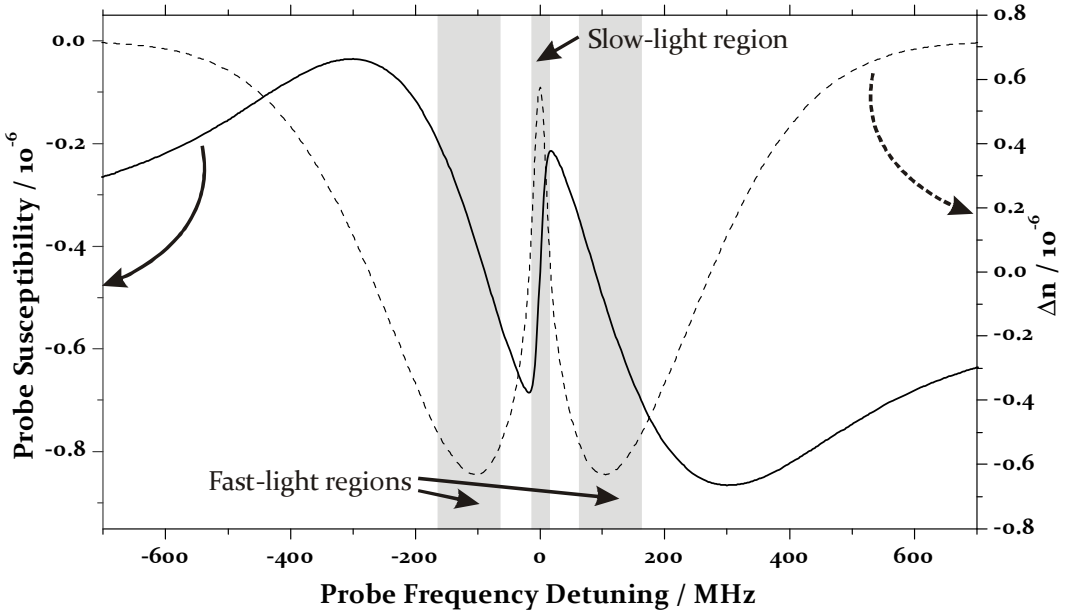

Figure 5-4: *Theoretical probe transmission (dashed curve) and change in refractive index (solid curve) illustrating the strong dispersion occurring across the frequency range of the induced transparency peak in an EIT system. Strong normal dispersion occurs across the region of induced transparency, opening possibilities for slow-light applications.*

For telecommunication applications, these effects must be available at wavelengths around ~1550 nm, and as we saw above, the $\nu_1 + \nu_3$ rovibronic overtone band of acetylene provides ~60 transitions in the 1510-1545 nm window.

These transitions allow the formation of both V and Λ energy level schemes by combining one transition from each of the P and R branches as illustrated in Figure 5-5. A lambda scheme is formed by the pair of transitions $R(J-1)$ & $P(J+1)$, and a vee scheme by the pair $R(J+1)$ & $P(J+1)$.

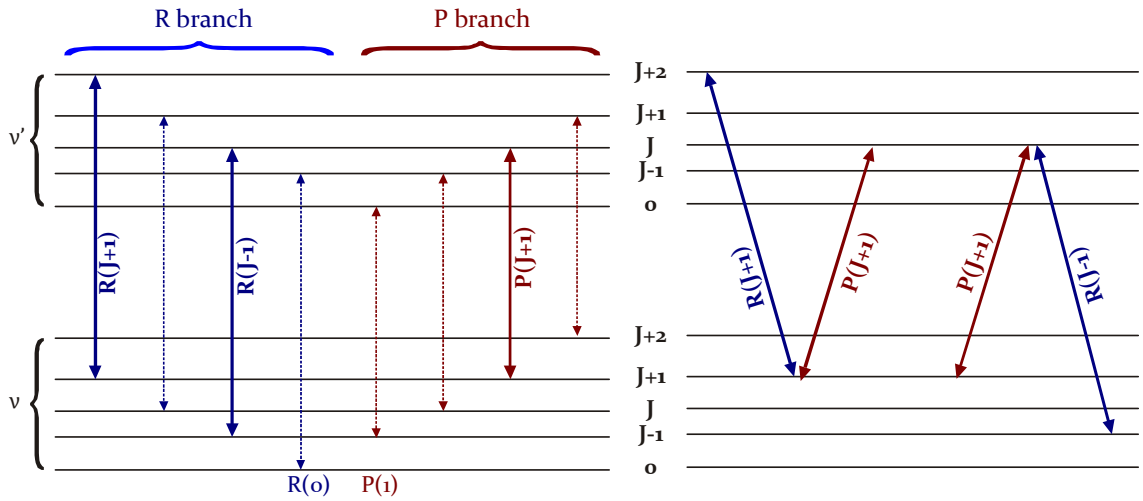

Figure 5-5: *(Left) Schematic energy level structure of acetylene showing the* $\nu_1 + \nu_3$ *transitions. (Right) Example of formation of three-level V and Λ schemes, both formed using the P(J+1) transition.*

The observation of EIT experimentally, as explained in section 3.1, requires a weak probe laser and strong coupling laser to co-propagate though the gas medium. The setup used is largely optical-fibre based, and is shown in Figure 5-6. One end of the HC-PCF host is hermetically sealed inside a gas control chamber, necessitating the use of free-space optics for detection of the probe at the output of the fibre. The acetylene pressure within the fibre is controlled by evacuation or addition of acetylene in the gas chamber.

The probe and coupling beams are provided by a pair of tuneable external cavity diode lasers (ECDLs). To achieve the required intensity of the coupling beam inside the fibre, a 1 W erbium-doped fibre amplifier (EDFA) is used to amplify the power from one ECDL. A fibre-optic coupler combines the probe and coupling beams, and a circulator prevents back-reflections to the lasers. An asymmetric splitting ratio 90:10 or 98:2 fibre-optic coupler is used to maximise the coupling power available, while still coupling sufficient probe power into the acetylene-filled fibre.

Free-space optics are employed at the output of the fibre for detection of the probe. Interference filters at the probe wavelength transmit the probe and attenuate remaining coupling power, before detection of the probe by a photodiode.

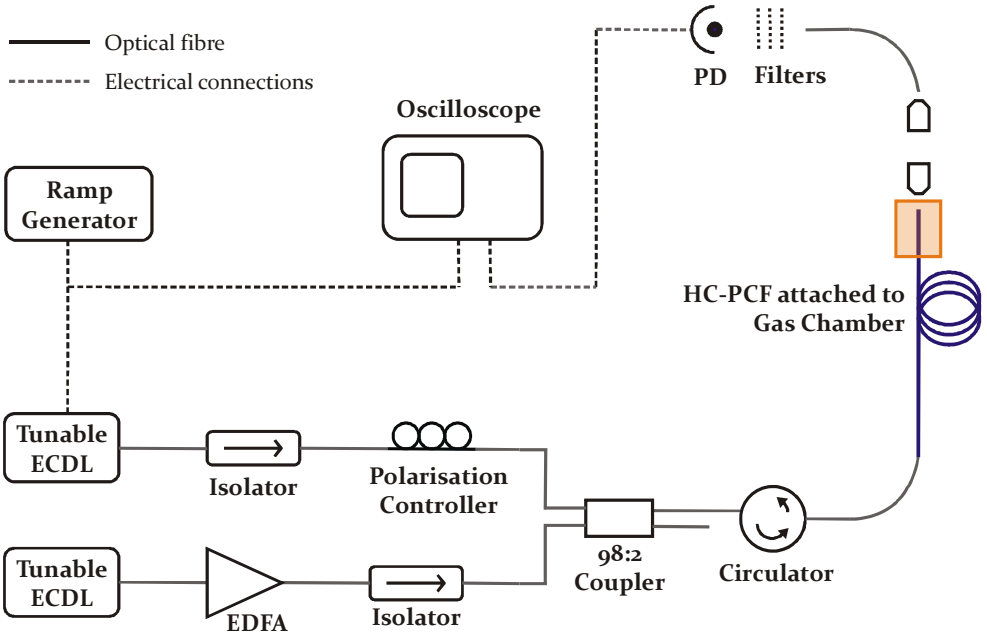

Figure 5-6: *Experimental setup for obtaining molecular electromagnetically induced transparency in HC-PCF. ECDL: external cavity diode laser; EDFA: erbium-doped fibre amplifier; PD: photo-diode.*

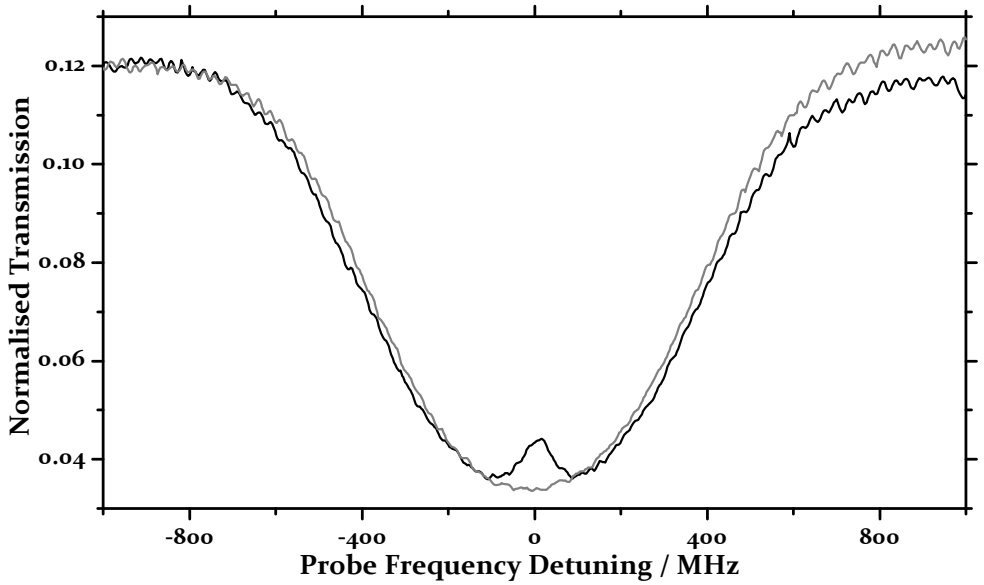

Figure 5-7: *Probe transmission spectrum showing electromagnetically induced transparency in acetylene filled HC-PCF at a pressure of 1 mbar. A lambda energy level scheme P(15)-R(13) is used, with a coupling power of ~500 mW.*

An EIT spectrum is obtained by sweeping the frequency of the probe laser by applying a triangular wave to the ECDL tuning mirror PZT. The typical sweep frequency is 20-30Hz. The grey curve in Figure 5-7 shows the probe transmission around the R(13) line in the

absence of the coupling beam, clearly showing a Doppler broadened absorption line. When the coupling laser is also coupled through the fibre, an EIT feature appears in the transmission spectrum, as seen by the peak of suppressed absorption in the black curve of Figure 5-7. The small oscillation seen across the spectrum is due to a low-finesse cavity formed by reflections at the gas chamber windows at either end of the fibre. A lower frequency oscillation due to beating between fundamental core modes of the fibre leads to the slight asymmetry observed in the spectrum (see Chapter 2 and section 5.8.2 later in this chapter).

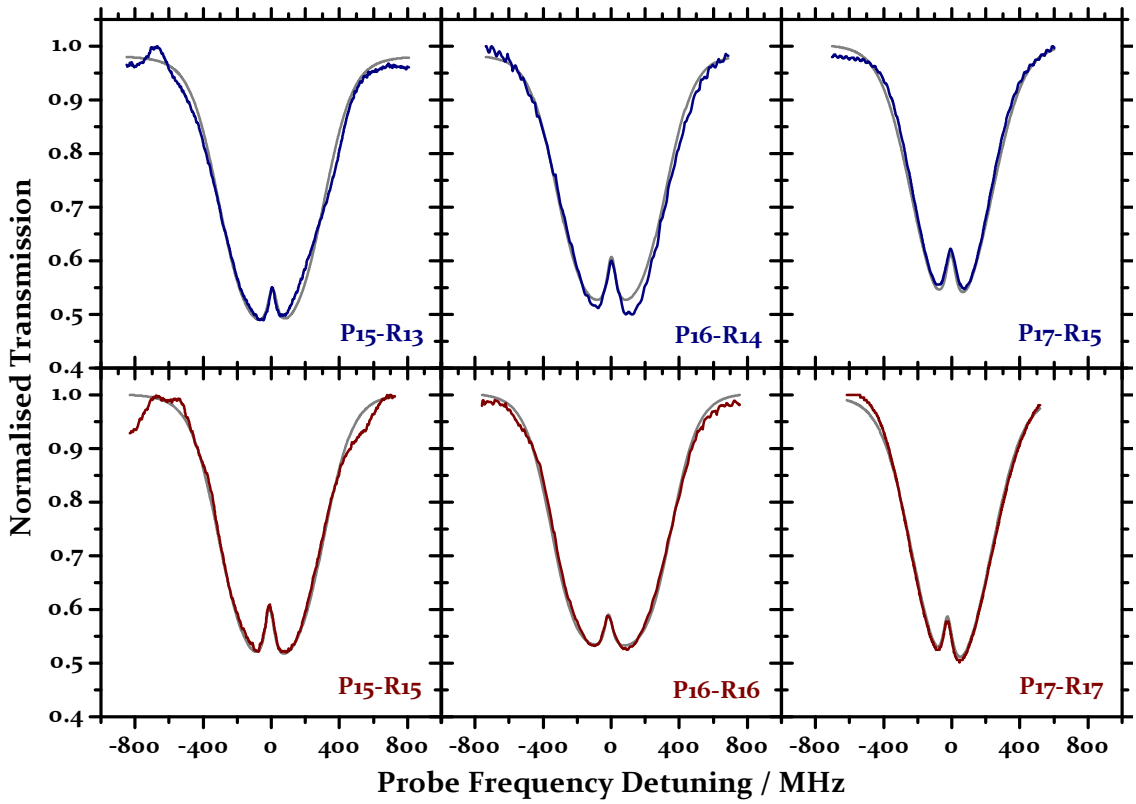

Figure 5-8: *EIT spectra obtained in acetylene filled fibre using three different coupling transitions (P15, P16, and P17 from left-to-right), and in Λ (top) and V (bottom) energy level schemes.*

In addition to the lambda scheme EIT in Figure 5-7, EIT has also been observed in the V energy scheme, using several transition pairs for the probe and coupling beams. Probe transmission spectra illustrating EIT in V and Λ configurations for three coupling transitions are shown in the grid of Figure 5-8.

The transparency induced in EIT can be characterised in a number of ways. It is conventional to consider the reduction in absorption on resonance with the coupling

beam present compared to the probe laser alone. This however fails to give any information about the transparency peak itself, and importantly we shall see later in section 5.5.1 that under certain conditions there may be no transparency *peak*, even though there is a reduction in absorption.

For characterisation of the induced transparency, it is convenient to define two parameters. The transparency height refers to ratio of the induced peak height to the total height, measured from minimum to maximum absorption in a given spectrum, as illustrated in Figure 5-9. Similarly, the transparency width refers to the full-width at half-height of the induced transparency peak. These definitions are chosen as they relate directly to properties that are important for applications, such as laser frequency stabilisation that require a narrow frequency reference.

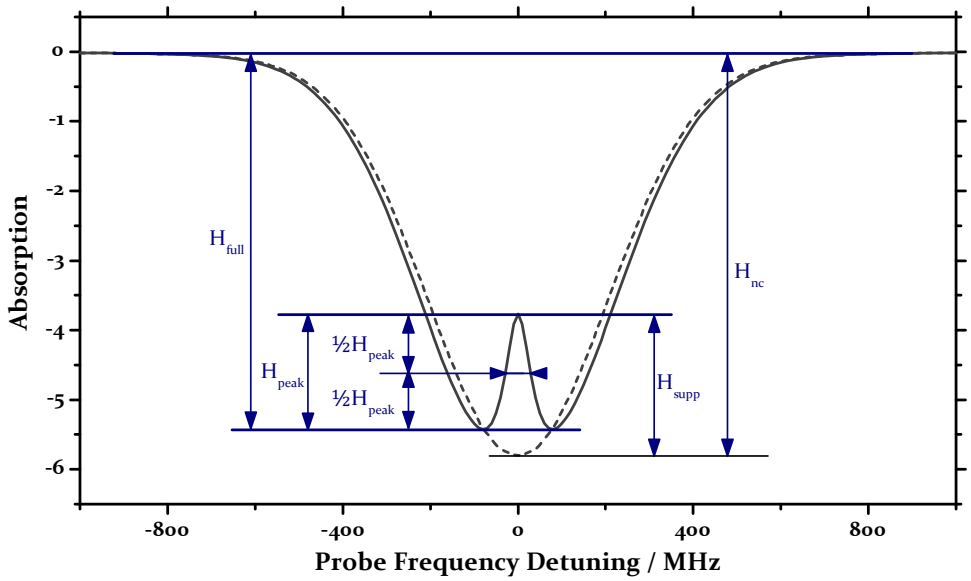

Figure 5-9: *Illustration of definitions used in text. Solid and dotted lines are probe transmission respectively in presence and absence of the coupling beam. H_{full} is height of spectrum from minimum to maximum absorption; H_{peak} is height from minimum absorption to on-resonance absorption; H_{supp} is suppressed absorption compared with spectrum in absence of the coupling beam; H_{nc} is total height in the absence of the coupling beam.*

Results obtained from a 2 m long HC-PCF filled with acetylene at ~1 mbar (such as those in Figure 5-8) show a typical transparency height of 10-15%, and width of 50-60 MHz. The relatively high acetylene pressure at which EIT is obtained demonstrates the effectiveness of HC-PCF as a host for such effects.

The effect of coupling power on the height and width of the induced transparency peak for the P(15)-R(13) Λ scheme is plotted in Figure 5-10. The peak height shows a strong dependence on the power of the coupling beam, with the height increasing from 4% to 17% as the coupling Rabi frequency is increased from 100 to 250 MHz. The dependence of linewidth on the coupling power is less pronounced, and remains ~52 MHz throughout. For coupling Rabi frequency above 260 MHz, the peak height is seen to plateau while there is a sudden increase in peak width. It is expected that this is due to the observed behaviour of the fibre amplifier at high power, resulting in increased linewidth of the coupling beam.

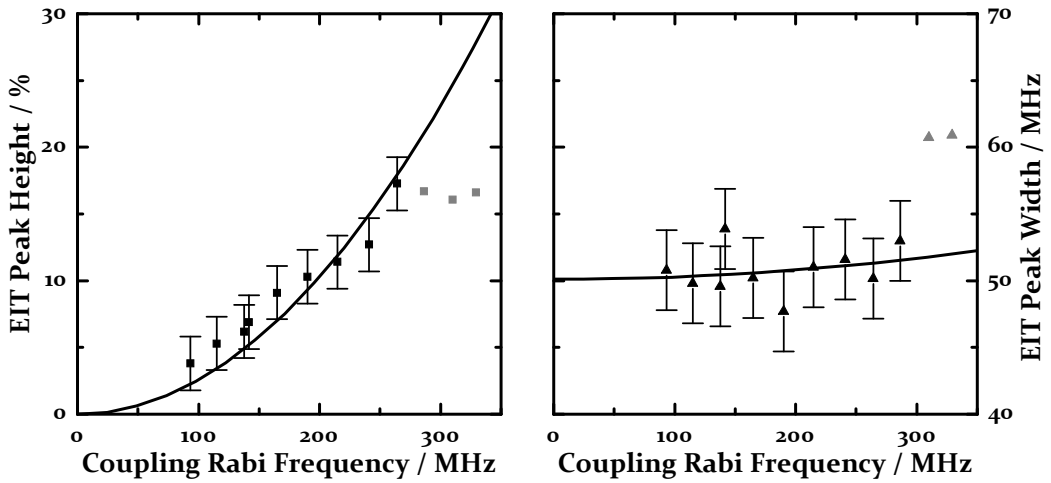

Figure 5-10: *Points: experimental EIT height and width as a function of coupling Rabi frequency for EIT observed in a Λ configuration using the P(15)-R(13) line-pair in acetylene-filled HC-PCF. Lines: fits to a simple theoretical model. Grey experimental points are excluded from the fit to this model for reasons explained in the main text.*

The curves on these plots represent fits to the experimental data based on a simple theoretical model designed to gain physical insight into the system. The model is based on that used by Gea-Banacloche et al. [91], derived for a cascade and lambda schemes under the assumption that in the absence of fields all population is in the ground state. It is also assumed that the system is closed, such that there is no population decay outside of the three coupled levels, and that the probe Rabi frequency is much less that of the coupling laser. The probe susceptibility is then given by equation 5-1.

$$\chi = \frac{ic\mu_c^2 N_0\sqrt{\pi}}{\varepsilon_0 \hbar u \omega_p} e^{z^2}[1 - \mathrm{erf(z)}]$$

5-1

$$z = \frac{c}{u\omega_p}\left[\Gamma_{od} - i\Delta_p + \frac{\Omega_c^2/4}{\Gamma_{gr} - i(\Delta_p - \Delta_c)}\right]$$

The error function $erf(z)$ appears as a result of integration over the Maxwellian velocity distribution of the molecules. μ_c is the dipole moment of the coupling transition, N_0 is the molecular density, u is the most probable molecular velocity, and ω_p is the probe laser frequency. The detuning of the probe and coupling from resonance are given by Δ_p and Δ_c respectively; Ω_c is the Rabi frequency of the coupling laser. Γ_{gr} gives the dephasing rate of the uncoupled transition, while Γ_{od} is that of the coupled transitions, partially due to the optical decay from the upper state of the lambda scheme.

From equation 5-1, approximate equations governing the height and width of the transparency peak are obtained (equations 5-2 and 5-3). It is important to note that these equations are based on a height defined as suppressed absorption, rather than the experimentally measured height shown in Figure 5-9; to a first approximation, however, these equations are valid.

5-2

$$H_{EIT} = \frac{\Omega_c^2}{2\Delta w_D \Gamma_{gr}}$$

5-3

$$W_{EIT} = 2\Gamma_{gr} + \frac{\Omega_c^2}{\Gamma_{\mathrm{od}}^*}$$

At large coupling Rabi frequencies the transparency width is dominated by the power broadening at a rate determined by Γ_{od}^*. This parameter is related to optical population decay from the upper level through $\Gamma_{\mathrm{od}}^* = \gamma_{\mathrm{od}}/V$, where γ_{od} is the rate of population decay from the excited state to ground state, and V is weighting due to the thermal velocity distribution of the acetylene molecules [92].

The solid lines in Figure 5-10 are the results of fitting the above equations to the experimental transparency heights and widths, with the decoherence rates as fit parameters. Independent fitting to the height and width data gives values of 20 MHz and 25 MHz respectively for the decoherence rate of the uncoupled transition (Γ_{gr}). These are in good agreement, considering the approximations made in the derivation of the expressions. The main sources of dephasing between levels 1 and 3, the lower states of the lambda scheme, are optical decay from the excited state 2, and collisional dephasing

due to collisions between acetylene molecules and the fibre core wall. The latter would be expected to dominate, since the lifetime of a vibrationally excited state is of the order of milliseconds; the calculated wall-collision rate for a fibre of core diameter 20 μm is 12 MHz (section 3.3.1). In addition, the finite laser linewidths of both probe and coupling lasers contribute to the dephasing rate, and are estimated to be ~2 MHz each. Γ_{od}^{*} is determined to be 9.6 GHz.

This results presented in this section were among the first observations of EIT in acetylene. During this work, Ghosh et al. published a similar observation of EIT in acetylene-filled HC-PCF [93], in a lambda energy level scheme and using a similar experimental setup.

In the following sections more detailed results, obtained using an acetylene photonic microcell, are presented and will be analysed in detail using a density matrix model.

5.3 EIT in Photonic Microcells

As seen in chapter 4, photonic microcells are all-fibre gas-cells suitable for integration directly into optical fibre based systems. In this, and following sections, we consider results obtained using a microcell formed from a 5 metre length of 19-cell HC-PCF with bandgap centred at 1550 nm. The use of a photonic microcell removes the need for bulky gas chambers, and simplifies the experimental setup for observing EIT to that shown in Figure 5-11. It also represents the first all-fibre system for this type of work.

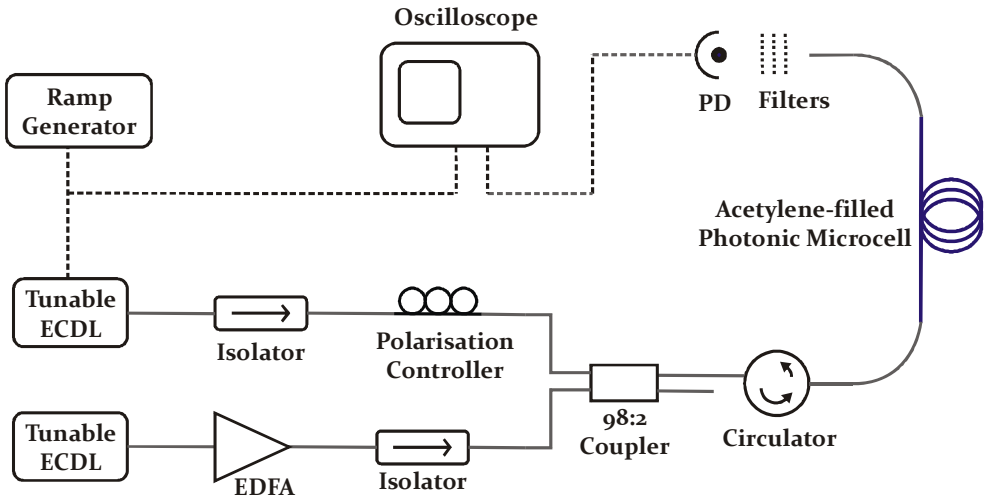

Figure 5-11: *Schematic experimental setup for investigation of EIT in an acetylene photonic microcell.*

An acetylene-filled photonic microcell is spliced to the forward-port of the circulator. While free-space optics are used as before for probe detection, their use here is not necessary; a fibre Bragg grating and a second fibre-circulator would provide an entirely optical fibre-based solution to separation of the probe beam from the coupling beam for detection.

A major advantage of photonic microcells is their lifetime. A single photonic microcell has been used in various experiments over a period of more than two years, and still displays the same characteristics as when it was initially fabricated.

Figure 5-12 displays a typical EIT profile obtained in an acetylene photonic microcell. The induced transparency peak is clearly visible at the centre of the Doppler-broadened acetylene absorption line. In this case the coupling laser is tuned to the P15 line at 1534.10 nm and the probe is sweeping across the R15 line at 1517.31 nm, forming a V energy level scheme. The probe and coupling powers are 10 μW and 406 mW respectively. The acetylene pressure within the photonic microcell is ~100 μbar, and this is the reason for the greater transparency height observed compared with that of figure Figure 5-7 for HC-PCF filled at a pressure of several millibar.

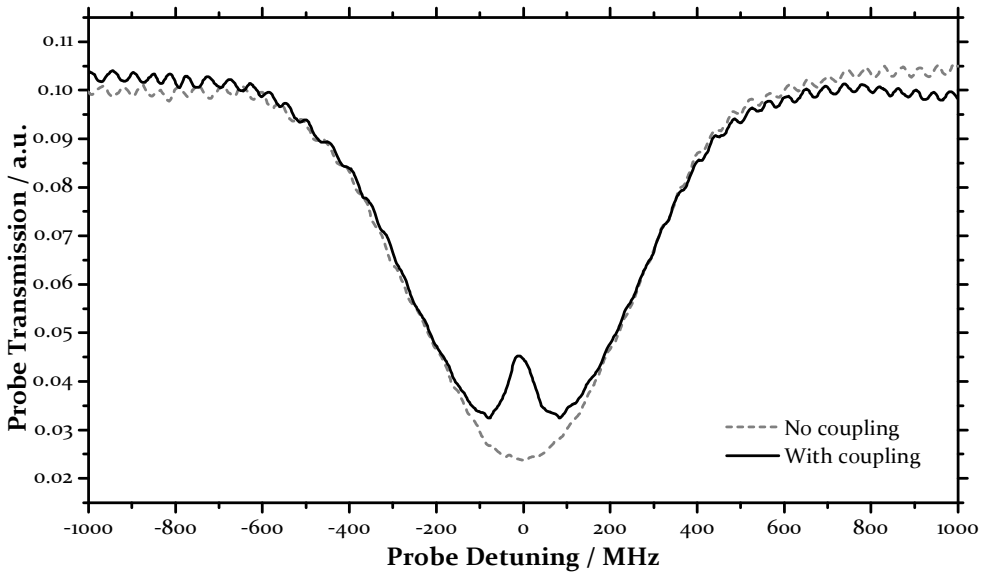

Figure 5-12: *Probe transmission profile through an acetylene photonic microcell displaying an electromagnetically induced transparency peak at the centre of the absorption line for the P15-R13 line pair (solid line) and for comparison the probe transmission in absence of the coupling beam (dashed line).*

The sinusoidal ripple that can be seen on this spectrum is due to a low-finesse cavity being formed by Fresnel reflections at the splices between HC-PCF and SMF in the

photonic microcell. The period corresponds to a frequency of ~40 MHz, and a cavity length of 3.8 m in air, the length of the HC-PCF forming the microcell. This effect can be significantly reduced by using a photonic microcell with an angled splice at one end as shown in section 4.3.3; doing so reduces the return-loss to -60dB, from -16dB for a standard splice.

For applications such as frequency metrology, a good understanding of the coherence in the EIT system is required. Due to the open nature of the acetylene system, a large amount of experimental data covering many configurations is required in order to accurately determine the coherences and optical decay rates involved. The photonic microcell is an important development in this study, as its use greatly simplifies the experimental setups, allowing concentration on the task of acquiring this data.

In order to evaluate this in the confined geometry of HC-PCF, a number of different experimental conditions are considered. Section 5.4 considers the usual co-propagating configuration that is commonly used for V and Λ energy level schemes, and compares the transparency that is obtained in each scheme across a selection of probe-coupling pairs. The use of counter-propagating probe and coupling beams is then considered in section 5.5, where it is found that an induced transparency peak is visible although the condition that the coupling Rabi frequency is greater than the two-photon Doppler width is not met.

In order to evaluate the coherence within the experimental systems, two density matrix models will be used, introduced in section 5.6.

5.4 Comparison of V and Λ Energy Level Schemes

As explained in section 3.1, the energy level structure of acetylene allows for the formation of V and Λ 3-level schemes. The sole difference between the schemes experimentally is the choice of probe transition; for each coupling transition both V and Λ schemes can be formed by appropriate choice of transition (Figure 5-5).

The results in this section make use of a single photonic-microcell, formed from 4 metres of 7-cell triangular-lattice HC-PCF with bandgap centred at 1550 nm. The acetylene pressure within the microcell is ~100 μbar, and other experimental details are as described in section 5.2.

EIT spectra obtained for both V and Λ schemes with coupling transitions P15, P16 and P17 are shown in Figure 5-11; each pair of spectra share a common coupling transition, with the probe transition chosen as appropriate to form the correct scheme. The maximum

coupling power available is used to obtain these spectra, which varies between 500 mW and 600 mW due to the wavelength dependent gain of the EDFA.

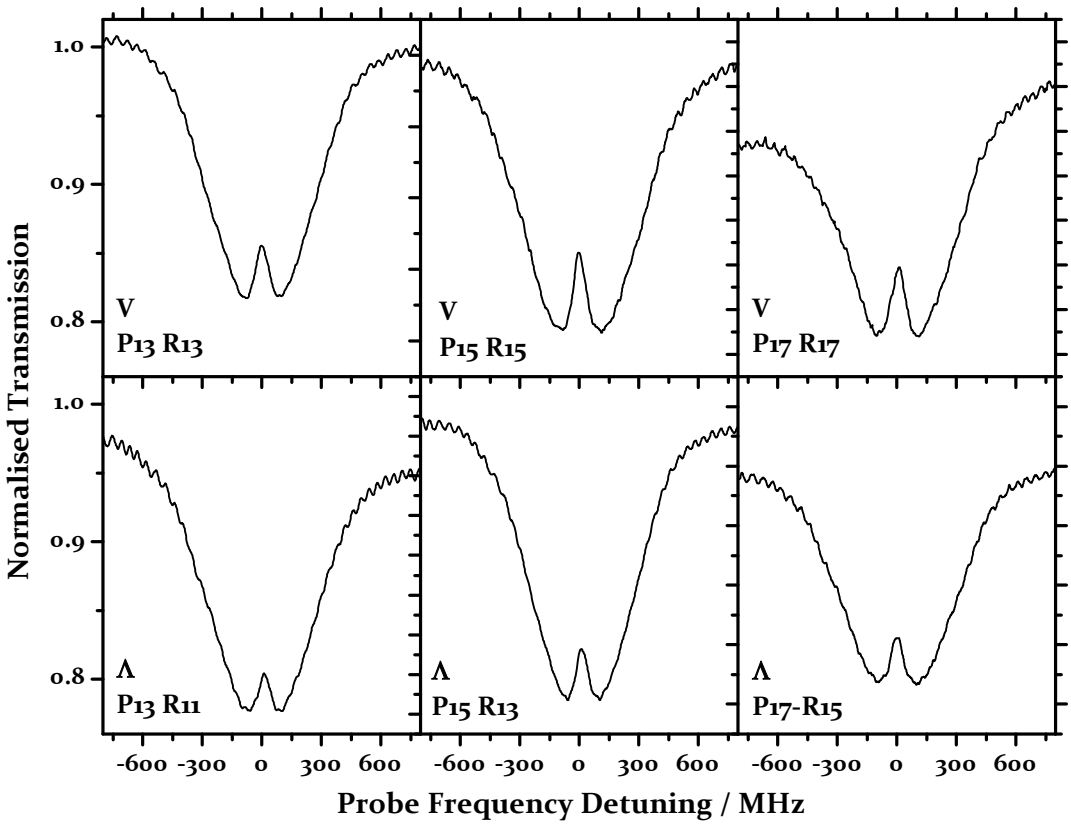

Figure 5-13: *Probe transmission spectra showing electromagnetically induced transparency for three coupling transitions and both V (top row) and Λ (bottom row) energy level schemes.*

The asymmetry seen in some of the spectra is due to mode-beating (see chapter 1), which results in a long-period variation in the measured probe transmission with frequency. This can be reduced by the use of kagomé structure fibre in place of bandgap HC-PCF, as will be seen later in this chapter.

To gain insight into these results it is useful to consider the evolution of the induced transparency peak shape with coupling laser power. This evolution of peak height and width are plotted in Figure 5-14 for six line-pairs, three of each energy level scheme. For ease of comparison the height and width are plotted against Rabi frequency (rather than coupling power), taking transitional dipole moments into account. The solid lines in the figure are the result of a fit to the closed-system model, and will be discussed further in section 5.6.

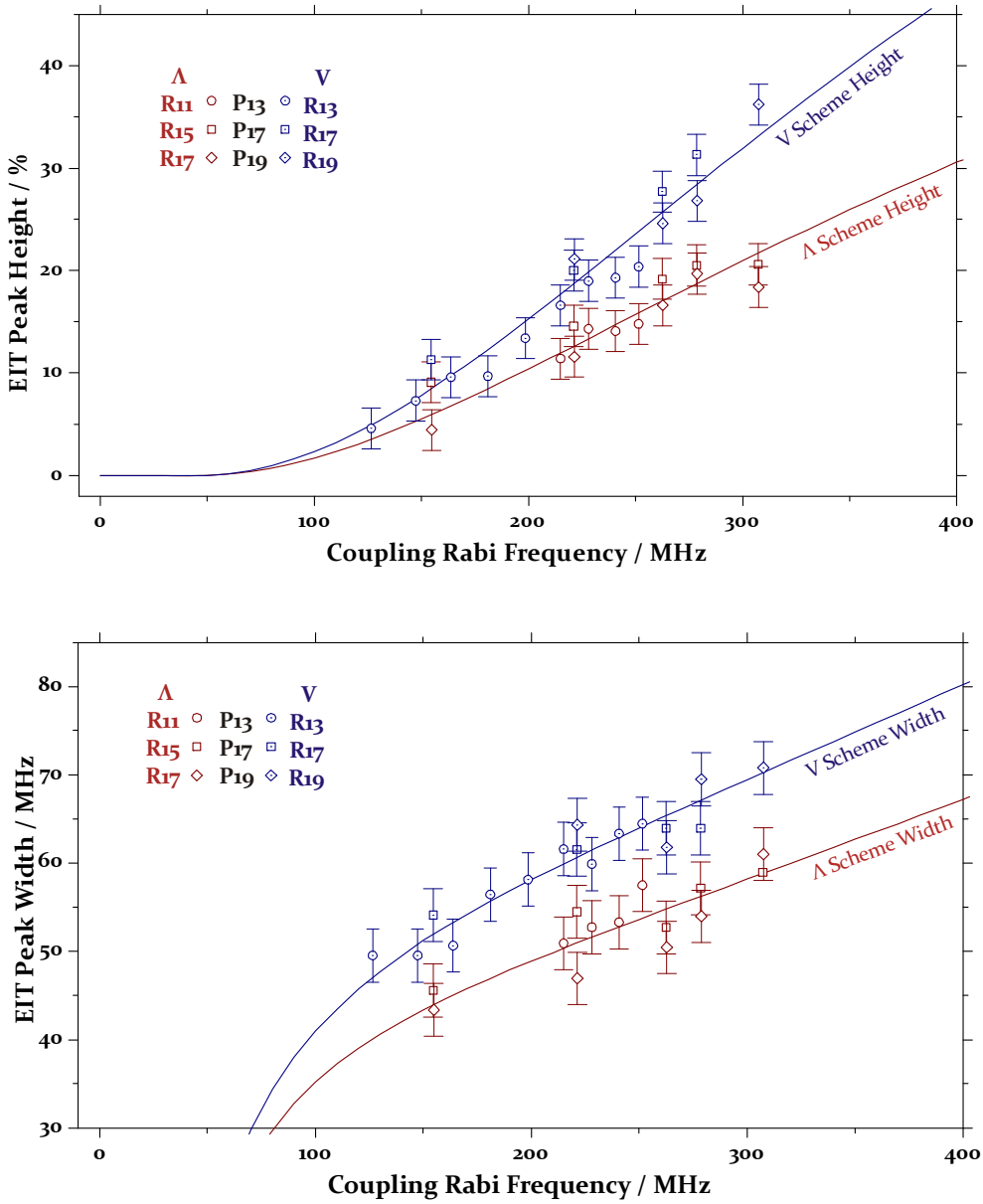

Figure 5-14: *Evolution of transparency peak height (top) and width (bottom) with coupling laser Rabi frequency for the three Λ schemes (open symbols) and three V schemes (centre dotted symbols). Symbols of the same shape share the same coupling transition as indicated in the legend. The solid curves are simulated curved from a closed-system model as discussed in the main text.*

There is no significant difference observed between the height and width of the transparency when comparing datasets for different line pairs of the same energy level scheme. Only a small difference would be expected due to the differing line frequencies leading to different Doppler shifts of the probe and coupling lasers for each line pair; however the change in transition frequency for the line pairs considered (~350 GHz) is insignificant compared with the actual optical transition frequencies (~200 THz). The

resulting change in transparency peak height and width would be significantly smaller than the uncertainty in measured height and width.

From Figure 5-14 it is clear that for two schemes sharing a common coupling transition, the V scheme achieves a greater transparency height than the Λ scheme, all other parameters remaining the same. For applications both height and width of the transparency peak are important, and it is seen that as transparency height increases, so does the width. This means there is a trade-off between a tall induced transparency, and narrow width. The correlation between transparency peak height and width in plotted in Figure 5-15.

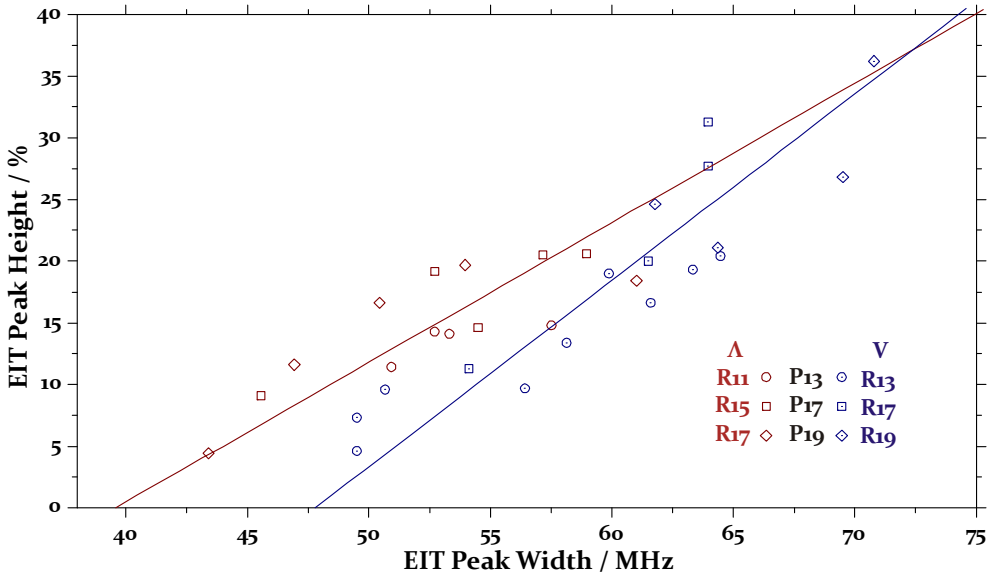

Figure 5-15: *Correlation between transparency height and width for the data in Figure 5-14, for V (dotted symbols) and Λ (open symbols) configurations.*

From this graph it is evident that for the range of coupling Rabi frequency investigated experimentally, for a given peak height the Λ scheme provides a narrower peak width than the V scheme. As an example, for a peak height of 20%, the width for V and Λ schemes is 61 MHz and 57 MHz respectively. The linear fits on the graph suggest that for peak height above ~37%, the V scheme would provide a narrower linewidth; this has not been verified experimentally however due to the limited coupling power available from the fibre amplifier. The equations of the fitted lines are given by equations 5-4, where W is the width in MHz, and H is transparency height in percent.

$$W_V = 47.8 + 0.66H_V$$

$$W_\Lambda = 39.6 + 0.88H_\Lambda \qquad 5\text{-}4$$

The reasons for the differences between the observed transparency heights and widths between the two energy level schemes will be considered in section 5.6, where density matrix models are used to determine the rates of decoherence within each system.

5.5 Counter-propagating EIT

In conventional experiments, a co-propagating probe and coupling beam configuration is chosen to observe EIT in V and Λ energy-level schemes. This choice is made in order to minimise the two-photon detuning when two lasers on resonance with their respective transitions for a stationary molecule are Doppler shifted for a molecule moving in the axis of propagation of the light. The Doppler shift is given by $\omega_D = kv$ where k is the wavevector and v the molecular velocity.

As highlighted in Figure 5-16, for co-propagating beams in V and Λ configurations the two Doppler shifts are of opposite sign and partially cancel. If probe and coupling frequencies were identical, this cancellation would be perfect; otherwise the degree of mismatch is characterised by the residual Doppler shift, $\Delta\omega_D = |k_c - k_p|u$. Here k_p and k_c are probe and coupling wave-vectors respectively. u is the most probable molecular velocity, determined by $u = \sqrt{2RT/M}$ where R is the universal gas constant, T temperature, and M molar mass. In the co-propagating configuration considered in the previous section, the relatively close frequency spacing of coupling and probe beams gives a small residual Doppler shift of ~30MHz.

With counter-propagating coupling and probe, the Doppler shifts of each laser add rather than cancel in V and Λ schemes, increasing the two photon detuning. For typical coupling and probe wavelengths used experimentally this configuration has a residual Doppler shift of ~4GHz, two orders of magnitude greater than the co-propagating scheme. In contrast, the ladder scheme, not considered here, requires counter-propagating beams in order to reduce the two-photon detuning and minimise the residual Doppler width (see Figure 5-16).

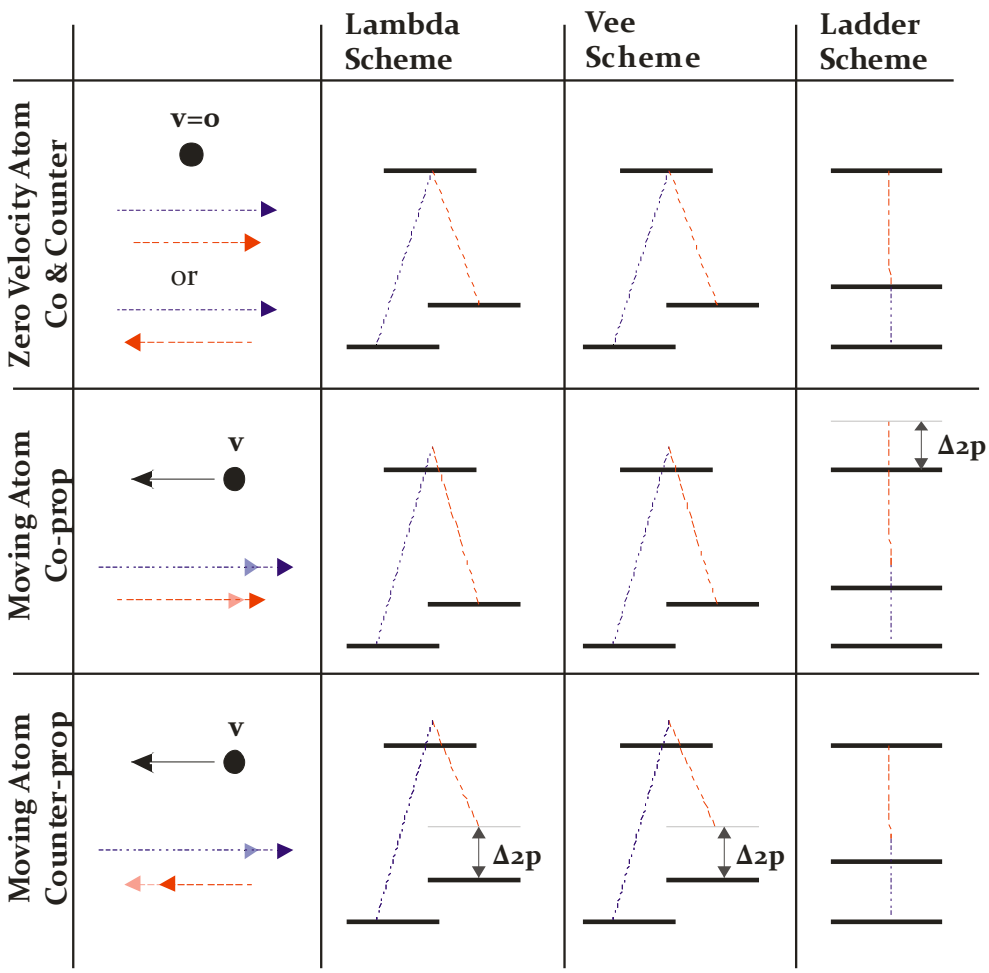

Figure 5-16: *Effect of Doppler shifts due to molecular motion in the configurations as labelled. The lambda scheme shows a large two photon detuning (Δ2p) in the counter-propagating case since one field is shifted to a higher frequency and the other to lower frequency. In contrast, these Doppler shifts minimise the two-photon detuning in a ladder scheme.*

To date, there have been no reported experimental results of either V or Λ scheme EIT in either molecular gases or atomic vapours with counter-propagating beams. The availability of such data however would be valuable in determining the decoherence sources within the acetylene system in a HC-PCF host.

Despite the large residual Doppler shift discussed above, EIT has been obtained in an acetylene photonic microcell with counter-propagating coupling and probe beams, using the experimental setup shown in Figure 5-17.

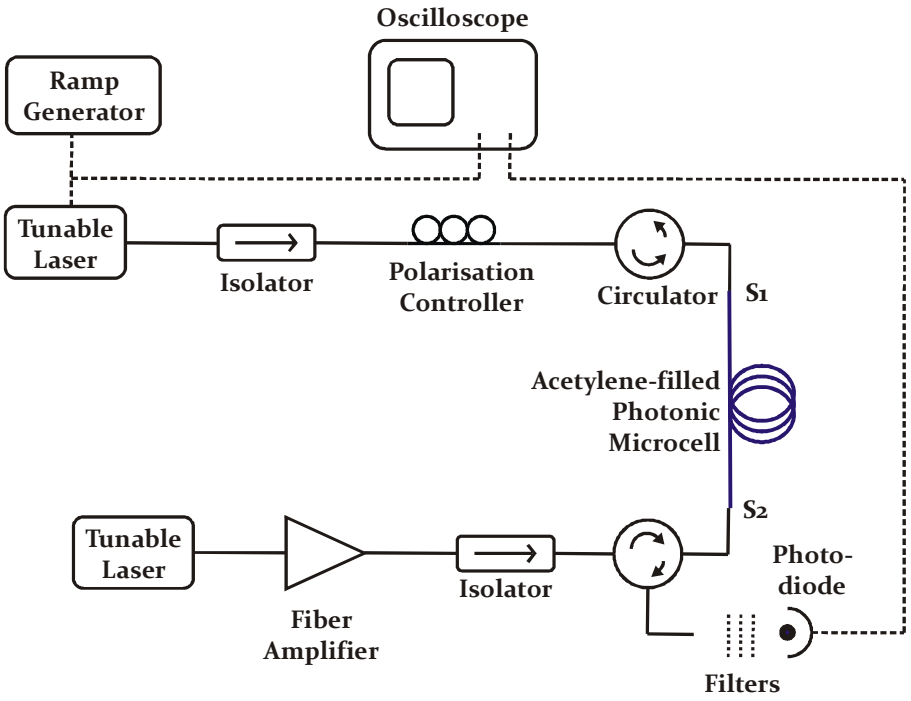

Figure 5-17: *Experimental setup for observing EIT in a counter-propagating coupling and probe beams configuration. S1, S2: splices between conventional single-mode fibre and hollow-core photonic crystal fibre; PC: polarization controller; EDFA: erbium-doped fibre amplifier; IF: interference filters; PD: photodiode.*

The acetylene photonic microcell is the same as that used in section 5.4, with a gas pressure of ~100 μbar. The coupling and probe beams are launched into the microcell from either end via fibre-optic circulators; in this way the probe can be detected at the output port of the appropriate circulator. Due to the reflections present at the splices between HC-PCF and SMF in the microcell (S1 and S2 in Figure 5-17), a small fraction of the coupling beam (~4%) is present at the probe output, necessitating the use of interference filters before the photodiode as was the case for the co-propagating geometry experiment. It should be noted that the coupling beam reflected at splice S2 will be co-propagating with the probe; however, even at the highest coupling power obtainable here, this reflected power would not be sufficient to give rise to a visible transparency peak with co-propagating beam geometry, as demonstrated by the earlier results. It would also be possible to significantly reduce the reflection using a microcell formed with angle splices (section 4.3.3).

A typical probe transmission spectrum obtained under these conditions is shown in Figure 5-18 (black curve) for a coupling power of 400 mW, and shows an induced transparency. It is immediately obvious that the induced transparency is broader and shorter than that obtained using co-propagating beams of the same power; for

comparison this is shown inset. The grey curves shows transmission in the absence of the coupling beam.

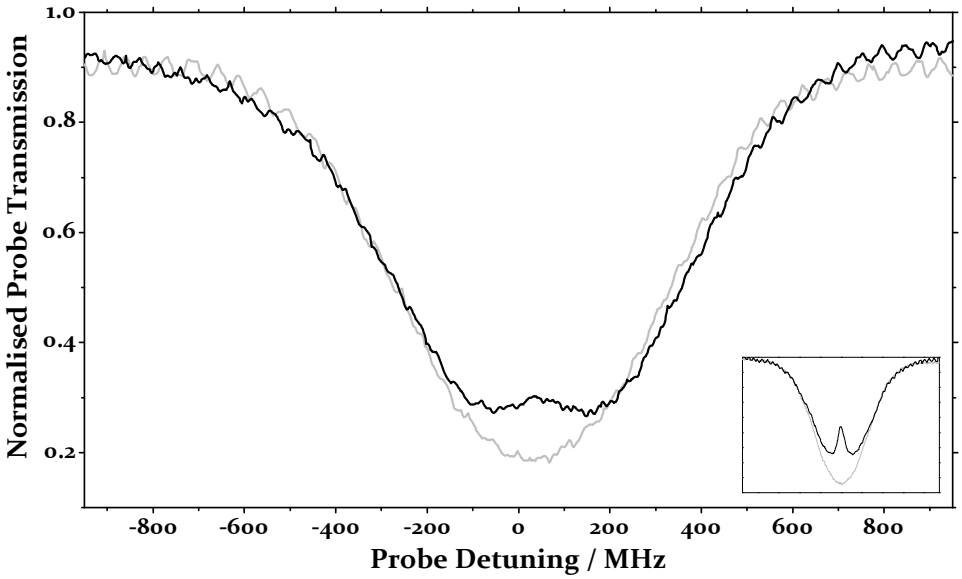

Figure 5-18: *Probe transmission spectrum displaying EIT in a counter-propagating coupling-probe configuration. For comparison the co-propagating EIT obtained in the same photonic microcell under the same conditions is shown inset.*

The peak height and width in counter-propagating geometry are 2.1% and 107.5 MHz respectively, in comparison with 29.2% and 69.7 MHz in the co-propagating geometry. For clarity Figure 5-19 shows a detail of the transparency peak in both geometries. As for the co-propagating geometry, data showing the evolution of the transparency peak height with coupling Rabi frequency has been obtained.

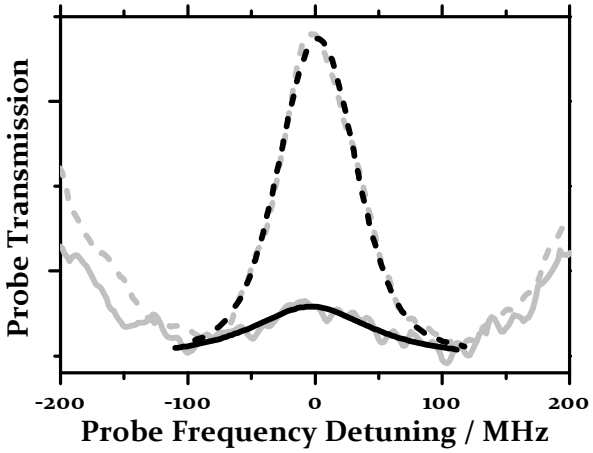

Figure 5-19: *Detail of the induced transparency peak in a co-propagating geometry (dashed grey line) and counter-propagating geometry (solid grey line) under otherwise identical conditions. Black lines are voigt fits to the transparency peaks.*

Before analysing these results with the aid of the open- and closed-system models (see section 5.6), it is useful to again consider why a co-propagating probe and coupling beam configuration is usually used: the probe transmission profile observed experimentally is the result of integration over the velocity distribution of acetylene molecules within the photonic microcell. It is therefore practical to consider the effect of each velocity class in explaining the result.

5.5.1 Absorption Density

To gain an insight into the difference between co-propagating and counter-propagating configurations, we consider here probe absorption not only as a function of probe detuning, but also molecular velocity.

Figure 5-20 and Figure 5-21 show theoretical probe absorption density plots for both propagation schemes. The shading on the plots represents absorption at a particular molecular velocity and probe detuning; the scale is linear with white representing zero absorption. The density is calculated using the closed-system density matrix model with a coupling Rabi frequency of 120 MHz and other parameters determined from the fitting to experimental data in section 5.7. It is calculated for a V energy level scheme at 298 K.

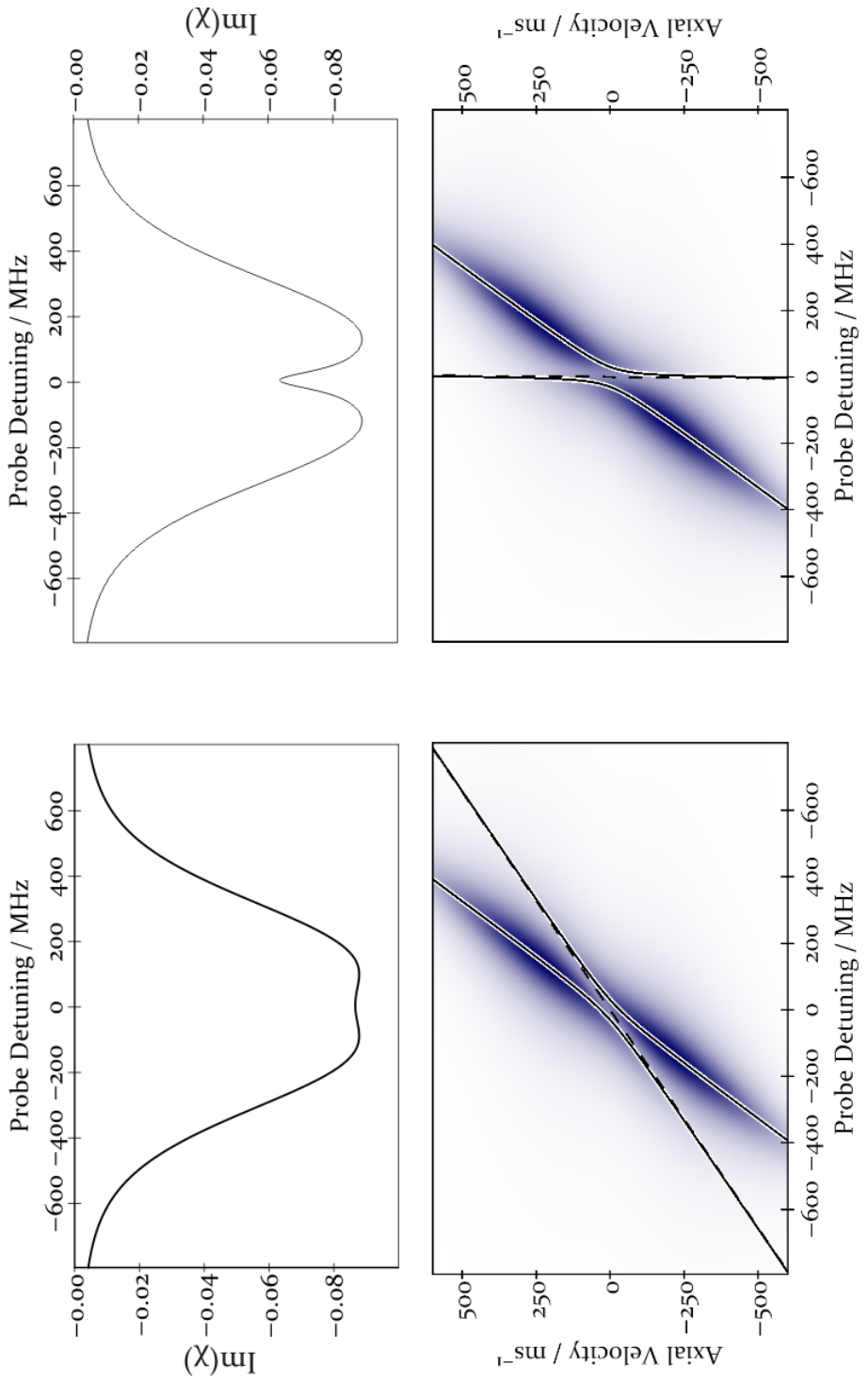

Figure 5-20: *Theoretical results for the counter-propagating scheme (left) and co-propagating scheme (right). The lower graphs plot probe absorption as a function of probe detuning and molecular axial velocity component for a coupling laser tuned to resonance for the zero-velocity class. The scale is linear, with white representing zero absorption, and dark blue maximum absorption. The upper graphs plot the imaginary part of susceptibility of the probe transition (proportional to probe absorption) as a function of probe detuning, obtained by integration over axial velocity.*

The solid lines on the plot show the Autler-Townes (AT) splitting components, calculated from equation 5-5, where $s = 1$ for the co-propagating case and $s = -1$ for the counter-propagating case [94]. This is an extension of the result seen in in section 3.1.1 to include detuning of both the coupling beam and probe beam from resonance with their respective transitions.

5-5 $$\Delta f_{AT} = \frac{v}{\lambda_p} - s\frac{v}{2\lambda_c} \pm \frac{1}{2}\left[\Omega_c^2 + \left(\frac{v}{\lambda_c}\right)\right]$$

AT splitting accounts for the Stark shift of the molecular levels in the presence of the strong coupling beam. The shape of the anti-crossing between AT components is determined by the detuning of the coupling laser frequency from the molecular resonance which in turn depends on the momentum mismatch between the laser frequency and that of the moving molecule. For a fixed value of velocity, the frequency difference between the two AT branches is the same for both beam geometries; it is only the relative position of the two components with respect to the optical frequency detuning that change between the two beam configurations. Finally, it should also be noted that in the absence of optical decay and dephasing, all absorption would occur along these lines, i.e. in the gap formed by the two AT branches, each molecule with a given velocity and frequency detuning would be transparent (off-resonance).

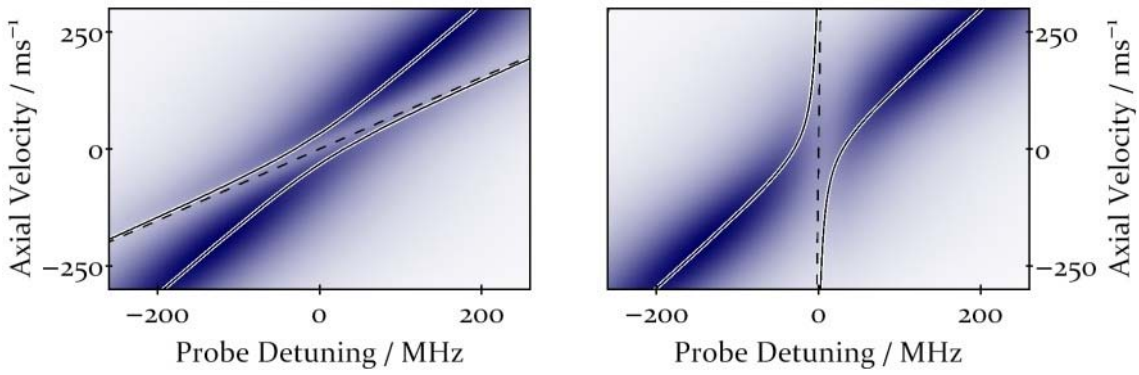

Figure 5-21: *Detail of the probe absorption density plots for both propagation configurations, with a coupling Rabi frequency of 120 MHz.*

In addition to the splitting resulting from the Autler-Townes effect, the occurrence of EIT requires a two-photon resonance. This is formulated for each molecular velocity by the momentum-matching condition which implies that $\Delta_\varphi = (\overrightarrow{k_p} - s\overrightarrow{k_c})\vec{v} = 0$, where k_p and k_c are probe and coupling wave-vectors respectively. It is at this point for each velocity class that the induced transparency occurs. In Figure 5-20 and Figure 5-21 zero two photon detuning locations are indicated by a dashed line.

Considering the co-propagating results in Figure 5-20, it can be seen that the two-photon detuning line (proportional to $k_p - k_c$) is close to vertical, indicating a very weak dependence on molecular velocity. Importantly, this creates a situation whereby the two-photon detuning line lies within the AT splitting gap for a large range of velocities, and where the transparency occurs at a similar probe detuning irrespective of molecular velocity; the central position shifts by only 7 MHz over the velocity range -500 ms^{-1} to 500 ms^{-1}, which covers the majority of acetylene molecules at room temperature. It should also be noted that the AT components, along which absorption occurs, remain away from zero probe detuning until the molecular velocity is above ~200 ms^{-1}. The combination of these two factors means that there is never a strong absorption at zero probe-detuning for co-propagating geometry at realistic molecular velocities.

A similar treatment for the counter-propagating plot in Figure 5-20 illustrates the reasons for the usual choice of co-propagating beam geometry. In this configuration, and unlike the co-propagating geometry, the two-photon detuning line does not cover a significant velocity range for any value of probe frequency detuning. Indeed, the two-photon detuning is proportional to $k_p + k_c$, and therefore has a very strong dependence on molecular velocity. The central transparency location shifts by ~1.2 GHz over the velocity range -500 ms^{-1} to 500 ms^{-1}, compared with just 7 MHz in the co-propagating geometry. Similarly, the Autler-Townes components show that the maximal absorption for zero-probe detuning occurs at a velocity of ~35 ms^{-1}. Since a significant fraction of molecules exist at this velocity, there is significant absorption at zero probe detuning.

A feature that is observed theoretically for the counter-propagating system is that as the coupling Rabi is increased slightly above that obtainable experimentally, the transparency peak height begins to decrease; this may be seen in Figure 5-25 later in this chapter. Although this may initially seem counter-intuitive, it must be remembered that it is the visible height, rather than suppressed absorption, that is considered. At higher Rabi-frequencies optical pumping has greater effect and although a transparency peak is no longer visible within the absorption line, the absolute probe absorption remains lower than in the absence of the coupling beam, or indeed in the presence of the coupling beam at lower Rabi frequencies. This is illustrated in Figure 5-22 which shows theoretical probe transmission spectra for a V scheme in the presence and absence of a 300 MHz Rabi frequency coupling laser; while there is suppressed absorption in the presence of the coupling beam, there is no visible transparency peak.

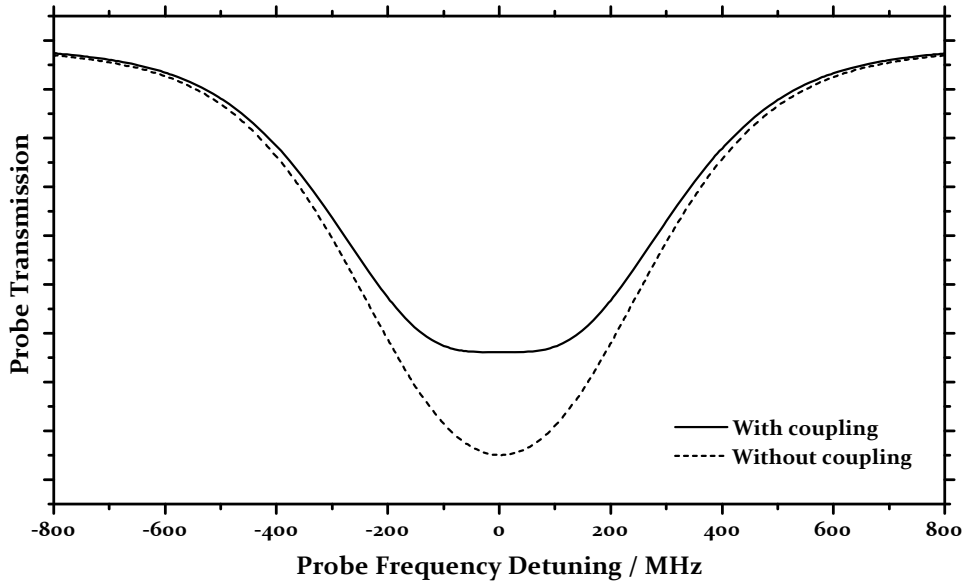

Figure 5-22: *Theoretical probe transmission for V-scheme counter-propagating geometry in the presence (solid line) and absence (dashed line) of a 30 MHz coupling beam, illustrating suppressed absorption without a transparency peak. Parameters for these curves are as determined in section 5.7.1 for the experimental systems.*

A parameter that is often used in determining whether the observation of EIT is possible (see for example [95]) is the residual Doppler width, $\Delta\omega_D = |k_c + sk_p|u$, where u is the most probable molecular velocity. It is often taken that if the residual Doppler width $\Delta\omega_D$ is greater than the coupling laser Rabi frequency, it is not possible to observe EIT since absorption at the Autler-Townes component for small probe-detuning becomes significant. The theoretical analysis above, corroborated by the experimental results show that a transparency is observable at coupling Rabi frequencies much lower that the two photon Doppler detuning. For the P15-R15 line-pair, at 1535.0987 nm and 1517.3145 nm respectively, the residual Doppler in a co-propagating configuration is 3.6MHz. In a counter-propagating configuration this increases to 646MHz. The condition on coupling Rabi frequency is not valid in this scheme, as we obtain EIT when the coupling Rabi frequency is much lower (150 MHz) than the residual Doppler width (646 MHz).

The observation of EIT in the counter-propagating configuration highlights the resolving power of the long interaction length photonic microcell used.

5.6 Modelling the Acetylene System

In section 5.2 we considered a basic model for the three-level Λ scheme, based on approximations that are not valid for the V scheme or counter-propagating beams that have been used for the experimental investigation of EIT in acetylene in the previous sections. In order to analyse the results and the coherence of the experimental system it is therefore necessary to consider more detailed models that capture the physical differences between the many experimental configurations.

In this section two theoretical models will be considered. Both models use the density matrix approach, introduced in section 3.2, as a means to evaluate the evolution of a system consisting of a bare atom and interacting fields; optical decay and rates of decoherence may be added to the matrix phenomenologically.

The first model (section 5.6.1) includes the assumption, as made in the earlier model, that the three-level EIT system is closed. This means that there can be no population decay to levels outside of the coupled energy levels, and equally that no uncoupled levels will decay into the closed-system. However, in order to take into account the 'open-ness' of the experimental system, a non-radiative population exchange mechanism is included, as detailed in the following section.

While the closed-system model is expected to give insight into the experimental system, it is clear that the system is not actually closed; for example, the excited states of the Λ scheme have dipole-allowed transitions to vibrational ground states outside of the three coupled levels. For this reason, in section 5.6.2, an open-system model is introduced. This will allow for population decay into and out of the three levels coupled by the probe and coupling lasers to be accounted for.

5.6.1 Closed System

Initially the experimental setup will be modelled as a fully-closed system; the parameters included in this model are shown schematically in Figure 5-23. A summary of the parameters is given in Table 5-2. In addition to the parameters in the table, the material properties of acetylene such as dipole moment, and physical properties of the system including fibre length and gas pressure are also included as is necessary to calculate the probe transmission.

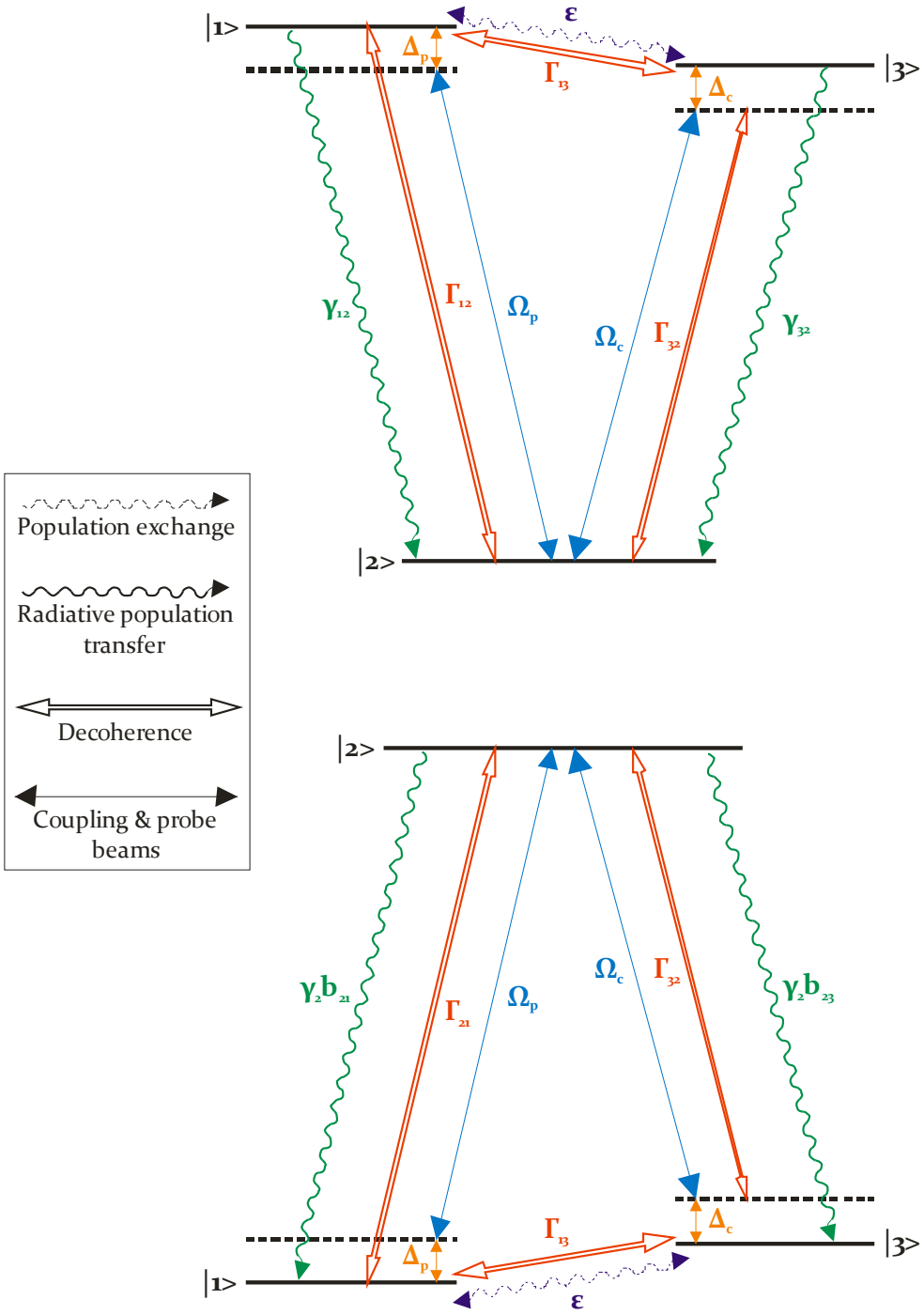

Figure 5-23: *Schematic diagrams of the parameters included in the closed-system model of the EIT system, for the V scheme (top) and Λ scheme (bottom).*

The first set of parameters in the table are related to the probe and coupling fields. The detuning of the lasers from resonance with their respective transitions is given by Δp and Δc respectively. All experimental data gathered in the preceding sections considers only an on-resonance coupling beam, and hence it is taken that $\Delta c = 0$. The power of the lasers is included through the Rabi frequencies Ω_c and Ω_p for coupling and probe

respectively. The Rabi frequency is also related to a particular transition through $\Omega = \mu E/\hbar$, where μ is the transitional dipole moment. The final parameter relating to the coupling laser is a scaling parameter c; this scales the experimental Rabi frequency in the fitting routine to take into account the uncertainty in exact loss at the input splice to the HC-PCF in the photonic microcell.

Parameter	Definition
Δp	Probe frequency detuning from resonance
Δc	Coupling frequency detuning from resonance
Ωp	Probe Rabi frequency
Ωc	Coupling Rabi frequency
c	Scaling of experimental Rabi frequency
Γ_{ij}	Total decoherence between levels i and j.
γ_i	Total population decay from level i.
ε	Rate of population exchange between levels 1 and 3.

Table 5-2: *Summary of parameters included in the closed-system model for EIT in acetylene. These are described in detail in the main text.*

Due to the system being closed, in this model all population decay from the upper levels of the V system is to the lower level of the system. For the Λ scheme it is assumed that radiative decay from the upper level populates the lower levels equally. The rate of decay of the excited state is given by the parameter γ.

In the experimental system it is expected that the presence of collisions between the acetylene molecules and the fibre core wall will lead not only to decay of coherence, but also a tendency to move towards a thermal population distribution. In order to approximate this effect within the closed-system model, a population transfer term is included between states 1 and 3, which both lie in the same vibrational band.

The full equations solved for the closed system are given in appendix A, but here we consider just the change in population of levels 1 and 3, as given by equations 5-6 for the Λ scheme.

$$\dot{\rho_{11}} = (-\gamma_1 - \varepsilon)\rho_{11} + \frac{i\Omega_p}{2}\rho_{12} - \frac{i\Omega_p}{2}\rho_{21} + \varepsilon\rho_{33}$$

5-6

$$\dot{\rho_{33}} = \varepsilon\rho_{11} - \frac{i\Omega_c}{2}\rho_{23} + \frac{i\Omega_c}{2}\rho_{32} + (-\gamma_3 - \varepsilon)\rho_{33}$$

The change in population of state 1 thus includes the terms $-\varepsilon\rho_{11} + \varepsilon\rho_{33}$, and similarly $\dot{\rho_{33}}$ includes the terms $-\varepsilon\rho_{33} + \varepsilon\rho_{11}$ such that total population of the three-level system is preserved.

The final parameters considered in the closed-system model are the rate of decay of decoherence between each of levels, Γ_{ij}. It is assumed that within each scheme the decoherence rate is identical for both transitions from ground to excited vibrational states (i.e. the transitions coupled by probe and coupling beams), but that the rate is different for the dipole-forbidden transition. The time evolution of the coherence between the uncoupled states in the V scheme is given by equation 5-7, which shows the coherence evolves as a result of the coherence induced between the coupled energy levels by the coupling and probe lasers.

$$\dot{\rho_{13}} = \frac{i\Omega_c}{2}\rho_{12} + [-\Gamma_{13} + i(\Delta p - \Delta c)]\rho_{13} - \frac{i\Omega_p}{2}\rho_{23} \qquad 5\text{-}7$$

The actual coherence dephasing rates are dependent on a number of experimental parameters, and the expected contributions to each decoherence term are given by equations 5-8. In these equations, δ_p and δ_c are the linewidths of the probe and coupling lasers respectively; ε is the population exchange rate introduced above. γ_{coll} is the rate of collisions of acetylene molecules with the fibre core wall, where it is assumed that all such collisions result in dephasing.

$$\Gamma_{12}^V = \Gamma_{21}^V = \gamma_{12}^V + \gamma_{coll} + \frac{\varepsilon}{2} + \delta_p + \delta_c$$

$$\Gamma_{32}^V = \Gamma_{23}^V = \gamma_{32}^V + \gamma_{coll} + \frac{\varepsilon}{2} + \delta_p + \delta_c$$

$$\Gamma_{13}^V = \Gamma_{31}^V = \gamma_{12}^V + \gamma_{32}^V + \gamma_{coll} + \varepsilon + \delta_p + \delta_c$$

$$\Gamma_{12}^\Lambda = \Gamma_{21}^\Lambda = \gamma_{21}^\Lambda + \gamma_{coll} + \frac{\varepsilon}{2} + \delta_p + \delta_c \qquad 5\text{-}8$$

$$\Gamma_{32}^\Lambda = \Gamma_{23}^\Lambda = \gamma_{23}^\Lambda + \gamma_{coll} + \frac{\varepsilon}{2} + \delta_p + \delta_c$$

$$\Gamma_{13}^\Lambda = \Gamma_{31}^\Lambda = \gamma_{21}^\Lambda + \gamma_{23}^\Lambda + \gamma_{coll} + \varepsilon + \delta_p + \delta_c$$

The full equations that are solved to determine the steady state probe absorption are given in Appendix A, which also discusses how the theoretical EIT width and height are determined. The result and discussion of this fit will be given in section 5.7.1.

5.6.2 Open System

The closed system described above is an approximation to the actual experimental system. As discussed earlier, the acetylene system contains many ro-vibrational lines, which are often closely spaced in frequency. Considering the wavelength range of interest here, 1510 nm – 1545 nm, in addition to the $\nu_1 + \nu_3$ overtone band there are other 'hot-band' transitions between vibrational states in this range. For the V scheme, even the excited states of the three coupled levels decay to ground states outside of the scheme. For these reasons an open-system model is described here, which takes into account these effects.

The open-system model is shown schematically in Figure 5-24. As for the closed system, a three level density matrix model is used, but provision is made for population decay out of the three-level system into a reservoir, representing states of the acetylene molecules not coupled to by either the probe or coupling lasers. Population is reintroduced into the three-level interaction system from the reservoir in a ratio at rates to be determined by fitting to the experimental data. The additional parameters compared to those of the closed system are summarised in Table 5-3.

Parameter	Definition
γ_i	Total population decay from level i.
b_{ij}	Ratio of population decay from i that decays to j.
w	Effective decay due to transit time.
G_i	Rate of gain to level i.

Table 5-3: *Summary of the additional parameters included in the open-system model. Refer to Table 5-2 for parameters that are in common with those of closed-system model.*

Since the system is open, true radiative population decay rates (γ_i) are introduced, representing the total decay rate to levels both within the interacting system, and to the reservoir of states outside of the interacting system. The branching ratios $\gamma_i b_{ij}$ determine the proportion of the total decay remaining with the three coupled levels, where b_{ij} is the fraction of the total decay from i that populates j. These terms can be seen in the evolution terms for the population of the ground state 2 and excited state 1 of the V scheme, given in equation 5-9.

$$\dot{\rho_{11}} = (-\gamma_1 - w)\rho_{11} + \frac{i\Omega_p}{2}\rho_{12} - \frac{i\Omega_p}{2}\rho_{21}$$

5-9

$$\dot{\rho_{22}} = (\gamma_1 b_{12})\rho_{11} - \frac{i\Omega_p}{2}\rho_{12} + \frac{i\Omega_p}{2}\rho_{21} - w\rho_{22} + \frac{i\Omega_c}{2}\rho_{23} - \frac{i\Omega_c}{2}\rho_{32} + (\gamma_3 b_{32})\rho_{33}$$

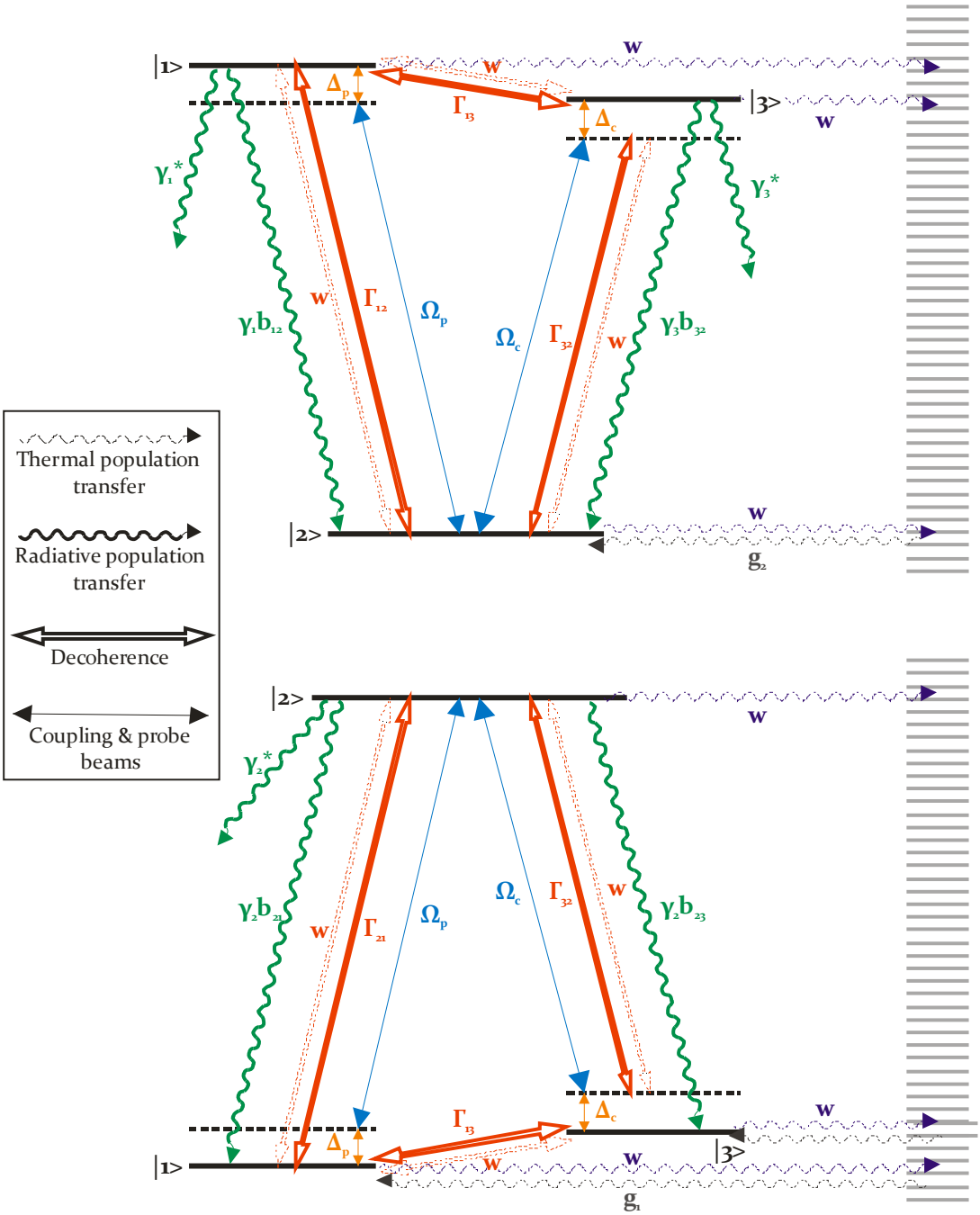

Figure 5-24: *Schematic diagram of the parameters included in the model of the experimentally observed EIT, for the V-scheme (top) and Λ-scheme (bottom). The parameters are explained in the main text.*

To compensate for the loss of population out of the three coupled levels, gain terms G_i are introduced to repopulate each level at a fixed rate, not dependent on the current population of the level.

Also of relevance in the open system is the transit time of molecules in the core region of the fibre before reaching the core wall. Molecules may become adsorbed on the silica core wall, and at a later time be released, losing phase information. A term w accounts for the transit time, and gives additional population decay from each level; this is taken to be identical for each energy level since the transit time is constant. This term should not be confused with dephasing due to wall collisions.

As for the closed-system model, the rate of decoherence between each pair of energy levels is considered. The decoherence sources discussed for the closed system model in the previous section apply equally to the open-system model, resulting in contribution to the decoherence terms as given by equation 5-10.

$$\Gamma_{12}^{V} = \Gamma_{21}^{V} = \frac{\gamma_{12}^{V}}{2} + \gamma_{coll} + \delta_p + \delta_c$$

$$\Gamma_{32}^{V} = \Gamma_{23}^{V} = \frac{\gamma_{32}^{V}}{2} + \gamma_{coll} + \delta_p + \delta_c$$

$$\Gamma_{13}^{V} = \Gamma_{31}^{V} = \frac{\gamma_{12}^{V}}{2} + \frac{\gamma_{32}^{V}}{2} + \gamma_{coll} + \delta_p + \delta_c$$

5-10

$$\Gamma_{12}^{\Lambda} = \Gamma_{21}^{\Lambda} = \frac{\gamma_{21}^{\Lambda}}{2} + \gamma_{coll} + \delta_p + \delta_c$$

$$\Gamma_{32}^{\Lambda} = \Gamma_{23}^{\Lambda} = \frac{\gamma_{23}^{\Lambda}}{2} + \gamma_{coll} + \delta_p + \delta_c$$

$$\Gamma_{13}^{\Lambda} = \Gamma_{31}^{\Lambda} = \frac{\gamma_{21}^{\Lambda}}{2} + \frac{\gamma_{23}^{\Lambda}}{2} + \gamma_{coll} + \delta_p + \delta_c$$

An additional parameter included in the open-system model is that of population gain from the reservoir. Separate gain terms G_i provide population gain at a constant rate to the three coupled energy levels. The gain arises from molecules adsorbed on the fibre core wall re-entering the system, and takes into account optical decay into the interacting system from other energy levels. The gain terms are independent of the state of the interacting system, and are thus not included in the density matrix. Instead, equation 5-11 is solved, with gain terms included in the vector G.

5-11 $$\boldsymbol{M}\rho + G = 0 \Longrightarrow \boldsymbol{M}\rho = -G$$

As for the closed system, the full matrices and equations for the open-system model are given in Appendix A.

The following section considers the fitting methods used to determine the free parameters of both open- and closed-system models based on the wide range of experimental configurations explored.

5.6.3 Fitting Technique

The experimental results obtained in this chapter will be used to determine the parameters included in the two models discussed above in order to access the decoherence sources within the experimental systems and the confined geometry of the HC-PCF host.

The experimental results consist of probe transmission spectra, spanning a region of probe detuning ~1 GHz about the resonant frequency. 36 sets of data have been chosen to represent the full range of experimental configurations. Due to the computation time required to calculate the full probe absorption profile theoretically, fitting the full transmission spectra is not realistic. However, as discussed in section 5.2, the induced transparency peak can be characterised by a height and width.

Rather than fitting the full transition profile, only the transparency height and width are considered for fitting, representing two parameters for each experimental configuration. Choosing to consider only the height and width has the advantage of reducing the amount of computation required for the fitting process, while still capturing the relevant feature of the EIT profiles. A total of 73 experimental points, height and width for each of the four experimental configurations, and used to determine the free parameters of each model.

These height and width must be obtained from the theoretical model in order to determine the fitting parameters; the method used to achieve this is detailed in Appendix A.

The equations presented in Appendix A for the open- and closed-system models are valid for only a single molecular velocity. Numerical integration over the acetylene molecular velocity distribution is required to obtain the full theoretical probe transmission profile. Determining the width of the theoretical transparency peak is computationally expensive since the probe transmission must be calculated for a broad range of probe frequency detuning. The methods used for determining theoretical transparency height and width are explained further in Appendix A.

To determine the free parameters within the models a multi-variate minimum of sum-of-squares fit is used. The fit is performed using the routine E04FCF from the Numerical Algorithms Group (NAG) Fortran 77 library. At each requested set of model parameters, the residual is calculated for the height and width of each experimental data point, and each residual returned to the NAG routine. The code used for calculating the height and width using the models, and performing the fit to experimental data, is included in Appendix B.

5.7 Analysis of Decoherence

In order to analyse the decoherence rates within the acetylene-filled HC-PCF, this section considers the full range of experimental data presented in the preceding sections. The decoherence rates are obtained by fitting the model parameters to the experimental results, using the method detailed in section 5.6.3.

A large amount of data is included, representing a total of 4 experimental configurations, including both co-propagating and counter-propagating geometries, For each configuration, data is included for V and Λ schemes each of the coupling transitions P13, P15, P17 and P19. For each scheme multiple points of coupling Rabi frequency are included between 100 MHz and 320 MHz. Both transparency peak height and width are fitted for each dataset. In total 73 experimental points are included in the fitting process, sufficient for determining the free parameters of each model with high accuracy. Furthermore, fits are obtained to both of the two models introduced in the previous section.

5.7.1 Closed System

Initially the approximate closed-system model introduced in section 5.6.1 is used. An unconstrained fit to the experimental data points results in the fitted parameter values shown in Table 5-4; all frequencies are non-angular.

Scheme	Parameter	Definition	Fitted Value
Both	c	Coupling Rabi freq. scaling	0.879
	$\gamma_2^V = \gamma_1^\Lambda = \gamma_3^\Lambda$	Excited state optical decay	110 MHz
V	$\Gamma_{12}^V = \Gamma_{32}^V$	Decoh. rate between coupled levels	32.1 MHz
	Γ_{13}^V	Decoh. rate between uncoupled levels	44.4 MHz
	ε^V	Population exchange rate	33.2 MHz
Λ	$\Gamma_{21}^\Lambda = \Gamma_{23}^\Lambda$	Decoh. rate between coupled levels	22.1 MHz
	Γ_{31}^Λ	Decoh. rate between uncoupled levels	55.7 MHz
	ε^Λ	Population exchange rate	18.2 MHz

Table 5-4: *Summary of the fitted parameters determined for the closed-system model. All values are non-angular.*

Theoretical curves of transparency height and width for the fitted values are shown in **Figure 5-25**.

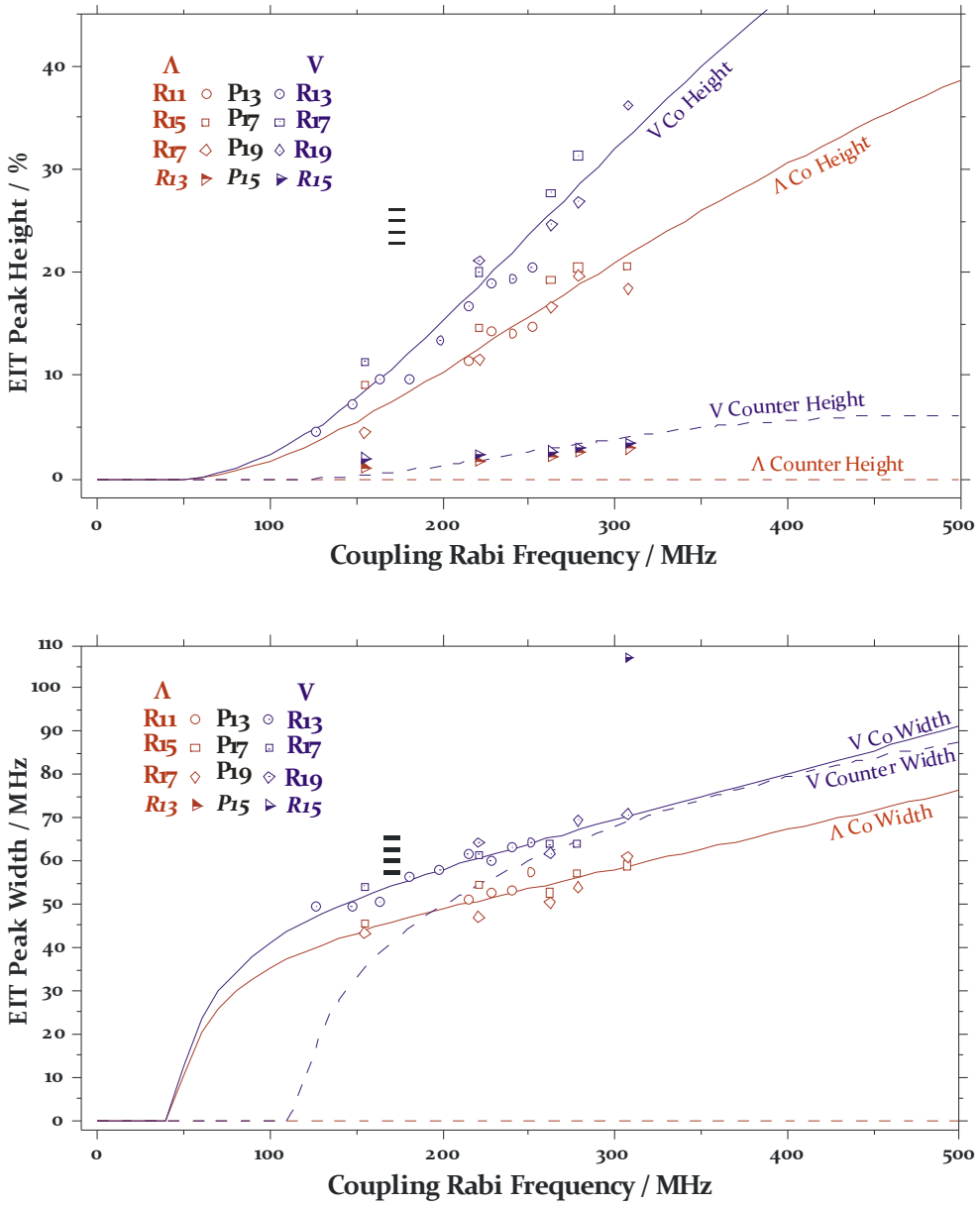

Figure 5-25: *Theoretical fits to the height (top) and width (bottom) of the transparency peak measured experimentally for a total of eight transitions and for a range of coupling Rabi frequencies. The fits are based on a model of a closed three-level system, as discussed in the main text.*

Figure 5-25 shows that the co-propagating data is fitted well, both in terms of peak height and width. The values of the parameters that provide this fit are discussed in the following paragraphs.

The scaling of the coupling Rabi frequency is included as a fitting parameter due to a small uncertainly in power coupled into the HC-PCF section of the photonic microcell. The total insertion loss is measured as 1.8 dB, and for the experimental data points the Rabi frequency is calculated based on a transmission loss of 0.9 dB at the splice between SMF and the acetylene filled fibre. This parameter therefore takes account of the possible difference in transmission loss at each splice in the microcell; the fitted value of 0.879 is within the expected range based on typical splice losses.

The fitted population decay from the vibrational excited state(s) (i.e. level 2 of the V scheme, and levels 1 and 3 of the Λ scheme) is 110 MHz. This is significantly larger than the radiative decay expected of such states, which is of the order of kilohertz, but can be explained by the fact that the excited molecules can decay back to the ground state via routes other than radiative optical decay. The population exchange term ε is fitted as 33.2 MHz and 18.2 MHz for the V and Λ schemes respectively. This term was introduced to describe the overall effect of population redistribution due to collisions of acetylene molecules with the fibre core wall, the rate of which is calculated to be 14 MHz for the 19-cell HC-PCF used experimentally.

The population decay and exchange terms together represent the total population transfer that is added phenomenologically to the density matrix model. In the physical system the vibrational excited states decay to further levels not included in the closed 3-level model, both radiatively and through collisions with the core wall. The large population decay obtained using the fit is likely to be the result of the approximate nature of the closed-system model, suggesting that the closed-system model does not fully capture the essential physics of the system. It is for this reason that an open-system model is considered in section 5.7.2.

The expected contributions to the dephasing rates were given in equation 5-8. In the lambda scheme the fitted decoherence values are 22.1 MHz and 55.7 MHz for coupled transitions (Γ_{21}, Γ_{23}) and uncoupled transitions (Γ_{13}) respectively. In the V scheme these values are 32.1 MHz and 44.4 MHz. Considering the contributions to each of these terms, the linewidths of the probe and coupling laser are expected to contribute no more than 5 MHz to each dephasing rate. The molecular collision rate γ_{coll} includes both inter-molecular collisions, as well as collisions with the core wall that dominate this term at the low experimental gas pressure. If the upper state population decay rate is excluded the fitted dephasing values are comparable with those expected on the basis of equations 5-8, with the fitted exchange rate and a collision rate of ~15 MHz. The fact that the experimental EIT linewidth at low Rabi frequencies is observed to be smaller than the Γ_{13} dephasing rate may be explained by the population exchange playing only a small role

[96]. The high fitted population decay rate is likely to be due to the experimental system not being fully-closed, and is another reason for using the open-system model in the next section.

In order to simplify the fitting process, only the height and width of the induced transparency peaks were considered in determining the parameters above. It is useful to also consider how well the model and experiment correspond for the full probe transmission profile. Figure 5-26 plots two of these for the P15-R15 V scheme and P15-R13 Λ scheme, both with a coupling Rabi frequency of 308 MHz.

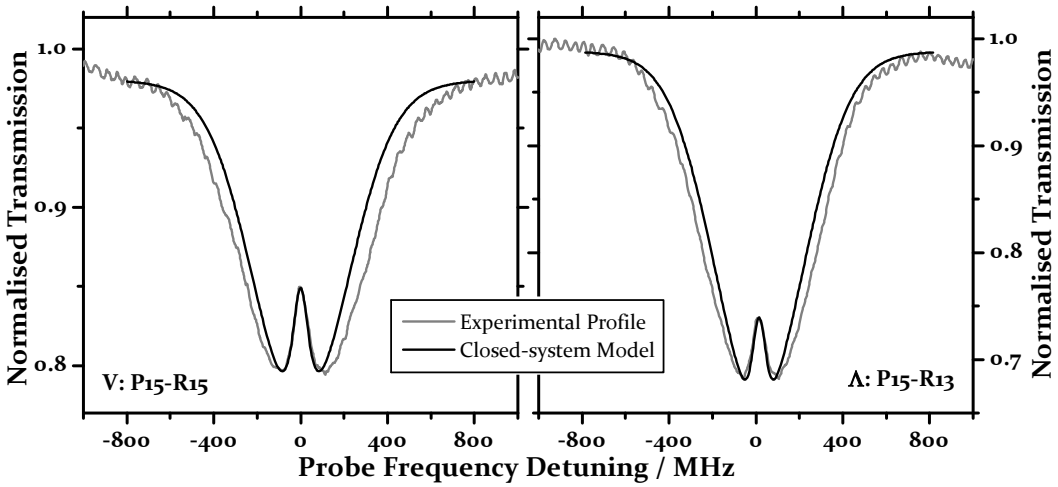

Figure 5-26: *Experimental (grey) and fitted theoretical (black) probe transmission profiles for (left) the P15-R15 V scheme and (right) the P15-R13 Λ schemes at a Rabi frequency of 308 MHz.*

It is observed that the experimental induced transparency peak (grey curve) is well fitted by the theoretical transmission (black curve). The Doppler broadened absorption line is however wider experimentally by ~80 MHz than the theoretical closed-system model profiles. This discrepancy is likely to be due to the closed-system model producing inaccurate population distributions.

Retuning to Figure 5-25, although the model fits the co-propagating data well, the model underestimates the linewidth of the counter-propagating EIT in the V scheme, and does not predict EIT in a Λ counter-propagating scheme at all. In order to more fully understand the dynamics of the system, an open-system model is considered in the next section, which allows for population transfer out of and into the three coupled energy levels of the system.

5.7.2 Open System

Here we consider the open-system introduced in section 5.6.2. For this system a constrained fit is used due to the large number of free parameters included. The result of the fit to the 73 data points representing the four distinct experimental configurations is shown in Figure 5-27. The fitted values and constraints applied are given in Table 5-5.

				Constraints	
Scheme	**Parameter**	**Definition**	**Fitted Value**	**Lower**	**Upper**
Both	c	Coupling field Rabi frequency scaling	0.832	0.5	2
	b	Branching ratio	0.0126	0.0001	0.5
	$\gamma_2^V = \gamma_1^\Lambda = \gamma_3^\Lambda$	Excited state population decay	52.5 MHz	0.001	50
	w	Effective decay (transit time)	21.9 MHz	0	50
V	$\Gamma_{12}^V = \Gamma_{32}^V$	Dephasing rate between coupled levels	15.3 MHz	10	200
	Γ_{13}^V	Dephasing rate between uncoupled levels	14.6 MHz	10	200
	g_2^V	Rate of gain into ground state level 2	50 MHz	0	400
Λ	$\Gamma_{21}^\Lambda = \Gamma_{23}^\Lambda$	Dephasing rate between coupled levels	21.1 MHz	10	200
	Γ_{31}^Λ	Dephasing rate between uncoupled levels	15.3 MHz	10	200
	g_1^Λ	Rate of gain into ground state level 1	180 MHz	0	400
	g_3^Λ	Rate of gain into ground state level 3	216 MHz	0	400

Table 5-5: *Summary of the fitted parameters determined for the open-system model. The right-hand columns give the constraints given to the NAG fitting algorithm. All frequencies are non-angular.*

As discussed in section 5.6.2, the open-system differs from the closed-system model in a number of ways. The population redistribution term ε is replaced by optical decay out of each of the three coupled levels, and population gain into each level through thermal atoms entering the system.

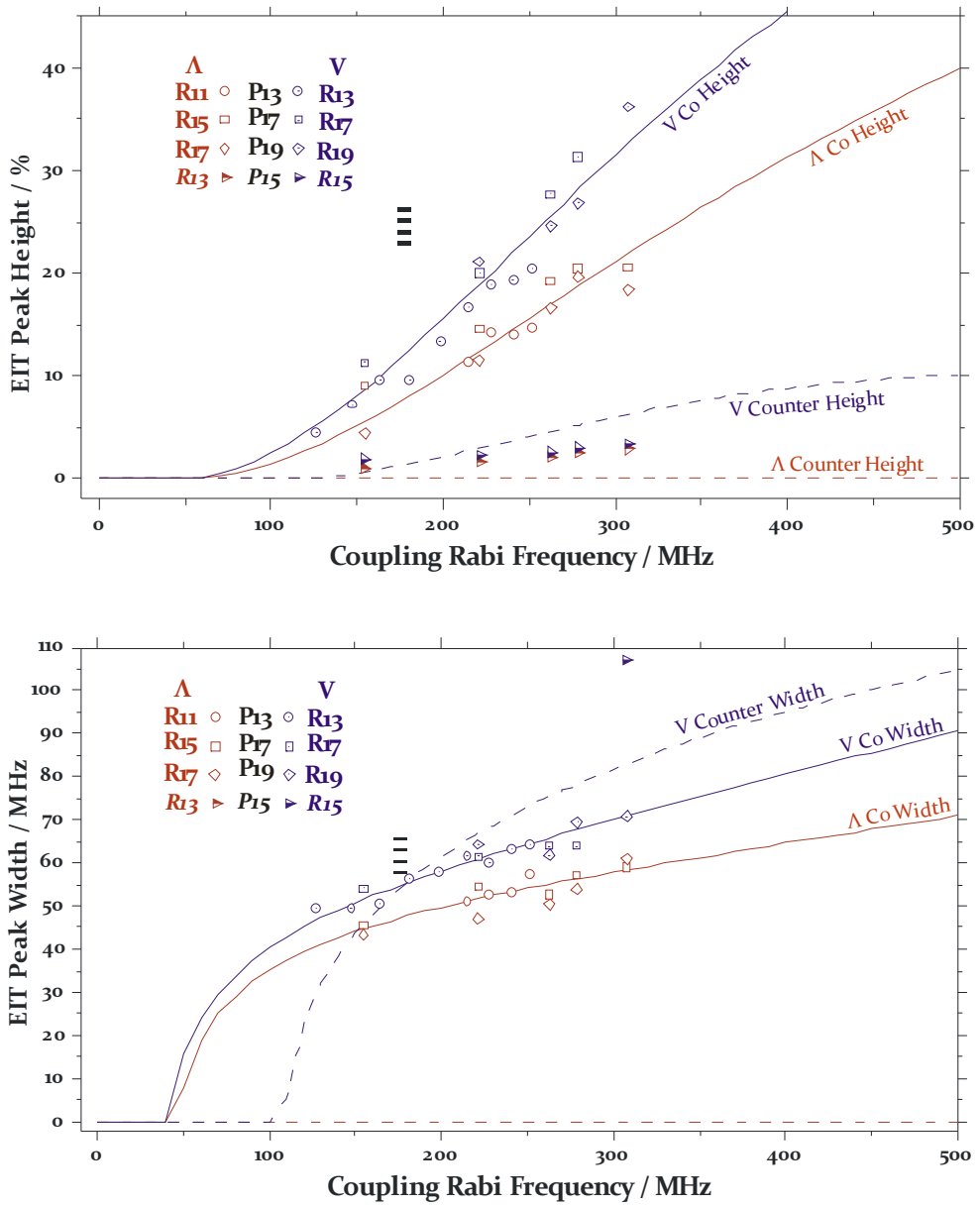

Figure 5-27: *Theoretical fits to the height (top) and width (bottom) of the transparency peak measured experimentally, using the open-system model described in the main text.*

The parameter *w* is an effective decay rate representing transit time introduced in section 5.6.2, justified by the fact that acetylene molecules may be adsorbed onto the silica core wall and lost from the system. This is fitted at ~22 MHz, a value that is greater than, but still comparable with, the expected 14 MHz collision rate of acetylene molecules with the fibre core wall.

The optical decay rate within the three-level system is determined by the overall optical decay values in combination with the branching parameter *b* that determines the ratio of

the total decay that remains within the three coupled levels. The radiative decay rate from the upper to lower states is thus given by γb and calculated to be 0.67 MHz.

Based on the above decay values and the equations given in section 5.6.2, each decoherence rate is expected to be of the order 20 MHz. The fitted values of decoherence agree well with this, with fitted rates of 15.3 MHz and 14.6 MHz for the dephasing on dipole-allowed and dipole-forbidden transitions of the V scheme respectively. For the lambda scheme the fitted dephasing rates are 21.1 MHz and 15.3 MHz respectively. These values correspond to wall-collisions rates of ~15-20 MHz.

Two full theoretical probe transmission profiles are shown in Figure 5-28, in comparison with experimentally obtained profiles for the same coupling power; the experimental profiles are the same line-pairs as compared for the closed-system model in Figure 5-26 (P15-R15 and P15-R13).

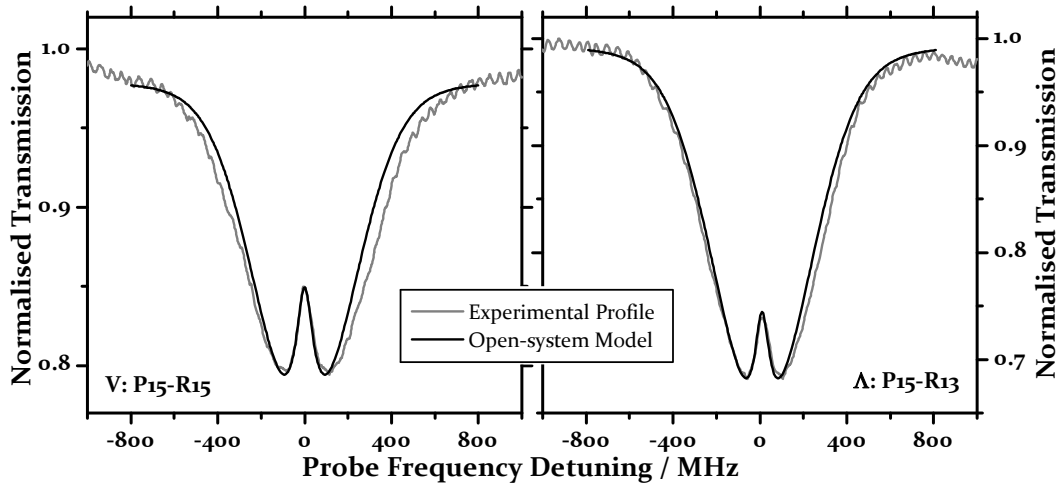

Figure 5-28: *Experimental (grey) and fitted theoretical (black) probe transmission profiles for (left) the P15-R15 V scheme and (right) the P15-R13 Λ schemes at a Rabi frequency of 308 MHz.*

The profiles obtained using the open-system fitted parameters more closely match the Doppler broadened absorption line profile than the closed-system model, and fit the transparency peak equally well. Importantly, the overall transmission profile calculated using the open-system is clearly a better fit to the experimental system than that obtained using the closed system model, particularly with regard to the width of the Doppler and power broadened absorption line.

5.8 Enhanced EIT Spectra

This section briefly considers how the induced transparency profiles obtained in photonic microcells in the configurations considered up to this point in the chapter may be improved. Applications such as laser frequency stabilisation call for a narrow frequency reference and clean signal, and it is these conditions that are considered below.

5.8.1 Low Temperature

The analysis of decoherence in an EIT system hosted by a photonic microcell in the previous section revealed that the major source of dephasing was the effective decay rate corresponding to the rate of collisions of acetylene molecule with the fibre core wall. Reducing the collision rate would thus be expected to reduce decoherence, and lead to a narrower and taller induced transparency peak.

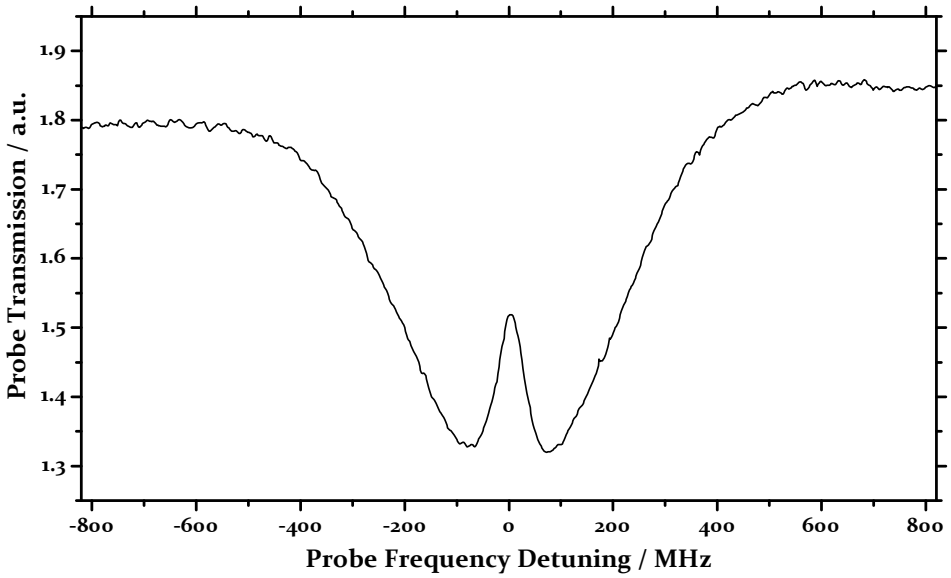

Figure 5-29: *EIT in a 4 m acetylene photonic microcell with 100 μbar pressure when at room temperature. The entire microcell is cooled to 230K, reducing both pressure and collision rates.*

A means by which the wall collision rate can be reduced is by lowering the temperature of the photonic microcell; the molecular velocity has a $\sqrt{T}$ dependence. In addition to reducing decoherence, the lower molecular velocity also reduces the Doppler width and therefore leads to a narrowing of the transparency (this can be seen by considering the relevant portion of the density plots in section 5.5.1).

Narrowing of the induced transparency to 56 MHz and increase in height to 42% is observed in the spectrum of Figure 5-29, obtained using a photonic microcell cooled to 250 K. The R(15)-P(15) V scheme is used, with a coupling Rabi frequency of 310 MHz. At room temperature in the same microcell the transparency width increases to 68 MHz, and the height is reduced to 34%. The reduction in temperature by ~70 K has thus resulted in a reduction in transparency linewidth of 12 MHz, or by 21% of the original width. In comparison the Doppler broadened absorption line is only reduced in width by 12%, corresponding to the expected reduction due to the $\sqrt{T}$ dependence of Doppler width.

5.8.2 Kagomé Fibre for EIT

Considering again the requirements for applications, a clean signal is required for applications such as laser frequency metrology. In the EIT spectra obtained from a photonic microcell presented in section 5.2, a sinusoidal variation in detected probe intensity with frequency was observed. The high frequency variation (at ~50 MHz) was attributed to a cavity formed from reflections at the two splices within the microcell, and it was demonstrated in section 4.3.3 that the use of an angle splice can remove this effect.

A second approximately sinusoidal variation in intensity with probe frequency, at a much lower frequency, is observed due to beating between guided modes of the fibre, predominantly the two polarisations of the fundamental mode. The numerically calculated difference in the propagation constants, or equivalently the beat length, for these modes is of the order $\Delta\beta$~2.5 m^{-1} (see section 2.4), which corresponds to a beat frequency ($c\Delta\beta$) of ~630 MHz. This beating is the reason for the asymmetry in the absorption line profile which may be seen, for example, in the transmission profiles of Figure 5-8.

This significance of this effect depends on the exact structure of the fibre, but is visible to an extent in all bandgap HC-PCF tested. It can be reduced significantly by control of the polarisation coupled into the HC-PCF such that only one fundamental mode is excited, but not eliminated completely.

The transmission of a 1-cell core kagomé fibre and a bandgap HC-PCF over a 20 GHz frequency span around the R(13) acetylene line are compared in **Figure 5-30**. The transmission of the bandgap fibre (grey line) exhibits oscillations that exceed 10% of the average transmitted fibre. The dotted line is the result of fitting two sine waves to the data in the region away from acetylene absorption lines; the fitted results correspond to beat frequencies of 84 MHz and 364 MHz, which in turn correspond to $\Delta\beta$ of 0.28 m^{-1}

and 1.2 m^{-1}. These are reasonable values for beating between the polarisation of the fundamental mode, and also between the higher-order HE21 modes that are also excited.

The kagomé fibre's transmission spectrum (black curve in Figure 5-30) is observed to be much flatter over the -10 GHz to -5 GHz span, where no absorption by the acetylene is expected. Hot bands are resolved on the shoulder and to the right of the main absorption line in the transmission spectrum[8].

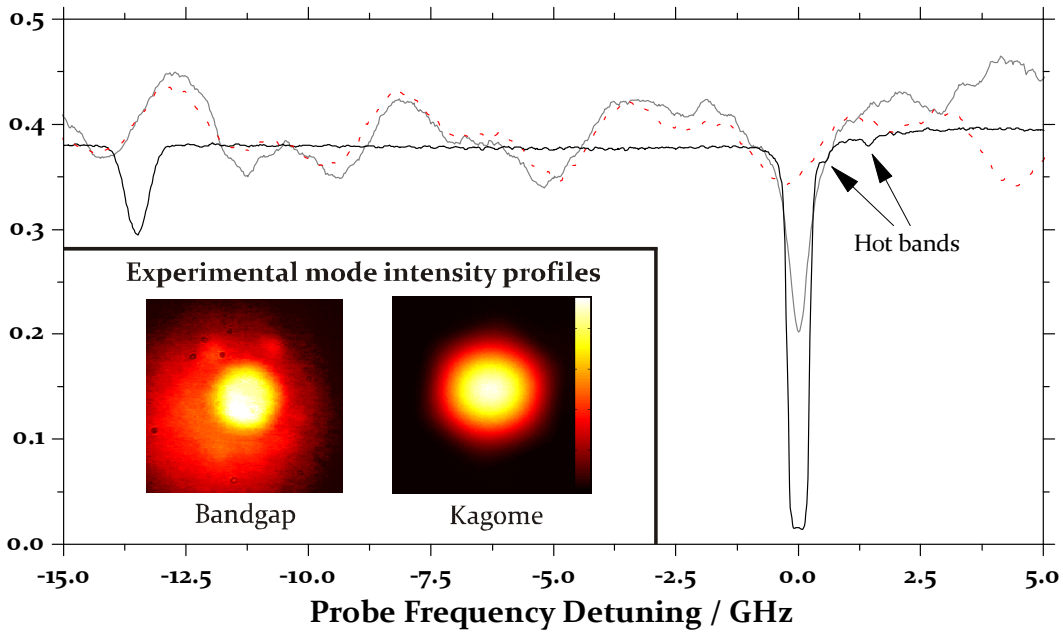

Figure 5-30: *Probe transmission through 7-cell triangular lattice HC-PCF (grey line) and 1-cell large pitch kagomé fibre (black line) over a broad frequency range. The R(13) acetylene absorption line is visible to the right of the spectrum. Both fibres are filled with acetylene at 1 mbar pressure. The inset figure shows pseudo-colour images of the experimental guided modes of the two fibres.*

The kagomé fibre does not exhibit the mode beating effect, and therefore is a candidate in situations in which the mode beating has a detrimental effect. However, kagomé fibre does also have a higher transmission loss (~1 dB/m) than bandgap fibre at 1550 nm; it also has a larger core diameter and therefore a lower intensity at a given power than bandgap fibre, by a factor of ~4. However, the greater loss is not significant for the several-metre long photonic microcells that are typically used, and the larger core offers a reduced wall collision rate and therefore reduced dephasing when used as a host for quantum optics.

[8] This work on the use of kagomé fibre for molecular EIT was carried out with Natalie Wheeler, also at the University of Bath.

The pseudo-colour near field intensity profiles of both fibres are also shown for comparison in Figure 5-30. These clearly highlight the relatively large power in the fundamental mode of the bandgap fibre than extends into the first ring of holes surrounding the core of the fibre. In contrast, the mode of the kagomé fibre is well confined to the core region of the structure.

To demonstrate the use of kagomé fibre for quantum optics, a 10 m acetylene-filled kagomé fibre has been used to observe EIT. This is significant as despite the relatively high optical loss, and reduced intensity for a given power than the bandgap fibre, a good induced transparency is obtained. The spectrum is shown by the black curve in Figure 5-31, which also shows the induced transparency obtain in a 7-cell bandgap fibre with 12 µm core diameter under the same experimental conditions. The probe is swept across the R(13) line with a power of 40 µW, with the coupling laser tuned to the P(13) with an input power of 250 mW.

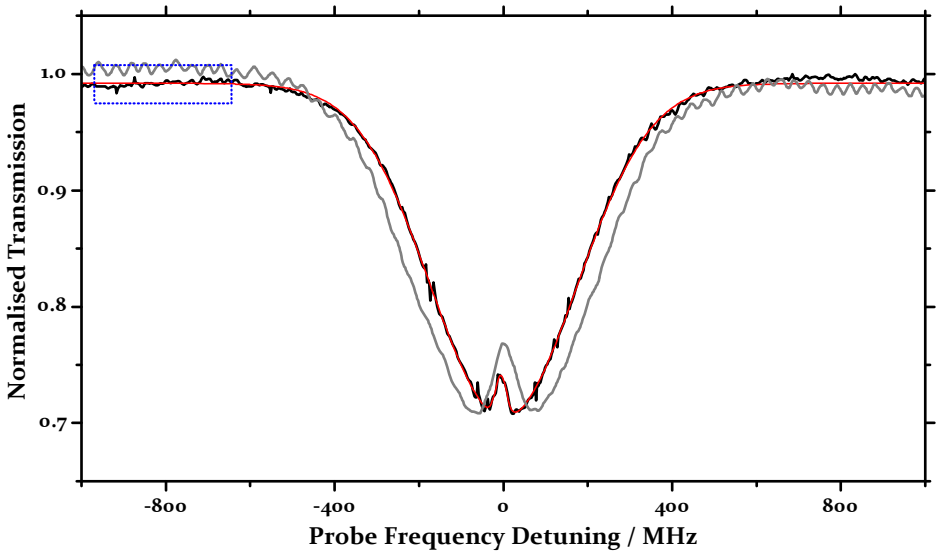

Figure 5-31: *EIT observed in acetylene gas in a kagomé structure fibre host (black curve). The fibre is 10 m in length with a 30 µm core diameter. The V scheme used is formed from the P13-R13 line pair, with a 250 mW coupling power and 40 µW probe power. For comparison EIT observed in a 4 m long 7-cell bandgap HC-PCF under the same conditions is shown by the grey curve.*

The height of the induced transparency achieved is smaller in the kagomé fibre due to the greater attenuation of the coupling beam than the bandgap fibre, which results in a significant decrease in coupling power along the length of the fibre; the total loss of the kagomé fibre is ~15 dB.

Although further measurements are required to confirm this, the transparency linewidth is expected to be narrower for the kagomé fibre due to the reduced rate of collisions with the fibre core wall resulting from its larger diameter. There is also opportunity to optimise the length of kagomé fibre used to balance signal-to-noise ratio which favours a long interaction length, and attenuation which favours a shorter fibre length.

The kagomé structure fibre clearly offers a cleaner transmission spectrum than bandgap HC-PCF, and as demonstrated is still suitable for observing quantum optical effects. The need for clean spectra will be seen clearly in the following section, where a saturated absorption signal is used to stabilise the frequency of a laser.

5.9 Saturated Absorption Spectroscopy

This chapter has thus far considered only electromagnetically induced transparency as a means to achieve a narrow frequency reference. An alternative technique used to obtain sub-Doppler peaks from an absorption line is that of saturated absorption. Experimentally this is achieved using counter-propagating beams of the same frequency, one a strong pump and the second a weaker probe. The stronger beam alters the population distribution for a particular velocity class by stimulated absorption when it is close to resonance, such that the ground and excited states are equal in population, and hence saturated. The counter-propagating probe beam, at the same frequency as the pump, will then not be absorbed. This suppressed absorption results in sub-Doppler peaks similar to those observed with EIT.

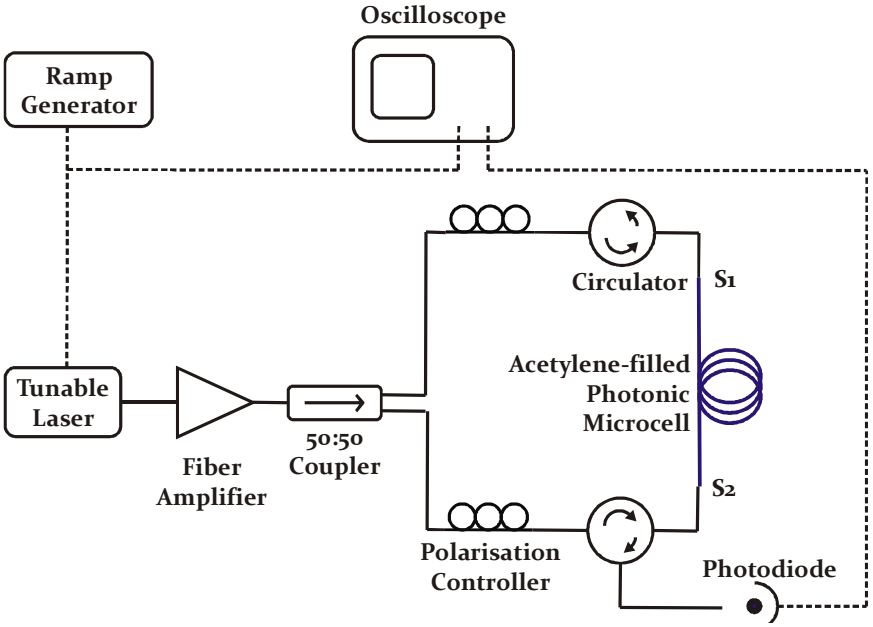

Figure 5-32: *Setup for observation of saturated absorption in a photonic microcell. S1 is a standard splice between HC-PCF and SMF. S2 is a splice between SMF and the collapsed end of a HC-PCF (used to seal the microcell), and has a transmission loss of ~10 dB.*

Here saturated absorption is observed in an acetylene photonic microcell. The setup is shown in Figure 5-32. The microcell used in this experiment was sealed using the collapse technique (section 4.3.3), and as such has a ~10 dB optical loss at one end; it is this loss that provides the required asymmetry in counter-propagating beam powers.

The detected probe transmission spectrum is shown in Figure 5-33, with the probe scanning across the P13 acetylene absorption line. The pump and probe powers inside the microcell are 200 mW and 25 mW respectively, taking the splice losses into account. A saturated absorption feature is visible close to the centre of the absorption line. As for an electromagnetically induced transparency peak, the width of the saturated absorption peak is limited by the rate of collisions between the acetylene molecules and fibre core wall; as discussed in section 3.2.1, for the 19-cell fibre used here the collision rate is 13 MHz.

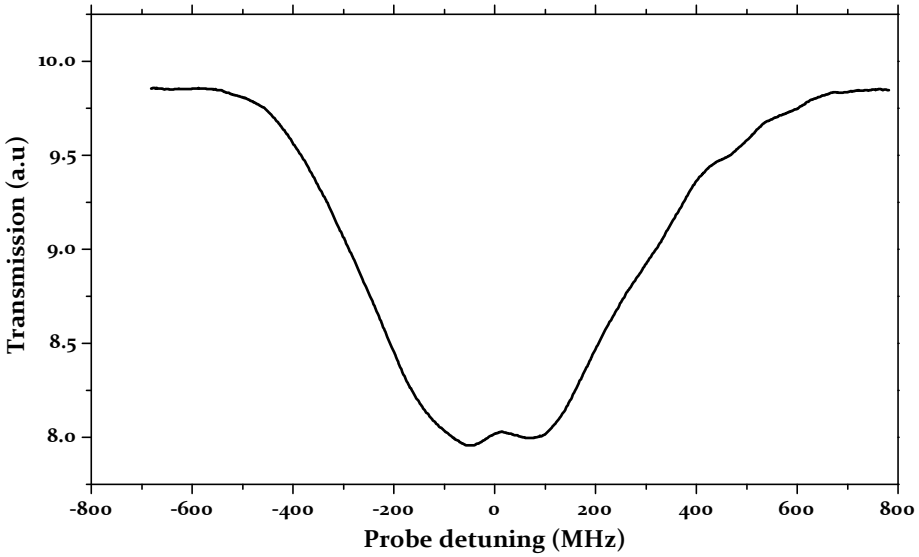

Figure 5-33: *Probe transmission profile across the acetylene P13 line displaying a sub-Doppler saturated absorption feature.*

The collisional rate can be reduced by use of fibre with a larger core diameter. Using kagomé-structure HC-PCF with 70 µm core diameter reduces the collisional rate to 1.5 MHz for acetylene pressure below ~100 mbar, compared with 13 MHz of the bandgap fibre. Results in such a fibre have been obtained by K. Knabe and K. L. Corwin of Kansas State University, and are summarised below.

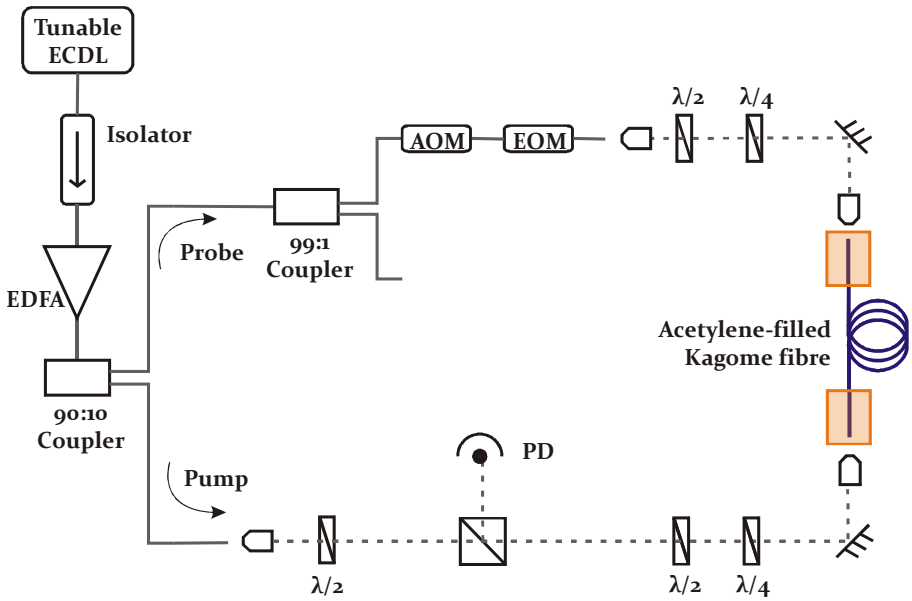

Figure 5-34: *Schematic setup for saturated absorption spectroscopy in kagomé structure HC-PCF. The fibre is attached to gas control chambers at both ends.*

The experimental setup is shown in Figure 5-34. As above, counter-propagating pump and probe beams are formed using a fibre-optic splitter, although in this setup an asymmetric splitting ratio (90:10) is used due to there being no significant difference in coupling loss at either end of the kagomé fibre.

The saturated absorption spectrum, obtained with a pump power of 150 mW measured at the probe output of the 1.4 m fibre, is shown in Figure 5-35. The 11 MHz linewidth of the saturated absorption feature is limited not by collisions between acetylene molecules and the wall, but rather by inter-molecular collisions, due to the relatively high operating pressure of 150 mbar.

In addition to obtaining saturated absorption in the large-core kagomé fibre, Knabe et al. used the sub-Doppler feature in a laser frequency stabilisation scheme, using the standard Pound-Drever-Hall frequency modulation technique [97].

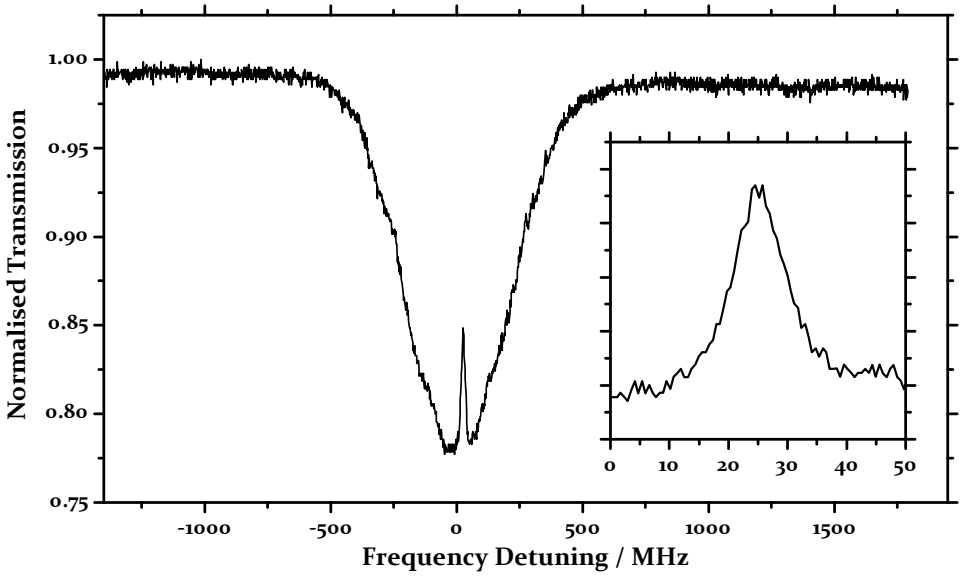

Figure 5-35: *Saturated absorption observed in kagomé fibre with 70 μm core diameter.*

The locking scheme is shown in Figure 5-36. An electro-optic modulator (EOM) adds sidebands spaced by f_m= 20 MHz to the probe laser. The probe output detected by a fast photodiode is mixed with the signal from a second synthesiser also modulating at f_m, which has an adjustable phase offset from that of the EOM synthesiser.

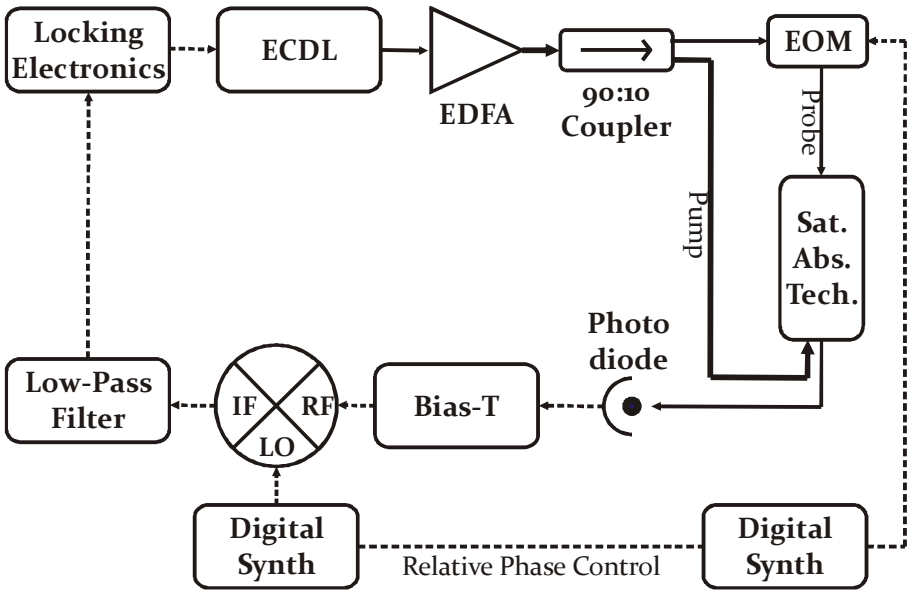

Figure 5-36: *Frequency modulation frequency stabilisation scheme using saturated absorption. EOM: electro-optic modulator; LO: local oscillator.*

The low frequency signal of interest is low-pass filtered and sent to side-locking servo electronics that provide feedback to the laser current. Using this setup the laser is locked to better than 200 kHz, as measured in-loop.

5.10 Summary

This chapter presented the first detailed study into the coherence properties of EIT in a molecular gas. The ability to observe EIT in such a gas is made possible by the long interaction lengths and tight confinement of light offered by HC-PCF.

The properties of the induced transparency have been compared in a number of configurations, including V and Λ energy level schemes. The use of counter-propagating probe and coupling beams to observe EIT in these schemes has been investigated experimentally for the first time.

Saturated absorption spectroscopy has also been achieved in an acetylene photonic microcell, and using large-core kagomé structure fibre linewidths of 10 MHz have been observed. The saturated absorption feature has also been used to stabilise the laser frequency to better than 200 kHz.

Chapter 6

Coherent Optics in Rubidium Vapour

Although for many applications the ease-of-use of molecular gases is desirable, for others the narrowest linewidths possible are required and operation with a single photon source desired.

This chapter explores the use of hollow-core photonic crystal fibre filled with the atomic vapour of rubidium. A polymer coating of the core of the fibre is used to reduce the effect of dephasing collisions between rubidium atoms and the silica wall.

Saturated absorption spectroscopy and narrow linewidth electromagnetically induced transparency are demonstrated.

6.1 Atomic vapour interactions in HC-PCF

While the use of molecular gases for applications such as laser-frequency stabilization is ideal due to the availability of many ro-vibrational absorption lines as discussed in section 5.1, there are many applications that require the properties of atomic vapours.

Atomic vapours have the advantage of providing more stable transitions and simpler energy structures. They also offer Debye-level dipole strengths and thus powers several orders of magnitude lower are sufficient for observing quantum optical effects than in molecular vapours; this feature is of utmost importance in single-photon coherent optics.

The use of atomic vapours for many applications is already proven, and it is therefore of interest to consider the advantages that HC-PCF can offer for quantum optics in atomic vapours. The drive to achieve smaller atomic clocks with the goal of implementing them in portable equipment such as GPS receivers has lead to the development of chip-scale devices [98]. Among the factors limiting the accuracy of these devices is the short interaction length that the millimetre scale cell offers. HC-PCF is able to provide metre scale interaction lengths in a compact device, dramatically increasing signal-to-noise

ratio and therefore improved frequency stability. As was discussed in section 4.3.2, there are different schemes in which atomic clocks may be realised in HC-PCF, including using CPT [99] or Raman-Ramsey fringes [100].

The long-interaction lengths of HC-PCF together with the large dipole-strength of atomic vapours should allow operation of devices at single-photon flux, and routine operation at picowatt powers; using low powers reduces the detrimental effects of power broadening [101]. In addition, the fibre may be made a source of single photons using a scheme based on stimulated Raman adiabatic passage developed and demonstrated in rubidium vapour by Hennrich *et al.* [102].

A major hurdle in the use of atomic vapours is the difficulty in loading them into the narrow core of the fibre due to their large mean-free-path, discussed below, and to the reactive nature of many atomic vapours of interest. The most commonly used vapours, such as rubidium and caesium are highly reactive alkali metals. Indeed, at room temperature rubidium is a solid and it is the use of its vapour that is of interest. The low vapour pressure necessitates the use of a of high-vacuum system. The successful loading of rubidium vapour into the core of a kagomé lattice fibre was shown in 4.4.2, and will be discussed in more detail in section 6.2 below.

Finally, another hurdle arises from the mean-free-path of vapour atoms being greater than the core-diameter of the fibre when operating at low pressures; at the vapour pressure of 1 μbar obtained at 90°C, the mean-free-path would be ~16 cm if wall collisions were neglected. The fact that the mean-free-path is greater than the core diameter gives a large collision rate of atoms with the silica core wall. These dephasing collisions lead to an increase in line-widths due to the loss of coherence. To reduce the number of dephasing collisions a technique was developed to coat the silica surface of the fibre with a polymer in order to provide spin-preserving collisions (see section 4.4).

Collisions with the silica core wall also result in the adsorption of the atomic vapour into the core wall, and therefore the loss of contrast. The use of a polymer coating in the core of the fibre is again a solution to this problem. Although atomic vapour will still be adsorbed onto the polymer coating (at a much lower rate than it is adsorbed onto silica), it has been shown that a large desorption rate can be obtained by illuminating the polymer with a weak incoherent and off-resonance light source in a process termed light-induced atomic desorption (LIAD) [103].

The main aim of the work in this chapter is to achieve narrow linewidth EIT, taking advantage of the long-interaction length offered by HC-PCF to dramatically improve the signal-to-noise ratio over conventional techniques. Ghosh et al. published results of EIT

in rubidium-filled HC-PCF using a V energy-level scheme [104]. Their paper does however raise some issues, which will be addressed here. One difficultly in interpreting experimental results in the configuration used is the effect of optical pumping between the two lower levels of the system, and this will be considered in section 6.3 which looks at optical pumping in a V energy level scheme. Based on these a Λ scheme is chosen for the experimental EIT results in section 6.4, to remove any ambiguity that the induced transparency involved is due to EIT and not an effect of optical pumping. A narrow transparency linewidth is obtained that is an order of magnitude lower than that obtained by Ghosh *et al.* and that shows the effectiveness of the anti-relaxation properties of the polymer core coating.

Although Ghosh et al. did not observe the reduction in linewidth that is expected from a polymer coating of the fibre core, they were able to observe the effects of LIAD. From this it seems likely that their polymer coating of the core resulted in a patchy coating, such that collisions with the silica were not prevented; an inconsistent coating would still allow desorption via LIAD.

6.2 Fibre Preparation and Rubidium Loading

Rubidium vapour has been chosen to demonstrate the loading of atomic vapour into HC-PCF. This choice was made due to its common use as a frequency standard, and its relative stability compared to caesium and other alkali metals. However, its reactivity with common gases and low vapour density impede the loading of rubidium vapour into HC-PCF. Figure 6-1 illustrates vapour density as a function of temperature for liquid rubidium [105]. A temperature of 90°C is needed to obtain a vapour density of only 1 μbar. For this reason low background pressures are required, and the gas-control chambers and fibre must both be heated during the loading process to keep the vapour density as high as possible.

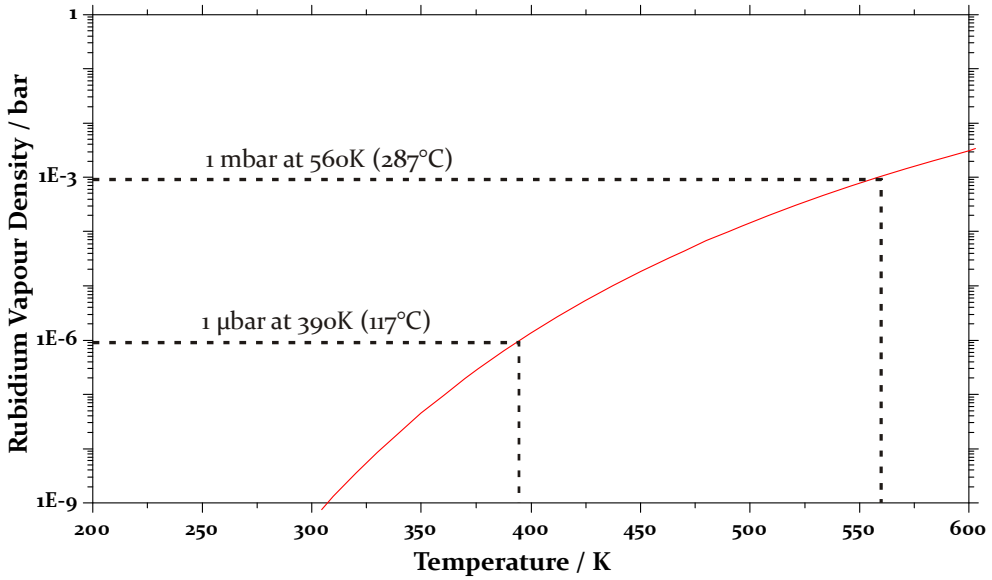

Figure 6-1: *Rubidium vapour density as a function of temperature. At room temperature the density is negligible; pressures of 1 microbar and 1 millibar are obtained at temperatures of 117°C and 287°C respectively.*

The loading of a bandgap HC-PCF with rubidium vapour has been achieved by running a vapour source at high current, in order to balance the large rate of loss of rubidium atoms due to their adsorption onto the silica core wall of the fibre. However, for observing quantum optical effects polymer coated kagomé lattice fibre is used.

The kagomé fibre was chosen over conventional triangular lattice bandgap HC-PCF because it offers a larger core diameter with similar transmission loss at around 800 nm. The diameter of the single-cell defect core of the kagomé fibre is 11 µm; a bandgap fibre operating at the required wavelength range would have a core diameter of only 6 µm. The advantages of the larger core in this instance are two-fold: the larger area reduces the difficulty of loading vapour inside the core, and also results in a lower rate of collisions between vapour atoms and the core wall by a factor of four. The larger core does also have the effect of reducing the light intensity, however this is of no consequence as the powers required are extremely low due to the large dipole-moments of the rubidium transition used.

Before loading kagomé fibre with rubidium vapour, the fibre must be prepared for use. As for filling the fibre with molecular gases, the fibre is first heated and flushed with argon or nitrogen, as described in section 4.3.1. An important stage in the preparation is the coating of the silica fibre core wall with a polymer. Polymers such as paraffin and PDMS have long been used in bulk gas reference cells due to their anti-relaxation properties, and their use in HC-PCF is of particular importance due to the large collision

rates of vapour atoms with the core wall that occur due to the small diameter of the fibre. The coating procedure is detailed in section 4.4.1.

Once coated the fibre is ready to be loaded with rubidium vapour. The basic procedure was described in section 4.4.2, but here we will consider monitoring of the loading process, and techniques to increase the flow of vapour into the fibre.

The initial loading process consists of releasing rubidium from a source in one gas-control chamber, after having first evacuated both chambers and fibre to below 10^{-6} mbar. The chamber without rubidium source is constantly evacuated to reduce contamination of the system through outgassing from the stainless steel chamber. Initially a current of 5.5 A is applied to the source until rubidium is observed inside the fibre.

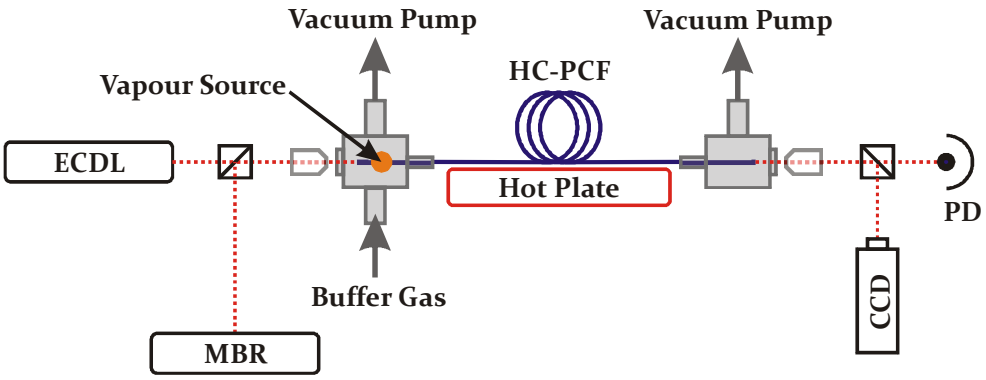

Figure 6-2: *Setup used for loading rubidium vapour into hollow-core fibre. The fibre and chambers are heated to increase the vapour pressure of the rubidium. PD: photodiode; ECDL: external cavity diode laser; MBR: monolithic block resonator Ti:sapphire laser, used for light-induced drift.*

The loading process is monitored by observation of the D2 absorption lines at 780nm (Figure 6-3); the structure of this spectrum will be explained in the following section. When using kagomé structure fibre it is possible to check that absorption observed is due to rubidium atoms within the fibre rather than that contained in the small path-length (~1 mm) between the gas-chamber window and fibre end by selectively coupling into a silica apex in the cladding (as seen in Figure 4-22(a)). When coupling in this way, a substantially reduced line contrast was observed, indicating that the rubidium had been successfully loaded into the fibre core.

During early stages of loading, reducing the vapour source current quickly reduces the contrast of the absorption lines. Over a period of days, however, it was found the current

could be gradually reduced to ~2.5 A, while maintaining contrast; at this stage the rate of release of rubidium from the source balances the rate of adsorption of the vapour onto the vacuum system walls, and reaction of the vapour with outgassing components from the vacuum system.

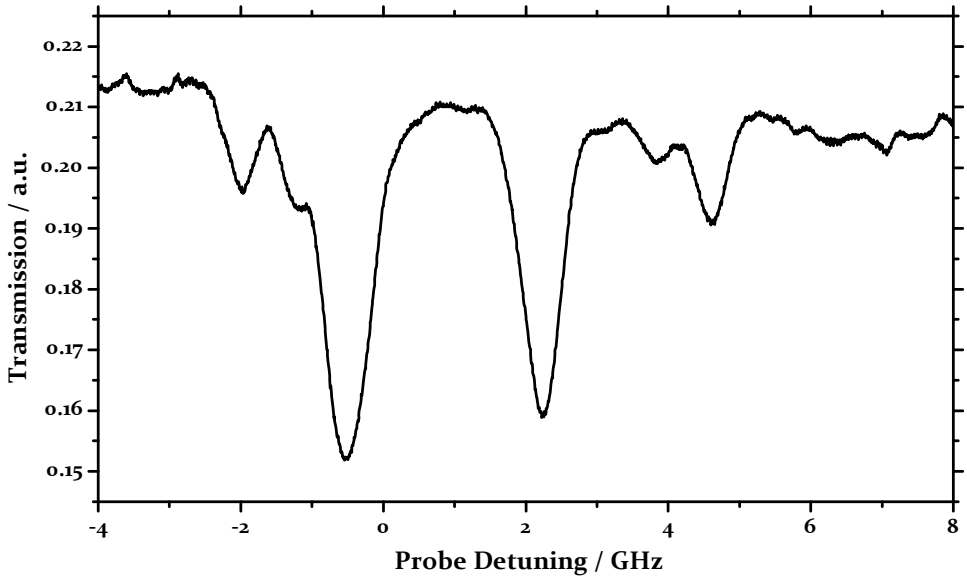

Figure 6-3: *Probe transmission through 30 cm of rubidium-loaded HC-PCF, showing the D2 absorption lines of both ^{85}Rb and ^{87}Rb.*

As was mentioned in section 4.4.2, there are several methods that may improve the slow loading rate of rubidium vapour into the fibre. One of these is light-induced drift [106]. This relies on the differential diffusion cross-section between atoms in their ground state and a buffer gas, and between atoms in an excited state and the same buffer gas; the collisional cross-section is typically larger for atoms in their excited state than those in the ground state. When a laser is red-detuned from resonance by ~1 GHz, absorbing atoms acquire a drift velocity in the same direction at the laser beam.

In bulk gas-cells this has been demonstrated experimentally to be very effective, with drift velocities obtained of the order of metres per second [107]. In millimetre scale capillaries it has been shown that the drift velocity is increased by orders of magnitude when the inner wall of the capillary is coated with a polymer (such as paraffin or PDMS) that reduces the interaction between the vapour and cell-wall [108].

During early stages of loading HC-PCF with Rb vapour an increase in line contrast was obtained when red detuning a Ti:sapphire laser by 2 GHz from the D_1 line with a power of 100 mW in the presence of ~100 μbar of argon as a buffer gas. After this initial increase no further effect of light-induced drift was observed.

A second more proven method to increase the loading rate of the fibre core with rubidium vapour is to take advantage of radiation pressure [109]. Renn was able to guide rubidium in a 40 μm diameter hollow capillary using a laser red detuned from a rubidium resonance by 1-30 GHz [110]. Using this method, the rubidium atoms are attracted to the high intensity region of the fundamental guided mode at the centre of the capillary. The fact that the atoms are kept away from the walls by the radiation pressure means that the atoms are guided around bends in the capillary. A similar demonstration of the effect in HC-PCF [111], where the effect is stronger due to the much reduced transmission loss, has been achieved using 5 μm diameter polystyrene spheres.

The applicability of this method to increasing the flux of Rb atoms entering the fibre requires further work, as the large velocity of atoms inside the gas chamber means it is unlikely to capture atoms passing through the beam as it enters the fibre.

The loading of rubidium vapour into hollow-core fibre has proved to be a time consuming process, taking several weeks including preparation of the system and the loading process itself. An alternative method of loading the fibre is proposed in chapter 7 with a view to easing and quickening the loading process.

6.3 Optical Pumping

Before considering quantum optical effects in the rubidium loaded fibre, it is useful to consider optical pumping effects that occur, particularly due to the small frequency spacing of the hyperfine structure.

Figure 6-4 shows the energy levels involved in the D_1 and D_2 transitions of both naturally occurring rubidium isotopes. The D_1 line at 795 nm represents transitions from $5S_{1/2}$ to $5P_{1/2}$, and the D_2 line transitions from $5S_{1/2}$ to $5P_{3/2}$. Throughout this chapter it is the rubidium-85 isotope that is studied experimentally, and thus we will consider that isotope here; the level structure of both isotopes is identical, with only the splitting values varying. In this figure the spacing of hyperfine levels within each band is shown to scale.

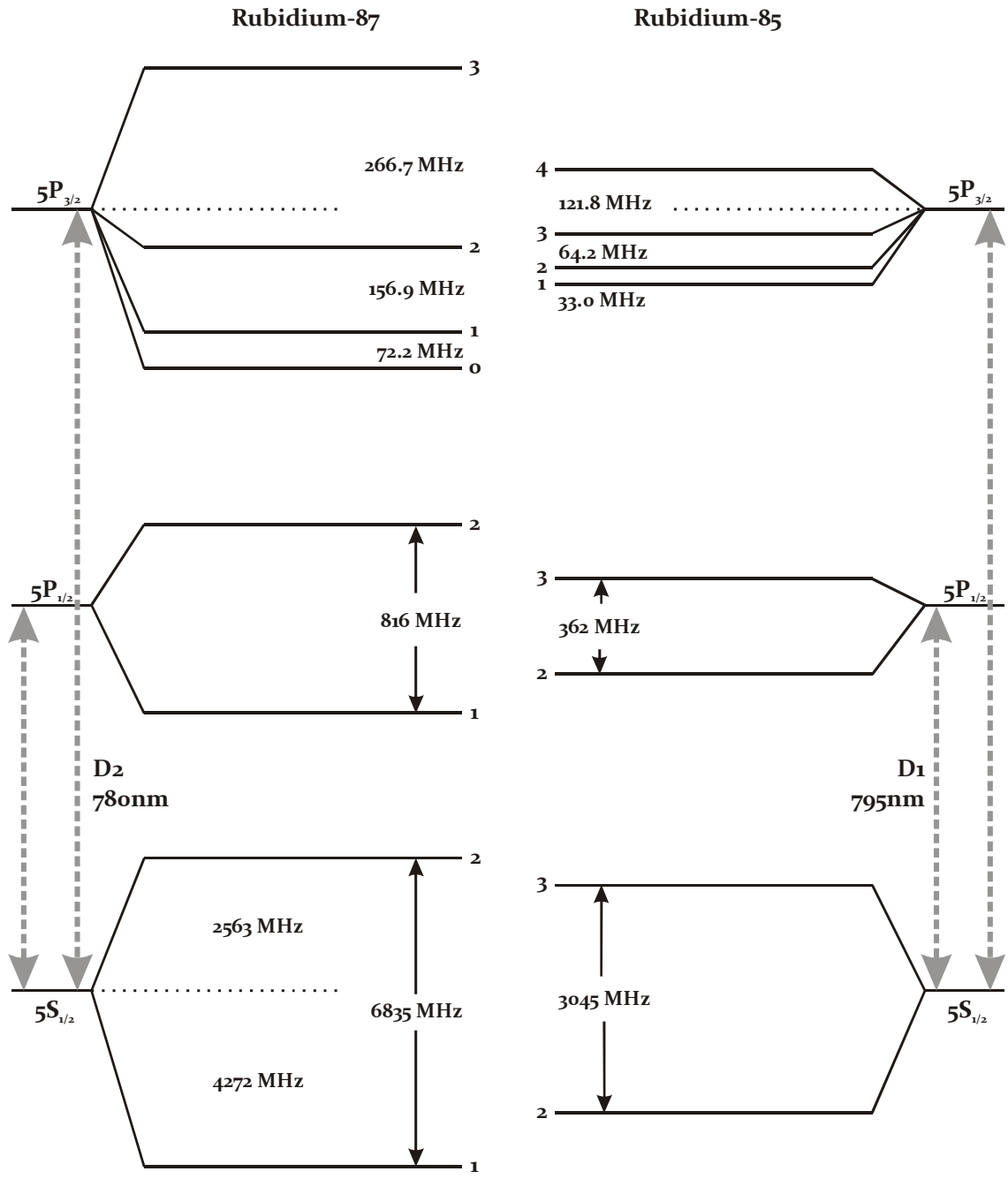

Figure 6-4: *Rubidium energy levels, showing D1 & D2 lines and their hyperfine structure. The structures for ^{87}Rb and ^{85}Rb are on the left and right respectively. The hyperfine structure is shown to scale within in each band.*

The splitting of the $5S_{1/2}$ ground state is 3.05 GHz. Importantly this is significantly more than the 517 MHz Doppler width at room temperature, which allows selective coupling from either hyperfine level to an excited state. The splitting of the $5P_{1/2}$ and $5P_{3/2}$ levels is however much smaller, and all four hyperfine levels of the $5P_{3/2}$ lie within one Doppler width. Considering a laser tuned to the $5S_{1/2}^{F=2} \rightarrow 5P_{3/2}^{F'=2}$ transition for zero velocity

atoms, the laser will be on resonance for transitions to $5P_{3/2}^{F'=1}$ and $5P_{3/2}^{F'=3}$ for a significant fraction at atoms at finite velocity (the transition to the final hyperfine level is dipole-forbidden).

This section explores the effects of optical pumping by a pump laser tuned to a single transition (for zero velocity atoms). The experimental setup is shown schematically in Figure 6-5.

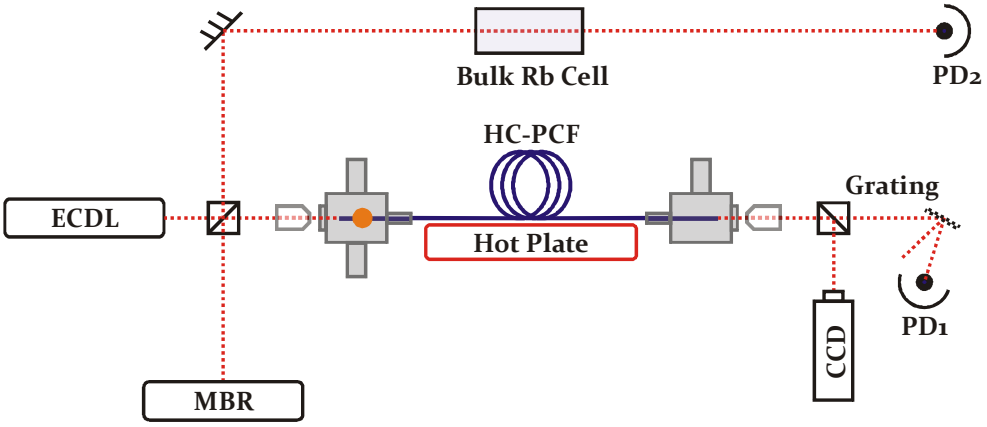

Figure 6-5: *Setup for rubidium loaded HC-PCF experiments. PD: photodiode; GTP: Glan-Thompson polarizer; NPBS: non-polarizing beam splitter; HWP: half-wave plate.*

To maintain a high vapour density, the chambers are kept heated to ~150°C, and the fibre at ~80°C. The pump laser is an external cavity diode laser, frequency locked to the required transition using a saturated absorption signal obtained by splitting off 50% of the laser power through a bulk rubidium reference cell (not shown in the figure). The probe laser is a sub-100 kHz linewidth Ti:Sapphire monolithic block resonator (MBR) laser. Both lasers are linearly polarised. The beams are combined at a non-polarising beam splitting before being coupled into the rubidium-loaded fibre via the coupling window in the gas chamber. At the output, pump and probe beams are separated at a grating, and the probe detected by a photodiode. The CCD camera is used ensure that both lasers are well coupled into the core of the fibre at all times.

To observe optical pumping the probe laser with a power of 5 nW is swept across all hyperfine levels of the D_1 transition ($5S_{1/2} \rightarrow 5P_{1/2}$), with a sweep frequency of 0.2 Hz. The pump laser with power of 3 μW is tuned to a D_2 transition, either $5S_{1/2}^{F=2} \rightarrow 5P_{3/2}^{F'=1}$ or $5S_{1/2}^{F=3} \rightarrow 5P_{3/2}^{F'=2}$. The probe transmission spectra for each pump transition are shown in the top and bottom graphs of Figure 6-6 respectively.

It is clear that the use of these schemes has resulted in sub-Doppler peaks of increased or decreased absorption. Before considering these it is useful to consider the effect the pump laser has on the Doppler broadened absorption lines.

By comparing the black and grey curves of Figure 6-6, showing probe transmission in the presence and absence of the pump beam, it can be seen that there is an overall change in absorption across the Doppler broadened D_1 transitions. As is expected from a rate equation approach, with the pump tuned to a D_2 transition from the lower ground state (as in the top graph), less absorption is seen on the D_1 transition from this state due to population being optically pumped into the upper ground state via optical decay from the $5P_{3/2}$ levels. Equivalently, greater absorption is observed on the D_1 transition from the upper ground state. For a pump tuned to a transition from the upper ground state the opposite is true, as seen in the lower graph.

The pump laser has the effect of producing a non-equilibrium population distribution amongst the hyperfine levels of the ground date.

Considering now the effect of the hyperfine structure of the excited states, the sub-Doppler structure of the $5S_{1/2}^{F=2} \rightarrow 5P_{1/2}$ transition in the presence of a pump tuned to a transition from the lower ground state is shown in detail in Figure 6-7. On this figure the approximate spacing of these peaks in frequency is labelled.

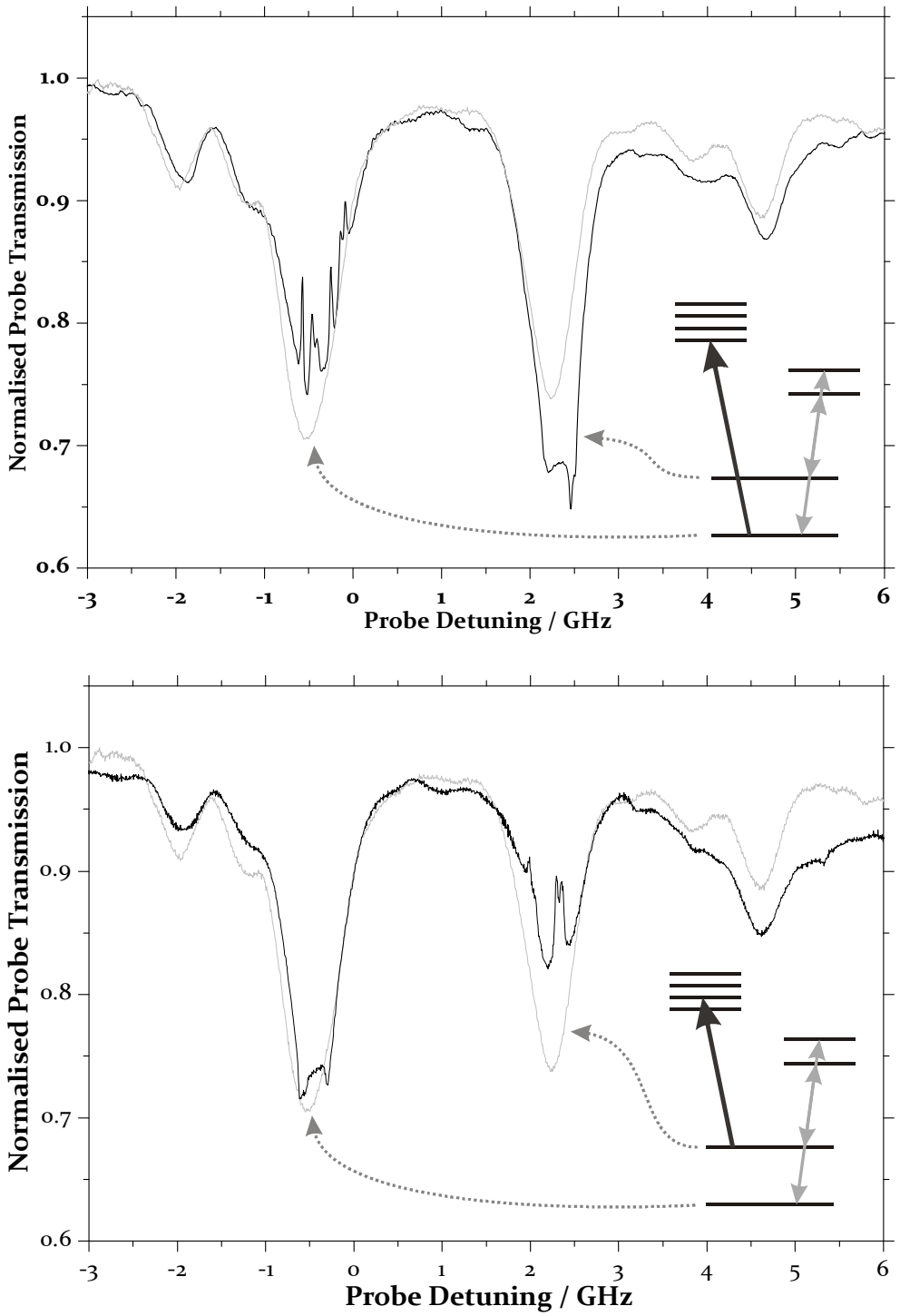

Figure 6-6: *Transmission of a probe beam swept across the rubidium D_1 transitions. Grey curves show transmission in the absence of the pump laser; black curves show probe transmission in presence of a pump tuned to the $5S_{1/2}^{F=2} \rightarrow 5P_{3/2}^{F'=1}$ transition (top) and $5S_{1/2}^{F=3} \rightarrow 5P_{3/2}^{F'=2}$ transition (bottom). The inset figure shows the schemes schematically, where the black and grey arrows represent pump and probe transitions respectively.*

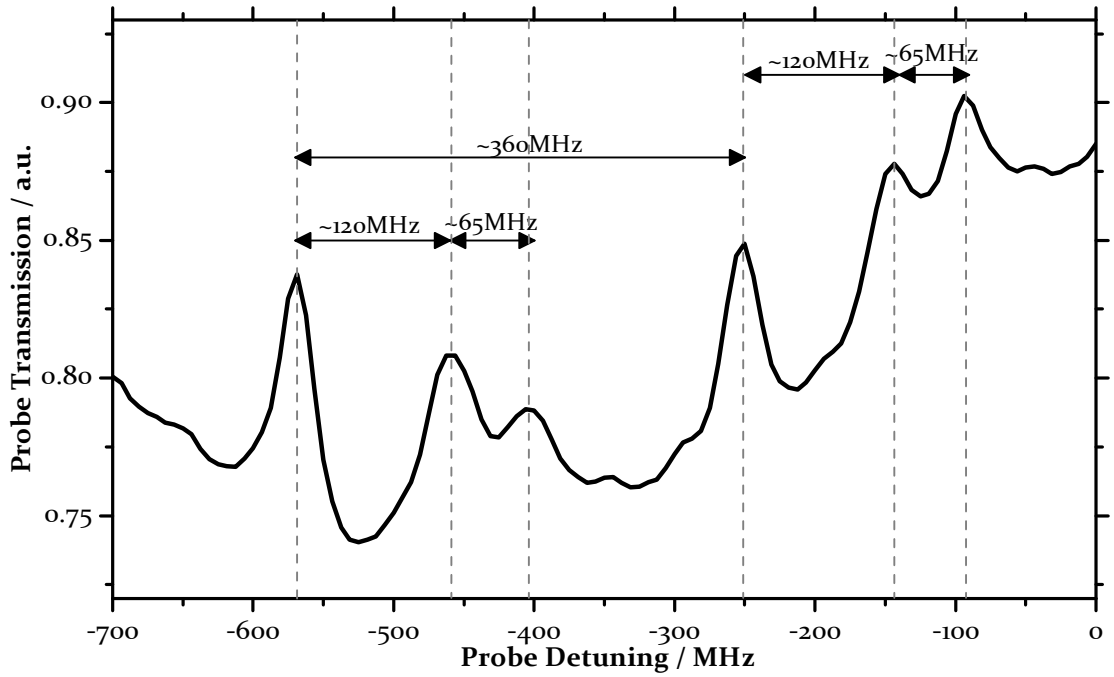

Figure 6-7: *Detail of Figure 6-6 (top graph) showing the frequency spacing of the sub-Doppler peaks observed in the Doppler broadened* $5S_{1/2}^{F=2} \rightarrow 5P_{1/2}$ *probe transition, in the presence of a pump tuned to a transition from the lower ground state. As illustrated, the six clearly visible peaks form two sets of three.*

The sub-Doppler peaks each have a line-width of ~30 MHz. The relative spacing of the peaks is determined by the hyperfine splitting of both excited states. From left-to-right, the peaks are separated by 120 MHz, 65 MHz, 175 MHz, 120 MHz and 65 MHz. The 120 MHz and 65 MHz spacings correspond to the spacing between the lower three hyperfine levels of the $5P_{3/2}$ state. It is also seen that the six peaks are formed by two repeated triplets, spaced by ~360 MHz corresponding to the hyperfine splitting of the $5P_{1/2}$ state. The reason for the formation of these six peaks (despite the fixed frequency of the pump) is the fact that three dipole-allowed transitions lie well within the Doppler width of the selected pump transition. This is in contrast to saturated absorption spectroscopy where the pump and probe are at the same frequency.

While the main interest in the spectra obtained here is to help with the interpretation of EIT spectra obtained in the next section, the results obtained demonstrate that sub-Doppler features have been achieved in rubidium loaded kagomé hollow-core fibre. The results show such fibre is promising as a compact and flexible replacement for bulk rubidium cells, offering a significant increase in interaction length. Of course, the ultimate aim of this work is to produce a rubidium vapour loaded photonic microcell, which would bring with it the advantages for applications discussed in chapter 4. The formation of a rubidium photonic microcell is discussed further in chapter 7.

6.4 Electromagnetically Induced Transparency

By considering the optical pumping results above, a configuration has been chosen in which to observe EIT in rubidium loaded kagomé fibre. It is useful first to consider the work of Ghosh *et al.* [104] who published results showing EIT in a rubidium loaded photonic bandgap HC-PCF. Their chosen V-type energy level scheme is shown in Figure 6-8. The reason given for this choice of scheme is that the $5P_{3/2}^{F=3}$ must decay to the upper ground state, since the transition to the lower hyperfine level of the ground state is dipole-forbidden; this would then preclude effects of optical pumping. However, the coupling beam will also couple to the nearby $5P_{3/2}^{F=2,1,0}$ levels due to Doppler shifts occurring due to the thermal distribution of atomic velocities. These levels are then allowed to radiatively decay to the lower-ground state, and will thus affect the equilibrium population distribution of the hyperfine level of the ground state.

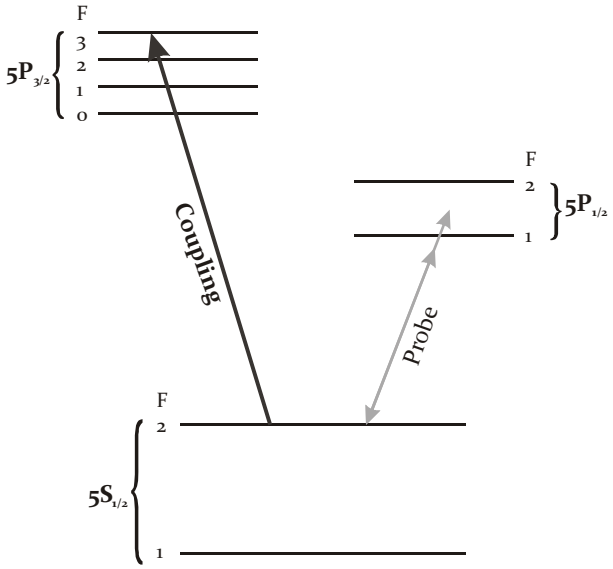

Figure 6-8: *The energy scheme used by Ghosh et al. for observation of EIT in a rubidium loaded HC-PCF.*

While the observation of EIT should indeed be possible in a configuration similar to that used by Ghosh, it is difficult to unambiguously identity the induced transparency peak amongst the numerous peaks expected due to optical pumping. For this reason a Λ scheme is chosen to demonstrate EIT in the rubidium loaded kagomé fibre. The scheme is shown in Figure 6-9. The coupling beam is tuned to a D_2 transition from the upper ground state, while the probe beams sweeps D_2 transitions from the lower ground state.

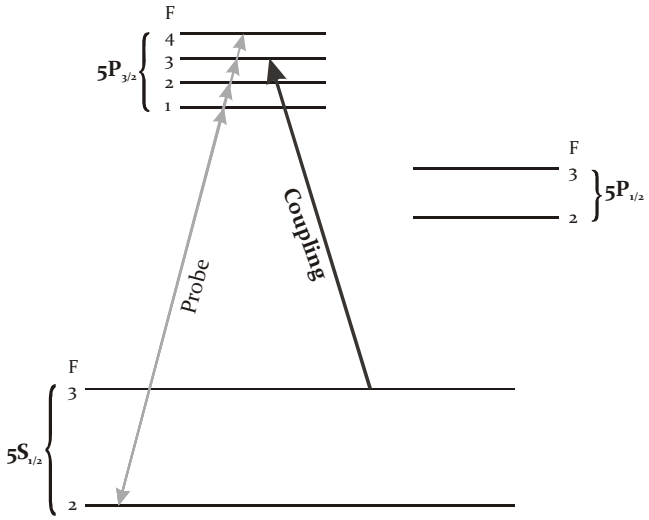

Figure 6-9: *Probe and coupling transition configuration for the observation of EIT in a Λ configuration in rubidium loaded kagomé fibre. The coupling laser is tuned to the* $5S_{1/2}^{F=3} \rightarrow 5P_{3/2}^{F'=3}$ *D_2 transition. The probe laser sweeps across the* $5S_{1/2}^{F=2} \rightarrow 5P_{3/2}$ *D_2 transitions.*

The use of this scheme allows any ambiguity between optical pumping effects and EIT to be removed. In this scheme optical pumping will produce dips in transmission instead of transparency peaks because population is pumped into the lower ground state. The experimental setup for EIT is very similar to that used in the previous section, and is shown in Figure 6-10.

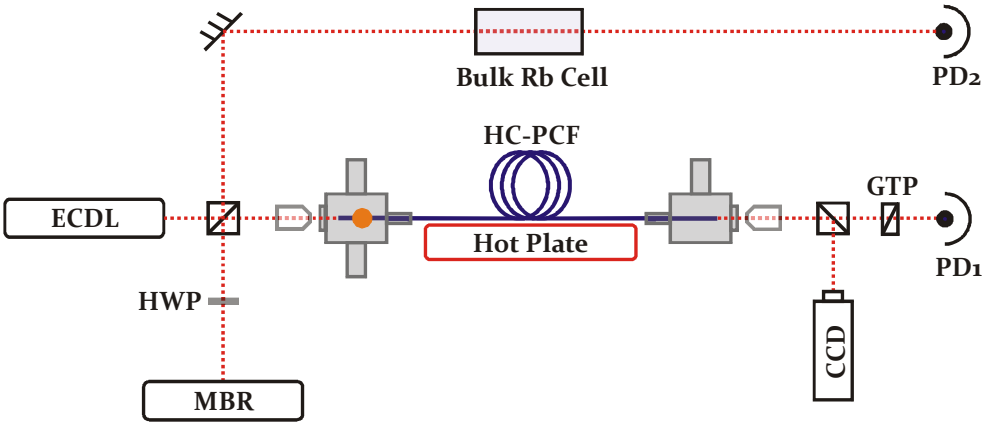

Figure 6-10: *Experimental setup for EIT in rubidium loaded kagomé fibre. HWP: half-wave plate; GTP: Glan-Thompson polariser.*

Due to the close frequency spacing of the probe and coupling beams, a diffraction grating, as used in the optical pumping setup, is not suitable for separation of the beams

as they exit the fibre. Instead, the beams are arranged to have orthogonal linear polarisations as they enter the fibre, and the probe is separated before detection by a Glan-Thompson polariser.

To observe EIT the 5 nW probe, provided by the ECDL, co-propagates through the fibre with the coupling beam from the MBR laser. They are tuned and swept across the transitions as illustrated in Figure 6-9.

Figure 6-11 shows the probe transmission in this configuration, with a coupling laser power of 1.6 μW coupled into the fibre. The induced transparency peak due to EIT is visible at zero probe detuning.

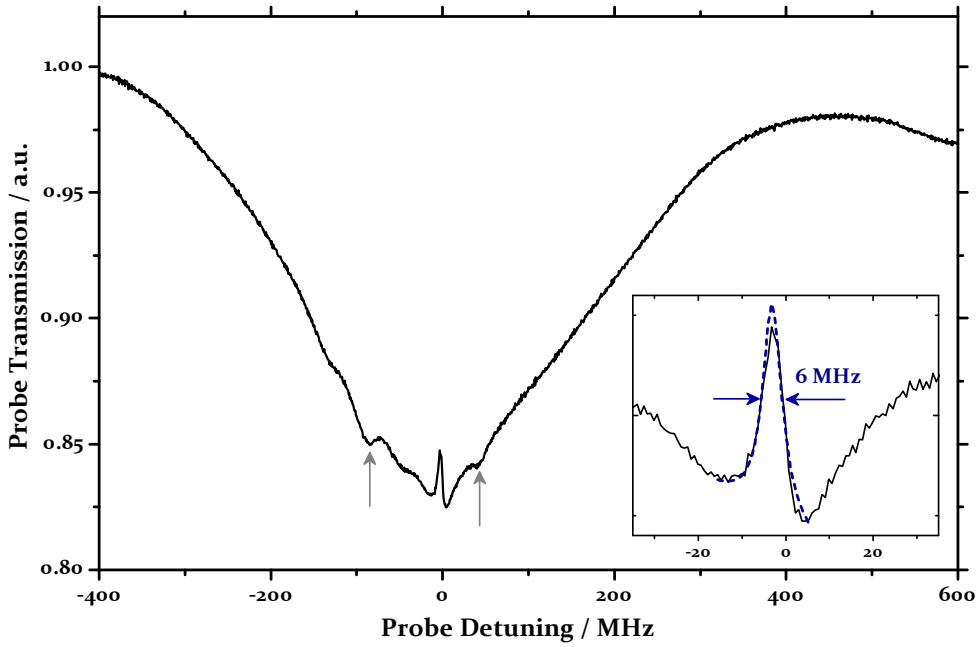

Figure 6-11: *Probe transmission showing narrow-linewidth EIT in rubidium loaded kagomé fibre in a Λ energy level scheme. The induced transparency peak is visible at zero detuning; troughs attributed to optical pumping are visible either side of the induced transparency, highlighted by grey arrows. Inset: detail of the induced transparency peak with Lorentzian fit.*

The induced transparency peak has a FWHM line-width of 6 MHz, as shown inset in Figure 6-11, and a height of nearly 6%. The evolution with coupling laser power of the height and width of the induced transparency has been measured experimentally, and is shown in Figure 6-12.

The line-width of the transparency peak remains approximately constant at 6 MHz, independent of the coupling Rabi frequency. The height increases linearly with coupling

Rabi frequency until ~1.3 GHz, where the height appears to saturate before asymptotically decreasing to 3% at 6 GHz (not plotted in the figure).

This turning point in height can be explained by the competing effect of optical pumping. In this Λ configuration optical pumping gives rise to additional absorption of the probe laser as can be seen either side of the induced transparency (marked by grey arrows in Figure 6-11) corresponding to the $F = 2$ and $F = 4$ levels of the $5P_{3/2}$ state. This additional absorption is also present at the location of the induced transparency, and thus has an effect on the characteristics of the transparency peak.

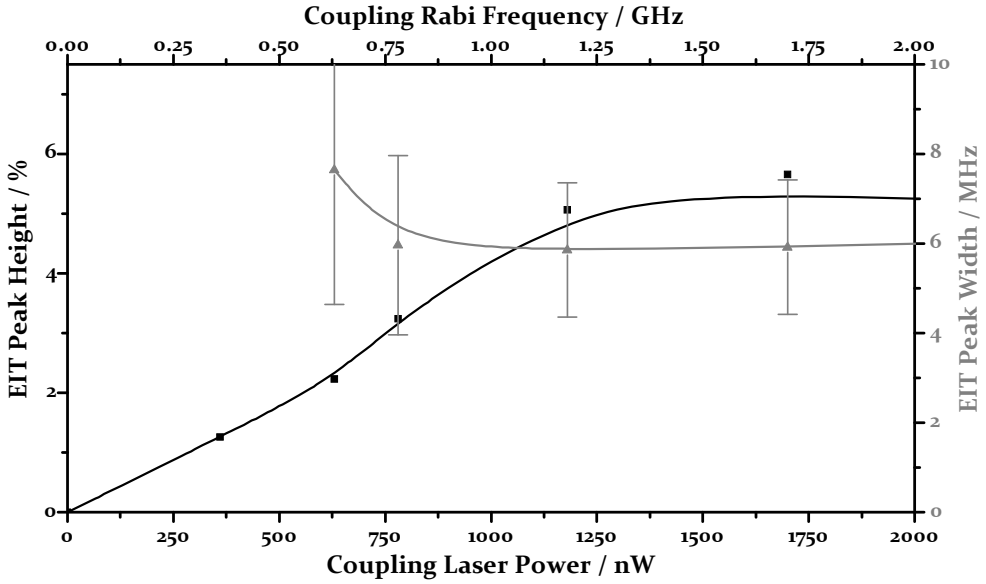

Figure 6-12: *Measured EIT peak visible height (black points) and width (grey points) as a function of the coupling laser power.*

The behaviour of the height and width evolution is in broad agreement with published experimental results [112], where the dependence of the EIT width on coupling laser intensity was investigated at Rabi frequencies much larger than the Doppler width. It is noteworthy that the earlier study required much higher power, of the order of 10 mW, to obtain the large Rabi frequency. This highlights an advantage of using HC-PCF as a host for the rubidium, where due to the tight confinement the required power is four orders of magnitude lower than conventional techniques.

The 6 MHz EIT width obtained is of particular interest due to the expected contribution to the width from collisions between rubidium atoms and the core wall. The collisional rate between rubidium atoms and core-wall for the fibre used with 11 μm core diameter is 7 MHz (section 3.3.1). In the absence of elastic collisions this would be expected to give the same contribution to the Lorentzian linewidth of the EIT peak.

This immediately suggests that the PDMS coating of the fibre's core wall does indeed have a beneficial effect. Moreover, if other sources of broadening of the peak are considered it is seen that the maximum contribution from wall collisions is significantly smaller than expected in an uncoated fibre. It was shown in [112] that at the Rabi frequency range explored here the EIT linewidth plateaus to a value around 3-4 MHz determined by the combination of optical broadening and optical pumping. The linewidth of the unstabilised diode laser contributes 1-2 MHz to the linewidth. This suggests a maximum contribution of only ~1 MHz from collision broadening.

Accurate quantification of the dephasing rate due to coated-wall collisions would require further measurements with a detection scheme more sensitive to low light level than the one used in the present experimental set-up. However, it is shown in principle that the coating is beneficial, and improvements in the coating technique may allow further reductions in linewidth. Future work planned in further investigating the properties of the coating is discussed in the following chapter.

6.5 Summary

The work in this chapter has demonstrated the successful loading of a kagomé structure HC-PCF with rubidium vapour. The loading process is time consuming, and therefore different techniques have been considered, and will be explained in the following chapter.

The hyperfine structure of excited states of rubidium has been resolved in pump-probe spectroscopy, similar to saturated absorption spectroscopy. Furthermore, electromagnetically induced transparency with narrow linewidth has been observed in the rubidium loaded fibre. The linewidths achieved are below those expected due to the high rate of dephasing that should result from the large collision rate of rubidium atoms with the fibre core wall. This suggests that the polymer coating applied to the wall has had the desired effect of achieving elastic collisions, and thus reducing the rate of dephasing.

Although further work is planned and required to access the properties of the coating, HC-PCF has been demonstrated as a capable host of quantum optical effects in atomic vapours. The next stage of this work is to create an atomic vapour photonic microcell, offering long interaction lengths and large signal-to-noise ratio in a compact and easy-to-use device.

Chapter 7

Summary and Future Work

This thesis has reported the development of photonic microcells based on hollow-core photonic crystal fibre, and experimentally demonstrated their suitability for quantum optical applications. This chapter provides a summary of the thesis and the work that remains to be done in exploiting the full potential of photonic microcells.

7.1 Summary

Photonic Crystal Fibre

The work is this thesis revolved around the use of HC-PCF. In Chapter 1 we saw how the fibre provides extremely efficient gas-laser interaction, maintaining small mode-area over metre or kilometre interaction lengths. It is this property of the fibre that makes its use for quantum optics so attractive. Chapter 2 looked at the linear optical characteristics of two distinct types of HC-PCF: bandgap and kagomé. The tailoring of the properties of drawn fibre by etching was demonstrated to be a technique with the potential to improve the properties of HC-PCF for particular applications.

Photonic Microcells

Chapter 4 explored the development of photonic microcells, consisting of gas-filled HC-PCF sealed by splicing to conventional optical fibre. Techniques have been developed that allow photonic microcells to be created at a wide range of gas-pressures, from sub-microbar to tens of bar, with very low insertion loss. The loading of a HC-PCF core with rubidium vapour has also been demonstrated, and is of particular interest for quantum optical applications, which have traditionally used atomic vapours.

Electromagnetically Induced Transparency

The use of HC-PCF has provided the first observation of EIT in a molecular gas, while the use of an acetylene photonic microcell provided a means to establish the coherence properties of such a system through an extensive range of experimental configurations.

In Chapter 6 EIT was demonstrated in a rubidium loaded HC-PCF. Importantly it was shown that by coating the silica core of the fibre with a polymer layer, spin-preserving collisions could be obtained resulting in a narrow linewidth EIT peak.

7.2 Future Work

Atomic Vapour Photonic Microcells

The rubidium EIT results in Chapter 6 were obtained using rubidium loaded HC-PCF attached to gas chambers. As for the acetylene work, sealed photonic microcells filled with atomic vapour are the ultimate aim, and would bring the same advantages as the molecular gas microcells.

The major difficulty in working with atomic vapours is the loading of the vapour into the HC-PCF due to their highly reactive nature. Further work is planned in finding more efficient vapour loading processes, for example by introducing rubidium into the fibre in the form of a metal-organic compound.

Further investigation of light-induced atomic desorption is also planned. This effect has the potential to allow a controllable vapour density within a rubidium photonic microcell, by control of the release of rubidium from the polymer core-wall coating.

Laser Cooling of Atoms in HC-PCF

The presence of collisions between atoms or molecules leads to dephasing of coherence when considering coherent optical effects such as EIT, leading to a broadening of line-widths. Clearly reduction in temperature of the gas or vapour will result in a corresponding decrease in collisional and dephasing rates, but cooling of an entire vapour-filled photonic microcell is an inefficient means of achieving this.

Instead, laser cooling offers a possible way to cool vapour atoms within a photonic microcell. Among the many methods of laser cooling [113] are two that when combined may be expected to be able to achieve efficient laser cooling of atoms within a photonic microcell. The two techniques of bichromatic laser cooling [114], which uses two laser fields symmetrically detuned from resonance of a two-level system, and Doppler cooling should be applicable in a HC-PCF system, and may allow for a great reduction in linewidths achievable in quantum optical effects in a fibre host.

Appendix A

Density Matrix

A.1 Three-level Density Matrix Derivation

This section shows the full density matrix calculated from the Liouville equation for a three energy-level system.

The levels have energies $\hbar\omega_1$, $\hbar\omega_2$ and $\hbar\omega_3$. A laser with frequency ω_A and Rabi frequency Ω_A couples levels 1 and 3, while a second field with frequency ω_B and Rabi frequency Ω_B couples levels 2 and 3.

The matrices below show the terms included for the full calculation with no approximations, after making the rotating-wave approximation, and after a second similar approximation to allow the steady-state conditions to be evaluated.

Hamiltonian:

$$H = \begin{pmatrix} \hbar\omega_1 & 0 & \hbar\Omega_A \mathrm{Exp}[+i\omega_A t] \\ 0 & \hbar\omega_2 & \hbar\Omega_B \mathrm{Exp}[+i\omega_B t] \\ \hbar\Omega_A \mathrm{Exp}[-i\omega_A t] & \hbar\Omega_B \mathrm{Exp}[-i\omega_B t] & \hbar\omega_3 \end{pmatrix}$$

Density matrix:

$$\rho = \begin{pmatrix} \rho 11[t] & \rho 12[t] & \rho 13[t] \\ \rho 21[t] & \rho 22[t] & \rho 23[t] \\ \rho 31[t] & \rho 32[t] & \rho 33[t] \end{pmatrix}$$

No approximations:

$$M = \begin{pmatrix} 0 & 0 & ie^{-it\omega A}\Omega A & 0 & 0 & 0 & -ie^{it\omega A}\Omega A & 0 & 0 \\ 0 & -i(\omega 1-\omega 2) & ie^{-it\omega B}\Omega B & 0 & 0 & 0 & 0 & -ie^{it\omega A}\Omega A & 0 \\ ie^{it\omega A}\Omega A & ie^{it\omega B}\Omega B & i(-\omega 1+\omega 3) & 0 & 0 & 0 & 0 & 0 & -ie^{it\omega A}\Omega A \\ 0 & 0 & 0 & i(\omega 1-\omega 2) & 0 & ie^{-it\omega A}\Omega A & -ie^{it\omega B}\Omega B & 0 & 0 \\ 0 & 0 & 0 & 0 & 0 & ie^{-it\omega B}\Omega B & 0 & -ie^{it\omega B}\Omega B & 0 \\ 0 & 0 & 0 & ie^{it\omega A}\Omega A & ie^{it\omega B}\Omega B & i(-\omega 2+\omega 3) & 0 & 0 & -ie^{it\omega B}\Omega B \\ -ie^{-it\omega A}\Omega A & 0 & 0 & -ie^{-it\omega B}\Omega B & 0 & 0 & i(\omega 1-\omega 3) & 0 & ie^{-it\omega A}\Omega A \\ 0 & -ie^{-it\omega A}\Omega A & 0 & 0 & -ie^{-it\omega B}\Omega B & 0 & 0 & i(\omega 2-\omega 3) & ie^{-it\omega B}\Omega B \\ 0 & 0 & -ie^{-it\omega A}\Omega A & 0 & 0 & -ie^{-it\omega B}\Omega B & ie^{it\omega A}\Omega A & ie^{it\omega B}\Omega B & 0 \end{pmatrix}$$

RWA:

$$M_{RWA} = \begin{pmatrix} 0 & 0 & i\Omega A & 0 & 0 & 0 & -i\Omega A & 0 & 0 \\ 0 & -i(\omega 1-\omega 2) & ie^{it(\omega A-\omega B)}\Omega B & 0 & 0 & 0 & 0 & -ie^{it(\omega A-\omega B)}\Omega A & 0 \\ i\Omega A & ie^{-it(\omega A-\omega B)}\Omega B & -i(\omega 1-\omega 3+\omega A) & 0 & 0 & 0 & 0 & 0 & -i\Omega A \\ 0 & 0 & 0 & i(\omega 1-\omega 2) & 0 & ie^{-it(\omega A-\omega B)}\Omega A & -ie^{-it(\omega A-\omega B)}\Omega B & 0 & 0 \\ 0 & 0 & 0 & 0 & 0 & i\Omega B & 0 & -i\Omega B & 0 \\ 0 & 0 & 0 & ie^{it(\omega A-\omega B)}\Omega A & i\Omega B & -i(\omega 2-\omega 3+\omega B) & 0 & 0 & -i\Omega B \\ -i\Omega A & 0 & 0 & -ie^{it(\omega A-\omega B)}\Omega B & 0 & 0 & i(\omega 1-\omega 3+\omega A) & 0 & i\Omega A \\ 0 & -ie^{-it(\omega A-\omega B)}\Omega A & 0 & 0 & -i\Omega B & 0 & 0 & i(\omega 2-\omega 3+\omega B) & i\Omega B \\ 0 & 0 & -i\Omega A & 0 & 0 & -i\Omega B & i\Omega A & i\Omega B & 0 \end{pmatrix}$$

Steady-state:

$$M_{SS} = \begin{pmatrix} 0 & 0 & i\Omega A & 0 & 0 & 0 & -i\Omega A & 0 & 0 \\ 0 & -i(\omega 1-\omega 2+\omega A-\omega B) & i\Omega B & 0 & 0 & 0 & 0 & -i\Omega A & 0 \\ i\Omega A & i\Omega B & -i(\omega 1-\omega 3+\omega A) & 0 & 0 & 0 & 0 & 0 & -i\Omega A \\ 0 & 0 & 0 & i(\omega 1-\omega 2+\omega A-\omega B) & 0 & i\Omega A & -i\Omega B & 0 & 0 \\ 0 & 0 & 0 & 0 & 0 & i\Omega B & 0 & -i\Omega B & 0 \\ 0 & 0 & 0 & i\Omega A & i\Omega B & -i(\omega 2-\omega 3+\omega B) & 0 & 0 & -i\Omega B \\ -i\Omega A & 0 & 0 & -i\Omega B & 0 & 0 & i(\omega 1-\omega 3+\omega A) & 0 & i\Omega A \\ 0 & -i\Omega A & 0 & 0 & -i\Omega B & 0 & 0 & i(\omega 2-\omega 3+\omega B) & i\Omega B \\ 0 & 0 & -i\Omega A & 0 & 0 & -i\Omega B & i\Omega A & i\Omega B & 0 \end{pmatrix}$$

A.2 Closed System Matrix

The following equation is represents that solved to obtain the steady state susceptibilities for the closed-system model used in Chapter 5 in the V scheme. At steady-state there is no time-dependence of the density vector, and the solution is therefore found by setting $\dot{\rho} = 0$.

$$\begin{pmatrix} \dot{\rho_{11}} \\ \dot{\rho_{12}} \\ \dot{\rho_{13}} \\ \dot{\rho_{21}} \\ \dot{\rho_{22}} \\ \dot{\rho_{23}} \\ \dot{\rho_{31}} \\ \dot{\rho_{32}} \\ \dot{\rho_{33}} \end{pmatrix} = \begin{pmatrix} -\gamma_1 - \varepsilon & i\Omega_p/2 & 0 & -i\Omega_p/2 & 0 & 0 & 0 & 0 & \varepsilon \\ i\Omega_p/2 & -\Gamma_{12} + i\Delta p & i\Omega_c/2 & 0 & -i\Omega_p/2 & 0 & 0 & 0 & 0 \\ 0 & i\Omega_c/2 & -\Gamma_{13} + i(\Delta p - \Delta c) & 0 & 0 & -i\Omega_p/2 & 0 & 0 & 0 \\ -i\Omega_p/2 & 0 & 0 & -\Gamma_{21} - i\Delta p & i\Omega_p/2 & 0 & -i\Omega_c/2 & 0 & 0 \\ \gamma_1 & -i\Omega_p/2 & 0 & i\Omega_p/2 & 0 & i\Omega_c/2 & 0 & -i\Omega_c/2 & \gamma_3 \\ 0 & 0 & -i\Omega_p/2 & 0 & i\Omega_c/2 & -\Gamma_{23} - i\Delta c & 0 & 0 & -i\Omega_c/2 \\ 0 & 0 & 0 & -i\Omega_c/2 & 0 & 0 & 0 - \Gamma_{31} + i(\Delta c - \Delta p) & i\Omega_p/2 & 0 \\ 0 & 0 & 0 & 0 & -i\Omega_c/2 & 0 & i\Omega_p/2 & -\Gamma_{32} + i\Delta c & i\Omega_c/2 \\ \varepsilon & 0 & 0 & 0 & 0 & -i\Omega_c/2 & 0 & i\Omega_c/2 & -\gamma_3 - \varepsilon \end{pmatrix} \begin{pmatrix} \rho_{11} \\ \rho_{12} \\ \rho_{13} \\ \rho_{21} \\ \rho_{22} \\ \rho_{23} \\ \rho_{31} \\ \rho_{32} \\ \rho_{33} \end{pmatrix} = \underline{0}$$

For the lambda scheme the equation becomes:

$$\begin{pmatrix} \dot{\rho_{11}} \\ \dot{\rho_{12}} \\ \dot{\rho_{13}} \\ \dot{\rho_{21}} \\ \dot{\rho_{22}} \\ \dot{\rho_{23}} \\ \dot{\rho_{31}} \\ \dot{\rho_{32}} \\ \dot{\rho_{33}} \end{pmatrix} = \begin{pmatrix} -\varepsilon & i\Omega_p/2 & 0 & -i\Omega_p/2 & \gamma_2 b_{21} & 0 & 0 & 0 & \varepsilon \\ i\Omega_p/2 & -\Gamma_{12} + i\Delta p & i\Omega_c/2 & 0 & -i\Omega_p/2 & 0 & 0 & 0 & 0 \\ 0 & i\Omega_c/2 & -\Gamma_{13} + i(\Delta p - \Delta c) & 0 & 0 & -i\Omega_p/2 & 0 & 0 & 0 \\ -i\Omega_p/2 & 0 & 0 & -\Gamma_{21} - wi\Delta p & i\Omega_p/2 & 0 & -i\Omega_c/2 & 0 & 0 \\ 0 & -i\Omega_p/2 & 0 & i\Omega_p/2 & -\gamma_2 & i\Omega_c/2 & 0 & -i\Omega_c/2 & 0 \\ 0 & 0 & -i\Omega_p/2 & 0 & i\Omega_c/2 & -\Gamma_{23} - i\Delta c & 0 & 0 & -i\Omega_c/2 \\ 0 & 0 & 0 & -i\Omega_c/2 & 0 & 0 & 0 - \Gamma_{31} + i(\Delta c - \Delta p) & i\Omega_p/2 & 0 \\ 0 & 0 & 0 & 0 & -i\Omega_c/2 & 0 & i\Omega_p/2 & -\Gamma_{32} + i\Delta c & i\Omega_c/2 \\ -\varepsilon & 0 & 0 & 0 & \gamma_2 b_{23} & -i\Omega_c/2 & 0 & i\Omega_c/2 & -\varepsilon \end{pmatrix} \begin{pmatrix} \rho_{11} \\ \rho_{12} \\ \rho_{13} \\ \rho_{21} \\ \rho_{22} \\ \rho_{23} \\ \rho_{31} \\ \rho_{32} \\ \rho_{33} \end{pmatrix} = \underline{0}$$

The sole difference between co-propagating and counter-propagating coupling-probe configurations is the sign of the Doppler shift of the probe laser; the matrices are thus adapted for the counter-propagating scheme by making the substitution $\Delta_p \rightarrow -\Delta_p$.

A.3 Open System Matrix

The complete equation solved for the open system in the V scheme is shown below:

$$\begin{pmatrix}\dot{\rho_{11}}\\ \dot{\rho_{12}}\\ \dot{\rho_{13}}\\ \dot{\rho_{21}}\\ \dot{\rho_{22}}\\ \dot{\rho_{23}}\\ \dot{\rho_{31}}\\ \dot{\rho_{32}}\\ \dot{\rho_{33}}\end{pmatrix} = \begin{pmatrix} -\gamma_1 - w & i\Omega_p/2 & 0 & -i\Omega_p/2 & 0 & 0 & 0 & 0 & 0\\ i\Omega_p/2 & -\Gamma_{12} - w + i\Delta p & i\Omega_c/2 & 0 & -i\Omega_p/2 & 0 & 0 & 0 & 0\\ 0 & i\Omega_c/2 & -\Gamma_{13} - w + i(\Delta p - \Delta c) & 0 & 0 & -i\Omega_p/2 & 0 & 0 & 0\\ -i\Omega_p/2 & 0 & 0 & -\Gamma_{21} - w - i\Delta p & i\Omega_p/2 & 0 & -i\Omega_c/2 & 0 & 0\\ \gamma_1 b_{12} & -i\Omega_p/2 & 0 & i\Omega_p/2 & -w & i\Omega_c/2 & 0 & -i\Omega_c/2 & \gamma_3 b_{32}\\ 0 & 0 & -i\Omega_p/2 & 0 & i\Omega_c/2 & -\Gamma_{23} - w - i\Delta c & 0 & 0 & -i\Omega_c/2\\ 0 & 0 & 0 & -i\Omega_c/2 & 0 & 0 & -\Gamma_{31} - w + i(\Delta c - \Delta p) & i\Omega_p/2 & 0\\ 0 & 0 & 0 & 0 & -i\Omega_c/2 & 0 & i\Omega_p/2 & -\Gamma_{32} - w + i\Delta c & i\Omega_c/2\\ \gamma_1 b_{13} & 0 & 0 & 0 & 0 & -i\Omega_c/2 & 0 & i\Omega_c/2 & -\gamma_3 - w \end{pmatrix} \begin{pmatrix}\rho_{11}\\ \rho_{12}\\ \rho_{13}\\ \rho_{21}\\ \rho_{22}\\ \rho_{23}\\ \rho_{31}\\ \rho_{32}\\ \rho_{33}\end{pmatrix} + \begin{pmatrix}G_1\\ 0\\ 0\\ 0\\ G_2\\ 0\\ 0\\ 0\\ G_3\end{pmatrix} = 0$$

For the Λ scheme the equation is:

$$\begin{pmatrix}\dot{\rho_{11}}\\ \dot{\rho_{12}}\\ \dot{\rho_{13}}\\ \dot{\rho_{21}}\\ \dot{\rho_{22}}\\ \dot{\rho_{23}}\\ \dot{\rho_{31}}\\ \dot{\rho_{32}}\\ \dot{\rho_{33}}\end{pmatrix} = \begin{pmatrix} -\mathrm{w} & i\Omega_\mathrm{p}/2 & 0 & -i\Omega_\mathrm{p}/2 & \gamma_2 b_{21} & 0 & 0 & 0 & \gamma_3 b_{31}\\ i\Omega_\mathrm{p}/2 & -\Gamma_{12} - \mathrm{w} + \mathrm{i}\Delta\mathrm{p} & i\Omega_\mathrm{c}/2 & 0 & -i\Omega_\mathrm{p}/2 & 0 & 0 & 0 & 0\\ 0 & i\Omega_\mathrm{c}/2 & -\Gamma_{13} - \mathrm{w} + \mathrm{i}(\Delta\mathrm{p} - \Delta\mathrm{c}) & 0 & 0 & -i\Omega_\mathrm{p}/2 & 0 & 0 & 0\\ -i\Omega_\mathrm{p}/2 & 0 & 0 & -\Gamma_{21} - \mathrm{w} - \mathrm{i}\Delta\mathrm{p} & i\Omega_\mathrm{p}/2 & 0 & -i\Omega_\mathrm{c}/2 & 0 & 0\\ 0 & -i\Omega_\mathrm{p}/2 & 0 & i\Omega_\mathrm{p}/2 & -\gamma_2 - \mathrm{w} & i\Omega_\mathrm{c}/2 & 0 & -i\Omega_\mathrm{c}/2 & 0\\ 0 & 0 & -i\Omega_\mathrm{p}/2 & 0 & i\Omega_\mathrm{c}/2 & -\Gamma_{23} - \mathrm{w} - \mathrm{i}\Delta\mathrm{c} & 0 & 0 & -i\Omega_\mathrm{c}/2\\ 0 & 0 & 0 & -i\Omega_\mathrm{c}/2 & 0 & 0 & 0 - \Gamma_{31} - \mathrm{w} + \mathrm{i}(\Delta\mathrm{c} - \Delta\mathrm{p}) & i\Omega_\mathrm{p}/2 & 0\\ 0 & 0 & 0 & 0 & -i\Omega_\mathrm{c}/2 & 0 & i\Omega_\mathrm{p}/2 & -\Gamma_{32} - \mathrm{w} + \mathrm{i}\Delta\mathrm{c} & i\Omega_\mathrm{c}/2\\ 0 & 0 & 0 & 0 & \gamma_3 b_{23} & -i\Omega_\mathrm{c}/2 & 0 & i\Omega_\mathrm{c}/2 & -\mathrm{w} \end{pmatrix} \begin{pmatrix}\rho_{11}\\ \rho_{12}\\ \rho_{13}\\ \rho_{21}\\ \rho_{22}\\ \rho_{23}\\ \rho_{31}\\ \rho_{32}\\ \rho_{33}\end{pmatrix} + \begin{pmatrix}G_1\\ 0\\ 0\\ 0\\ G_2\\ 0\\ 0\\ 0\\ G_3\end{pmatrix} = 0$$

The steady state solution for this open system model is found by solving $\dot{\rho} = -G$, where G is the vector containing the population gain terms for each energy level.

A.4 Determination of Theoretical Transparency Characteristics

To find the height and width of the transparency peak experimentally it is necessary to integrate over the molecular velocity distribution. This is achieved by considering the Doppler shifts due to molecular velocity, i.e. the terms Δc and Δp in the matrices of the previous section. The susceptibility is calculated at small intervals of velocity, weighted according to the Maxwellian distribution at the appropriate temperature, and summed to give the overall susceptibility.

Obtaining the height of the induced transparency simply required evaluation of the on-resonance probe absorption with the coupling beam present, and again in its absence.

Calculation of the theoretical width is slightly more involved. First it is necessary to determine the probe frequency detuning of the turning point in the probe transmission curve that indicates the point of maximum absorption. Then it is necessary to find the probe detuning, lying between zero and the point of maximum absorption, that the absorption is half-way between maximum and the on-resonance value. In the software developed, NAG library routines are used to perform both of these steps efficiently. However, determining the width sufficiently accurately is a computation expensive task due to the need to integrate over the velocity distribution for the evaluation of susceptibility at each probe detuning point.

Appendix B

EIT Modelling Code

This appendix contains the C# code used in calculation of probe transmission in the presence of EIT.

B.1 EIT Class

This class represents a three-level system, and solves the equations defined above to calculate the probe transmission.

```
using System;
using System.Collections.Generic;
using System.Text;
using Paraxial.Evaluator;
using Exocortex.DSP;

namespace Paraxial
{
    public partial class MathLibrary
    {

        public class VLEIT
        {

            #region --- Parameters ---

            // Total decay out of each level
            public ExpressionClass DecayL1;
            public ExpressionClass DecayL2;
            public ExpressionClass DecayL3;
            public ExpressionClass DecayV1;
            public ExpressionClass DecayV2;
            public ExpressionClass DecayV3;

            // Gain into each level
            public ExpressionClass GainL1;
            public ExpressionClass GainL2;
            public ExpressionClass GainL3;
            public ExpressionClass GainV1;
            public ExpressionClass GainV2;
            public ExpressionClass GainV3;

            // Loss from each level
            public ExpressionClass LossL1;
            public ExpressionClass LossL2;
            public ExpressionClass LossL3;
            public ExpressionClass LossV1;
            public ExpressionClass LossV2;
            public ExpressionClass LossV3;

            // Fraction of total decay
```

```
            public ExpressionClass BranchL21;
            public ExpressionClass BranchL23;
            public ExpressionClass BranchL31;
            public ExpressionClass BranchV12;
            public ExpressionClass BranchV32;
            public ExpressionClass BranchV13;

            // Decoherence
            public ExpressionClass DecoherenceL12;
            public ExpressionClass DecoherenceL13;
            public ExpressionClass DecoherenceL23;
            public ExpressionClass DecoherenceV12;
            public ExpressionClass DecoherenceV13;
            public ExpressionClass DecoherenceV23;

            // Effective decay
            public ExpressionClass EffectiveDecay;

            // Exchange between 1 & 3
            public ExpressionClass ExchangeL13;
            public ExpressionClass ExchangeV13;

            // Closed or open system
            public bool OpenSystem;

            // Direction
            public enum EITDirections { Copropagating, Counterpropagating }
            public EITDirections Direction;

            // Scheme
            public enum EITSchemes
            public EITSchemes Scheme;

            // Temperature, pressure, gas etc.
            public double Temperature { get { return vars["temperature"]; } set {
vars["temperature"] = value; } }
            public double Pressure { get { return vars["pressure"]; } set { vars["pressure"] =
value; } }
            public double FibreLength { get { return vars["fibrelength"]; } set {
vars["fibrelength"] = value; } }
            public double MolarWeight { get { return vars["molarweight"]; } set {
vars["molarweight"] = value; } }
            public double DipoleMoment { get { return vars["dipolemoment"]; } set {
vars["dipolemoment"] = value; } }

            // Velocity integration range
            public double MinimumVelocity;
            public double MaximumVelocity;
            public int VelocitySteps;

            // Coupling
            public double CouplingRabiFrequency;
            public double CouplingDetuning;
            public double CouplingWavelength;

            // Probe
            public double ProbeRabiFrequency;
            public double ProbeDetuning;
            public double ProbeWavelength;

            // Most probable molcules speed
            public ExpressionClass MedianSpeed;

            // Variables
            public Variables vars;

            #endregion

            #region --- Constructor ---

            public VLEIT()
            {
                // Create new variable class + add some constants
                vars = new Variables();
                vars["c"] = 2.99792458e8;
```

```
            vars["h"] = 6.626068e-34;
            vars["hbar"] = 1.05457148e-34;
            vars["e0"] = 8.854187817e-12;
            vars["Nav"] = 6.0221367e23;
            vars["kb"] = 1.3806503e-23;
            vars["R"] = 8.314472;

            // Attach vars to each expression
            DecayL1 = new ExpressionClass("0", vars);
            DecayL2 = new ExpressionClass("0", vars);
            DecayL3 = new ExpressionClass("0", vars);
            DecayV1 = new ExpressionClass("0", vars);
            DecayV2 = new ExpressionClass("0", vars);
            DecayV3 = new ExpressionClass("0", vars);

            GainL1 = new ExpressionClass("0", vars);
            GainL2 = new ExpressionClass("0", vars);
            GainL3 = new ExpressionClass("0", vars);
            GainV1 = new ExpressionClass("0", vars);
            GainV2 = new ExpressionClass("0", vars);
            GainV3 = new ExpressionClass("0", vars);

            LossL1 = new ExpressionClass("0", vars);
            LossL2 = new ExpressionClass("0", vars);
            LossL3 = new ExpressionClass("0", vars);
            LossV1 = new ExpressionClass("0", vars);
            LossV2 = new ExpressionClass("0", vars);
            LossV3 = new ExpressionClass("0", vars);

            BranchL21 = new ExpressionClass("0.5", vars);
            BranchL23 = new ExpressionClass("0.5", vars);
            BranchL31 = new ExpressionClass("0", vars);
            BranchV12 = new ExpressionClass("0.5", vars);
            BranchV32 = new ExpressionClass("0.5", vars);
            BranchV13 = new ExpressionClass("0", vars);

            DecoherenceL12 = new ExpressionClass("0", vars);
            DecoherenceL13 = new ExpressionClass("0", vars);
            DecoherenceL23 = new ExpressionClass("0", vars);
            DecoherenceV12 = new ExpressionClass("0", vars);
            DecoherenceV13 = new ExpressionClass("0", vars);
            DecoherenceV23 = new ExpressionClass("0", vars);

            EffectiveDecay = new ExpressionClass("0", vars);

            ExchangeL13 = new ExpressionClass("0", vars);
            ExchangeV13 = new ExpressionClass("0", vars);

            // Set some required expressions
            MedianSpeed = new ExpressionClass("(2*kb*temperature*Nav/molarweight)^0.5",
vars);
        }

        #endregion

        #region --- Density matrix without detuning terms ---

        public Complex[,] CreateDensityMatrixNoDetuning(bool EnforcePopulationConservation)
        {
            // Create new 9x9 matrix
            Complex[,] DensityMatrix = new Complex[9, 9];

            //Setup complex density matrix
            DensityMatrix[0, 1] = new Complex(0, ProbeRabiFrequency / (2 * 6.28318531));
            DensityMatrix[0, 3] = new Complex(0, -ProbeRabiFrequency / (2 * 6.28318531));

            DensityMatrix[1, 0] = new Complex(0, ProbeRabiFrequency / (2 * 6.28318531));
            DensityMatrix[1, 2] = new Complex(0, CouplingRabiFrequency / (2 * 6.28318531));
            DensityMatrix[1, 4] = new Complex(0, -ProbeRabiFrequency / (2 * 6.28318531));

            DensityMatrix[2, 1] = new Complex(0, CouplingRabiFrequency / (2 * 6.28318531));
            DensityMatrix[2, 5] = new Complex(0, -ProbeRabiFrequency / (2 * 6.28318531));

            DensityMatrix[3, 0] = new Complex(0, -ProbeRabiFrequency / (2 * 6.28318531));
            DensityMatrix[3, 4] = new Complex(0, ProbeRabiFrequency / (2 * 6.28318531));
```

```
                DensityMatrix[3, 6] = new Complex(0, -CouplingRabiFrequency / (2 * 6.28318531));

                DensityMatrix[4, 1] = new Complex(0, -ProbeRabiFrequency / (2 * 6.28318531));
                DensityMatrix[4, 3] = new Complex(0, ProbeRabiFrequency / (2 * 6.28318531));
                DensityMatrix[4, 5] = new Complex(0, CouplingRabiFrequency / (2 * 6.28318531));
                DensityMatrix[4, 7] = new Complex(0, -CouplingRabiFrequency / (2 * 6.28318531));

                DensityMatrix[5, 2] = new Complex(0, -ProbeRabiFrequency / (2 * 6.28318531));
                DensityMatrix[5, 4] = new Complex(0, CouplingRabiFrequency / (2 * 6.28318531));
                DensityMatrix[5, 8] = new Complex(0, -CouplingRabiFrequency / (2 * 6.28318531));

                DensityMatrix[6, 3] = new Complex(0, -CouplingRabiFrequency / (2 * 6.28318531));
                DensityMatrix[6, 7] = new Complex(0, ProbeRabiFrequency / (2 * 6.28318531));

                DensityMatrix[7, 4] = new Complex(0, -CouplingRabiFrequency / (2 * 6.28318531));
                DensityMatrix[7, 6] = new Complex(0, ProbeRabiFrequency / (2 * 6.28318531));
                DensityMatrix[7, 8] = new Complex(0, CouplingRabiFrequency / (2 * 6.28318531));

                DensityMatrix[8, 5] = new Complex(0, -CouplingRabiFrequency / (2 * 6.28318531));
                DensityMatrix[8, 7] = new Complex(0, CouplingRabiFrequency / (2 * 6.28318531));

                // Decay & Decoherence
                switch (Scheme)
                {
                    case EITSchemes.Lambda:
                        // Decay
                        DensityMatrix[0, 0] += new Complex(-EffectiveDecay.Evaluate(), 0);
                        DensityMatrix[0, 4] += new Complex(DecayL2.Evaluate() *
BranchL21.Evaluate(), 0);
                        DensityMatrix[0, 8] += new Complex(DecayL3.Evaluate() *
BranchL31.Evaluate(), 0);
                        DensityMatrix[4, 4] += new Complex(-DecayL2.Evaluate() -
EffectiveDecay.Evaluate(), 0);
                        DensityMatrix[8, 4] += new Complex(DecayL2.Evaluate() *
BranchL23.Evaluate(), 0);
                        DensityMatrix[8, 8] += new Complex(-DecayL3.Evaluate() -
EffectiveDecay.Evaluate(), 0);

                        // Exchange
                        DensityMatrix[0, 0] += new Complex(-ExchangeL13.Evaluate(), 0);
                        DensityMatrix[0, 8] += new Complex(ExchangeL13.Evaluate(), 0);
                        DensityMatrix[8, 0] += new Complex(ExchangeL13.Evaluate(), 0);
                        DensityMatrix[8, 8] += new Complex(-ExchangeL13.Evaluate(), 0);

                        // Decoherence
                        DensityMatrix[3, 3] += new Complex(-DecoherenceL12.Evaluate() -
EffectiveDecay.Evaluate(), 0);
                        DensityMatrix[6, 6] += new Complex(-DecoherenceL13.Evaluate() -
EffectiveDecay.Evaluate(), 0);
                        DensityMatrix[1, 1] += new Complex(-DecoherenceL12.Evaluate() -
EffectiveDecay.Evaluate(), 0);
                        DensityMatrix[7, 7] += new Complex(-DecoherenceL23.Evaluate() -
EffectiveDecay.Evaluate(), 0);
                        DensityMatrix[2, 2] += new Complex(-DecoherenceL13.Evaluate() -
EffectiveDecay.Evaluate(), 0);
                        DensityMatrix[5, 5] += new Complex(-DecoherenceL23.Evaluate() -
EffectiveDecay.Evaluate(), 0);

                        // Loss
                        if (OpenSystem)
                        {
                            DensityMatrix[0, 0] -= new Complex(LossL1.Evaluate(), 0);
                            DensityMatrix[4, 4] -= new Complex(LossL2.Evaluate(), 0);
                            DensityMatrix[8, 8] -= new Complex(LossL3.Evaluate(), 0);
                        }
                        break;

                    case EITSchemes.V:
                        // Decay
                        DensityMatrix[0, 0] += new Complex(-DecayV1.Evaluate() -
EffectiveDecay.Evaluate(), 0);
                        DensityMatrix[4, 0] += new Complex(DecayV1.Evaluate() *
BranchV12.Evaluate(), 0);
                        DensityMatrix[4, 4] += new Complex(-EffectiveDecay.Evaluate(), 0);
```

```
                        DensityMatrix[4, 8] += new Complex(DecayV3.Evaluate() *
BranchV32.Evaluate(), 0);
                        DensityMatrix[8, 0] += new Complex(DecayV1.Evaluate() *
BranchV13.Evaluate(), 0);
                        DensityMatrix[8, 8] += new Complex(-DecayV3.Evaluate() -
EffectiveDecay.Evaluate(), 0);

                        // Exchange
                        DensityMatrix[0, 0] += new Complex(-ExchangeV13.Evaluate(), 0);
                        DensityMatrix[0, 8] += new Complex(ExchangeV13.Evaluate(), 0);
                        DensityMatrix[8, 0] += new Complex(ExchangeV13.Evaluate(), 0);
                        DensityMatrix[8, 8] += new Complex(-ExchangeV13.Evaluate(), 0);

                        // Decoherence
                        DensityMatrix[3, 3] += new Complex(-DecoherenceV12.Evaluate() -
EffectiveDecay.Evaluate(), 0);
                        DensityMatrix[6, 6] += new Complex(-DecoherenceV13.Evaluate() -
EffectiveDecay.Evaluate(), 0);
                        DensityMatrix[1, 1] += new Complex(-DecoherenceV12.Evaluate() -
EffectiveDecay.Evaluate(), 0);
                        DensityMatrix[7, 7] += new Complex(-DecoherenceV23.Evaluate() -
EffectiveDecay.Evaluate(), 0);
                        DensityMatrix[2, 2] += new Complex(-DecoherenceV13.Evaluate() -
EffectiveDecay.Evaluate(), 0);
                        DensityMatrix[5, 5] += new Complex(-DecoherenceV23.Evaluate() -
EffectiveDecay.Evaluate(), 0);

                        // Loss
                        if (OpenSystem)
                        {
                            DensityMatrix[0, 0] -= new Complex(LossV1.Evaluate(), 0);
                            DensityMatrix[4, 4] -= new Complex(LossV2.Evaluate(), 0);
                            DensityMatrix[8, 8] -= new Complex(LossV3.Evaluate(), 0);
                        }
                        break;
                }

                // Population conservation for closed system (overwrites redundant equation
since p11+p22+p33=constant)
                if (EnforcePopulationConservation)
                {
                    DensityMatrix[8, 0] = new Complex(1, 0);
                    DensityMatrix[8, 1] = new Complex(0, 0);
                    DensityMatrix[8, 2] = new Complex(0, 0);
                    DensityMatrix[8, 3] = new Complex(0, 0);
                    DensityMatrix[8, 4] = new Complex(1, 0);
                    DensityMatrix[8, 5] = new Complex(0, 0);
                    DensityMatrix[8, 6] = new Complex(0, 0);
                    DensityMatrix[8, 7] = new Complex(0, 0);
                    DensityMatrix[8, 8] = new Complex(1, 0);
                }

                return DensityMatrix;
            }

            #endregion

            #region --- Susceptibility calculation ---

            public class SuscResult
            {
                public double SusRe;
                public double SusIm;
                public SuscResult(double re, double im) { SusRe = re; SusIm = im; }
            }

            public SuscResult Susceptibility()
            {
                // Create density matrix with constant values
                Complex[,] DM_NoDetuning = CreateDensityMatrixNoDetuning(!OpenSystem);

                // Calc velocity interval for integration
                double velocityinterval = (MaximumVelocity - MinimumVelocity) / (VelocitySteps -
1);
```

```
                // Temporary variables
                double DelC, DelP = 0;

                // Velocity sign
                double VelSign = 0;
                switch (Direction)
                {
                    case EITDirections.Copropagating: VelSign = -1; break;
                    case EITDirections.Counterpropagating: VelSign = 1; break;
                }

                // Scheme sign
                double SchSign = 0;
                switch (Scheme)
                {
                    case EITSchemes.V: SchSign = -1; break;
                    case EITSchemes.Lambda: SchSign = 1; break;
                }

                // Steady state vector (rhodot+gain=0 => ss=-gain)
                Complex[] DensityVector = new Complex[9];

                if (OpenSystem)
                {
                    // Include gain
                    switch (Scheme)
                    {
                        case EITSchemes.Lambda:
                            DensityVector[0] -= new Complex(GainL1.Evaluate(), 0);
                            DensityVector[4] -= new Complex(GainL2.Evaluate(), 0);
                            DensityVector[8] -= new Complex(GainL3.Evaluate(), 0);
                            break;
                        case EITSchemes.V:
                            DensityVector[0] -= new Complex(GainV1.Evaluate(), 0);
                            DensityVector[4] -= new Complex(GainV2.Evaluate(), 0);
                            DensityVector[8] -= new Complex(GainV3.Evaluate(), 0);
                            break;
                    }
                }
                else
                {
                    // Enforce constant total population
                    DensityVector[8] = new Complex(1, 0);
                }

                // Vector for solution (Ax=B)
                Complex[] Solution;

                // Current velocity
                double velocity = 0;

                // Full density matrix
                Complex[,] DM;

                // Store total probe density
                Complex rho12 = new Complex(0, 0);

                // Calculate most prob speed
                double u = MedianSpeed.Evaluate();

                // Integrate over velocity distribution
                for (int Step = 0; Step < VelocitySteps; Step++)
                {
                    velocity = MinimumVelocity + Step * (MaximumVelocity - MinimumVelocity) /
(VelocitySteps - 1);

                    // Calculate probe/coupling detuning including Doppler shifts
                    DelP = SchSign * (ProbeDetuning - velocity / ProbeWavelength);
                    DelC = SchSign * (CouplingDetuning + (VelSign * velocity) /
CouplingWavelength);

                    // Copy 'no-detuning' matrix
                    DM = (Complex[,])DM_NoDetuning.Clone();

                    // Detunings
```

```
                    DM[1, 1] += new Complex(0, DelP);
                    DM[2, 2] += new Complex(0, DelP - DelC);
                    DM[3, 3] += new Complex(0, -DelP);
                    DM[5, 5] += new Complex(0, -DelC);
                    DM[6, 6] += new Complex(0, DelC - DelP);
                    DM[7, 7] += new Complex(0, DelC);

                    Solution = new Complex[9];
                    NAG.F04ADF(ref DM, ref DensityVector, ref Solution); // Solve Ax=B

                    // Add susceptibility (weighted by normalised Maxwell-Boltzmann distributon)
                    rho12 += SchSign * Solution[1] * velocityinterval * Math.Exp(-
Math.Pow(velocity, 2) / Math.Pow(u, 2)) / (u * Math.Pow(Math.PI, 0.5));
                }

                // Transform to susceptibility (lab book P26)
                Complex chi12 = -rho12 * ((Math.Pow(DipoleMoment, 2) * (Pressure / (1.3806503e-
23 * Temperature))) / (0.5 * 8.85418782e-12 * ProbeRabiFrequency * 1.05457148e-34));

                // Return susceptibiliy
                return new SuscResult(chi12.Re, -Math.Abs(chi12.Im));
            }

            #endregion

            #region --- Transparency shape calculation ---

            public class EITShape { public double VisibleHeight; public double VisibleWidth;
public double SuppressedAbsorption; }

            private double HalfHeight = 0;

            public EITShape Shape(double AbsoluteAccuracy)
            {
                EITShape Shape = new EITShape();

                double tempp = ProbeDetuning;
                ProbeDetuning = 0;
                double OnResonanceAbs = Susceptibility().SusIm;
                double tempc = CouplingRabiFrequency;
                CouplingRabiFrequency = 0;
                double OnResonanceAbsNoCoupling = Susceptibility().SusIm;
                CouplingRabiFrequency = tempc;
                Shape.SuppressedAbsorption = 100.0 * (OnResonanceAbs - OnResonanceAbsNoCoupling)
/ (1 - OnResonanceAbsNoCoupling);

                double e1 = 1e-11;
                double e2 = AbsoluteAccuracy;
                double a = 0;
                double b = 200e6;
                int maxcal = 100;
                double x = 0;
                double f = 0;
                int ifail = 1;
                NAG.E04ABF(new NAG.E04ABF_Function_Delegate(E04ABF_Function_Height), ref e1, ref
e2, ref a, ref b, ref maxcal, ref x, ref  f, ref ifail);
                //if (ifail != 0) MessageBox.Show("ifail=" + ifail.ToString() + " in height
calculation.");
                Shape.VisibleHeight = 100 * (OnResonanceAbs - f) / (0 - f);

                e1 = 1e-11;
                e2 = AbsoluteAccuracy;
                a = 0;
                b = x;
                maxcal = 100;
                ifail = 1;
                HalfHeight = (OnResonanceAbs + f) / 2;
                NAG.E04ABF(new NAG.E04ABF_Function_Delegate(E04ABF_Function_Width), ref e1, ref
e2, ref a, ref b, ref maxcal, ref x, ref  f, ref ifail);
                //if (ifail != 0) MessageBox.Show("ifail=" + ifail.ToString() + " in width
calculation.");
                Shape.VisibleWidth = 2 * x;

                ProbeDetuning = tempp;
                return Shape;
```

```
            }

            public void E04ABF_Function_Height(ref double xc, ref double fc)
            {
                ProbeDetuning = xc;
                fc = Susceptibility().SusIm;
            }

            public void E04ABF_Function_Width(ref double xc, ref double fc)
            {
                ProbeDetuning = xc;
                fc = Math.Abs(Susceptibility().SusIm - HalfHeight);
            }

            #endregion

        }

    }

}
```

B.2 Fitting Routine

```
using System;
using System.Collections.Generic;
using System.ComponentModel;
using System.Data;
using System.Drawing;
using System.Text;
using System.Windows.Forms;
using System.IO;
using Paraxial;
using System.Runtime.InteropServices;

namespace DensityMatrixEIT
{
    public partial class FitWindow : Form
    {
        public FitWindow()
        {
            InitializeComponent();
        }

        private EITIO.EITFit FitEIT;

        private List<ExperimentalPoint> ExperimentalPoints;

        double[] InitialFitValues;

        StreamWriter outfile;

        //TODO: Provide an EIT stucture with the constant values to use
        public void RunFit(EITIO.EITFit e,string pointsfile)
        {
            FitEIT = e;

            List<double> ExpLCoHX = new List<double>();
            List<double> ExpLCoHY = new List<double>();
            List<double> ExpLCoWX = new List<double>();
            List<double> ExpLCoWY = new List<double>();
            List<double> ExpVCoHX = new List<double>();
            List<double> ExpVCoHY = new List<double>();
            List<double> ExpVCoWX = new List<double>();
            List<double> ExpVCoWY = new List<double>();
            List<double> ExpLCounterHX = new List<double>();
            List<double> ExpLCounterHY = new List<double>();
            List<double> ExpVCounterHX = new List<double>();
            List<double> ExpVCounterHY = new List<double>();

            // Load fit points
            // File format: Scheme,Direction,Rabi,W/H,Value,Weight
            ExperimentalPoints = new List<ExperimentalPoint>();
            StreamReader infile = new StreamReader(pointsfile);
            do
            {
                ExperimentalPoint NewPoint = new ExperimentalPoint();
                string[] NewPointStr = infile.ReadLine().Split(',');
                if (NewPointStr[0].ToLower() == "v") { NewPoint.Scheme =
ExperimentalPoint.Schemes.V; } else { NewPoint.Scheme = ExperimentalPoint.Schemes.L; }
                if (NewPointStr[1].ToLower() == "co") { NewPoint.Direction =
ExperimentalPoint.Directions.Co; } else { NewPoint.Direction =
ExperimentalPoint.Directions.Counter; }
                NewPoint.CouplingRabiFrequency = 1e6 * double.Parse(NewPointStr[2]);
                if (NewPointStr[3].ToLower() == "width") { NewPoint.Type =
ExperimentalPoint.Types.Width; } else
                NewPoint.Value = double.Parse(NewPointStr[4]);
                NewPoint.Weight = double.Parse(NewPointStr[5]);
                ExperimentalPoints.Add(NewPoint);
                if (NewPoint.Type == ExperimentalPoint.Types.Height && NewPoint.Scheme ==
ExperimentalPoint.Schemes.L && NewPoint.Direction == ExperimentalPoint.Directions.Co)
                {
                    ExpLCoHX.Add(NewPoint.CouplingRabiFrequency / 1e6);
                    ExpLCoHY.Add(NewPoint.Value);
                }
```

```
                if (NewPoint.Type == ExperimentalPoint.Types.Height && NewPoint.Scheme ==
ExperimentalPoint.Schemes.V && NewPoint.Direction == ExperimentalPoint.Directions.Co)
                {
                    ExpVCoHX.Add(NewPoint.CouplingRabiFrequency / 1e6);
                    ExpVCoHY.Add(NewPoint.Value);
                }
                if (NewPoint.Type == ExperimentalPoint.Types.Width && NewPoint.Scheme ==
ExperimentalPoint.Schemes.L && NewPoint.Direction == ExperimentalPoint.Directions.Co)
                {
                    ExpLCoWX.Add(NewPoint.CouplingRabiFrequency / 1e6);
                    ExpLCoWY.Add(NewPoint.Value);
                }
                if (NewPoint.Type == ExperimentalPoint.Types.Width && NewPoint.Scheme ==
ExperimentalPoint.Schemes.V && NewPoint.Direction == ExperimentalPoint.Directions.Co)
                {
                    ExpVCoWX.Add(NewPoint.CouplingRabiFrequency / 1e6);
                    ExpVCoWY.Add(NewPoint.Value);
                }
                if (NewPoint.Type == ExperimentalPoint.Types.Height && NewPoint.Scheme ==
ExperimentalPoint.Schemes.V && NewPoint.Direction == ExperimentalPoint.Directions.Counter)
                {
                    ExpVCounterHX.Add(NewPoint.CouplingRabiFrequency / 1e6);
                    ExpVCounterHY.Add(NewPoint.Value);
                }
                if (NewPoint.Type == ExperimentalPoint.Types.Height && NewPoint.Scheme ==
ExperimentalPoint.Schemes.L && NewPoint.Direction == ExperimentalPoint.Directions.Counter)
                {
                    ExpLCounterHX.Add(NewPoint.CouplingRabiFrequency / 1e6);
                    ExpLCounterHY.Add(NewPoint.Value);
                }
            } while (!infile.EndOfStream);

            label1.Text = "Fitting to " + ExperimentalPoints.Count.ToString() + " experimental
points.";

            // Set initial fit parameters
            InitialFitValues = (double[])FitEIT.FitValues.Clone();

            // Create log file
            string file = pointsfile.Substring(pointsfile.LastIndexOf('\\')+1,
pointsfile.LastIndexOf('.') - pointsfile.LastIndexOf('\\') - 1);
            outfile = new StreamWriter(pointsfile.Substring(0,3) + DateTime.Now.Ticks.ToString()
+ ".csv");
            foreach (string str in FitEIT.ParaRecord) outfile.WriteLine(str);
            outfile.AutoFlush = true;
            outfile.Write("#");
            foreach (string st in FitEIT.FitParameters) outfile.Write("," + st);
            outfile.WriteLine(",Sum(Res^2)");

            // Do fitting in a new thread
            System.Threading.Thread FitThread = new System.Threading.Thread(FitScript);
            FitThread.Start();
        }

        private void FitScript()
        {
            int ifail = 0;

            // Call NAG fitting routine
            if (FitEIT.LowerBounds.Length > 0)
            {
                // Use bounds
                double[] x = new double[InitialFitValues.Length];
                double[] ub = new double[InitialFitValues.Length];
                double[] lb = new double[InitialFitValues.Length];

                for (int i = 0; i < x.Length; i++)
                {
                    x[i] = 1;
                    ub[i] = FitEIT.UpperBounds[i] / InitialFitValues[i];
                    lb[i] = FitEIT.LowerBounds[i] / InitialFitValues[i];
                }


                //E04UCF
```

```
                NAG.E04UEF("NoList *Disable output");
                NAG.E04UEF("Derivative Level 0 *No derivatives");
                NAG.E04UEF("Major Print Level 0 *No info");
                NAG.E04UEF("Minor Print Level 0 *No info");
                NAG.E04UEF("Function Precision 0.00000001 *Total residual precision");
                ifail = NAG.E04UCF(x, lb, ub, new
NAG.E04UCF_ObjectFunct_Delegate(CalculateResidualE04UCF));

                //Add results to listview
                AddToListView(new string[] { "" });
                List<string> subitems = new List<string>();
                subitems.Add("");
                for (int i = 0; i < x.Length; i++) subitems.Add((x[i] *
InitialFitValues[i]).ToString("f10"));
                subitems.Add("(ifail=" + ifail.ToString() + ")");
                AddToListViewBold(subitems.ToArray());
            }
            else
            {
                // No bounds

                // Array for NAG fit values (all set to 1 initally, since scaled by true initial
value in calculation)
                double[] x = new double[InitialFitValues.Length];
                for (int i = 0; i < x.Length; i++) x[i] = 1;

                ifail = NAG.E04FCF(ref x, ExperimentalPoints.Count, 2000, 0.5, 1e-4, 100000,
                    new NAG.E04FCF_Function_Delegate(CalculateResidualE04FCF), new
NAG.E04FCF_Monitor_Delegate(MonitorE04FCF));

                //Add results to listview
                AddToListView(new string[] { "" });
                List<string> subitems = new List<string>();
                subitems.Add("");
                for (int i = 0; i < x.Length; i++) subitems.Add(x[i].ToString("f10"));
                subitems.Add("(ifail=" + ifail.ToString() + ")");
                AddToListViewBold(subitems.ToArray());
            }

            // Close file
            System.Threading.Thread.Sleep(1000);
            outfile.Close();
        }

        private class ExperimentalPoint
        {
            public enum Schemes { V, L }
            public enum Directions { Co, Counter }
            public enum Types { Height, Width }
            public Schemes Scheme;
            public Directions Direction;
            public Types Type;
            public double Value;
            public double CouplingRabiFrequency;
            public double Weight = 1;

            public ExperimentalPoint() { }

            public ExperimentalPoint(Schemes s, Directions d, double rabi, Types t, double v,
double w)
            {
                Scheme = s;
                Direction = d;
                CouplingRabiFrequency = rabi;
                Type = t;
                Value = v;
                Weight = w;
            }
        }

        public void MonitorE04FCF(ref int m, ref int n, IntPtr xc, IntPtr fvecc, IntPtr fjacc,
            ref int ljc, IntPtr s, ref int igrade, ref int niter, ref int nf, IntPtr iw, ref int
liw, IntPtr w, ref int lw)
        {
            double SumResSq = 0;
```

```
            double[] Res = new double[m];
            Marshal.Copy(fvecc, Res, 0, m);
            for (int i = 0; i < Res.Length; i++) SumResSq += Math.Pow(Res[i], 2);
            List<string> Subitems = new List<string>();
            Subitems.Add(niter.ToString());
            for (int i = 0; i < InitialFitValues.Length; i++) Subitems.Add("");
            Subitems.Add(SumResSq.ToString("f10"));
            AddToListViewBold(Subitems.ToArray());
        }

        public void CalculateResidualE04JYF(ref int n, IntPtr pVariables, ref double result,
IntPtr iuser, IntPtr ruser)
        {
            //Create array of variables to use
            double[] NAGValues = new double[n];
            Marshal.Copy(pVariables, NAGValues, 0, n);

            result = CalculateResidual(CalculateResiduals(NAGValues));
        }

        public void CalculateResidualE04UCF(ref int mode, ref int n, IntPtr pVariables, ref
double result, IntPtr objgrd,
            ref int nstate, IntPtr iuser, IntPtr ruser)
        {
            if (mode != 1)
            {
                Count++;

                //Create array of variables to use
                double[] NAGValues = new double[n];
                Marshal.Copy(pVariables, NAGValues, 0, n);

                //Add parameters to log
                List<string> subitems = new List<string>();
                subitems.Add(Count.ToString());
                for (int i = 0; i < NAGValues.Length; i++) subitems.Add((NAGValues[i] *
InitialFitValues[i]).ToString("f10"));
                subitems.Add("(Calculating...)");
                AddToListView(subitems.ToArray());

                result = CalculateResidual(CalculateResiduals(NAGValues));

                //Add total residual to log
                UpdateListView(result.ToString("f10"));

                if (RequestStop) mode = -1;
            }
        }

        int Count = 0;

        public void CalculateResidualE04FCF(ref int iflag, ref int m, ref int n, IntPtr
pVariables, IntPtr fvecc,
            IntPtr iw, ref int liw, IntPtr w, ref int lw)
        {
            //Increase count
            Count++;

            //Create array of variables to use
            double[] NAGValues = new double[n];
            Marshal.Copy(pVariables, NAGValues, 0, n);

            //Add parameters to log
            List<string> subitems = new List<string>();
            subitems.Add(Count.ToString());
            for (int i = 0; i < NAGValues.Length; i++) subitems.Add((NAGValues[i] *
InitialFitValues[i]).ToString("f10"));
            subitems.Add("(Calculating...)");
            AddToListView(subitems.ToArray());

            //Calculate residuals
            double[] Residuals = CalculateResiduals(NAGValues);

            //Copy managed array to memory location
            Marshal.Copy(Residuals, 0, fvecc, Residuals.Length);
```

```
            //Add total residual to log
            UpdateListView(CalculateResidual(Residuals).ToString("f10"));

            //Set iflag negative if stop request to terminate NAG routine
            if (RequestStop) iflag = -1;
        }

        public double CalculateResidual(double[] Residuals)
        {
            double TotalResidual = 0;
            foreach (double res in Residuals) TotalResidual += Math.Pow(res, 2);
            return TotalResidual;
        }

        public double[] CalculateResiduals(double[] Parameters)
        {
            double[] residuals = new double[ExperimentalPoints.Count];

            // Calculate residual
            int PointNumber = 0;
            foreach (ExperimentalPoint P in ExperimentalPoints)
            {
                if (P.Direction == ExperimentalPoint.Directions.Co) FitEIT.EIT.Direction =
Paraxial.MathLibrary.VLEIT.EITDirections.Copropagating;
                if (P.Direction == ExperimentalPoint.Directions.Counter) FitEIT.EIT.Direction =
Paraxial.MathLibrary.VLEIT.EITDirections.Counterpropagating;
                if (P.Scheme == ExperimentalPoint.Schemes.L) FitEIT.EIT.Scheme =
MathLibrary.VLEIT.EITSchemes.Lambda;
                if (P.Scheme == ExperimentalPoint.Schemes.V) FitEIT.EIT.Scheme =
MathLibrary.VLEIT.EITSchemes.V;
                FitEIT.EIT.CouplingRabiFrequency = P.CouplingRabiFrequency *
FitEIT.EIT.vars["RabiScaling"];

                SetEITParameters(Parameters);

                // Calc visible height/width
                Paraxial.MathLibrary.VLEIT.EITShape Shape = FitEIT.EIT.Shape(1e-3);

                // Calc. residual and add to result
                // Absolute
                if (P.Type == ExperimentalPoint.Types.Height) residuals[PointNumber] = P.Weight
* (Shape.VisibleHeight - P.Value);
                if (P.Type == ExperimentalPoint.Types.Width) residuals[PointNumber] = P.Weight *
((Shape.VisibleWidth / 1e6) - P.Value);

                PointNumber++;
                UpdateProgress(PointNumber);
            }

            return residuals;
        }

        public double[] CalculateValues(double[] Parameters)
        {
            double[] values = new double[ExperimentalPoints.Count];

            // Calculate residual
            int PointNumber = 0;
            foreach (ExperimentalPoint P in ExperimentalPoints)
            {
                if (P.Direction == ExperimentalPoint.Directions.Co) FitEIT.EIT.Direction =
Paraxial.MathLibrary.VLEIT.EITDirections.Copropagating;
                if (P.Direction == ExperimentalPoint.Directions.Counter) FitEIT.EIT.Direction =
Paraxial.MathLibrary.VLEIT.EITDirections.Counterpropagating;
                if (P.Scheme == ExperimentalPoint.Schemes.L) FitEIT.EIT.Scheme =
MathLibrary.VLEIT.EITSchemes.Lambda;
                if (P.Scheme == ExperimentalPoint.Schemes.V) FitEIT.EIT.Scheme =
MathLibrary.VLEIT.EITSchemes.V;
                FitEIT.EIT.CouplingRabiFrequency = P.CouplingRabiFrequency *
FitEIT.EIT.vars["RabiScaling"];

                SetEITParametersUnscaled(Parameters);

                // Calc visible height/width
```

```
                Paraxial.MathLibrary.VLEIT.EITShape Shape = FitEIT.EIT.Shape(1e-3);

                if (P.Type == ExperimentalPoint.Types.Height) values[PointNumber]
=Shape.VisibleHeight;
                if (P.Type == ExperimentalPoint.Types.Width) values[PointNumber] =
Shape.VisibleWidth / 1e6;

                PointNumber++;
                UpdateProgress(PointNumber);
            }

            return values;
        }

        private void SetEITParameters(double[] Parameters)
        {
            for (int para = 0; para < FitEIT.FitParameters.Length; para++)
                FitEIT.EIT.vars[FitEIT.FitParameters[para]] = Parameters[para] *
InitialFitValues[para];
        }

    }

}
```

Publications

Journal Papers

Y. Wang, P. S. LIGHT and F. Benabid, "Core-surround Shaping of Hollow-Core Photonic Crystal Fiber via HF Etching," Photonics Technol. Lett. **20** (2008) 1018-1020.

F. Couny, F. Benabid and P. S. LIGHT, "Subwatt threshold cw raman fiber-gas laser based on H-2-filled hollow-core photonic crystal fiber," Phys. Rev. Lett. **99** (2007) 143903

F. Couny, F. Benabid, P. J. Roberts, P. S. LIGHT and M. G. Raymer, "Generation and photonic guidance of multi-octave optical-frequency combs," Science **318** (2007) 1118-1121

F. Couny, F. Benabid and P. S. LIGHT, "Reduction of fresnel back-reflection at splice interface between hollow core PCF and single-mode fiber," IEEE Photonics Technol. Lett. **19** (2007) 1020-1022

P. S. LIGHT, F. Benabid, M. Maric, A. N. Luiten and F. Couny, "Electromagnetically induced transparency in Rb-filled coated hollow-core photonic crystal fiber," Opt. Lett. **32** (2007) 1323-1325

F. Couny, F. Benabid and P. S. LIGHT, "Large-pitch kagome-structured hollow-core photonic crystal fiber," Opt. Lett. **31** (2006) 3574-3576

P. S. LIGHT, F. Couny and F. Benabid, "Low optical insertion-loss and vacuum-pressure all-fiber acetylene cell based on hollow-core photonic crystal fiber," Opt. Lett. **31** (2006) 2538-2540

F. Couny, P. S. LIGHT and F. Benabid, "Electromagnetically induced transparency and saturable absorption in all-fiber devices based on $^{12}C_2H_2$-filled hollow-core photonic crystal fiber," Opt. Commun. **263** (2006) 28-31

F. Benabid, P. S. LIGHT, F. Couny, and P. St. J. Russell, "Electromagnetically-induced transparency grid in acetylene-filled hollow-core PCF," Opt. Express **13** (2005) 5694-4087

Conference Papers

P. S. LIGHT, P. J. Roberts, P. Mirault and F. Benabid, "Observation of Anti-Crossing Events via Mode-Pattern Rotation in HC-PCF," Conference on Lasers and Electro-optics (CLEO) 2008, Paper CThEE3

P. S. LIGHT, F. Benabid, M. Maric, A. N. Luiten and F Couny, "Electromagnetically Induced Transparency in Rubidium-Filled Kagome HC-PCF," Conference on Lasers and Electro-optics (CLEO) 2008, Paper QThB7

N. V. Wilding, P. S. LIGHT, F. Couny and F. Benabid, "Experimental Comparison of Electromagnetic Induced Transparency in Acetylene-Filled Kagome and Triangular Lattice Hollow Core Photonic Crystal Fiber," Conference on Lasers and Electro-optics (CLEO) 2008, Paper JFA3

F. Benabid, P. S. LIGHT and F. Couny, "Quantum Coherent Effects with Hollow-Core Photonic Crystal Fibers," Conference on Lasers and Electro-optics (CLEO) 2008, Paper JFE1

Y. Wang, P. S. LIGHT and F. Benabid, "Core-Surround Shaping of Hollow Core Photonic Crystal Fiber via Fiber Etching," Conference on Lasers and Electro-optics (CLEO) 2008, Paper JFE2

G. Humbert, Y. Wang, P. S. LIGHT, F. Benabid, and P. J. Roberts, "Nonlinear Effects in a Silica-Node of a Hollow-Core Photonic Crystal Fiber within the Photonic Bandgap," Conference on Lasers and Electro-optics (CLEO) 2008, Paper JTuA79

F. Couny, F. Benabid and P. S. LIGHT, "Sub-Watt Threshold CW Raman Fiber-Gas-Laser Based on H2-Filled Hollow-Core Photonic Crystal Fiber," Conference on Lasers and Electro-optics (CLEO) 2008, Paper CTuL4

K. Knabe, A. Jones, K. L. Corwin, F. Couny, P. S. LIGHT and F. Benabid, "Saturated Absorption Spectroscopy of C2H2 inside a Hollow, Large-Core Kagome Photonic Crystal Fiber," Conference on Lasers and Electro-optics (CLEO) 2008, Paper JFA5

P. J. Roberts, F. Benabid, F. Couny and P. S. LIGHT, "Dispersion Properties of "Kagome" Hollow-Core Fibers," Conference on Lasers and Electro-optics (CLEO) 2008, Paper JFG2

F. Couny, F. Benabid, P. J. Roberts, P. S. LIGHT, M. G. Raymer, "Generation of Multi-Octave Optical-Frequency Combs in a Kagome Lattice Hollow Core Photonic Crystal Fiber," Conference on Lasers and Electro-optics (CLEO) 2008, Paper JFC2

B. Beaudou, F. Couny, Y. Wang, P. S. LIGHT and F. Benabid, "Tapered Hollow-Core Photonic Crystal Fiber for Cascaded Stimulated-Raman-Scattering," Conference on Lasers and Electro-optics (CLEO) 2008, Paper JFC5

F. Couny, F. Benabid and P. S. Light, "Sub-Watt Threshold CW Raman Fiber-Gas-Laser Based on H2-Filled HC-PCF," 33rd European Conference and Exhibition on Optical Communication (ECOC) 2007, Post-deadline Paper

F. Benabid, P. S. LIGHT and F. Couny, "Low insertion-loss (1.8 dB) and vacuum-pressure all-fiber gas cell based on hollow-core PCF," CLEO/Europe-IQEC 2007, Paper CH-3-MON

P. S. LIGHT, F. Benabid, M. Maric, A. N. Luiten and F. Couny, "Electromagnetically induced transparency in Rubidium-Filled HC-PCF," CLEO/Europe-IQEC 2007, Paper CK9-3-WED

F. Couny, F. Benabid and P. S. LIGHT, "Large pitch kagome-structured hollow-core PCF," CLEO/Europe-IQEC 2007, Paper CE5-1-WED

C. R. Locke, T. M. Fortier, J. J. McFerran, P. S. LIGHT, F. Benabid, E. N. Ivanov and A. N. Luiten, "High-bandwidth frequency stabilization of a fibre-laser frequency comb," Frequency Control Symposium, 2007

P. S. LIGHT, F. Couny and F. Benabid, "Low Insertion-Loss (1.8 dB) and Vacuum-Pressure All-Fiber Acetylene Cell Based on Hollow-Core PCF," Conference on Lasers and Electro-optics (CLEO) 2007, Paper CThKK4

P. S. LIGHT, F. Benabid, F. Couny, G. J. Pearce and D. M. Bird, "EIT with Counter Propagating Probe-Coupling Beams in Acetylene Filled HC-PCF," Conference on Lasers and Electro-optics (CLEO) 2007, Paper QMC7

P. S. LIGHT, F. Benabid, F. Couny, G. J. Pearce and D. M. Bird, "Experimental Study Comparing EIT in V and Λ Schemes in Acetylene-Filled HC-PCF," Conference on Lasers and Electro-optics (CLEO) 2007, Paper CMI2

F. Couny, F. Benabid and P. S. LIGHT, "Control of the Transient Regime of Stimulated Raman Scattering in Hollow-Core Photonic Crystal Fiber," Conference on Lasers and Electro-optics (CLEO) 2007, Paper CWO1

F. Couny, F. Benabid and P. S. LIGHT, "Large Pitch Kagome-Structured Hollow-Core PCF," Conference on Lasers and Electro-optics (CLEO) 2007, Paper CWF1

F. Couny, F. Benabid, P. J. Roberts and P. S. LIGHT, "Fresnel Zone Imaging of Bloch-Modes from a Hollow-Core Photonic Crystal Fiber Cladding," Conference on Lasers and Electro-optics (CLEO) 2007, Paper CWF5

F. Couny, F. Benabid and P. S. Light, "Large Pitch Kagome-Structured Hollow-Core PCF," 32nd European Conference and Exhibition on Optical Communication (ECOC) 2006, Post-deadline Paper

P. S. LIGHT, F. Couny and F. Benabid, "EIT Decoherence Sources in Acetylene-Filled Hollow-Core PCF," Conference on Lasers and Electro-optics (CLEO) 2006, Paper CMO6

F. Couny, P. S. LIGHT and F. Benabid, "Electromagnetically-Induced Transparency and Saturable Absorption in All-Fiber Devices Based on Acetylene-Filled Hollow-Core PCF," Conference on Lasers and Electro-optics (CLEO) 2006, Paper CTuK7

P. S. LIGHT, F. Couny, F. Benabid and P. St. J. Russell, "Electromagnetically-Induced Transparency and Saturable Absorption in All-Fiber Devices Based on Acetylene-Filled Hollow-Core PCF," 31st European Conference and Exhibition on Optical Communication (ECOC) 2005, Post-deadline Paper

Conference Posters

F. Benabid, P. S. LIGHT and F. Couny, "Low insertion-loss (1.8 dB) and vacuum-pressure all-fiber gas cell based on hollow-core PCF," CLEO/Europe-IQEC 2007, Paper CH-3-MON

W. Zhong, C. Marquardt, G. Leuchs, U. L. Andersen, P. S. LIGHT, F. Couny and F. Benabid, "Squeezing by self induced transparency in Rb filled hollow core fibers," CLEO/Europe-IQEC 2007, Paper IA-4-MON

References

[1] K. Tsujikawa, K. Tajima, and H. Zhou, *"Intrinsic Loss of Optical Fibers,"* Optical Fiber Tech. **11** (2005) 319-331.

[2] E. A. J. Marcatili, and R. A. Schmetzer, *"Hollow Metallic and Dielectric Waveguides for Long Distance Optical Transmission and Lasers,"* Bell Syst. Tech. J. **43** (1964) 1783.

[3] P. Yeh, A. Yariv, and C. S. Hong, *"Electromagnetic Propagation in Periodic Stratified Media .1. General Theory,"* J. Opt. Soc. Am. **67** (1977) 423-438.

[4] P. Yeh, *Optical Waves in Layered Media* (Wiley-Interscience, Hoboken, N.J., 1998).

[5] P. Yeh, A. Yariv, and E. Marom, *"Theory of Bragg Fiber,"* J. Opt. Soc. Am. **68** (1978) 1196-1201.

[6] Y. Fink, D. J. Ripin, S. H. Fan *et al.*, *"Guiding Optical Light in Air Using an All-Dielectric Structure,"* J. Lightwave Tech. **17** (1999) 2039-2041.

[7] S. G. Johnson, M. Ibanescu, M. Skorobogatiy *et al.*, *"Low-Loss Asymptotically Single-Mode Propagation in Large-Core Omniguide Fibers,"* Opt. Express **9** (2001) 748-779.

[8] B. Temelkuran, S. D. Hart, G. Benoit *et al.*, *"Wavelength-Scalable Hollow Optical Fibres with Large Photonic Bandgaps for Co2 Laser Transmission,"* Nature **420** (2002) 650-653.

[9] K. Kuriki, O. Shapira, S. D. Hart *et al.*, *"Hollow Multilayer Photonic Bandgap Fibers for Nir Applications,"* Opt. Express **12** (2004) 1510-1517.

[10] P. Russell, *"Photonic Crystal Fibers,"* Science **299** (2003) 358-362.

[11] T. A. Birks, P. J. Roberts, P. S. J. Russel *et al.*, *"Full 2-D Photonic Bandgaps in Silica/Air Structures,"* Electron. Lett. **31** (1995) 1941-1943.

[12] S. John, *"Strong Localization of Photons in Certain Disordered Dielectric Superlattices,"* Phys. Rev. Lett. **58** (1987) 2486-2489.

[13] E. Yablonovitch, *"Inhibited Spontaneous Emission in Solid-State Physics and Electronics,"* Phys. Rev. Lett. **58** (1987) 2059-2062.

[14] F. Benabid, J. C. Knight, G. Antonopoulos *et al.*, *"Stimulated Raman Scattering in Hydrogen-Filled Hollow-Core Photonic Crystal Fiber,"* Science **298** (2002) 399-402.

[15] F. Benabid, and P. J. Roberts, *"Guidance Mechanisms in Hollow-Core Photonic Crystal Fiber,"* Proc. SPIE: Photonic Crystal Materials and Devices VII **6901** (2008)

[16] T. D. Hedley, *Modelling of Photonic Crystal Fibre,* (Thesis, Department of Physics, University of Bath, 2006)

[17] F. Couny, F. Benabid, P. J. Roberts *et al.*, *"Generation and Photonic Guidance of Multi-Octave Optical-Frequency Combs,"* Science **318** (2007) 1118-1121.

[18] M. A. Duguay, Y. Kokubun, T. L. Koch *et al.*, *"Antiresonant Reflecting Optical Wave-Guides in Sio2-Si Multilayer Structures,"* Appl. Phys. Lett. **49** (1986) 13-15.

[19] N. M. Litchinitser, A. K. Abeeluck, C. Headley *et al.*, *"Antiresonant Reflecting Photonic Crystal Optical Waveguides,"* Opt. Lett. **27** (2002) 1592-1594.

[20] N. M. Litchinitser, S. C. Dunn, B. Usner *et al.*, *"Resonances in Microstructured Optical Waveguides,"* Opt. Express **11** (2003) 1243-1251.

[21] T. A. Birks, G. J. Pearce, and D. M. Bird, *"Approximate Band Structure Calculation for Photonic Bandgap Fibres,"* Opt. Express **14** (2006) 9483-9490.

[22] N. W. Ashcroft, and N. D. Mermin, *Solid State Physics* (Holt, Rinehart and Winston, New York; London, 1977).

[23] A. W. Snyder, and X. H. Zheng, *"Optical Fibers of Arbitrary Cross-Sections,"* J. Opt. Soc. Am. A **3** (1986) 600-609.

[24] F. Couny, F. Benabid, P. J. Roberts *et al.*, *"Identification of Bloch-Modes in Hollow-Core Photonic Crystal Fiber Cladding,"* Opt. Express **15** (2007) 325-338.

[25] F. Couny, F. Benabid, and P. S. Light, *"Large-Pitch Kagome-Structured Hollow-Core Photonic Crystal Fiber,"* Opt. Lett. **31** (2006) 3574-3576.

[26] J. von Neumann, and W. Wigner, *"Unusual Discrete Eigenvalues,"* Phys. Z **30** (1929) 465.

[27] F. Capasso, C. Sirtori, J. Faist *et al.*, *"Observation of an Electronic Bound-State above a Potential Well,"* Nature **358** (1992) 565-567.

[28] C. M. Soukoulis, *Photonic Crystals and Light Localization in the 21st Century* (Kluwer Academic, Boston, 2001).

[29] J. C. Knight, T. A. Birks, P. S. Russell *et al.*, *"All-Silica Single-Mode Optical Fiber with Photonic Crystal Cladding,"* Opt. Lett. **21** (1996) 1547-1549.

[30] J. K. Ranka, R. S. Windeler, and A. J. Stentz, *"Visible Continuum Generation in Air-Silica Microstructure Optical Fibers with Anomalous Dispersion at 800 Nm,"* Opt. Lett. **25** (2000) 25-27.

[31] P. J. Roberts, F. Couny, H. Sabert *et al.*, *"Ultimate Low Loss of Hollow-Core Photonic Crystal Fibres,"* Opt. Express **13** (2005) 236-244.

[32] L. G. Cohen, *"Comparison of Single-Mode Fiber Dispersion Measurement Techniques,"* J. Lightwave Tech. **3** (1985) 958-966.

[33] A. W. Snyder, and J. D. Love, *Optical Waveguide Theory* (Chapman and Hall, London, 1983).

[34] *Boe® Premixed Etchants: A Complete Range of Useful Thermal Oxide Etching Rates,* General Chemical Corporation (2000)

[35] Q. Y. Tong, Q. Gan, G. Fountain *et al.*, *"Low-Temperature Bonding of Silicon-Oxide-Covered Wafers Using Diluted Hf Etching,"* Appl. Phys. Lett. **85** (2004) 2762-2764.

[36] R. Amezcua-Correa, N. G. R. Broderick, M. N. Petrovich *et al.*, *"Optimizing the Usable Bandwidth and Loss through Core Design in Realistic Hollow-Core Photonic Bandgap Fibers,"* Opt. Express **14** (2006) 7974-7985.

[37] S. H. Autler, and C. H. Townes, *"Stark Effect in Rapidly Varying Fields,"* Phys. Rev. **100** (1955) 703-722.

[38] U. Fano, *"Effects of Configuration Interaction on Intensities and Phase Shifts,"* Phys. Rev. **124** (1961) 1866-1878.

[39] N. F. Ramsey, *"A Molecular Beam Resonance Method with Separated Oscillating Fields,"* Phys. Rev. **78** (1950) 695.

[40] J. C. Bergquist, S. A. Lee, and J. L. Hall, *"Saturated Absorption with Spatially Separated Laser Fields - Observation of Optical Ramsey Fringes,"* Phys. Rev. Lett. **38** (1977) 159-162.

[41] M. M. Salour, and C. Cohentannoudji, *"Observation of Ramseys Interference-Fringes in Profile of Doppler-Free 2-Photon Resonances,"* Phys. Rev. Lett. **38** (1977) 757-760.

[42] G. Alzetta, A. Gozzini, L. Moi *et al.*, *"Experimental-Method for Observation of Rf Transitions and Laser Beat Resonances in Oriented Na Vapor,"* Nouvo Cimento Soc. Ital. Fis. B-Gen. Phys. Relativ. Astron. Math. Phys. Methods **36** (1976) 5-20.

[43] R. M.]Whitley, and C. R. Stroud, *"Double Optical Resonance,"* Phys. Rev. A **14** (1976) 1498-1513.

[44] E. Arimondo, and G. Orriols, *"Non-Absorbing Atomic Coherences by Coherent 2-Photon Transitions in a 3-Level Optical-Pumping,"* Lettere Al Nuovo Cimento **17** (1976) 333-338.

[45] K. Bergmann, H. Theuer, and B. W. Shore, *"Coherent Population Transfer among Quantum States of Atoms and Molecules,"* Rev. Mod. Phys. **70** (1998) 1003-1025.

[46] F. T. Hioe, and J. H. Eberly, *"N-Level Coherence Vector and Higher Conservation-Laws in Quantum Optics and Quantum-Mechanics,"* Phys. Rev. Lett. **47** (1981) 838-841.

[47] U. Gaubatz, P. Rudecki, S. Schiemann *et al.*, *"Population Transfer between Molecular Vibrational Levels by Stimulated Raman-Scattering with Partially Overlapping Laserfields - a New Concept and Experimental Results,"* J. Chem. Phys. **92** (1990) 5363-5376.

[48] K. J. Boller, A. Imamoglu, and S. E. Harris, *"Observation of Electromagnetically Induced Transparency,"* Phys. Rev. Lett. **66** (1991) 2593-2596.

[49] O. A. Kocharovskaya, and Y. I. Khanin, *"Coherent Amplification of an Ultrashort Pulse in a 3-Level Medium without a Population-Inversion,"* JETP Lett. **48** (1988) 630-634.

[50] S. E. Harris, *"Lasers without Inversion - Interference of Lifetime-Broadened Resonances,"* Phys. Rev. Lett. **62** (1989) 1033-1036.

[51] S. E. Harris, J. E. Field, and A. Imamoglu, *"Nonlinear Optical Processes Using Electromagnetically Induced Transparency,"* Phys. Rev. Lett. **64** (1990) 1107-1110.

[52] C. Cohentannoudji, and S. Reynaud, *"Dressed-Atom Description of Resonance Fluorescence and Absorption-Spectra of a Multilevel Atom in an Intense Laser-Beam,"* J. Phys. B **10** (1977) 345-363.

[53] J. P. Marangos, *"Topical Review Electromagnetically Induced Transparency,"* J. Mod. Phys. **45** (1998) 471-503.

[54] U. Fano, *"Description of States in Quantum Mechanics by Density Matrix and Operator Techniques,"* Rev. Mod. Phys. **29** (1957) 74-93.

[55] H. Lee, and M. O. Scully, *"The Physics of Eit and Lwi in V-Type Configurations,"* Found. Phys. **28** (1998) 585-600.

[56] B. S. Ham, P. R. Hemmer, and M. S. Shahriar, *"Efficient Electromagnetically Induced Transparency in a Rare-Earth Doped Crystal,"* Opt. Communications **144** (1997) 227-230.

[57] A. V. Turukhin, V. S. Sudarshanam, M. S. Shahriar *et al.*, *"Observation of Ultraslow and Stored Light Pulses in a Solid,"* Phys. Rev. Phys. **88** (2002) 023602.

[58] M. S. Bigelow, N. N. Lepeshkin, and R. W. Boyd, *"Observation of Ultraslow Light Propagation in a Ruby Crystal at Room Temperature,"* Phys. Rev. Lett. **90** (2003) 113903.

[59] E. Cussler, *Diffusion: Mass Transfer in Fluid Systems* (Cambridge University Press, Cambridge, 1984).

[60] H. G. Robinson, E. S. Ensberg, and H. G. Demelt, Bull. Am. Phys. Soc. **3** (1958)

[61] M. Delabachelerie, K. Nakagawa, Y. Awaji *et al.*, *"High-Frequency-Stability Laser at 1.5 Mu-M Using Doppler-Free Molecular Lines,"* Opt. Lett. **20** (1995) 572-574.

[62] T. Zanon, S. Guerandel, E. de Clercq *et al.*, *"High Contrast Ramsey Fringes with Coherent-Population-Trapping Pulses in a Double Lambda Atomic System,"* Phys. Rev. Lett. **94** (2005) 193002.

[63] A. Nagel, L. Graf, A. Naumov *et al.*, *"Experimental Realization of Coherent Dark-State Magnetometers,"* Europhysics Lett. **44** (1998) 31-36.

[64] S. E. Harris, J. E. Field, and A. Kasapi, *"Dispersive Properties of Electromagnetically Induced Transparency,"* Phys. Rev. A **46** (1992) R29-R32.

[65] J. E. Field, K. H. Hahn, and S. E. Harris, *"Observation of Electromagnetically Induced Transparency in Collisionally Broadened Lead Vapor,"* Phys. Rev. Lett. **67** (1991) 3062-3065.

[66] M. Xiao, Y. Q. Li, S. Z. Jin *et al.*, *"Measurement of Dispersive Properties of Electromagnetically Induced Transparency in Rubidium Atoms,"* Phys. Rev. Lett. **74** (1995) 666-669.

[67] L. V. Hau, S. E. Harris, Z. Dutton *et al.*, *"Light Speed Reduction to 17 Metres Per Second in an Ultracold Atomic Gas,"* Nature **397** (1999) 594-598.

[68] F. Benabid, F. Couny, J. C. Knight *et al.*, *"Compact, Stable and Efficient All-Fibre Gas Cells Using Hollow-Core Photonic Crystal Fibres,"* Nature **434** (2005) 488-491.

[69] *Gas Reference Cells, (*http://www.thorlabs.com/newGroupPage9.cfm; accessed on 14 February, 2008)

[70] M. M. Grunina, *"Mathematical-Model for Estimating the Conditions for Filling Acetylene Cylinders,"* Chemical and Petroleum Engineering **30** (1994) 317-320.

[71] F. Sharipov, and V. Seleznev, *"Data on Internal Rarefied Gas Flows,"* J. Phys. Chem. Ref. Data **27** (1998) 657-706.

[72] C. I. Weng, W. L. Li, and C. C. Hwang, *"Gaseous Flow in Microtubes at Arbitrary Knudsen Numbers,"* Nanotechnology **10** (1999) 373-379.

[73] R. Thapa, K. Knabe, K. L. Corwin *et al.*, *"Arc Fusion Splicing of Hollow-Core Photonic Bandgap Fibers for Gas-Filled Fiber Cells,"* Opt. Express **14** (2006) 9576-9583.

[74] V. Dangui, M. J. F. Digonnet, and G. S. Kino, *"Determination of the Mode Reflection Coefficient in Air-Core Photonic Bandgap Fibers,"* Opt. Express **15** (2007) 5342-5359.

[75] F. Benabid, *"An Optical Assembly of a Hollow Core Fibre Gas Cell Spliced to Fibre Ends and Methods of Its Production,"* (Patent, PCT/GB2006/000229 (WO/2006/077437))

[76] P. Light, F. Couny, and F. Benabid, *"Low Optical Insertion-Loss and Vacuum-Pressure All-Fiber Acetylene Cell Based on Hollow-Core Photonic Crystal Fiber,"* Opt. Lett. **31** (2006) 2538-2540.

[77] S. Dushman, and J. M. Lafferty, *Scientific Foundations of Vacuum Technique* (John Wiley & Sons, New York, London, Sydney, 1962).

[78] B. K. Dutta, D. Biswas, B. Ray *et al.*, *"Semi-Classical Analysis of Helium Broadened Acetylene (Nu(1)+3 Nu(3)) Band Transitions Measured by a Nir Diode Laser Spectrometer,"* European Phys. J. D **13** (2001) 337-344.

[79] W. C. Swann, and S. L. Gilbert, *"Pressure-Induced Shift and Broadening of 1510-1540-Nm Acetylene Wavelength Calibration Lines,"* J. Opt. Soc. Am. B **17** (2000) 1263-1270.

[80] M. A. Bouchiat, and J. Brossel, *"Relaxation of Optically Pumped Rb Atoms on Paraffin-Coated Walls,"* Phys. Rev. **147** (1966) 41-54.

[81] H. G. Robinson, and C. E. Johnson, *"Narrow Rb-87 Hyperfine-Structure Resonances in an Evacuated Wall-Coated Cell,"* Appl. Phys. Lett. **40** (1982) 771-773.

[82] *Itu-T G.694.1*, International Telecommunication Union (2002)

[83] R. Felder, *"Practical Realization of the Definition of the Metre, Including Recommended Radiations of Other Optical Frequency Standards (2003),"* Metrologia **42** (2005) 323-325.

[84] G. B. B. M. Sutherland, *"The Infrared Absorption Bands of Acetylene,"* Phys. Rev. **43** (1933) 883-886.

[85] B. Girard, N. Billy, J. Vigue *et al.*, *"Evidence for a Dynamical Stark-Effect in Co(A1-Pi) 2-Photon Excitation,"* Chem. Phys. Lett. **102** (1983) 168-173.

[86] B. Girard, G. O. Sitz, R. N. Zare *et al.*, *"Polarization Dependence of the Ac Stark-Effect in Multiphoton Transitions of Diatomic-Molecules,"* J. Chem. Phys. **97** (1992) 26-41.

[87] M. A. Quesada, A. M. F. Lau, D. H. Parker *et al.*, *"Observation of Autler-Townes Splitting in the Multiphoton Ionization of H-2 - Measurement of Vibronic Transition Moments between Excited Electronic States,"* Phys. Rev. A **36** (1987) 4107-4110.

[88] J. B. Qi, G. Lazarov, X. J. Wang *et al.*, *"Autler-Townes Splitting in Molecular Lithium: Prospects for All-Optical Alignment of Nonpolar Molecules,"* Phys. Rev. Lett. **83** (1999) 288-291.

[89] A. M. Lyyra, H. Wang, T. J. Whang *et al.*, *"Cw All-Optical Triple Resonance Spectroscopy,"* Phys. Rev. Lett. **66** (1991) 2724-2727.

[90] J. Qi, F. C. Spano, T. Kirova *et al.*, *"Measurement of Transition Dipole Moments in Lithium Dimers Using Electromagnetically Induced Transparency,"* Phys. Rev. Lett. **88** (2002) 173003.

[91] J. Geabanacloche, Y. Q. Li, S. Z. Jin *et al.*, *"Electromagnetically Induced Transparency in Ladder-Type Inhomogeneously Broadened Media - Theory and Experiment,"* Phys. Rev. A **51** (1995) 576-584.

[92] E. Arimondo, in *Progress in Optics*, edited by E. Wolf (Elsevier Science and Technology, 1996), pp. 257-354.

[93] S. Ghosh, *"Resonant Optical Interactions with Molecules Confined in Photonic Band-Gap Fibers,"* Phys. Rev. Lett. **94** (2005) 093902.

[94] M. Erhard, and H. Helm, *"Buffer-Gas Effects on Dark Resonances: Theory and Experiment,"* Phys. Rev. A **63** (2001) 043813.

[95] M. Fleischhauer, A. Imamoglu, and J. P. Marangos, *"Electromagnetically Induced Transparency: Optics in Coherent Media,"* Rev. Mod. Phys. **77** (2005) 633-673.

[96] E. Figueroa, F. Vewinger, J. Appel *et al.*, *"Decoherence of Electromagnetically Induced Transparency in Atomic Vapor,"* Opt. Lett. **31** (2006) 2625-2627.

[97] R. W. P. Drever, J. L. Hall, F. V. Kowalski *et al.*, *"Laser Phase and Frequency Stabilization Using an Optical-Resonator,"* Appl. Phys. B **31** (1983) 97-105.

[98] S. Knappe, P. D. D. Schwindt, V. Gerginov *et al.*, *"Microfabricated Atomic Clocks and Magnetometers,"* J. Opt. A **8** (2006) S318-S322.

[99] J. Vanier, *"Atomic Clocks Based on Coherent Population Trapping: A Review,"* Appl. Phys. B **81** (2005) 421-442.

[100] S. Guerandel, T. Zanon, N. Castagna *et al.*, *"Raman-Ramsey Interaction for Coherent Population Trapping Cs Clock,"* IEEE Trans. Instr. and Meas. **56** (2007) 383-387.

[101] F. Benabid, P. S. Light, F. Couny *et al.*, *"Electromagnetically-Induced Transparency Grid in Acetylene-Filled Hollow-Core Pcf,"* Opt. Express **13** (2005) 5694-5703.

[102] M. Hennrich, T. Legero, A. Kuhn *et al.*, *"Vacuum-Stimulated Raman Scattering Based on Adiabatic Passage in a High-Finesse Optical Cavity,"* Phys. Rev. Lett. **85** (2000) 4872-4875.

[103] S. N. Atutov, V. Biancalana, P. Bicchi *et al.*, *"Light-Induced Diffusion and Desorption of Alkali Metals in a Siloxane Film: Theory and Experiment,"* Phys. Rev. A **60** (1999) 4693-4700.

[104] S. Ghosh, A. R. Bhagwat, C. K. Renshaw *et al.*, *"Low-Light-Level Optical Interactions with Rubidium Vapor in a Photonic Band-Gap Fiber,"* Phys. Rev. Lett. **97** (2006)

[105] R. Gary, *Vapor Pressure of the Chemical Elements* (Elsevier, Amsterdam, 1963).

[106] F. K. Gelmukhanov, L. V. Ilichov, and A. M. Shalagin, *"Kinetic-Theory of Light-Induced Drift of Gas Particles,"* Physica A **137** (1986) 502-530.

[107] H. G. C. Werij, J. P. Woerdman, J. J. M. Beenakker *et al.*, *"Demonstration of a Semipermeable Optical Piston,"* Phys. Rev. Lett. **52** (1984) 2237-2240.

[108] E. Mariotti, J. H. Xu, M. Allegrini *et al.*, *"Light-Induced-Drift Stationary States,"* Phys. Rev. A **38** (1988) 1327-1334.

[109] A. Ashkin, *"Acceleration and Trapping of Particles by Radiation Pressure,"* Phys. Rev. Lett. **24** (1970) 156.

[110] M. J. Renn, D. Montgomery, O. Vdovin *et al.*, *"Laser-Guided Atoms in Hollow-Core Optical Fibers,"* Phys. Rev. Lett. **75** (1995) 3253-3256.

[111] F. Benabid, J. C. Knight, and P. S. Russell, *"Particle Levitation and Guidance in Hollow-Core Photonic Crystal Fiber,"* Opt. Express **10** (2002) 1195-1203.

[112] C. Y. Ye, A. S. Zibrov, Y. V. Rostovtsev *et al.*, *"Unexpected Doppler-Free Resonance in Generalized Double Dark States,"* Phys. Rev. A **65** (2002) 043805.

[113] H. J. Metcalf, and P. van der Straten, *"Laser Cooling and Trapping of Atoms,"* J. Opt. Soc. Am. B **20** (2003) 887-908.

[114] J. Soding, R. Grimm, Y. B. Ovchinnikov *et al.*, *"Short-Distance Atomic Beam Deceleration with a Stimulated Light Force,"* Phys. Rev. Lett. **78** (1997) 1420-1423.